

Assessment of Blast Energy Usage and the Extent of Blast Damage in Hard Rock Open-pit Mines

By

Magreth Sungwa Dotto

A thesis submitted in partial fulfillment of the requirements for the degree of

Doctor of Philosophy

in

Mining Engineering

Department of Civil and Environmental Engineering

University of Alberta

© Magreth Sungwa Dotto, 2024

ABSTRACT

Blasting fragmentation influences the cost and productivity of downstream processes such as loading, hauling, crushing, and milling. Interaction between the rock mass and explosive energy determines blast outcomes. This research aims to enhance the understanding of the blasting process by examining key factors that influence blast outcomes specifically, the explosive strength, rock mass strength, and rock structures such as rock contacts and joints. The research estimates damage zones around blasthole and evaluates fragmentation patterns using the analytical approach and numerical simulation. These methods are applied to the data from an existing mining operation collected through laboratory tests and field measurements. The results are validated through comparisons with field measurements and estimations from other verified approaches.

Key findings of the research indicate that explosive selection is a crucial aspect of blast design and should be based on the rock mass properties and the desired outcomes. The formation and size of damage zones around the blasthole are influenced by the explosive's energy and rock mass strength. Stronger explosives are more effective in hard rock, creating longer and more extended fractures, while less powerful explosives result in a more uniform distribution of fractures in both soft and hard rocks, although with a reduced extent in hard rocks.

Structural properties influence how explosive energy and fractures are distributed in the rock mass. The propagation of stress waves at the interface between different rock types depends on the impedance difference between the rocks, the intensity of the incident stress wave, and its direction. When a stress wave moves from soft to hard rock, it is enhanced and attenuates in the opposite direction. Despite this attenuation, cracks can easily propagate from hard rock to soft rock.

In a jointed rock mass, the type and size of the infill material, along with fracture frequency, significantly impact how explosive energy and fractures are distributed. When comparing empty joints with clay-filled joints, the empty joints reflect most of the stress wave energy, whereas clay-filled joints allow better energy transfer. Energy transmission decreases as joint width and fracture frequency increase, leading to reduced fracturing: by 9% when fracture frequency increases from one to four and by 13% when joint width increases from 3 to 10 cm. Other factors like joint continuity, distance from the charge, and joint orientation and randomness further intensify these effects.

Blast design is the art of carefully balancing explosive strength, energy propagation, and confinement to maximize rock fracturing. This is achieved by selecting explosives that match the rock's strength and adjusting the pattern design and initiation sequencing and delays to maximize energy usage. Understanding how rock mass properties influence blast outcomes allows for better design adjustments. Common adjustments include changing explosive strength properties, increasing the powder factor, changing the pattern size, and varying initiation sequences and delays. The study found that increasing the powder factor by increasing the blasthole diameter did not improve fracturing in jointed rock masses. However, altering delays and sequencing significantly enhanced fracturing: 10% in intact rock, 14% in jointed rock, and 7% at rock contacts.

The research is valuable to the industry as it provides practical guidelines for blast design, particularly in complex rock masses where standard approaches may be insufficient. The insights gained offer a basis for refining predictive models and exploring innovative blasting techniques.

PREFACE

This thesis is an original work by Magreth Dotto under the supervision of Dr. Yashar Pourrahimian and Dr. Tim Joseph. A version of this thesis's chapters has been published as three journal papers and two conference papers. At the time of the publication of this thesis, the journal publications and conference papers with their status are as follows:

Peer-Reviewed Journal Papers

1. Dotto, MS., Apel, D., and Pourrahimian, Y. (2024), "Investigating the influence of discontinuity parameters on blast-induced fragmentation", *International Journal of Mining, Reclamation, and Environment*, 1-25. <https://doi.org/10.1080/17480930.2024.2347128>
2. Dotto, MS. and Pourrahimian, Y. (2024), "The Influence of Explosive and Rock Mass Properties on Blast Damage in a Single-Hole Blasting". *Mining*, 4(1), 168-88. <https://doi.org/10.3390/mining4010011>.
3. Dotto, MS., Pourrahimian, Y., Joseph, T., and Apel, D. (2022), "Assessment of blast energy usage and induced rock damage in hard rock surface mines", *CIM Journal*, 13(4), 166-80. <https://doi.org/10.1080/19236026.2022.2126924> .

Conference Papers

1. Dotto, MS. and Pourrahimian, Y. (2023), "The effects of rock mass properties on explosive energy in rock blasting" The Application of Computers and Operations Research in the Mineral Industry (APCOM 2023), Society for Mining, Metallurgy and Explosives (SME) June 25-28, Rapid City, SD.

2. Dotto, MS., Pourrahimian, Y., and Joseph, T. (2022), "Assessment of Blast Energy Usage and Induced Rock Damage in a Hard Rock Blasting", *48th Annual Conference on Explosives and Blasting Techniques*, International Society of Explosives Engineers (ISEE); Jan. 28 to Feb. 2, Las Vegas, Nevada.

Magreth Dotto has carried out all the work presented in this thesis. As a supervisor, Dr. Yashar Pourrahimian has reviewed all parts of the work.

This Thesis Is Proudly Dedicated To My Mother

Maria Mombo Majanga

(1963-2023)

May Your Loving Soul Rest in Eternal Peace.

ACKNOWLEDGMENT

I am thankful to those who supported me throughout my Ph.D. journey. I am immensely grateful to Dr. Yashar Pourrahimian and Dr. Tim Joseph for allowing me to work with them and for their immeasurable guidance, support, and encouragement throughout.

This research work would not have been possible without the funding from the graduate students' awards and scholarships at the University of Alberta, the University of Dar es Salaam, and the International Society of Explosives Engineers (ISEE).

My gratitude to the supervisory committee formed by my supervisor Dr. Yashar Pourrahimian, Co-Supervisor Dr. Tim Joseph, and Dr. Derek Apel, to the facility and technical staff in the Department of Civil and Environmental Engineering for their invaluable knowledge, technical support, and encouragement.

Special thanks to the management of Anglo Gold Ashanti - Geita Gold Mine and Shanta Gold - New Luika Gold Mine for allowing me access to the mines for data collection. I sincerely thank the geologists, engineers, technicians, and surveyors at Orica, Capital Drill, AECI Mining Explosives from GGM and Shanta mines for the technical support, expert insights, and accommodation during the visits. It was an absolute pleasure and honor to work with all of you.

I am thankful to fellow graduate students in and out of the Mining and Rock Science Development and Innovation Lab (MRDIL) and Mining Optimization Lab (MOL) for making my journey wonderful and memorable and to my community friends for their

love and understanding. Special thanks to the Kizito Family for always being there for me and my family. You are a true definition of love and community.

Lastly, I thank my awesome family, my lovely husband and best friend **Allen Matari** for his love, support, and patience throughout my studies. Without him, I would not have made it with our amazing sons Nathan and Nolan Matari. Thank you, my lovely parents: Baba Bernard Dotto Majanga (The HERO) and Mama Maria Mombo Majanga, and my mother-in-law Mary Matari, for your encouragement and prayers. To my siblings Albert, Benjamin, Edgar, Editha, Emelda, and Brigitha and your families, I acknowledge your love and support.

TABLE OF CONTENTS

ABSTRACT	II
PREFACE.....	IV
ACKNOWLEDGMENT	VII
LIST OF TABLES	XII
LIST OF FIGURES	XIII
LIST OF ABBREVIATIONS.....	XVI
CHAPTER 1	1
1.1 Background	2
1.2 Statement of the problem.....	4
1.3 Hypothesis	5
1.4 Summary of Literature Review	6
1.5 Objectives of the study.....	7
1.6 Scope and Assumptions of the Study.....	8
1.7 Research Methodology.....	9
1.8 Scientific Contributions and Industrial Significance of the Research.....	11
1.9 Organization of Thesis	12
CHAPTER 2	14
2.1 Introduction	15
2.2 Blast design and explosive properties	16
2.2.1 Blast design	17
2.2.2 Explosive properties	19
2.3 Explosive energy and detonation parameters	22
2.3.1 Explosive detonation and energy partition.....	23
2.3.2 Detonation parameters	25
2.4 Explosive energy interaction with the rock and formation of damage zones.....	28
2.4.1 Shock wave properties.....	30
2.4.2 Stress wave properties (parameters)	35
2.4.3 Loading rate dependency and fracture mechanisms of rock material	42
2.5 Blast damage prediction.....	44
2.5.1 Empirical/theoretical approach for damage zone prediction	45
2.5.2 Numerical approach for damage prediction	48
2.6 Summary of the chapter and Remarks.....	56
CHAPTER 3	58
3.1 Introduction	59
3.2 Determination of rock mass properties	59
3.3 Borehole pressure estimation	60

3.4	Analytical approach to estimate damage zones.....	61
3.5	A numerical approach to damage zone estimation	63
3.6	Summary and Conclusion	66
CHAPTER 4		68
4.1	Introduction	69
4.2	Blast parameters.....	69
4.2.1	Rock's physical and mechanical properties	69
4.2.2	Structural mapping	76
4.2.3	Point load test.....	77
4.2.4	Blast design and explosive properties.....	82
4.3	Blast monitoring	85
4.4	Analytical approach to estimating damage zones	88
4.4.1	Crushed zone estimation	89
4.4.2	Fracture zone estimation	92
4.5	Finite element modelling of blast-induced fragmentation.....	93
4.5.1	Determination of RHT model parameters	95
4.5.2	Explosive parameters.....	100
4.5.3	Damage mechanisms on the intact rock and model verification.....	100
4.5.4	Model validation	102
4.6	Full-scale model to 2D model comparison.....	104
4.7	Summary and Conclusion	106
CHAPTER 5		108
5.1	Introduction.....	109
5.2	Explosive properties.....	110
5.3	Explosive energy transmission through rock contacts.....	115
5.4	The effects of joint parameters on blast fragmentation	120
5.4.1	Joint infill material.....	120
5.4.2	Joint width and persistence	123
5.4.3	Joint distance from the blasthole	125
5.4.4	Joint orientation angle.....	127
5.4.5	Joint spacing (fracture frequency).....	129
5.5	Summary of the analysis	132
5.6	Comparison of results with fragmentation analysis	134
5.7	Chapter summary and conclusion.....	140
CHAPTER 6		142
6.1	Introduction	143
6.2	Blast-induced fragmentation modelling.....	144
6.2.1	Energy balance	144
6.2.2	Influence of rock mass properties	146
6.3	Initiation delays and sequencing.....	150

6.3.1 Intact rock delays analysis	152
6.3.2 Stress wave interaction and delays across rock contacts	156
6.3.3 Stress wave interaction across the joint.....	160
6.3.4 Initiation delays and sequencing summary.....	163
6.4 Chapter summary and conclusion	165
CHAPTER 7	168
7.1 Summary and conclusion	169
7.1.1 Limitations of the study	172
7.2 Contributions of the Research	173
7.3 Recommendations for Future Research.....	174

LIST OF TABLES

Table 2-1: Hugoniot Elastic Limit for Rock Materials.....	34
Table 4-1: P-wave speed measurements	72
Table 4-2: Brazilian tensile strength test results	73
Table 4-3: UCS and density for rock types	75
Table 4-4: Poisson’s ratio and Young’s modulus for rock types	75
Table 4-5: The joint sets summary	77
Table 4-6: Relationship between UCS and $I_{s(50)}$	80
Table 4-7: Estimated rock dynamic properties	82
Table 4-8: Blast design parameters.....	83
Table 4-9: Explosive properties.....	84
Table 4-10: VOD and explosive density measurements	85
Table 4-11: Vibration monitoring.....	88
Table 4-12: Input parameters to damage zone prediction.....	90
Table 4-13: Damage zones estimated	91
Table 4-14: Crushed zone parameters comparison	92
Table 4-15: Stemming parameters for soil material model	94
Table 4-16: Mechanical properties under various confining pressure.....	98
Table 4-17: RHT model parameters for BIF rock	99
Table 4-18: High explosive material model parameters and JWL constants for Fortis extra	100
Table 4-19: Results comparison with field measurements and estimations	104
Table 5-1: High explosive material model parameters and JWL constants for ANFO explosive	111
Table 5-2: Sandstone physical and mechanical properties	111
Table 5-3: Sandstone RHT material model parameters	112
Table 5-4: Air material parameters.....	120
Table 5-5: Clay material parameters.....	121
Table 5-6: Block reduction factor estimations	139

LIST OF FIGURES

Figure 1-1: Traditional blast improvement flowchart.....	5
Figure 1-2: Proposed blast improvement flowchart.....	5
Figure 1-3: Summary of methodology.....	10
Figure 2-1: Ideal detonation after Brinkmann (1990)	23
Figure 2-2: Non-ideal detonation after Brinkmann (1990)	24
Figure 2-3: Energy partition in blasting after Udy and Lownds (1990).....	24
Figure 2-4: Continuous VOD measurement with MREL’s Micro-Trap Data Recorder, after MREL (2022) ..	28
Figure 2-5: Zones around a blasthole (Damage Zone = crushed zone + fractured zone).....	30
Figure 2-6: Wave propagation in an interface.....	37
Figure 2-7: Wave propagation in two rock types, after Zhang (2016).....	40
Figure 2-8: Regression curve for compressive strength strain rate increase, after Xie et al. (2017)	43
Figure 2-9: Regression curve for tensile strength strain rate increase, after Xie et al. (2017)	43
Figure 2-10: P-Q equation of state after Borrvall and Riedel (2011).....	52
Figure 2-11: Stress limit surfaces and loading scenario after Borrvall and Riedel (2011)	53
Figure 3-1: Analytical approach to estimate damage zones.....	62
Figure 3-2: Numerical simulation flowchart	65
Figure 3-3: Consideration factors and design parameters in the blast-induced fragmentation model	67
Figure 4-1: Nyankanga pit pushback 8 design showing the study bench.....	70
Figure 4-2: Nyankanga Pit Cut 8 Bench 920_910 lithology distribution.	71
Figure 4-3: Uniaxial compressive strength test setup.....	74
Figure 4-4: Loading rate effect on UCS for DHP rock.....	76
Figure 4-5: The stereonet of the mapped structures.....	77
Figure 4-6: Specimen shapes suggested by ISRM 1985.....	79
Figure 4-7: Point Load Strength index test setup	80
Figure 4-8: Blast design layout.....	83
Figure 4-9: VOD measurement from blasthole EC3	84
Figure 4-10: Vibration monitoring shot NY8_910_04	86
Figure 4-11: Resultant peak particle velocity on Shot 910#4	87
Figure 4-12: Particle velocity attenuation with scaled distance.....	88
Figure 4-13: Damage zones estimated using the analytical approach	93
Figure 4-14: Full-size simulation model of an intact rock.....	96

Figure 4-15: Damage distribution from the simulation of single blasthole blasting	102
Figure 4-16: Comparison of the simulated pressure and PPV curves with field measurements	103
Figure 4-17: Stress wave comparison in full-scale and 2D simulation models	105
Figure 4-18: Damage distribution comparison for 3D and 2D simulation models	106
Figure 4-19: Pressure of stress wave at the free-face along burden and spacing.....	106
Figure 5-1: Pressure and PPV attenuations in soft and hard rock	114
Figure 5-2: Damage zone extents in soft and hard rock.....	114
Figure 5-3: Damage percentage distributions for various explosives and rocks.....	115
Figure 5-4: General models for the simulation of contacts between soft and hard rock	116
Figure 5-5: Pressure curves across the interfaces of soft and hard rock	117
Figure 5-6: PPV curves across the interface of soft and hard rock.....	118
Figure 5-7: Damage propagation beyond the contacts between soft and hard rock	119
Figure 5-8: The effect of empty joint and clay as joint infill material on the extent of damage.....	122
Figure 5-9: Cumulative damage distribution for empty joint and clay as infill material	122
Figure 5-10: Pressure across a 3 mm joint with clay and air-infill materials.....	123
Figure 5-11: Damage distribution and pressure curves for 3 cm and 10 cm joint widths	124
Figure 5-12: Variability in stress and damage distribution with joint continuity.....	125
Figure 5-13: Damage distribution for variable joint distances from the blasthole.....	126
Figure 5-14: Influence of joint orientations on damage distribution	128
Figure 5-15: Joint dipping angle and its effect on fracturing.....	129
Figure 5-16: Fracture frequency and joints randomness influence on rock mass fracturing	131
Figure 5-17: Summary of the effect of joint parameters on rock mass fracturing.....	134
Figure 5-18: Blast movement from tie-up plan	135
Figure 5-19: Mapped structures on Shot 910_6.....	136
Figure 5-20: Locations for fragmentation analysis with associated structures	137
Figure 5-21: Fragmentation sample set analysis.....	138
Figure 5-22: Fragmentation along burden in various monitoring locations	139
Figure 6-1: Pressure attenuation comparison for various rock masses	147
Figure 6-2: Damage distribution on various rock mass properties and the effect of PF increase	149
Figure 6-3: Damage intensity with delays for the intact rock.....	152
Figure 6-4: Velocity vectors between blastholes for various initiation delays	153
Figure 6-5: Stress curves mid-bench for various initiation delays.....	153
Figure 6-6: Stress curves around the blastholes for various initiation delays.....	154

Figure 6-7: Damage extents and interference illustration for various initiation delays.....	155
Figure 6-8: General model for rock contacts analysis.....	156
Figure 6-9: Damage distribution when firing from hard rock to soft rock at various delays.....	156
Figure 6-10: Borehole peak stresses and overall damage for hard to soft initiation sequence.....	157
Figure 6-11: Damage distribution with the interface is close to soft rock and firing from soft to hard....	158
Figure 6-12: Blasthole peak stresses and damage when firing from soft to hard rock.....	158
Figure 6-13: Damage distribution when firing from soft to hard rock with a longer interface.....	159
Figure 6-14: Borehole peak stresses and damage on a longer interface firing from soft to hard rock	160
Figure 6-15: Damage extents across the joint for various delays and sequence	161
Figure 6-16: Damage extents comparison when changing firing sequence across a clay joint.....	162
Figure 6-17: Pressure contours for 1 ms delay when changing firing sequence through an empty joint .	162
Figure 6-18: Damage extents for various delays and sequences with air joint on adjacent blastholes ...	163
Figure 6-19: Damage across an empty joint in various firing sequences and delays	163
Figure 6-20: Summary of damage variations in variable rock masses for various delays and sequence .	164

LIST OF ABBREVIATIONS

Parameter	Definition
ALE	Arbitrary Lagrangian-Eulerian
ANFO	Ammonium Nitrate Fuel Oil
ASTM	American Society for Testing and Materials
BRF	Block Reduction Factor
DEM	Discrete Element Method
DIF	Dynamic increase factor
EOS	Equation of State
FEM	Finite Element Method
HEL	Hugoniot Elastic Limit
HJC	Holomquist–Johnson–Cook
ISRM	International Society for Rock Mechanics
JWL	Jones-Wilkins-Lee
PF	Powder factor
PPV	Peak particle velocity
PVS	Peak vector sum
RBS	Relative bulk strength
REE	Relative Effective Energy
RHT	Riedel–Hiermaier–Thoma
RWS	Relative weight strength
SD ₂	Square root scaled distance
UCS	Uniaxial compressive strength
USBM	United States Bureau of Mines
VOD	Velocity of detonation

CHAPTER 1

INTRODUCTION

Chapter 1 is an introduction to the research thesis, offering an overview of the background, problem statement, a summary of pertinent literature, the objectives of the study, and its existing limitations. Additionally, it presents a detailed explanation of the research methodology employed and highlights the innovative contributions made by this work. In the end, the organization of the thesis is outlined.

1.1 Background

Fragmentation by blasting is a key process in hard rock mining. The approach to blasting has evolved with time from being just an effective rock-breaking mechanism to accommodating the need for downstream processes and protecting the integrity of the remaining structure. Blasting is considered the first step in comminution, which is cheaper and more efficient than crushing and grinding. Effective blast design and implementation are connected to downstream processes' economy and technical success. Good fragmentation is linked to easier loading, improved cycle times, less equipment wear and tear on load and haul, as well as lower energy consumption and improved throughput in crushing and milling.

The rock mass is an anisotropic and heterogeneous medium. Due to the complex nature of the rock mass and blast process, the use of standard blast design (rule of thumb) leads to unsatisfactory outcomes. Each rock mass is unique, but some features influence the blast energy similarly, leading to similar outcomes. Having analyzed these features and their influence on blast results, they can be incorporated into the blast design to achieve better outcomes.

Conventionally, blasting in mines is designed to break the rock into a manageable size for trucks and shovels, typically aiming for fragmentation smaller than 1/3 of the shovel bucket's lip length, while also minimizing the costs associated with drilling and explosives. In this process, the blast design is tailored to the specific rock type being blasted, with design parameters adjusted to achieve an average powder factor usually determined based on previous experience or professional judgment. Mine-to-mill optimization studies have transformed blast efficiency focus to include minimization of comminution costs and increase overall mine productivity. These studies have shown that it is possible to improve downstream processes and costs by improving

blast designs (Kanchibotla et al., 1999, Nielsen and Malvik, 1999, McKee, 2013). To enhance blast outcomes, it is crucial to have a grasp on the rock mass and how it interacts with the energy released during blasting.

Blast energy is typically divided into shock wave energy, pulse energy, and gas pressure, which are essential for initiating cracks and fragmenting rock. The energy partitioning depends on the properties of the explosive and the conditions during detonation. The term "shock wave pressure" is commonly used to describe the intensity of pressure and stress waves generated by explosive detonation, which propagate through the rock mass, causing fracturing and fragmentation. In this study, shock wave pressure will primarily be referred to as explosive energy.

The use of explosive energy to fragment rock is a complex process, influenced by high-stress levels, rapid loading rates, and the variable properties of the rock mass. Blast-induced fragmentation studies for over three decades aimed to improve understanding and provide theories on the interaction between rock mass and blast energy (Blair and Minchinton, 1997, Sun, 2013, Bhandari, 1996). The areas of interest have been the non-ideal detonation of commercial explosives used in blasting, the response of rock mass to higher stresses and loading rates, and the effect of structures.

Rock properties such as in-situ rock mass strength, density, elastic constants, and the nature of discontinuities, their frequency, and orientations contribute significantly to the blast outcomes, predominantly the fragmentation and stability of the remaining rock mass. Past researchers have observed that in brittle material such as rock, the confining pressure and loading rates alter the rock strength and fracture mechanism (Zhang et al., 2000, Kimberley et al., 2013). Rock strength and density govern the intensity of stress wave required to cause fracturing, while the nature and

properties of discontinuities influence wave propagation, its attenuation in the rock mass, cracks propagation, and gas pressure effectiveness. This thesis aims to understand the influence of variable explosive and rock properties, such as rock strength and structures like rock contacts and joint parameters, on blast-induced damage to predict blast outcomes. The findings of this thesis offer valuable insights into the blasting process and can be used to improve blast fragmentation prediction models and guide blast design for various rock masses and explosive properties, as outlined in Section 1.2.

1.2 Statement of the problem

Designing an effective blast in mining is challenging due to the complex nature of the rock mass and the complicated interaction between explosive energy and the rock, particularly when structural features are present. Higher stress levels and loading rates during blasting cause the rock to break at greater strengths. The presence of structural features can alter the distribution of explosive energy, leading to variable outcomes. To achieve good blast results, it is crucial to thoroughly understand the blasting process and the influence of these structures and to incorporate this knowledge into the blast design.

Over the years, drill and blast improvements have been focused on improving rock fragmentation, minimizing structures damage, and environmental impacts. Traditional blast design incorporates geological, structural, and explosive properties as input parameters while adjusting the pattern size and occasionally the type of explosive, sequencing, and firing delays to meet specific objectives. This improvement process is illustrated in a flowchart presented by Hustrulid (1999) in Figure 1-1. Design parameters have traditionally been adjusted based on professional experience or trial and error. However, with recent technological advancements, computer

modeling has largely replaced this approach. Now, design parameters are simulated until they produce acceptable outcomes before being implemented in the field with validation and refinement done after the blast.

Several methods have been developed to predict blast outcomes, ranging from empirical approaches (Cunningham, 2005, Ouchterlony, 2005) to numerical models (Esen et al., 2003). However, these methods often overlook or generalize the properties of the rock mass (Ohadi, 2018). Each rock type is unique in its physical, mechanical, and structural properties, which influence fracturing and energy propagation in different ways. Understanding these unique rock properties and how they affect the rock mass interaction with explosive energy is essential for accurately predicting blasting outcomes and designing effective blast strategies. This can be achieved by thoroughly characterizing the rock mass and the explosive energy produced and assessing their interaction as proposed in a modified flowchart in Figure 1-2.

1.3 Hypothesis

Rock mass properties and the desired outcomes dictate explosive selection and blast design. Variability in physical and mechanical properties of rock mass governs how it responds to blast energy from explosive detonation, energy usage in rock fragmentation, and attenuation in the rock mass, which define the overall outcomes. The complexity of rock mass and limited understanding of rock response to higher stresses and loading rates have limited blast energy studies to intact and homogeneous rock masses.

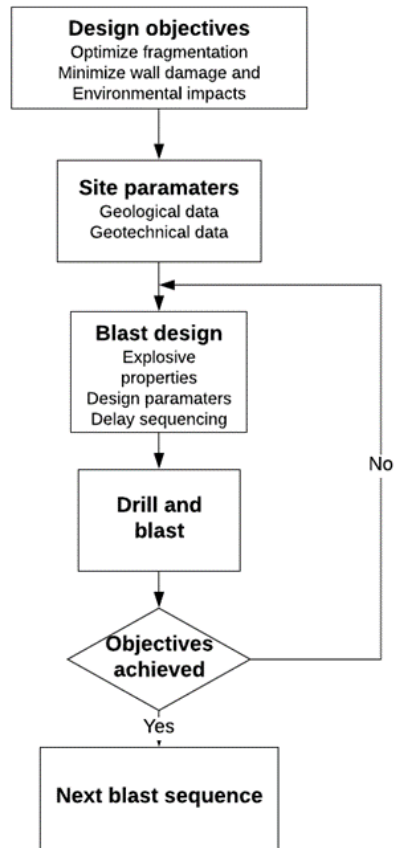


Figure 1-1: Traditional blast improvement flowchart

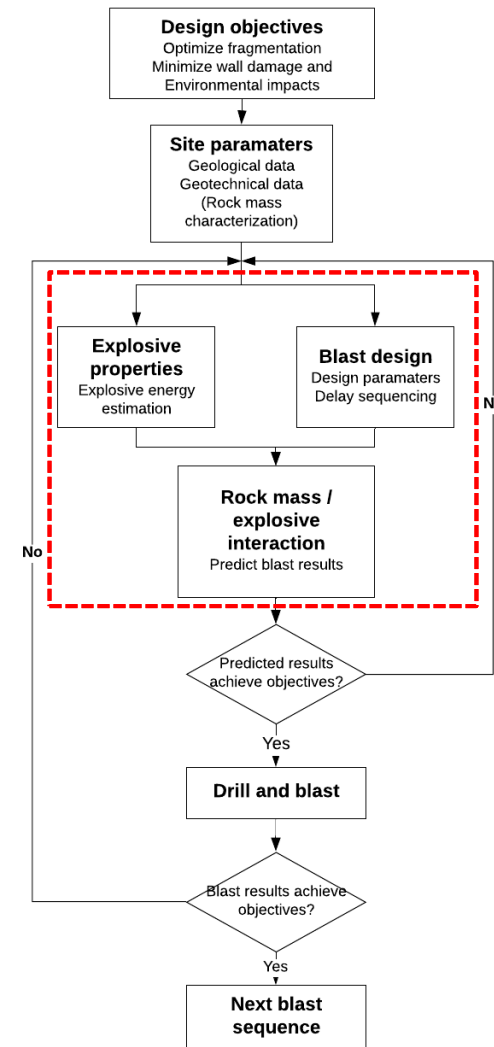


Figure 1-2: Proposed blast improvement flowchart

This research demonstrates that integrating rock mass properties enhances understanding of how energy is used in fragmenting rock and hence enables blast results prediction. Estimating the energy available at any distance from the charge requires the knowledge of explosive properties, intact rock properties, and properties of encountered discontinuities. In other words, a rock mass's variability can lead to different blast outcomes if the same explosive with the same energy properties is used in the same blast design.

1.4 Summary of Literature Review

A comprehensive literature review is available in Chapter 2. Chapter 2 covers relevant studies on stress wave properties and blast-induced fracturing. The review includes a discussion of controllable factors of rock blasting, such as blast design, explosive properties, and initiation type and sequence, and how they can be used to improve fragmentation. It also covers the discussion of uncontrollable factors such as rock physical and mechanical properties, presence and distribution of structures, their influence on blast outcomes, and how they are currently accommodated during the blast design.

Most studies aimed at improving blast-induced fragmentation have primarily focused on intact rock blasting. For heterogeneous and jointed rock masses, improvements in blast designs are often achieved through experience or trial and error. The common engineering tools currently used to predict fragmentation from blasting tend to overlook the presence and properties of encountered structures. Since each rock property is unique and affects blasting energy distribution and the outcomes differently, it is crucial to analyze each property independently, understand their combined influence, and incorporate them into the blast design process.

Blast fragmentation is subjected to higher confinement and loading rates where the rock can withstand higher forces before failure, altering the fracture toughness, strength, and mechanisms. Strain rate (measured in per second, s^{-1}) which is the rate at which rock deformation (strain) occurs under stress governs material behavior, especially under conditions of higher deformation. Rapid changes in material behavior are observed beyond the critical strain rate which is studied to be $10 s^{-1}$ (Zhang and Zhao, 2014). Most laboratory tests in the field are conducted under quasi-static loading. The review presents the range of strain rates experienced during blasting from previous studies and the relationships to estimate rock dynamic properties from the values obtained under static loading.

Several approaches are currently used to estimate damage zones around the charge and predict fragmentation distribution ranging from experimental, empirical/analytical approaches, numerical simulations, and with the improvements of computer power the use of machine learning and artificial intelligence. This study uses the analytical approach and finite element numerical simulation to investigate the effects of variable explosive and rock mass properties on the extent and intensity of fracturing in the rock mass. Both approaches are reviewed in depth in Chapter 2.

1.5 Objectives of the study

The primary aim of this thesis is to study the influence of variable explosive and rock mass properties on the distribution and utilization of explosive energy in order to quantify blast-induced damage. The analytical approach utilizes rock mass properties, borehole pressure, and its attenuation from the blasthole (as measured through vibration monitoring) to estimate the extent of fractures and damage zones. This estimation considers the ability of stress waves to induce fracturing and the relevant fracture mechanisms.

Estimating the limit of effective energy in causing fracturing accurately is crucial for determining design parameters. Such analysis informs decisions on explosive selection, pattern size, and blasthole sequencing to achieve the desired outcomes and optimize the use of explosive energy. The results can also be used to develop a model for predicting blast-induced fragmentation. To extend this analysis, numerical modeling is employed, particularly because the analytical approach has limitations in assessing the influence of rock properties and structures. Numerical modeling is used exclusively in this section.

The specific objectives of this study are as follows:

1. To estimate the energy generated from the explosive detonation in a blasthole.
2. To seek a correlation between the explosive energy and the rock mass damage induced.
3. To estimate damage zones around the blasthole and assess the variation in damage for various explosive and rock mass properties.
4. To model blast-induced fragmentation and investigate techniques to improve fracturing in intact rock, across contacts between hard and soft rock, and in jointed rock masses.

The ultimate goal of this study is to accurately estimate the damage around the charge, explain the interaction between explosive energy and the rock mass, provide insight into blast outcomes, and present techniques to maximize fracturing across variable explosives and rock masses.

1.6 Scope and Assumptions of the Study

Although there are many methods to estimate damage from explosive energy, this study focuses on assessing stress wave attenuation and estimating damage potential based on peak particle velocity (PPV), pressure, and dynamic stress experienced by the rock. Data from a hard rock open-

pit mine was analyzed to study the influence of rock mass characteristics and explosive energy on stress wave propagation and fracture extension. Stress wave monitoring depended on far-field vibration measurements, though this method has limitations in accurately predicting stress wave attenuation near the blasthole.

Since fragmentation by blasting involves multiple mechanisms and variables, a series of laboratory tests and field measurements were conducted in the field to characterize the rock mass and estimate explosive energy. Due to the inability to perform high-loading rate rock strength tests, empirical formulas were used to estimate rock strengths under dynamic loading conditions. Additional insights into rock mechanical properties were obtained from lab tests conducted at the University of Alberta's Surface Mining Research Lab. The results are provided in APPENDIX B of this study.

Due to the unavailability of testing equipment, laboratory tests using explosives could not be performed either in the field or in the university laboratory. Instead, explosive properties reported by manufacturers or estimated from studies of similar explosives were used to estimate explosive energy in both the analytical approach and numerical modelling. Similarly, established empirical equations were employed to estimate damage zones around the charge in the analytical approach, with efforts made to understand the methods used to develop them, and make necessary modifications where appropriate.

1.7 Research Methodology

To achieve the objectives of this study, the methodology outlined in the flowchart in Figure 1-3 was applied in a hard rock open-pit mine for analysis and validation of the study's approaches.

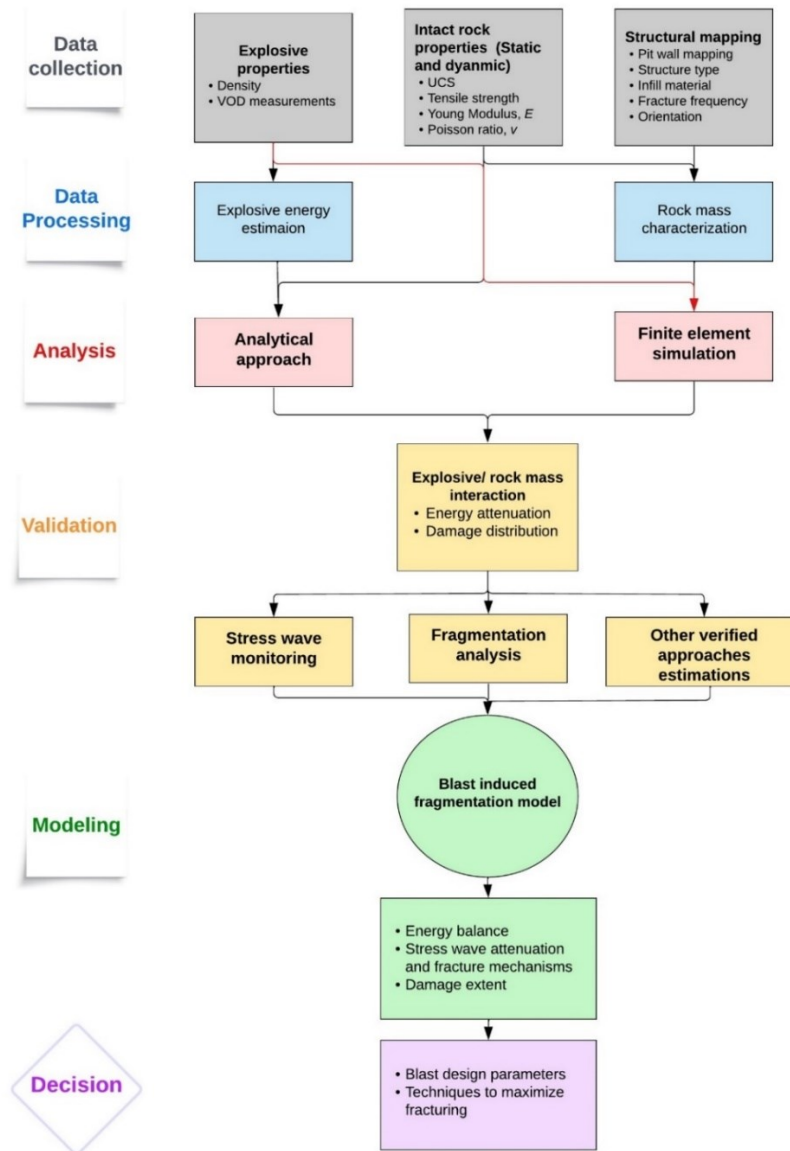


Figure 1-3: Summary of methodology

The methodology is divided into several steps: estimating blast energy, characterizing the rock mass, assessing failure mechanisms, and evaluating rock damage. Key aspects of the study include estimating blast energy based on explosive density and VOD measurements, evaluating the interaction between explosive energy and the rock using both the analytical approach and finite element simulation to aid the prediction of damage zones, and finally, formulating a blast-induced fragmentation model.

Energy attenuation, crack propagation, and the extent of damage zones around a blasthole are investigated in both analytical and numerical approaches. Field measurements, including stress wave monitoring and the analysis of fragmentation distribution, are performed to validate the models. Various explosive strengths and rock mass properties are assessed through finite element simulation to understand their influence on blast outcomes. The analysis is then used to provide an overview of the blast-induced fragmentation model, including steps for selecting design parameters and techniques to improve fracturing.

1.8 Scientific Contributions and Industrial Significance of the Research

Blasting is a critical operation in hard rock mining. The size distribution of fragmentation resulting from blasting directly impacts overall mine productivity, energy consumption, and comminution-related costs. Approximately 67% of the total mine processing costs are estimated to be associated with comminution (Spathis, 2015). Optimized blast design, achieved through an understanding of the interaction between explosive energy and the rock mass, can significantly enhance the productivity and cost efficiency of mine operations.

Blast outcomes are highly influenced by the characteristics of the encountered rock mass. This study expands the understanding of rock mass behavior under high stresses and loading rates, as well as the effects of explosive strength and structural properties, which play a crucial role in defining blast outcomes. The findings of this research could enhance the prediction of blast outcomes through computer modeling, including machine learning and artificial intelligence, and provide valuable insights into the blasting process, leading to improved blast designs. Specific contributions of the research are presented in Chapter 7.

1.9 Organization of Thesis

Chapter 1 of this thesis mainly contains background information, research objectives, a description of the gap the research is going to address, and the scope and assumptions of the study. A brief description of the research methodology is also presented.

Chapter 2 contains the literature survey, which outlines the major concepts and theories on rock mass fragmentation by blasting. It covers the fundamental parameters affecting blast outcomes, including explosive energy production, propagation, and attenuation in variable rock masses. This chapter also discusses the shortcomings of current approaches in predicting fragmentation and estimating damage zones. The two approaches used in this study are discussed in detail, including the concepts behind the formulations.

Chapter 3 presents the methodology used to achieve the objectives of this study. It details the data collection process from laboratory tests and field measurements, as well as the subsequent analysis of this data. The chapter also explains how the collected data is utilized in numerical modeling and analytical approaches to estimate the damage zones around blastholes.

Chapter 4 presents the data collection process and the estimation of parameters that cannot be measured directly in the field. This chapter also covers the estimation of damage zones using both analytical and numerical approaches, along with the verification and validation of these methods.

Chapter 5 analyzes the explosive strength properties and their influence on the fracturing of various rock masses. The rock mass varies in rock strength and structural properties, mainly the contact of soft and hard rock and the various joint/discontinuity properties. The insights gained from this analysis are used to explain the variability in fragmentation observed in field blasts.

Chapter 6 builds on the analysis from Chapter 5 by presenting the steps and considerations for modeling blast-induced fragmentation in variable rock masses. It also explores techniques to maximize fracturing when various rock properties are encountered in heterogeneous rock mass.

Finally, Chapter 7 provides a summary of the research, discusses the contributions made by this study, and offers suggestions for future work.

CHAPTER 2

LITERATURE REVIEW

This chapter outlines the major concepts and theories on rock mass fragmentation by blasting. It covers the fundamental parameters affecting blast outcomes such as explosive energy production and propagation, attenuation in variable rock masses, and the expected outcomes i.e. fragmentation distribution and pit wall formation.

2.1 Introduction

Energy consumption is a major capital and operating cost in mineral beneficiation. In the mine-to-mill optimization strategy, blasting is considered the first step in comminution, and its performance impacts the energy consumption and efficiency of the downstream processes. Conventionally, blast patterns are designed to break the rock mass within the boundaries of the shot to achieve the desired fragmentation size distribution while preserving the integrity of the pit wall. In mine-to-mill optimization, the focus extends beyond just mining, where the whole system economics is evaluated to come up with a design that ensures maximum shock/heave energy use and overall minimum cost.

There is substantial evidence that investing in blasting reduces overall costs and improves mining, crushing, and milling productivity. Cottee (2001), Tosun et al. (2012), and Brunton et al. (2003) determined that the productivity, power consumption, and general performance of a mining system are dependent on the fragmentation size distribution and muck-pile looseness achieved by blasting. Increasing the powder factor up to a certain threshold leads to improved fragmentation, resulting in better loading productivity, lower excavation and comminution costs, and reduced equipment wear and tear. However, the balance between increasing explosive energy and the benefits to downstream processes must be carefully analyzed. If not, these benefits may not be realized. For instance, once the loading equipment reaches its capacity, additional drilling and blasting costs may not be justified by the marginal increase in productivity. Additionally, ore losses can occur when finer fragments sink and are left behind on the bench floor.

Michaux and Djordjevic (2005) observed increased crusher and mill performance by increasing explosive energy, which was attributed to the increase in fragmentation and blast-induced pre-

conditioning. The study by Scott et al. (1999) observed an increase of over 10% in mill throughputs when the powder factor was increased by 50%. Further increases failed to produce benefits and instead increased the critical size of material in the mill.

Rock mass properties are of particular interest when it comes to blast outcomes. Several approaches have been developed to explain the blasting mechanisms, provide insight into underlying physical processes, and predict blast outcomes ranging from empirical methods (Kuznetsov, 1973, Cunningham, 2005, Ouchterlony, 2005), experimental blasts (Bhandari, 1996), numerical modelling (Furtney et al., 2009, Dehghan Banadaki and Mohanty, 2012) to machine learning and artificial intelligence techniques (Amoako et al., 2022, Nguyen et al., 2022). Although these approaches are useful in understanding the influence of blast design parameters on blast outcomes, the influence of rock mass properties is often overlooked or generalized.

This chapter reviews the theories and concepts related to rock breakage by explosive energy, with a focus on the factors that influence the process. It examines key elements such as explosive properties, the detonation process, design parameters, and the effects of high loading rates and rock structures on stress wave propagation and fracturing. Additionally, the chapter discusses the approaches used in this study and their formulation, providing a broad understanding of the mechanics of blast-induced rock breakage.

2.2 Blast design and explosive properties

Blast performance depends on the design parameters (blasthole diameter, depth, spacing, burden, charge column, and stemming height and material), explosive properties, the powder factor, initiation sequence and delays, and rock properties. Since rock properties cannot be changed and

the desired outcomes define the blast performance, blast improvements are limited to varying design parameters, explosive properties, and blasthole initiation and sequencing.

2.2.1 Blast design

Blast design parameters define the boundaries the explosive charge is expected to break depending on the explosive strength and rock characteristics. The blast performance is evaluated by how efficiently the explosive energy is used to fragment the rock. Due to the low reaction rate, the performance of commercial explosives depends on the blasthole diameter and confinement. Each explosive has a critical diameter, the smallest diameter at which the reaction can sustain itself once the explosive is detonated. An increase in explosive diameter increases its detonation velocity (VOD) until the ideal detonation velocity is reached.

The energy level and distribution depend on the blasthole diameter, which limits the amount of explosive per hole and governs the decision on the burden size, spacing, and stemming height. The energy distribution is essential to achieving the required fragmentation distribution. Smaller diameters with smaller burdens improve explosive energy distribution than bigger ones, though this option can be costly and less practical for operations with higher production requirements.

The burden distance is defined as the distance between rows or the distance between the charge and a free face, and spacing is the distance between holes in the direction perpendicular to the burden. The burden should equal the length of radial cracks formed from the explosion to achieve the desired fragmentation. Less burden distance can result in flyrock, air blast (venting), and finer fragmentation than required wasting a significant amount of explosive energy. Higher burden distance, on the other hand, causes excessive ground vibrations, poor fragmentation, and less

muckpile movement leading to hard digging. Spacing is usually greater than the burden to allow rock movement along the burden; it usually ranges from 1.1 to 1.5 times the burden.

The depth of a blasthole depends on the bench height, and the sub-drill is usually drilled to achieve a smooth floor on the lower bench. The top of the hole is usually filled with stemming material to contain explosive energy. The gas pressure has to be contained long enough to expand and extend cracks and displace rock before venting. It is believed that shockwaves are responsible for radial cracks within 20 to 30 times the blasthole diameter; more fragmentation is created by the expansion of gases into cracks, making the confinement necessary (ISEE, 2011). Insufficient stemming height may cause premature venting of explosive gases and fly rocks, while excessive stemming reduces explosive energy distribution, resulting in poor fragmentation around the collar. The stemming height usually ranges from 18 to 30 times the blasthole diameter. Scott et al. (1999) suggested that the crushed rock used as stemming material should be of a size ranging from 0.04 to 0.06 times the blasthole diameter. It is important to note that rock mass geological and structural features can contribute significantly to defining energy confinement ability.

A free face (free surface) is required for a blasted rock to move and expand as well as for the reflection of shockwaves, which, when strong enough, cause further fragmentation. The size of the burden and firing sequence is important in ensuring a balance between confinement and relief and hence controlling flyrock and vibrations, rock movement, and the degree of fragmentation (ISEE, 2011). Proper timing should ensure minimum interference and adequate fracturing between holes, which means there should be enough time for the predecessor hole to break and loosen the rock before the next charge. Lopez et al. (1995) explained that the fragmentation increases with each row fired at an interval because the radial cracks around the explosive column are almost

totally formed before the next row is detonated, creating a more free face. It is essential to determine the optimum delay, which is the function of the rise and duration of the stress pulse, the stress wave speed, and crack propagation in the rock mass (Saadatmand Hashemi and Katsabanis, 2020).

The powder factor represents the amount of explosive required for a unit volume of rock to be blasted. For the given type of explosive, the decision on powder factor depends on rock properties, particularly compressive strength, toughness, and joint structure, and usually ranges from 0.25 to 1.0 kg/m³ (Gokhale, 2011). While the powder factor increases with the increase in rock mass strength, with more free faces or when blasting in a more fractured rock mass powder factor can be lowered. The weight of the explosive per hole depends on the length of the charge column, coupling ratio, and loading density, which is the weight of charge per unit length of the blasthole. Loading density is a function of explosive density and the blasthole diameter. The coupling ratio influences energy transfer to the blasthole wall and is commonly used in controlling energy, especially in pre-split blasts.

2.2.2 Explosive properties

Explosives have been a primary method of breaking and loosening rock in hard rock mining. When properly initiated, explosives are converted into gases at very high temperatures and pressure, causing extremely high strain on the rock. Variable proportions of shock energy and gas pressure released from the detonation depend on the explosive composition and the quantity, which also define their ability to fragment and displace rock. Surface mines use bulk explosives initiated by high explosive primers (detonators or boosters). Bulk explosives are categorized into four main

groups: ANFO types (blasting agents), water gel, emulsion, and slurry explosives. In this review, only ANFO and emulsions are covered.

The most common way of comparing explosive strength is through their effective energy, which is the calculated theoretical total energy released. The relative weight strength (RWS) and relative bulk strength (RBS) are calculated as the total energy produced per unit mass or volume of explosives compared to the weight strength of equal weight or volume of standard ANFO. Most fragmentation prediction models use RWS to define explosive strength/ability to fragment the rock. Such analysis can be inaccurate since RWS does not account for the proportions of shock energy or gas pressure released, which play distinctive roles in actual fragmentation.

Explosive properties such as VOD, detonation pressure, and total energy produced differentiate one explosive type from the other and influence their selection for particular applications. Energy release depends on how the explosive is formulated, primed, confined, and protected from external influences. The explosive performance depends on the energy release rate and its effectiveness in fragmenting the rock mass (ISEE, 2011). The role of blast design is to ensure the effective use of explosive energy to fragment the rock mass and the safety of the structures while mitigating losses in the form of excessive air overpressure, ground vibrations, and the generation of excessive fines.

The theoretical energy applied per unit rock for commercial explosives ranges from 0.42 – 1.88 kJ/kg. Energy has to be high enough to overcome rock tensile strength and generate pressure high enough to expand and extend fractures. Elements must completely oxidize for higher energy generation, i.e., carbon has to be completely converted to carbon dioxide, hydrogen to water, and solid nitrogen to gaseous nitrogen. Excess oxygen from less fuel results in the formation of

nitrogen oxides, which reduces the reaction's energy. While the formation of nitrogen gas generates energy, the formation of nitrogen oxides absorbs energy. On the other hand, oxygen deficiency due to a high proportion of fuel results in the formation of carbon monoxide and free carbon with less than ideal energy. Too much fuel causes up to 6% less energy, while less fuel (formation of nitrogen oxides) causes up to 42% energy loss (Konya and Walter, 1991).

Explosive density controls the amount of explosives that can be charged in the hole. The density also affects performance characteristics such as critical diameter, sensitivity, and VOD. Most explosives' densities range between 800 to 1,350 kg/m³. Ammonium nitrate is a common ingredient in explosives. Standard ANFO is a mixture of ammonium nitrate prills (AN) and fuel oil (FO) at a weight ratio of 94.5:5.5 respectively and 800 kg/m³ density (ISEE, 2011). The energy output depends on oxygen balance. A decrease in particle size of ammonium nitrate prills increases the density and velocity of detonation which is the speed at which the detonation wave travels through a charge column. Above 1,200 kg/m³ ANFO sensitivity decreases. The description of the ANFO reaction is presented in APPENDIX C2.

Emulsions are homogeneous explosive mixtures composed of finely dispersed ammonium nitrate solution in fuel oil, widely used in mining, quarrying, and construction for rock blasting. The fine particle size of the oxidizer and its intimate mixing with the fuel oil lead to a higher velocity of detonation and, consequently, more energy output. Emulsions can be mixed with ANFO to create heavy ANFO, offering higher density and energy output. The optimal emulsion/ANFO ratio ranges from 35% to 40%. To improve water resistance, the emulsion percentage in the mixture should exceed 50% (Evans and Taylor, 1987).

The VOD for commercial explosives ranges from 3,000 m/s to 7,600 m/s. Explosives with the same weight strength can perform differently during the blast if they have different VOD. VOD determines the detonation pressure and shock energy produced by the explosive. Explosives with higher VOD have higher shock energy and less gas energy, making them suitable for massive homogeneous rock masses. The maximum/ideal VOD can be achieved by the size of the reaction zone and confinement. With the increased reaction zone, the relief wave behind the detonation front slows down so that the energy produced does not support the detonation wave, hence lowering VOD. Particle size determines the reaction zone; with increased particle size, the size of the reaction zone increases and hence lower VOD. An increase in confinement and charge diameter decreases lateral losses on the curvature, resulting in higher VOD (ISEE, 2011).

2.3 Explosive energy and detonation parameters

Explosive energy is released during detonation, a rapid self-sustaining exothermic reaction that produces a shock wave ahead of the reaction supporting it. Detonation reaction results in shock, heat, and a large volume of gaseous products. There are several ways to estimate explosive energy, ranging from simple calculations and field tests to extremely complex computations that involve studies of chemistry and reaction thermodynamics (ISEE, 2011). The two common methods to quantify shock energy and gas pressure are a combined theory of gas expansion and measurements of shock and bubble energy properties underwater in ideal conditions and controlled environments (Lang and Favreau, 1972, Hustrulid, 1999). These methods develop theoretical pressure-volume curves of the energy partition, provide insight into blasting, and help quantify the effect of rock mass (Lizotte and Scoble, 1994).

2.3.1 Explosive detonation and energy partition

Explosive properties and detonation conditions govern explosive energy release (Brinkmann, 1990, Udy and Lownds, 1990). The theory behind explosive detonation indicates that, upon detonation, the reaction produces a shockwave from high-pressure and temperature gases. The shock front bounds the reaction zone on one end, and the Chapman-Jouquet (C-J) plane on the rear. Figure 2-1 shows the ideal detonation, the concept developed by Chapman-Jouquet, (Cook, 1958). The reaction zone is extremely small ahead of the C-J plane, with no afterburning in the expansion zone, producing higher VOD and borehole pressure.

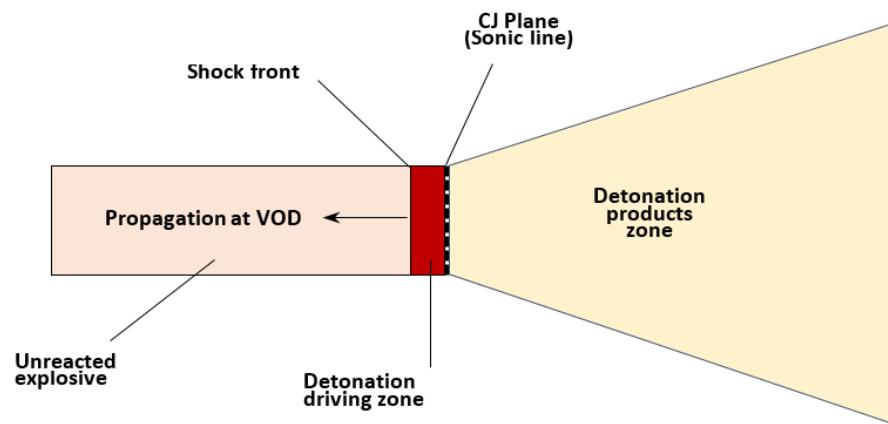


Figure 2-1: Ideal detonation after Brinkmann (1990)

Most commercial explosives exhibit non-ideal behaviour where VOD and borehole pressure are affected by the change in charge diameter and confinement. Figure 2-2 shows non-ideal explosive detonation. The detonation energy is released partly within the C-J plane and some during the lateral expansion of product gases. Although both energies are available to fragment rock, in a non-ideal explosive VOD is reduced, resulting in a different partition of energy between shock energy and gas pressure (Udy and Lownds, 1990). With adequate priming, VOD varies with

borehole diameter or confinement related to stemming, surrounding rock strength and density, and discontinuities.

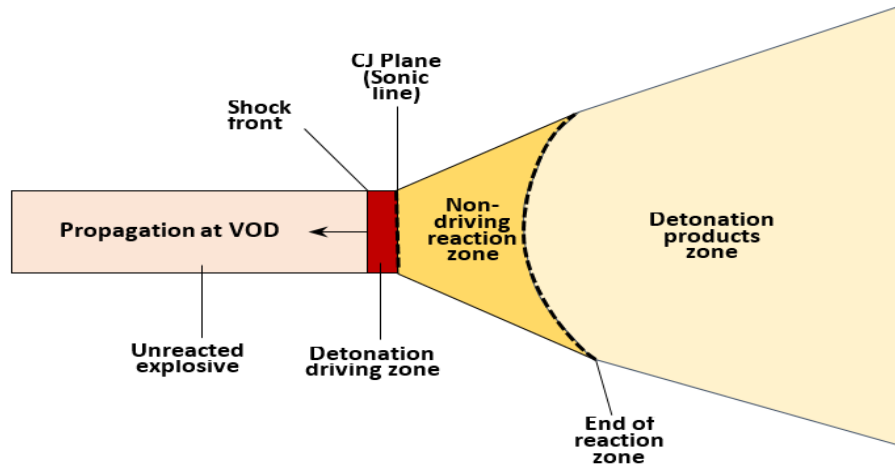


Figure 2-2: Non-ideal detonation after Brinkmann (1990)

Explosive energy partition is essential in causing fragmentation and material displacement. Figure 2-3 illustrates a simplified model of explosive energy partition and explosive-rock interaction as described by Udy and Lownds (1990).

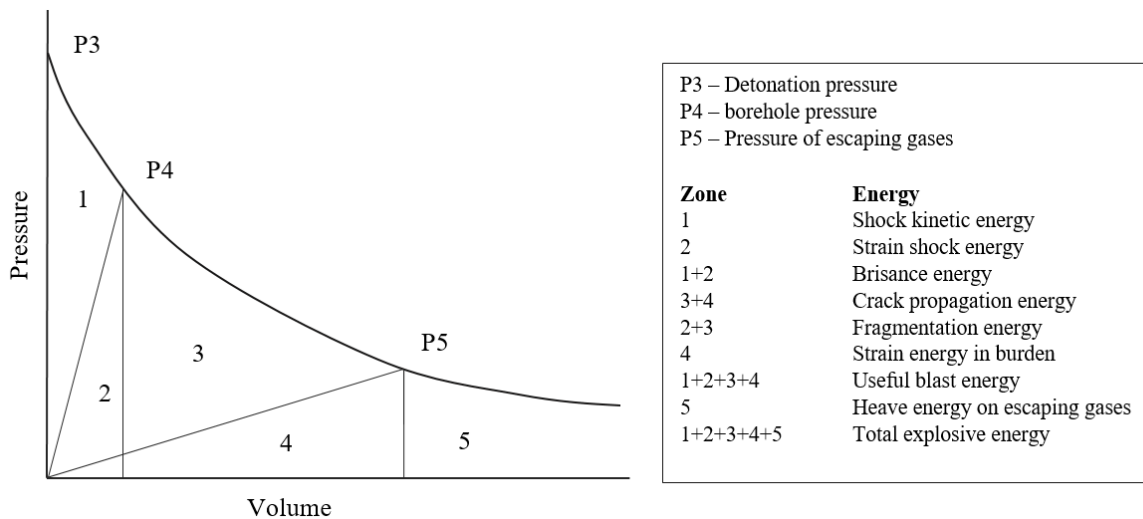


Figure 2-3: Energy partition in blasting after Udy and Lownds (1990)

They explained that the brisance energy is the work done during expansion, which is composed of strain energy stored in the rock and shock wave kinetic energy. While strain energy is used to generate cracks, shock wave kinetic energy is spent in the crushed zone around the blasthole and propagates stress waves in the ground. Explosion gas products extend the cracks and cause rock movement. The energy used in wave propagation, fracturing, crack propagation, and rock movement is the only useful energy in rock blasting; the rest is wasted as heat, flyrock, air blast, noise, and ground vibrations.

2.3.2 Detonation parameters

Selection of an explosive for a particular rock mass and given objectives depends on the ability to characterize the performance of different explosives, including the total energy produced per weight of the explosive, the rate at which this energy is released, and the energy partition. The total energy released (heat of explosion) is the difference between the heat of the formation of products and the heat of the breakdown of explosive ingredients, as presented in the equation (2.1) (Hustrulid, 1999). In an ideal and complete reaction, the gas pressure developed is proportional to the explosive mixture and temperature of the gases.

$$Q_E + Q_R = Q_P \quad (2.1)$$

Where Q_E is the heat of explosion in kCal/mole, Q_P is the total energy released in forming products and Q_R is the energy of breakdown of ingredients. The energy released, Q per unit mass, m (kCal/kg) is given by;

$$Q = \frac{Q_E}{m} \quad (2.2)$$

From the heat of explosion Q , the temperature of explosion products, T_E can be obtained from;

$$T_E = \frac{Q}{\bar{C}_V} + T_1 \quad (2.3)$$

$$\bar{C}_V = \sum_1^n n_i \bar{C}_{V_i} \quad (2.4)$$

\bar{C}_V is the average specific heat (kCal/°K-kg) over temperature T_1 to T_E , n_i is the number of moles in *ith* component (moles/kg), \bar{C}_{V_i} is the average specific heat of *ith* component (kCal/°K-kg) from initial temperature, T_1 (usually 300°K) to final blasthole temperature T_E . When T_E is obtained, gas pressure P_g can be calculated from the Gas Equation as;

$$P_g v_E = nRT_E \quad (2.5)$$

Where n is the summation of moles of gas per kilogram of explosive, R is gas constant (0.0821 L-atm/°K-mol) and v_E is the volume occupied by gases. Gas pressure is defined as the pressure exerted by expanding gases into the borehole walls (borehole pressure, P_b or P_g).

Another way to estimate gas pressure is from detonation pressure. Detonation pressure P_d (Pa), is the pressure released on the reaction zone as the result of detonation and can be estimated from explosive density, ρ_e (kg/m³), and measured VOD (m/s) using Equation (2.6) (ISEE, 2011). Pressure formed from explosive detonation can be up to 20 GPa at the front of the detonation wave and is normally from 5 to 10 GPa for a fully coupled charge. The pressure exerted on the boreholes is less than detonation pressure due to the wall acceleration outwards (Persson et al., 1994). Gas pressure impinging on the borehole wall for a fully coupled hole has been estimated at 45% to 50% of the theoretical detonation pressure (ISEE, 2011). A recent analysis by Barreto (2020) indicates that this value can be as low as 15%. For uncoupled charges, this value is much lower.

$$P_d = \frac{\rho_e VOD^2}{4} \quad (2.6)$$

Several methods are used to measure VOD. VOD can be used to indicate several explosive performance characteristics, such as consistency of detonation, adequacy in priming, the effects of hydrostatic pressure, explosive density, or contamination along the charge column (Chiappetta, 1998). VOD can be used to determine detonation pressure and shock energy produced by the ideal explosive as described in the equation (2.6). The correlation of VOD, rock mass encountered, and fragmentation distribution can offer useful information on the influence of rock mass properties on blast energy.

Two common systems used to measure VOD are point-to-point systems and continuous systems. Point-to-point systems give the average VOD between two discrete points where sensors are placed. Point-to-point measurement has limitations in providing information on the malfunction of explosives and determining transit VODs in the explosive column. They can be used to determine if the hole detonated or not but cannot provide further information on explosive malfunction or fault on the initiation system in case the hole does not detonate.

Continuous VOD systems overcome the limitations presented by the point-to-point system, whereas continuous systems can measure VOD between any two points (Crosby et al., 1991). The commonly used continuous VOD measurement is the resistance wire method developed by the United States Bureau of Mines (USBM) in the 1960s. Figure 2-4 shows a similar system; the MREL's MicroTrap Data Recorder. The system operates under constant resistance wire theory using basic Ohm's law, ($V = RI$), where V (Volts) is Voltage, R is Resistance (Ohms), and I is Current (Amps). A constant current is supplied to known resistance wire, and upon detonation; a change

in resistance indicates the explosive reaction. Since the constant current is supplied, a voltage drop indicates the distance initiated, and the VOD is calculated with time.

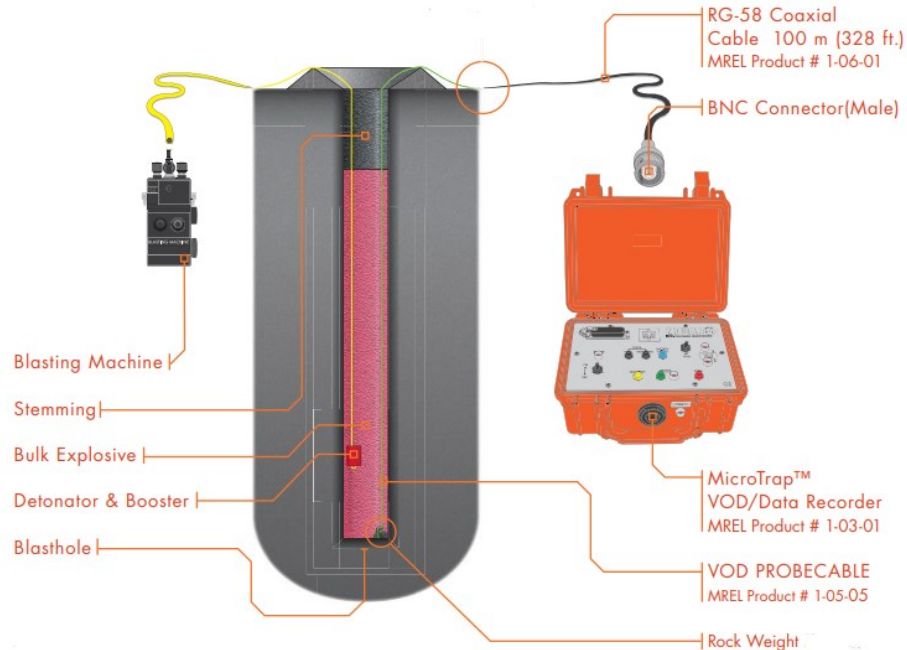


Figure 2-4: Continuous VOD measurement setup for MREL's Micro-Trap Data Recorder, after MREL (2022)

2.4 Explosive energy interaction with the rock and formation of damage zones

Blasting in mining aims to fracture rock by providing energy that exceeds rock strength or elastic limit. Rock deformation occurs by a change in volume by compression or shape by shear. Material resistance to deformation is bulk modulus (modulus of incompressibility) if the deformation is in compression or shear modulus (modulus of rigidity) if it is shear. Upon detonation, a strong shockwave is transferred to a rock mass, causing crushing around the charge. The shock waves quickly decay into stress waves further out, forming radial cracks.

The theory of rock fracture and fragmentation due to blasting suggests an overall combined damage mechanism, where intensity, propagation, and interaction of stress waves are responsible for initially fracturing the rock (conditioning), while the ensuing gas pressure predominantly

affects fragmentation breakage and displacement beyond the immediate borehole region. The induced shock front precedes the gas pressure, causing the borehole's initial crushed zone and dissipating the fracture zone. While the crushed zone is formed due to higher compressive stresses after the stress wave travels through a distance and the rock yields, the tangential stress changes from compressive to tensile forming radial cracks in the fracture zone (Zhu et al., 2007). These are the two major zones that contribute to fragmentation in mining, and in this study, they are referred to as damage zones.

It is commonly observed in a normal blast that under 10% of broken volume breaks in shear due to compression, while the remaining over 90% is broken by tensile stresses (Hustrulid, 1999). The further the wave travels radially outwards, the amplitude decreases and it becomes an elastic wave. The energy in elastic waves can deform but not fracture the rock, instigating ground vibrations. Upon encountering the free surface, the wave is reflected and when it is higher or equal to the tensile strength of the rock, spalling occurs.

The zones around a single blasthole with continuous rock mass in all directions are described by Hustrulid (1999), as shown in Figure 2-5. The size of the damage zones depends on explosive energy and rock strength. For example, using ANFO in medium-strength rock, a crushed zone can extend up to 6 times a blasthole diameter, a fracture zone up to 20, and an influenced zone up to 60 times the diameter (Hustrulid, 1999). It is important to note that rock breakage can significantly vary from this example due to variations in blast geometry and the interaction of stress waves with the discontinuity boundaries. The common feature of the influenced zone is minor fractures, which are insignificant as far as fragmentation is concerned but can affect stability of the remaining structure.

The damage potential of a stress wave can be determined if the wave attenuation in the rock mass is known by assuming that the peak pressure and peak particle velocity (PPV) are proportional to dynamic stress experienced by the rock mass (Yang et al., 1994, Onederra and Esen, 2004, Mojtabai and Beattie, 1996, Personn, 1997). Using the example of ANFO in medium-strength rock Hustrulid (1999) obtained the boundaries of the damage zones correspond to peak particle velocities of 20 m/s in the crushed zone, 5 m/s in the fractured zone, and 1.5 m/s in the influenced zone.

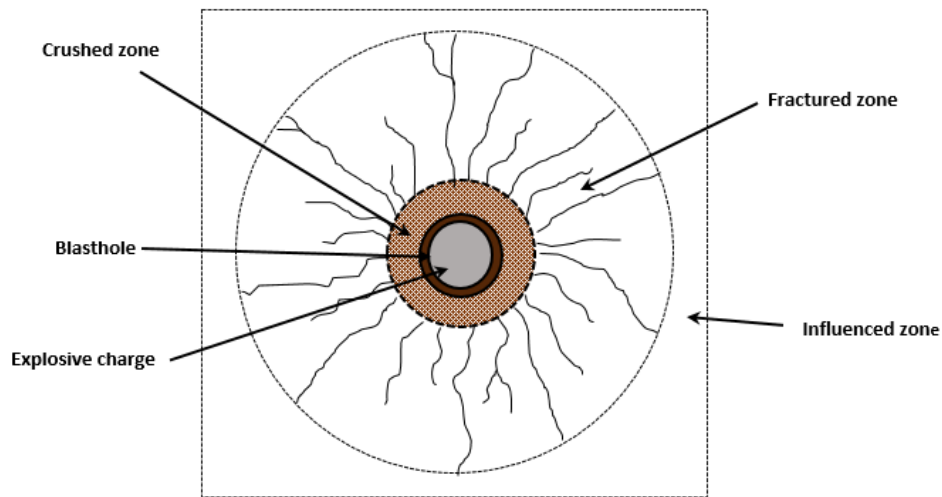


Figure 2-5: Zones around a blasthole (Damage Zone = crushed zone + fractured zone)

Section 2.4 reviews the properties of the shock waves and stress wave and their interaction with the rock mass which is the foundation of the formation of damage zones around the blasthole.

2.4.1 Shock wave properties

In fully coupled charges, shock waves are produced and transmitted outward from the explosive axis. They are characterized by higher stress beyond the elastic limit, vertical or nearly vertical wavefront, and an increase in entropy. With way higher stress and particle velocity, the shock wave velocity is also higher than the elastic wave velocity in the rock. When the wave impinges the rock,

the rarefaction wave is formed traveling in the opposite direction to the shock front while detonation products push the borehole wall outside. Since it is subjected to higher stress, the rock is stressed way beyond its elastic limit and fails by plastic deformation. Upon shock wave arrival, the rock status changes from undisturbed to shocked status with the rapid temperature, pressure, and density increase. The initial rock parameters P_o (pressure), u_o (particle velocity), ρ_o (density), v_o (specific volume), and e_o (specific internal energy) change to shocked states P_1 , u_1 , ρ_1 , v_1 , and e_1 . Rankine-Hugoniot jump equations which consider fundamental laws of physics for mass, momentum, and energy conservations in equations (2.7),(2.8), and (2.9) are used to formulate shock discontinuity propagation in the rock, (Henrych, 1979, Cooper, 1996).

From the law of energy conversation;

$$e_1 - e_o = \frac{1}{2}(P_1 + P_o)(v_o - v_1) \quad (2.7)$$

Mass equation;

$$\frac{\rho_1}{\rho_o} = \frac{v_o}{v_1} = \frac{VOD}{VOD - u_1} \quad (2.8)$$

Momentum conservation

$$P_1 - P_o = \rho_o (u_1 - u_o)(VOD - u_o) = u_1 VOD \quad (2.9)$$

Internal specific energy can be calculated from the equation (2.10). γ is an isentropic exponent with values ranging from $2.54 \leq \gamma \leq 3$ depending on the kind of explosive. The particle velocity at the interface of the borehole hole (u_r) is estimated from the equation (2.11), where P_r is shock pressure at the rock interface (Henrych, 1979).

$$e = \frac{P(v)}{\gamma + 1} \quad (2.10)$$

$$u_r = \frac{VOD}{1 + \gamma} \left(1 - \sqrt{2\gamma} \frac{\frac{P_r}{P_d} - 1}{\sqrt{[(1 + \gamma)] \frac{P_r}{P_d} + (\gamma - 1)}} \right) \quad (2.11)$$

The shock velocity V_r in rock interface can also be estimated by Hugoniot Equation (2.12) Cooper (1996).

$$V_r = C_o + s u_r \quad (2.12)$$

The initial rock pressure (P_o) and particle velocity (u_o) before the shock wave are assumed zero. If ρ_r is rock density, the shock wave pressure in the rock interface P_r is estimated from the conservation of momentum in the equation (2.9) as shown in the equation (2.13);

$$P_r = \rho_r V_r u_r \quad (2.13)$$

C_o and s are Hugoniot parameters. From the experiments, it was observed that shock velocity was linear to particle velocity. The constant C_o is the bulk sound speed in rock (km/s) or the y-intercept, and S (dimensionless) is the slope (Cooper, 1996). The value of s can be estimated from the material with similar physical and chemical properties, such as crystal structure, density, and chemical formation. The Hugoniot slope for a variety of rocks ranges from 1.0 to 1.7, and for sulphide minerals, s can be considered 1.4 (Liu and Katsabanis, 1993). C_o and s values for emulsion explosives are 2.04 km/s and 1.91 (Lee et al., 1989).

Liu and Katsabanis (1993) and Liu and Tidman (1995) derived an expression in the equation (2.14) to estimate the particle velocity at the rock interface, (u_r) for a fully coupled blasthole assuming

an adiabatic process where V_d is the shock wave velocity. Assuming that rock density in front of the shock front is constant in cylindrical charges, they developed a hydrodynamic model to estimate pressure, (P_r) at the rock/explosive interface in the equation (2.15).

$$u_r = \frac{2V_d}{\gamma-1} \left(1 - \left(\frac{P_r}{P_d} \right)^{\frac{\gamma-1}{2\gamma}} \right) \quad (2.14)$$

$$P_r = 1.62 \rho_e VOD^2 \left(\frac{\rho_r V_p}{\rho_e VOD} \right)^{0.25} \text{ kbar} \quad (2.15)$$

The coupling ratio affects shock wave transfer to the rock. In uncoupled charges, the shock intensity induced in the rock reduced significantly. The shock wave peak pressure decays rapidly from the rock interface and acts over a short range, depending on the material properties encountered. Hino (1956) suggested that the shock wave produced by the charge could be divided into two parts; a crushing shock wave that prevails in the crushed zone and a stress wave beyond the crushed zone. Properties of shock waves within the crushed zone can be calculated using Rankine-Hugoniot equations and the peak pressure, P at any distance from the charge be estimated from the equation (2.16).

$$P = P_r \left(\frac{r_o}{R} \right)^\beta \quad (2.16)$$

Where r_o is the radius of the charge cross-section, R is the distance from the charge, and β is the wave attenuation index for the cylindrical charge, which is assumed to range from 2 to 3 close to the charge. Henrych (1979) suggested that the value of β depends on explosive and rock properties and for most rocks β is approximately 1.5. Sun (2013) presented modified expressions

used by Dai (2002) to estimate the attenuation index in the shock wave zone (β_1) and stress wave zone (β_2) as shown in equations (2.17) and (2.18), where ν is the rock's Poisson ratio.

$$\beta_1 = 2 \left(1 + \frac{\nu}{1-\nu} \right) \quad (2.17)$$

$$\beta_2 = 2 \left(1 - \frac{\nu}{1-\nu} \right) \quad (2.18)$$

The change from plastic deformation in the crushed zone to elastic deformation in the fracture zone by stress waves can also be explained by the Hugoniot Elastic Limit (HEL) concept, which is based on the decrease in amplitude of shock waves. Ahrens and Gregson (1964) cited HEL for various rocks and minerals as shown in Table 2-1. Rosenberg (1993) developed a relationship between Hugoniot Elastic Limit Stress σ_{HEL} and the dynamic compressive strength of the rock (UCS_d) in the equation (2.19).

$$\sigma_{HEL} = \frac{1-\nu}{(1-2\nu)^2} UCS_d \quad (2.19)$$

Table 2-1: Hugoniot Elastic Limit for Rock Materials

Rock materials	σ_{HEL} value (GPa)
Quartzite and Novaculite	4 to 9
Plagioclase	4 to 5
Calcite	1.5 to 2.5
Limestone and sandstone	~0.5

When propagating from low to high impedance material, since the shock wave pressure in high impedance material is higher than in low impedance material the shock wave is strengthened. An example of such a scenario is when the shock wave propagates from the blasthole to the rock

mass. Similarly, when propagating from high to low impedance, the shock wave induced on low impedance is lower than the initial. When travelling from the material to a free surface, the particle velocity on the free surface is double that in the material (Zhang, 2016).

2.4.2 Stress wave properties (parameters)

Beyond the proximity to the blasthole, the waves induced by blasting are generally elastic waves (Zhang, 2016). Elastic waves are characterized by stress that is within the material's elastic limit, constant wave speed, and no change in entropy. Within the elastic limit, the strain produced by the material is proportional to the stress applied to it. Beyond elastic limit, the material is loaded beyond its elastic limit and plastic deformation occurs, similar to shock wave action from an explosion.

The waves formed are categorized into body waves and surface waves. Body waves travel through the rock mass and can either be compressional waves or shear waves. Compressional waves (P-waves) cause compression and dilation and they travel in the direction of wave travel. The wave P-velocity, V_p can be estimated using equation (2.20).

$$V_p = \sqrt{\frac{E(1-\nu)}{\rho_r(1+\nu)(1-2\nu)}} \quad (2.20)$$

Shear waves (S-waves) or distortional waves travel perpendicular to the direction of wave travel causing displacement normal to the direction of wave propagation. Under three-dimensional conditions, the velocity of the shear wave is estimated using the equation (2.21). The ratio between shear and compressional wave velocities can be calculated from the equation (2.22). As most rocks have ν between 0.25 and 0.33, the ratio of P-wave to S-wave is around 1.7 to 2.

Propagation of P- and S- wave in intact rock depends on material properties, including mineral content and size, and the presence of pores or micro-cracks which influence rock density and Young's Modulus. Shear waves travel in solids and not fluids, making their propagation more influenced by rock mass cavities and joints. In cases where these joints are perpendicular to wave travel, shear waves decrease greatly or disappear. Surface waves travel on the surface of the rock mass. They form when body waves reach a free surface. These waves carry high energy and are the cause of ground motions. Surface waves can be either Rayleigh waves or Love waves.

$$V_s = \sqrt{\frac{E}{2\rho_r(1+\nu)}} \quad (2.21)$$

$$\frac{V_s}{V_p} = \sqrt{\frac{1-2\nu}{2(1-\nu)}} \quad (2.22)$$

The stress wave generated from an explosion can be categorized into three orthogonal motion components. The longitudinal or radial component is aligned parallel to the plane between the blasthole and the monitoring point, the transverse component is perpendicular to the longitudinal plane, and the vertical component is aligned in the vertical plane.

Wave parameters such as displacement, period, frequency, amplitude, and wavelength describe wave propagation in a rock mass. The properties of the medium in which the wave travels affect its propagation. Figure 2-6 shows that as the stress wave travels through an interface it can be transmitted, reflected, or refracted following the same principles as light. Refraction occurs when the wave passes through material with different densities, causing a wave speed and direction change. The wave energy can also be partitioned into transmitted and reflected waves at the

interface. This partition depends on acoustic impedance, Z in the equation (2.23) which is related to the sonic speed of the material, (V_p), and its density, (ρ_r).

$$Z = \rho_r V_p \quad (2.23)$$

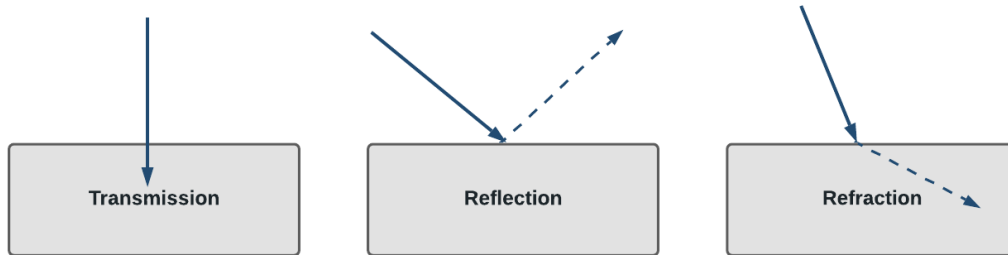


Figure 2-6: Wave propagation in an interface

Considering a longitudinal deformational wave travelling from the source across the rock mass. According to Persson et al. (1994), the stress through the section (σ) can be estimated from the particle velocity (u), P-velocity (V_p), and rock density (ρ_r) from;

$$\sigma = \rho_r V_p u \quad (2.24)$$

Also from Hooke's Law

$$\sigma = E \varepsilon \quad (2.25)$$

Where ε the strain and E is Young's modulus. The strain and strain rate (ε^*) can be estimated if the particle velocity and particle acceleration (a_p) are known from equation (2.26).

$$\varepsilon = \frac{\partial u}{\partial x} = \frac{\partial u}{\partial t} \frac{\partial t}{\partial x} = \frac{u}{V_p} \quad (2.26)$$

$$\varepsilon^* = \frac{a_p}{V_p}$$

Then from equations (2.24) and (2.25)

$$\sigma = \rho V_p u = E \varepsilon = E \frac{u}{V_p} \quad (2.27)$$

$$V_p = \sqrt{\frac{E}{\rho_r}} \quad (2.28)$$

As well, as equations (2.23) and (2.27),

$$E = V_p Z_p \quad (2.29)$$

2.4.2.1 Wave propagation across the rock mass

When propagating in the rock, the stress wave amplitudes attenuate by geometrical spreading as the wave radiates from the source and due to material properties with the rate depending on the size and frequency of the wave and the properties of the medium. Attenuations due to medium are caused by induced deformation, internal friction, and reflection of the wave on the interface. Rock masses are made up of intact rock and structures such as joints, bedding planes, etc., which dominate rock mass response to static and dynamic loadings and the fragmentation process (Goodman, 1976).

Wave propagation in intact rock depends on its Young's modulus and density. The wave velocity is higher in dense and compact rock. Mineral composition affects the wave's speed, where large grains cause a decrease in wave speed (Vutukuri, 1978); pores and micro-cracks also lower the wave speed especially when empty.

When passing through an interface, the wave attenuates both by decreasing amplitude and high-frequency pulse filtering (Myer et al., 1990). The wave frequency determines how much is reflected or transmitted across the interface. With high frequency, a high proportion of the wave is reflected. This effect is negligible in intact rock or tightly closed joints (high-stiffness joints).

The joints with lower stiffness reflect more, causing higher attenuations by decreasing wave amplitude and high-frequency pulse filtering. Complex rock texture and the presence of structures cause higher blast wave attenuation as a result of partial wave reflection, transmission, and energy absorption in the joints' deformation.

Joint parameters such as joint width, roughness, infill material type and thickness, orientation, shear and compressive strength of the contact, fracture frequency, and spacing between the joints affect wave transmissions (Zhu et al., 2007). An increase in joint spacing improves burden breakage by reducing the number of joints from which the wave is disrupted. On a highly jointed rock mass wave propagation undergoes several reflections and refraction making its analysis complex, (Zhao et al., 2006). As the joint width increases, fracturing on the opposite side of the joint decreases and increases on the incident side due to wave reflection. Empty joints hinder the transmission of stress waves and no cracks pass through joints causing minimum to no damage on the opposite side of the joint. Water content in the rock improves the transmission of waves through joints. The angle of incidence governs the proportions of reflected and transmitted waves. Ma and An (2008) observed that when the joint orientation is parallel to the free face, the block between the free face and joint can be fragmented from reflected tensile fractures at the free face. This is not a possibility when the joints are normal to free face.

2.4.2.2 Wave transmission and reflection at an interface

When blast waves propagate in a rock mass, an S-wave and P-wave are formed. When the waves meet an interface at an oblique angle, they can be transmitted as P-wave, reflected as P-wave, transmitted as S-wave, and reflected as S-wave. If the incidence angle is normal to the interface only S-waves or P-waves are induced depending on the incident wave (i.e. P-wave or S-wave),

(Zhang, 2016). Assuming a wave propagating from one rock to the other of the same cross-section area and with the densities (ρ) and longitudinal wave velocities (V_p) as described in Figure 2-7, the stress and the particle velocity of the incidence (σ_i, u_i) reflected (σ_r, u_r), and transmitted (σ_t, u_t) waves can be estimated.

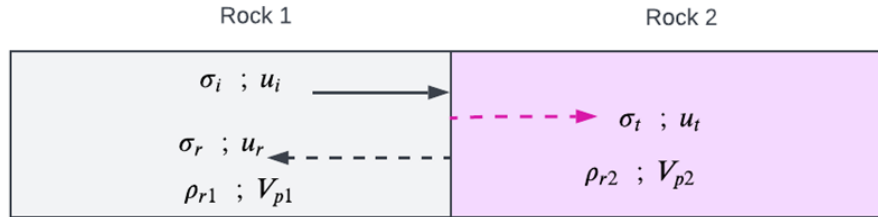


Figure 2-7: Wave propagation in two rock types, after Zhang (2016)

Assuming that the stress across the interface is continuous, the velocities and stresses on the opposite sides of the interface are equal.

$$u_i + u_r = u_t \quad (2.30)$$

$$\sigma_i + \sigma_r = \sigma_t \quad (2.31)$$

σ_r and u_r carry negative signs as they are moving in the opposite direction from the incident wave.

Using equations (2.24) and (2.30) becomes;

$$\frac{\sigma_i}{\rho_{r1} V_{p1}} - \frac{\sigma_r}{\rho_{r1} V_{p1}} = \frac{\sigma_t}{\rho_{r2} V_{p2}} \quad (2.32)$$

Substitution equation (2.31) for σ_t and using equation (2.23) for material impedance, Z:

$$\sigma_r = \left(\frac{\rho_{r2} V_{p2} - \rho_{r1} V_{p1}}{\rho_{r2} V_{p2} + \rho_{r1} V_{p1}} \right) \sigma_i = \left(\frac{Z_2 - Z_1}{Z_2 + Z_1} \right) \sigma_i \quad (2.33)$$

Substitution equation (2.31) for σ_r and using equation (2.23) for material impedance, Z:

$$\sigma_t = \left(\frac{2\rho_{r2}V_{p2}}{\rho_{r2}V_{p2} + \rho_{r1}V_{p1}} \right) \sigma_i = \left(\frac{2Z_2}{Z_2 + Z_1} \right) \sigma_i \quad (2.34)$$

With the substitution of equation (2.24) on the right side of equations (2.33) and (2.13):

$$u_r = \left(\frac{\rho_{r2}V_{p2} - \rho_{r1}V_{p1}}{\rho_{r2}V_{p2} + \rho_{r1}V_{p1}} \right) u_i = \left(\frac{Z_2 - Z_1}{Z_2 + Z_1} \right) u_i \quad (2.35)$$

$$u_t = \left(\frac{2\rho_{r1}V_{p1}}{\rho_{r2}V_{p2} + \rho_{r1}V_{p1}} \right) u_i = \left(\frac{2Z_1}{Z_2 + Z_1} \right) u_i \quad (2.36)$$

When the wave propagates from soft to hard rock $Z_2 > Z_1$ the stress of the transmitted wave is stronger than the incident wave, and it is the opposite when propagating from hard to soft. In cases where the wave propagates from a weaker to a very strong rock where $Z_2 \gg Z_1$ from equations (2.33) to (2.36):

$$\sigma_r = \sigma_i, \quad \sigma_t = 2\sigma_i, \quad u_r = -u_i, \quad u_t = 0 \quad (2.37)$$

On the other hand, when $Z_2 \ll Z_1$, similar to when the blast wave reaches a free surface, from equations (2.33) to (2.36):

$$\sigma_r = -\sigma_i, \quad \sigma_t = 0, \quad u_r = u_i, \quad u_t = 2u_i \quad (2.38)$$

On the free surface, the particle velocity of the transmitted wave doubles the incident wave particle velocity while all the stress is reflected, and none is transmitted. As the wave is reflected on a free surface, the incident wave interacts with the reflected wave and superimposition occurs. If the incident wave compressive stress is less than the dynamic tensile strength of material $\sigma_i < \sigma_{Td}$, the reflected wave stress will be less than the dynamic tensile strength of the rock and no damage occurs. In cases where the incident wave is higher than the dynamic tensile strength of

the rock but lower than the dynamic compressive strength of the rock, the reflected wave will be equal to the tensile strength of the rock and spalling occurs at the free surface, (Zhang, 2016).

2.4.3 Loading rate dependency and fracture mechanisms of rock material

The rapid release of energy from explosive detonation in the rock mass results in shock waves at a high loading rate/strain rate propagating radially from the blasthole. The studies have shown that brittle material properties such as rock are strain rate sensitive, meaning their properties improve with the increase in strain rate. Blast-induced fragmentation is particularly influenced by rock dynamic strength; with increasing confinement and loading rate, the rock can withstand higher forces before failure (Zhang, 2016, Persson et al., 1994). Fracture toughness and fracture mechanisms also vary with loading rate; beyond critical strain rate, significant changes are observed (Ramesh et al., 2015, Hogan et al., 2016, Gong et al., 2019). Fracture mechanisms for rocks vary where rock failure changes from single fracture, or multiple fractures to pulverization with the increase in strain rate. The critical strain rate for tensile and compressive strength is between 1s^{-1} and 10s^{-1} (Liu et al., 2018, Zhang and Zhao, 2014).

The dynamic-to-static strength ratio is defined as the dynamic increase factor (DIF); for rocks is reported to be more than 5 in compression and more than 6 in tension (Liu et al., 2018). Prasad (2000) observed the dynamic compressive strength for 12 different rock types to be 2.5 to 4.6 times the static values. Mohanty (1987) and Cho et al. (2003) observed that dynamic tensile strength is 2 to 12 times higher than static tensile strength for various rock types.

Zhang and Zhao (2014) summarize data from several studies on tensile and compressive strength under various strain rates and Xie et al. (2017) used their findings to perform curve regression and developed a relationship between strain rate and dynamic uniaxial compressive strength in

Figure 2-8 and the dynamic tensile strength in Figure 2-9. Equations (2.39) and (2.40) show the increase factor for compressive strength (DIF_c) and tensile strength (DIF_t), respectively with strain rate.

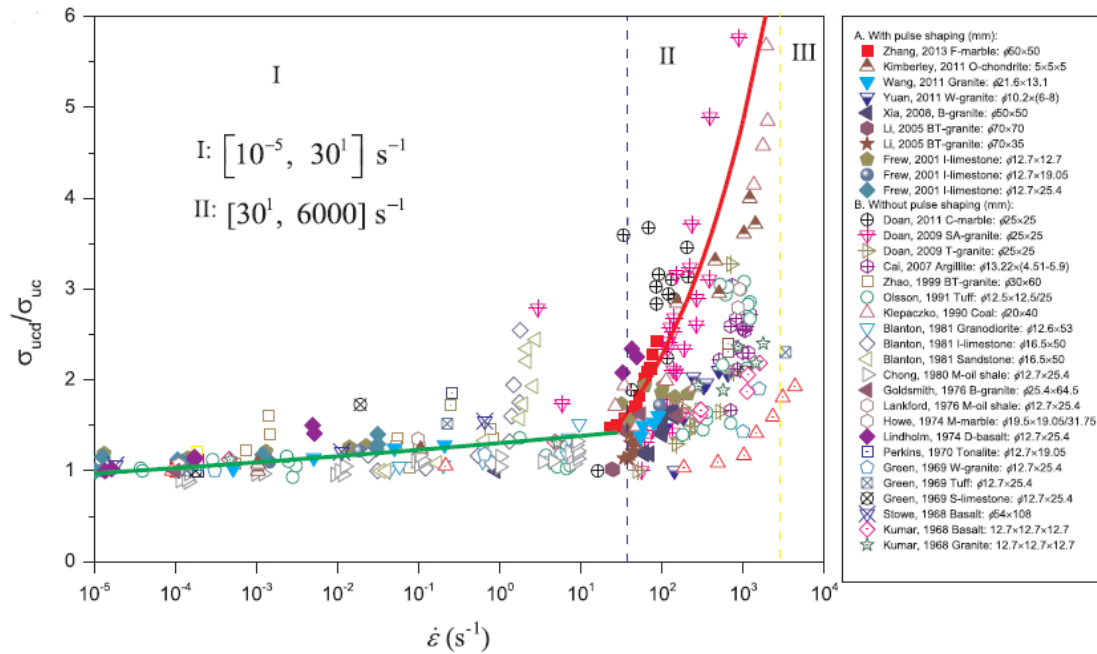


Figure 2-8: Regression curve for compressive strength strain rate increase factor, after Xie et al. (2017)

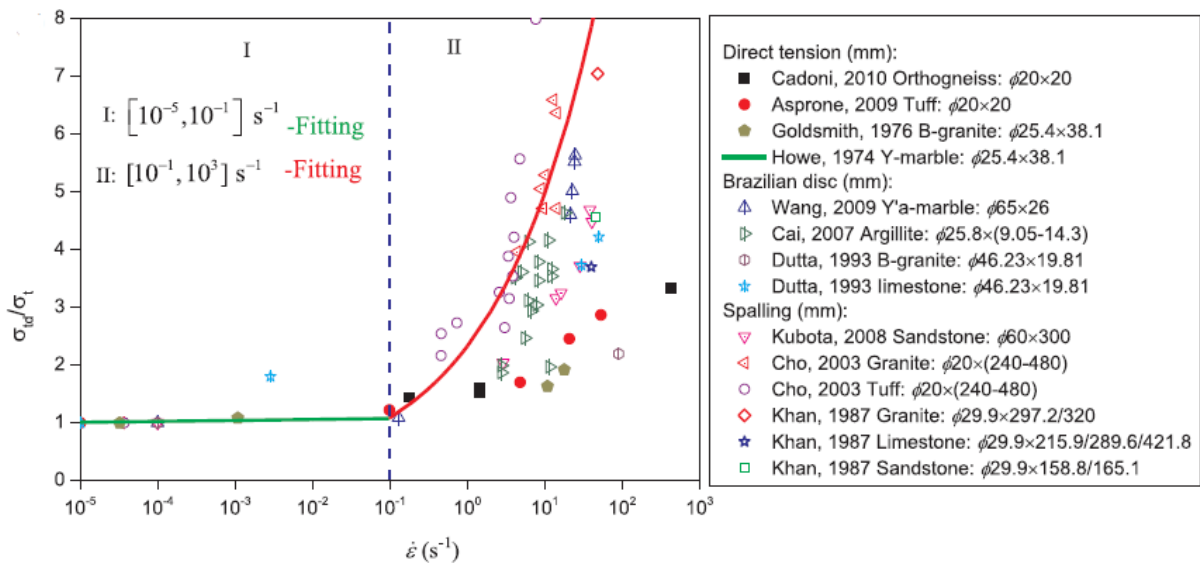


Figure 2-9: Regression curve for tensile strength strain rate increase factor, after Xie et al. (2017)

$$DIF_c = \begin{cases} 0.512\varepsilon_p^{\bullet 1/3} & \text{for } \varepsilon_p^{\bullet} > 30s^{-1} \\ (\varepsilon_p^{\bullet} / \varepsilon_0^{\bullet c})^{0.0026} & \text{for } \varepsilon_p^{\bullet} \leq 30s^{-1} \end{cases} \quad (2.39)$$

$$DIF_t = \begin{cases} 2.4\varepsilon_p^{\bullet 1/3} & \text{for } \varepsilon_p^{\bullet} > 10 s^{-1} \\ (\varepsilon_p^{\bullet} / \varepsilon_0^{\bullet t})^{0.007} & \text{for } \varepsilon_p^{\bullet} \leq 10 s^{-1} \end{cases} \quad (2.40)$$

ε_p^{\bullet} is the strain rate, $\varepsilon_0^{\bullet c}$ is the reference strain rate in compression equal to $3 \times 10^{-5} s^{-1}$, and $\varepsilon_0^{\bullet t}$ is the reference strain rate in tension equal to $3 \times 10^{-6} s^{-1}$. From over five decades worth of data from several studies, Liu et al. (2018) also developed equations to predict DIF over a wide range of strain rates for compressive (DIF_c) and tensile (DIF_t) strengths of rocks as seen in the equation (2.41) and (2.42), respectively. ε_c^{\bullet} is the compressive strain rate between 10^{-6} and $10^4 s^{-1}$ and ε_t^{\bullet} is the tensile strain rate between 10^{-6} and $10^3 s^{-1}$.

$$DIF_c = \begin{cases} 1 + 0.15\varepsilon_c^{\bullet 0.30} & \text{for } \varepsilon_c^{\bullet} < 10 s^{-1} \\ 1 + 0.10\varepsilon_c^{\bullet 0.50} & \text{for } \varepsilon_c^{\bullet} \geq 10 s^{-1} \end{cases} \quad (2.41)$$

$$DIF_t = \begin{cases} 1 + 0.70\varepsilon_t^{\bullet 0.18} & \text{for } \varepsilon_t^{\bullet} < 10 s^{-1} \\ 1 + 0.70\varepsilon_t^{\bullet 0.55} & \text{for } \varepsilon_t^{\bullet} \geq 10 s^{-1} \end{cases} \quad (2.42)$$

2.5 Blast damage prediction

Several approaches have been developed to describe blast-induced fragmentation and estimate the damage around the blasthole. Techniques such as theoretical estimations and empirical/analytical models have been developed from the theories and experiments. With computer advancements, numerical models and machine learning in artificial intelligence are emerging to predict outcomes with substantial use in blasting. Analytical approaches use parameters such as PPV (Fleetwood et al., 2009, Persson et al., 1994) or borehole pressure (Sun, 2013) to estimate the damage zones. Numerical modelling uses algorithms such as the Discrete Element Method (DEM), Finite Element Method (FEM), etc., to analyze stress fields around the

charge and estimate the damage zones. Machine learning uses the already-established relationships between input and output data to train the model to predict outcomes from a given set of data.

Review from several studies (Zhu et al., 2007, Dehghan Banadaki and Mohanty, 2012, Zhang, 2016, Yang et al., 2018, Zhu, 2011) provide a meaningful insight into factors affecting blasting outcomes. Such include the influence of explosive and rock mass strength on fracture mechanisms and the extent of damage and rock structures on stress wave and fracture distribution in the rock mass. Still, little work has been done on how various explosives and rock mass properties, specifically rock contacts and other discontinuity properties, affect the blasting process. This analysis is important in predicting blast outcomes and in improving the accuracy of predicting models and guiding blast designs.

Several theoretical and empirical formulations to estimate blast wave energy and damage zones are reviewed in section 2.5.1 and later used to estimate damage zones. Since the theoretical and empirical formulas have limitations when dealing with varying rock mass, numerical modelling is implemented to extend the study of the influence of structures on stress waves and crack propagations.

2.5.1 Empirical/theoretical approach for damage zone prediction

Prior studies indicate that the crushed zone to borehole radius ratio ranges from 2 to 6 (Brady and Brown, 2006, Hustrulid, 1999, Liu and Katsabanis, 1993). Esen et al. (2003) suggested that the radius of the crushed zone is a function of blasthole radius (r_o), borehole pressure (P_b), and dynamic properties of rock. From the analysis of 92 blasting tests on the concrete of variable strengths, they established a model to predict the radius of the crushed zone (r_c) in Equations

(2.43) and (2.44). K is stiffness (Pa), σ_c is the uniaxial compressive strength (Pa), E_d is the dynamic Young's modulus (Pa) and ν_d is the dynamic Poisson's ratio. Although the approach was developed using concrete, which is a man-made material with different conditions from the rock mass, validation of results has demonstrated its applicability to production blasting.

Equation (2.45) estimates the dynamic Young's modulus (Eissa and Kazi, 1988) from the static Young's modulus (E_s) in GPa and rock density (ρ_r) in g/cm³. The dynamic Poisson ratio can also be estimated from P-wave velocity (V_p) and S-wave velocity (V_s) using the expression in the equation (2.46). This expression is suitable for low-stress waves (Sun, 2013).

$$\frac{r_o}{r_c} = 1.231(CZI)^{-0.219} \quad (2.43)$$

$$CZI = \frac{P_b^3}{K\sigma_c^2}, \quad K = \frac{E_d}{1+\nu_d} \quad (2.44)$$

$$\log E_s = 0.02 + 0.77 \log(\rho_r E_d) \quad (2.45)$$

$$\nu_d = \frac{V_p^2 - 2V_s^2}{2(V_p^2 - V_s^2)} \quad (2.46)$$

The pressure experienced at the limit of the crushed zone (P_{eq}) may be estimated from a peak pressure attenuation function developed by Liu and Katsabanis (1993). P_{eq} in Equation (2.47) is derived from borehole pressure P_b , borehole radius r_o , the radius of pulverized zone r_c , and pressure decay factor ϕ . The pressure decay factor is an empirical curve that fits the function of the rock and its explosive properties. This function was developed from several rock samples, including concrete, and is proved to agree with computed blast results with a standard deviation of 1.45%.

$$P_{eq} = P_b \left(\frac{r_c}{r_o} \right)^\phi, \quad \phi = -1.54 \left(\frac{V_p}{VOD} \right)^{-0.33} \quad (2.47)$$

Peak particle velocity at the limit of a crushed zone, PPV_{eq} is estimated using Equation (2.48) for the stress in a plane, adopted from Persson et al. (1994) who assumed that the rock is intact and continuous without any structure. This assumption can be valid under high loading rates where, the entire distribution of flaws is activated and dependency on the weak links decreases (Kimberley et al., 2013).

$$u_{eq} = \frac{P_{eq} V_d}{E_d} \quad (2.48)$$

From the analysis conducted by Nicholls et al. (1971), attenuation characteristics of the stress waves in a rock mass beyond the crushed zone for a given explosive charge may be estimated by a square root scaled distance (SD_2) function of maximum charge mass detonated within any eight milliseconds, (W) in kg, and distance between the blast centroid and monitoring point, (R) in m as seen in the equation (2.49). When scaled distance, SD_2 is combined with the PPV monitoring, site-specific rock mass-influenced empirical constants A and B may be established. A is suggested to be indicative of the type of rock mass geology, while B is the ability of vibrations to attenuate in the rock mass.

$$SD_2 = \frac{R}{W^{0.5}}, \quad PPV = A(SD_2)^{-B} \quad (2.49)$$

Forsyth (1993) presented an expression to determine the critical PPV that can induce fresh tensile fractures in a rock mass given the rock mass 'pseudo' elastic properties in the equation (2.50), where PPV_{cr} is critical PPV, above which the rock mass would prospectively fail by tension (mm/s), σ_t is the uniaxial tensile strength of rock (Pa), and ϵ_{tcr} is the critical tensile strain. The use of

Young's modulus in tensile failure, which assumes that the rock is homogeneous and isotropic, and deriving tensile strength and fracture mechanism under quasi-static unconfined conditions are the two inherent flaws in this expression. To rectify this, the dynamic properties of the rock are calculated and used to reflect blast experienced strengths.

$$u_{cr} = \varepsilon_{tcr} \times V_p = \frac{\sigma_t}{E} \times V_p \quad (2.50)$$

2.5.2 Numerical approach for damage prediction

Numerical modelling, both finite element modelling (FEM) (Ma and An, 2008, Dehghan Banadaki and Mohanty, 2012) and discrete element modelling (DEM) (Yoon and Jeon, 2010, Onederra et al., 2013) have been used as the most economical and effective techniques to simulate the blasting process and optimize blast fragmentation. In DEM, the rock mass is represented as an assembly of bonded elements with specified tensile or shear strength. Failure is achieved when the stress exceeds this value (Yoon and Jeon, 2010). This approach can successfully track crack evolution and fracture patterns, but without some modifications and assumptions, it falls short in tracking explosive gas dispersion (Yoon and Jeon, 2010). In FEM, the damage mechanics is due to the growth and nucleation of cracks in the brittle rock mass defined by the appropriate damage evolution law (Wang et al., 2018).

Most blast-induced fragmentation studies are based on two dimensions (2D) analysis. Although they simplify the computation process and provide a significant understanding of the fragmentation process and the influence of discontinuities along the 2D plane, they do not capture the spatial stress distribution and blast damage in the three-dimensional (3D) setup. In this study, both 2D and 3D numerical simulation models are used in various applications.

LS-DYNA, a nonlinear transient finite element code with an explicit integration scheme capable of implementing dynamic problems, has been used for blasting modelling (Livermore Software Technology Corporation, 2018). LS-DYNA can successfully model the interaction between the solid material and fluid and gas flow using the Lagrangian algorithm and Arbitrary Lagrangian-Eulerian (ALE). LS-DYNA can incorporate coupling between the Lagrangian and ALE interfaces. Boundary conditions to restrict elements' movements can also be applied as needed. Two main damage models commonly used to simulate the damage evolution of rock mass under blasting loads in LS-DYNA are the Holmquist–Johnson–Cook (HJC) model (Holmquist et al., 1993) and the Riedel–Hiermaier–Thoma (RHT) model (Riedel et al., 1999). From the study conducted by Wang et al. (2021), the RHT model is observed to define damage distribution in rock well and describe the formation of the crushed zone and propagation of radial tensile cracks. The latter could not be captured in the HJC model.

2.5.2.1 The RHT material model

The Riedel-Hiermaier-Thoma (RHT) material model is an advanced brittle plasticity model for impulsive and dynamic loadings of brittle materials such as concrete, rock, or metals. The RHT model has been used extensively to model blast-induced fragmentation in rocks (Wang et al., 2021, Xie et al., 2017, Yi et al., 2017) since the rock has numerous randomly distributed pores and micro-cracks and behaves nonlinearly under compression. In the RHT material model, the shear and pressure components are coupled. Mie-Gruneisen equation of state (EOS) with a polynomial Hugoniot curve describes pressure, which also accounts for porous compaction. Mie-Gruneisen EOS shows the relationship between the pressure (P), volume (v_L), and energy (e) of the solid material expressed as;

$$P = f(v_L, e) \quad (2.51)$$

The change in pressure can be defined as

$$dP = \left(\frac{\partial p}{\partial v_L} \right)_e dv_L + \left(\frac{\partial p}{\partial e} \right)_{v_L} de \quad (2.52)$$

The integration can be done first at constant energy from V_{L0} to V_{L1} and then at constant volume from e_0 to e_1 as;

$$P = P_0 + \int_{V_{L0}}^{V_{L1}} \left(\frac{\partial p}{\partial e} \right)_e dv_L + \int_{e_0}^{e_1} \left(\frac{\partial p}{\partial e} \right)_{v_L} de \quad (2.53)$$

The term $v_L \left(\frac{\partial p}{\partial e} \right)_{v_L} = \Gamma$ is defined as Gruneisen gamma (Autodyn, 2005), making the second part of the integration,

$$\int \left(\frac{\partial p}{\partial e} \right)_{v_L} de = \frac{\Gamma(V_L)}{V_L} [e_1 - e_0] \quad (2.54)$$

From the first part of the integration in equation (2.53)

$$\int_{V_{L0}}^{V_{L1}} \left(\frac{\partial p}{\partial e} \right)_e dv_L = P - P_0 \quad (2.55)$$

The final output becomes;

$$P = P(V_L) + \frac{\Gamma(V_L)}{V_L} [e_1 - e_0] \quad (2.56)$$

Equation (2.56) is known as the Mie-Gruneisen equation of state and in this case P varies linearly with e at constant V_L , (Autodyn, 2005).

The polynomial equation of state used to define the pressure for fully compacted material is expressed in equation (2.57); where B_0 and B_1 are material constants, α_0 is the initial porosity, ρ_0

is the rock density, μ is the volumetric strain and A_1 , A_2 , and A_3 are Hugoniot polynomial coefficients, (Borrvall and Riedel, 2011). The porous material pressure is scaled using the porosity (α) value referencing fully compacted material; see equation (2.61).

$$P = \frac{1}{\alpha} \left((B_0 + B_1 \mu) \alpha_0 \rho_0 e + A_1 \mu + A_2 \mu^2 + A_3 \mu^3 \right) \quad (2.57)$$

From equation (2.57), the Gruneisen parameter $\Gamma(V)$ can be described as seen in equation (2.58), (Autodyn, 2005).

$$\Gamma(V) = \frac{B_0 + B_1 \mu}{1 + \mu} \quad (2.58)$$

The volumetric strain can be estimated from the initial and final density and porosity as;

$$\mu = \frac{\alpha_1 \rho_1}{\alpha_0 \rho_0} - 1 \quad (2.59)$$

B_0 and B_1 can be estimated for $\Gamma(v) = 0$ as $B_0 = B_1 = 2s - 1$. The Hugoniot polynomial coefficients A_1 , A_2 , and A_3 according to Xie et al. (2017) can be estimated using momentum and mass conservation equations from equations (2.9), (2.12), and (2.13) as shown in equation (2.60).

$$\begin{aligned} T_1 &= A_1 = \alpha_0 \rho_0 V_p^2 \\ A_2 &= \alpha_0 \rho_0 V_p^2 (2s - 1) \\ A_3 &= \alpha_0 \rho_0 V_p^2 (3s - 1)(s - 1) \end{aligned} \quad (2.60)$$

The pressures between P_{crush} and P_{comp} , can be scaled using equation (2.61); where N is the porosity exponent. For the fully compacted material P will be equal to P_{comp} . P_{crush} is 2/3 of the uniaxial compressive strength (Borrvall and Riedel, 2011).

$$P = f(\rho, \alpha, e) \quad \text{with } \alpha = 1 + (\alpha_0 - 1) \left[\frac{P_{comp} - P}{P_{comp} - P_{crush}} \right]^N \quad (2.61)$$

Figure 2-10 describes the p - α compaction model. Pore crush pressure (P_{crush}) and compaction pressure (P_{comp}) define failure modes in the model. Below the P_{crush} , the model is elastic. Beyond P_{crush} , with pressure increase, porous compaction occurs accompanied by a reduction in the effective bulk modulus of the material and volumetric stiffness. The relationship between pressure and volumetric strain is non-linear. Above the pore crush pressure, unloading occurs along current elastic stiffness, resulting in permanent volumetric strain at zero pressure. Pore crushing is defined by the porosity, which is the rock and the pore spaces ratio. Porosity decreases with increased pressure, and the value ranges from 0 to 1, from pore crush pressure to compaction pressure. When the pressure reaches the P_{comp} , the material is fully compacted, and the conventional equation of the state model governs the damage evolution (Borrvall and Riedel, 2011).

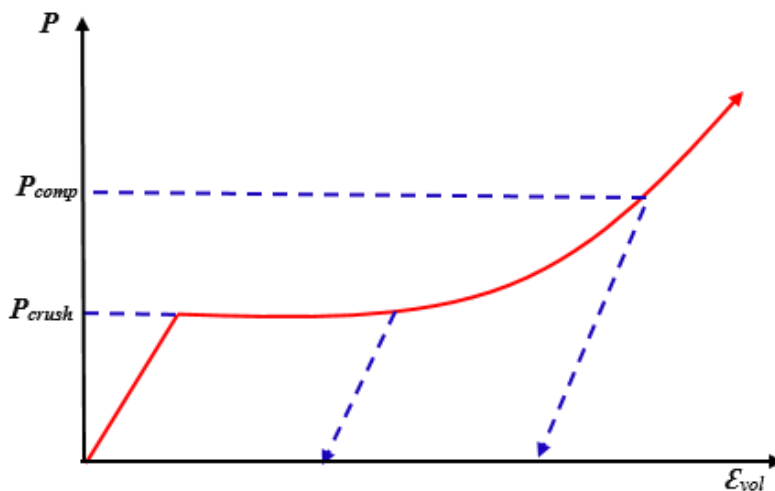


Figure 2-10: P-Q equation of state after Borrvall and Riedel (2011)

Three limit surfaces define the stress state of material in the RHT strength model; the initial elastic yield surface, residual friction surface, and failure surface, which depend on the hydrostatic pressure and the strain rate effect. The surfaces represent the reduction in material strength in different meridians and the strain rate effect. Surface material failure is achieved when its ultimate compressive, shear, or tensile strength is reached. Figure 2-11 illustrates an example of static compressive meridian surfaces; P_t is the pressure at time and P_u is the current pore crush pressure. It shows that the model is elastic until it reaches the initial yield surface, beyond which plastic strain prevails. The failure surface in compression is defined as a function of strength along the compression meridian, regularized yield function, and William-Warnke function, representing reduced strength on shear and tensile meridian presented in equation (2.62).

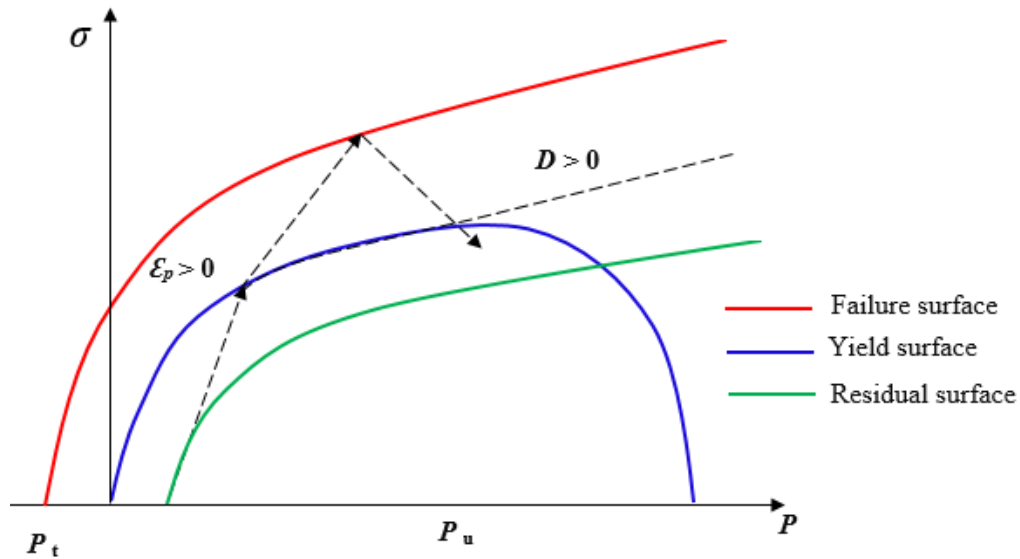


Figure 2-11: Stress limit surfaces and loading scenario after Borrvall and Riedel (2011)

$$\sigma_y(P_o^*, \varepsilon_p^*, \varepsilon_p^*) = f_c \sigma_y^*(P_o, F_r(\varepsilon_p^*), \varepsilon_p^*) R_3(\theta_1, P_o^*) \quad (2.62)$$

Where σ_y^* is the normalized yield function $\sigma_y^* = \sigma_y / f_c$, f_c is uniaxial compressive strength (UCS), P_o^* is the normalized pressure $P_o^* = P_o / f_c$, P_o is hydrostatic pressure.

$$P_o = (\sigma_1 + 2\sigma_3) / 3 \quad (2.63)$$

$$\sigma_f = \sigma_1 - \sigma_3 \quad (2.64)$$

σ_1 and σ_3 are the maximum and minimum principal stress. F_r is the dynamic strain rate increase factor, $\dot{\varepsilon}_p$ is the strain rate, $\dot{\varepsilon}_p^*$ is the effective plastic strain, R_3 is the William Warnke function, and θ_l is the lode angle. Equation (2.65) defines the dependency of the strength in the strain rate in this model.

$$F_r(\dot{\varepsilon}_p, P) \begin{cases} \left(\frac{\dot{\varepsilon}_p^*}{\dot{\varepsilon}_o^{*c}} \right)^{\beta_c} & P \geq f_c / 3 \\ \frac{P + f_t / 3}{f_c / 3 + f_t / 3} \left(\frac{\dot{\varepsilon}_p^*}{\dot{\varepsilon}_o^{*t}} \right)^{\beta_c} - \frac{P - f_c / 3}{f_c / 3 + f_t / 3} \left(\frac{\dot{\varepsilon}_p^*}{\dot{\varepsilon}_o^{*c}} \right)^{\beta_t} & -f_t / 3 < P < f_c / 3 \\ \left(\frac{\dot{\varepsilon}_p^*}{\dot{\varepsilon}_o^{*t}} \right)^{\beta_c} & P \leq -f_t / 3 \end{cases} \quad (2.65)$$

Where $\dot{\varepsilon}_o^{*c}$ is the reference strain rate in compression = $3 \times 10^{-5} \text{ s}^{-1}$ and $\dot{\varepsilon}_o^{*t}$ is the reference strain rate in tension = $3 \times 10^{-6} \text{ s}^{-1}$, f_t is tensile strength, P is the pressure, and β_c and β_t are material constants in compression and tension, obtained from equations (2.66) and (2.67), respectively (Borrvall and Riedel, 2011). Equation (2.68) defines the failure surface.

$$\beta_c = 4 / (20 + 3f_c) \quad (2.66)$$

$$\beta_t = 2 / (20 + f_c) \quad (2.67)$$

$$\sigma_f^*(P_o^*, F_r) = A \left(P_o^* - F_r / 3 + (A / F_r)^{-1/N} \right)^N \quad 3P_o^* \geq F_r \quad (2.68)$$

Where σ_i^* is normalized strength, $\sigma_i^* = \sigma_i / f_c$, and N and A are failure surface parameters obtained experimentally.

In the RHT material model, the reduction of strength along the tensile meridian is governed by the relative pressure;

$$Q(P_o^*) = Q_o + BP_o^* \quad (2.69)$$

Where Q_o is the ratio between tensile and compressive radii meridians ranging from $0.51 \leq Q_o \leq 1$ and B is the lode angle dependency factor (Borrvall and Riedel, 2011). Q_o and B define material behavior under different stress states, where Q_o influences the material's resistance to failure under tensile stress and B influences how the material's tensile strength is reduced or modified along the tensile meridian.

When stress reaches the failure surface, damage strain accumulation governs damage evolution.

The damage variable of the RHT model (D) is calculated using equation (2.70).

$$D = \sum \frac{\Delta \varepsilon_m^P}{\varepsilon_f^P} \quad (2.70)$$

Where ε_m^P is the accumulated plastic strain and ε_f^P the plastic strain failure. When the hardening state reaches the ultimate strength of the rock, the damage accumulated from further inelastic loading is controlled by plastic strain. The plastic strain at failure is calculated using equation (2.71).

$$\varepsilon_f^P \begin{cases} D_1 (P_o^* - (1-D)P_t^*)^{D_2} & P_o^* \geq (1-D)P_t^* + (\varepsilon_m^P / D_1)^{\frac{1}{D_2}} \\ \varepsilon_m^P & P_o^* < (1-D)P_t^* + (\varepsilon_m^P / D_1)^{\frac{1}{D_2}} \end{cases} \quad (2.71)$$

Where P_t^* is failure cut-off pressure, and $D_1 = 0.04$ and $D_2 = 1.0$ are damage constants. More references on the RHT model can be found in Livermore Software Technology Corporation (2018) and Borrvall and Riedel (2011).

2.5.2.2 Explosive material modelling

Upon explosive detonation in the blasthole, the chemical reaction transforms the explosive material into explosion gases at very high pressure and temperature. There are different ways blast loads can be introduced into a simulation model. One is using the high explosive burn material and Jones-Wilkins-Lee (JWL) EOS to model explosive charge detonation. The JWL equation of state is a high-energy combustion model that can reliably predict higher explosion pressures. The model defines the pressure of detonation products P_{cj} using equation (2.72) (Lee et al., 1968)

$$P_{cj} = A \left(1 - \frac{\omega}{R_1 V_1} \right) e^{-R_1 V_1} + B \left(1 - \frac{\omega}{R_2 V_1} \right) e^{-R_2 V_1} + \frac{\omega E}{V_1} \quad (2.72)$$

A , B , R_1 , and R_2 and ω are material constants, E is detonation energy per unit volume, and V_1 is the relative specific volume of detonation products.

2.6 Summary of the chapter and Remarks

This chapter reviewed relevant material on rock fracturing and fragmentation by blasting, addressing several factors that affect blast outcomes and exploring the theories developed over the years to predict blast-induced fragmentation. It was noted that the effect of rock mass properties is often overlooked in predicting damage zones around the blasthole, fragmentation, and the resulting excavation. The review covered theories on wave properties, propagation, and

the influence of interfaces, which will be utilized in the upcoming chapters to discuss the effects of discontinuities.

The impact of higher loading rates on rock strengths and fracturing mechanisms was also examined, including studies on higher strain rates and the relationships used to estimate rock strengths under the strain rates experienced during blasting. Finally, the review discussed various approaches to estimating damage zones around the charge, with a detailed focus on the empirical/analytical approach and numerical simulations that will be employed in this study. An overview of the required data and how it is obtained was presented, including the relationships used to estimate parameters that are not commonly measured directly in the field. Detailed discussions on data collection and estimations will be covered in Chapter 4.

CHAPTER 3

METHODOLOGY

This chapter outlines the methodology employed in the study to estimate damage zones and model blast-induced fracturing. It provides a summary of the processes involved, including data collection, processing, analysis, and modelling.

3.1 Introduction

Blast fragmentation is influenced by several rock factors such as rock's physical and mechanical properties such as dynamic strength (tensile, compressive, and shear), density, Young's modulus, and Poisson's ratio, presence of structures, their properties and distribution, and the ability of the rock to absorb and transmit blast energy. Rock factors determine the type and quantity of explosive to use along with the geometrical design of the blast, the initiation type, and firing sequence and delays.

In blast design, engineers have control over the design and explosive choice and none over the geology and structures associated with the rock mass. To achieve the required outcomes, the designs and explosive choice must be matched to the encountered rock mass, and therefore, the knowledge of the interaction between the rock mass and explosive energy is essential. This chapter outlines the approaches used to assess the interaction between explosive energy and the rock mass to estimate the damage zones around the blasthole and model blast-induced rock fragmentation. The following sections summarize the steps involved in data collection, processing, analysis, and modelling. The study is based on field measurements and laboratory tests conducted at an open-pit hard-rock mine.

3.2 Determination of rock mass properties

Rock physical and mechanical properties govern the fragmentation process and distribution of blast energy in the rock mass. During blasting, the rock around the blasthole is pulverized, forming the crushed zone. The crushed zone extends to where the pressure falls below the dynamic compressive strength of the rock. The fracture zone is formed beyond the crushed zone and extends to where the pressure falls below the rock's dynamic tensile strength. Blastwave propagation depends on the rock density and Young's modulus. Rock's mechanical and structural

properties are necessary for evaluating the rock mass's transmissivity properties and estimating the extent of damage zones around the blasthole.

Laboratory tests and physical measurements for intact rock are performed to derive the rock's physical and mechanical properties, such as the density, the UCS, and tensile strength. These tests and inferences are used to estimate static elastic constants such as Young's Modulus and Poisson's ratio. Measurements of rock's strengths in the field are commonly done under static loading. The dynamic strengths can be estimated using relationships like those discussed in section 2.4.3.

The presence of discontinuities and their properties governs the stress wave propagation, gas pressure confinement, and effectiveness, and eventually, the overall fragmentation size distribution. The extent of damage zones is also impacted by the presence of structures. To accurately assess these effects, pit wall mapping is conducted to define rock structural features such as faults, joints, and rock contacts. Information such as structure types, orientation, size and type of infill material, persistence, groundwater conditions, and fracture frequency are collected.

3.3 Borehole pressure estimation

Explosive detonation produces a shock wave which is characterized by the shock wave pressure, particle velocity, and shock wave velocity and frequency. The shock wave pressure on the borehole wall is termed borehole pressure. There are several ways to obtain borehole pressure. It can be measured or estimated based on shock wave mechanics (section 2.4.1) or from the explosion pressure (section 2.3.2). Explosive density and the VOD are required to estimate detonation pressure from the expression in the equation (2.6). Detonation pressure acting on the borehole wall for a fully coupled hole is estimated to be 50% of the theoretical detonation

pressure. VOD and density measurements are usually conducted in the field as part of quality control to regulate explosive mixing and determine the efficiency of explosive detonation.

3.4 Analytical approach to estimate damage zones

To estimate the damage zones around the charge, the analytical approach in Figure 3-1 is suggested and implemented using the data collected from the mines. The approach is divided into steps to estimate the borehole pressure, estimate rock dynamic properties, determine stress wave attenuation, evaluate failure mechanisms, and estimate damage zones. Fundamental aspects of this approach include estimating borehole pressure from VOD and density measurements and blast energy-rock mass interaction through vibration monitoring to aid damage prediction. Energy attenuation, the sizes of damage zones around a blasthole, and the extent of useful energy are estimated from the steps and equations illustrated in Figure 3-1. Review of the analytical approach is presented in detail in section 2.5.1.

To compute the size of the crushed zone, which is estimated as the radius from the center of the blasthole, borehole pressure and the dynamic properties of the rock such as the UCS, Young's modulus, and Poisson's ratio are required. This calculation uses equations (2.43) to (2.46) while equations (2.39) to (2.42) are used to estimate the dynamic strengths. Although previous studies (Liu et al., 2018, Xie et al., 2017) show that these estimations can provide reasonable results, they have limitations due to variations in loading rates or material behavior. For critical applications, direct dynamic testing is recommended. The pressure at the end of the crushed zone is calculated using the pressure attenuation function in equation (2.47) which takes into account borehole pressure, crushed zone radius, P-wave velocity, and the VOD. The peak particle velocity (PPV) at the end of the crushed zone is then computed using equation (2.48).

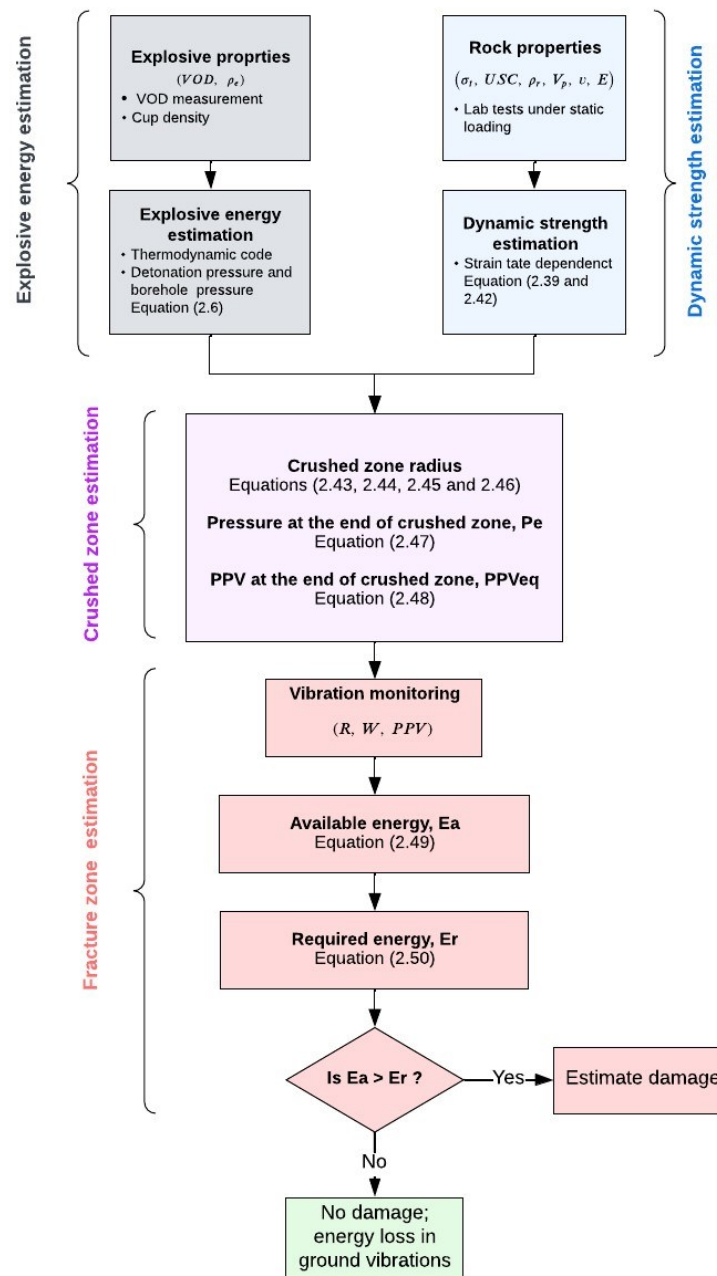


Figure 3-1: Analytical approach to estimate damage zones

Beyond the crushed zone, the fractured zone is estimated by determining the peak particle velocity (PPV) damage limit using the Forsyth equation (2.50), which calculates the strain energy required to initiate fracturing. The PPV attenuation from the blasthole is estimated using the square root scaled distance (SD_2) in equation (2.49). Factors such as the quantity of charge detonated, the

distance from the charge to the monitoring point, and the properties of the rock mass influence the PPV. PPV can be measured through near-field or far-field vibration monitoring. The attenuation function is derived from a fitted curve of PPV against the scaled distance, which allows PPV to be calculated at any distance from the charge.

When the PPV exceeds the critical threshold, new tensile fractures are formed. This critical PPV is determined by the dynamic tensile strength, Young's modulus, and longitudinal wave velocity. The size of the fractured zone is then estimated using equation (2.50). The estimations derived from the analytical method are validated through field blast measurements and by comparisons with estimations from other verified approaches, as discussed in Chapter 4.

3.5 A numerical approach to damage zone estimation

Due to data analysis limitations and the rock mass's complex nature, numerical modelling has been used to investigate stress wave behaviour and the response of rock material under blast loads. Simulations provide a better insight into the fragmentation process in a more simplified and controlled environment. The RHT constitutive material model introduced by Borrvall and Riedel (2011), which has features capable of modelling the dynamic behaviour of concrete, is useful in simulating rock fragmentation by blasting. This constitutive model involves interdependence between several micromechanical effects such as stress, strain, plastic strain, strain rate, damage, and material failure and can be implemented in general-purpose finite element code such as LS-DYNA.

The porous compaction model and the strength model govern the RHT model. The porous compaction model describes the material behavior under compression, accounting for the compaction of pores in the material. Governed by the increase in pressure, the porous compaction

model starts in the elastic region where the loading process is reversible. Beyond the pore crush pressure, porous compaction occurs accompanied by the material's reduced bulk modulus and volumetric stiffness. When the pressure reaches compaction pressure, the material is fully compacted; refer to Figure 2-10.

The strength model defines the material's resistance to deformation and failure under various stresses. The strength of the material, experienced stress, and strain rate effects govern the strength model. Surface failure is governed by parameters defining the ultimate strength of the rock in terms of compression, shear, and tension. Three limit surfaces define the strength model; the residual surface, yield surface, and failure surface, depending on the pressure, as seen in Figure 2-11. The model is elastic until it reaches the yield surface beyond which plastic strain dominates. The material's plastic strain and hardening properties are required to interpolate between the surfaces. When the failure surface is reached, the damage model governs damage evolution driven by material plastic strain.

Laboratory experiments and calculations are conducted to estimate the parameters needed for the RHT material model and the explosive properties to be used in the simulation. The detonation of the explosive charge is modeled using a high explosive burn material model, with the Jones-Wilkins-Lee EOS parameters derived from the explosive properties. The simulation model results, such as the pressure and PPV attenuations as well as the extent of damage zones around the blasthole, are obtained. These results are validated through field blast measurements and by comparing them with estimations from other verified approaches.

Figure 3-2 summarizes the whole process in a flowchart with the steps used to prepare the simulation models, the validation, the variables analyzed, and the outcomes. The details for the

modelling parameters are discussed in section 2.5.2. The model's parameters estimations, simulation, verification, and validation are covered in Chapter 4. Chapter 5 covers the analysis of variable explosives and rock mass properties on blast outcomes and Chapter 6 the blast-induced fragmentation modelling and techniques to maximize fracturing in the jointed rock mass.

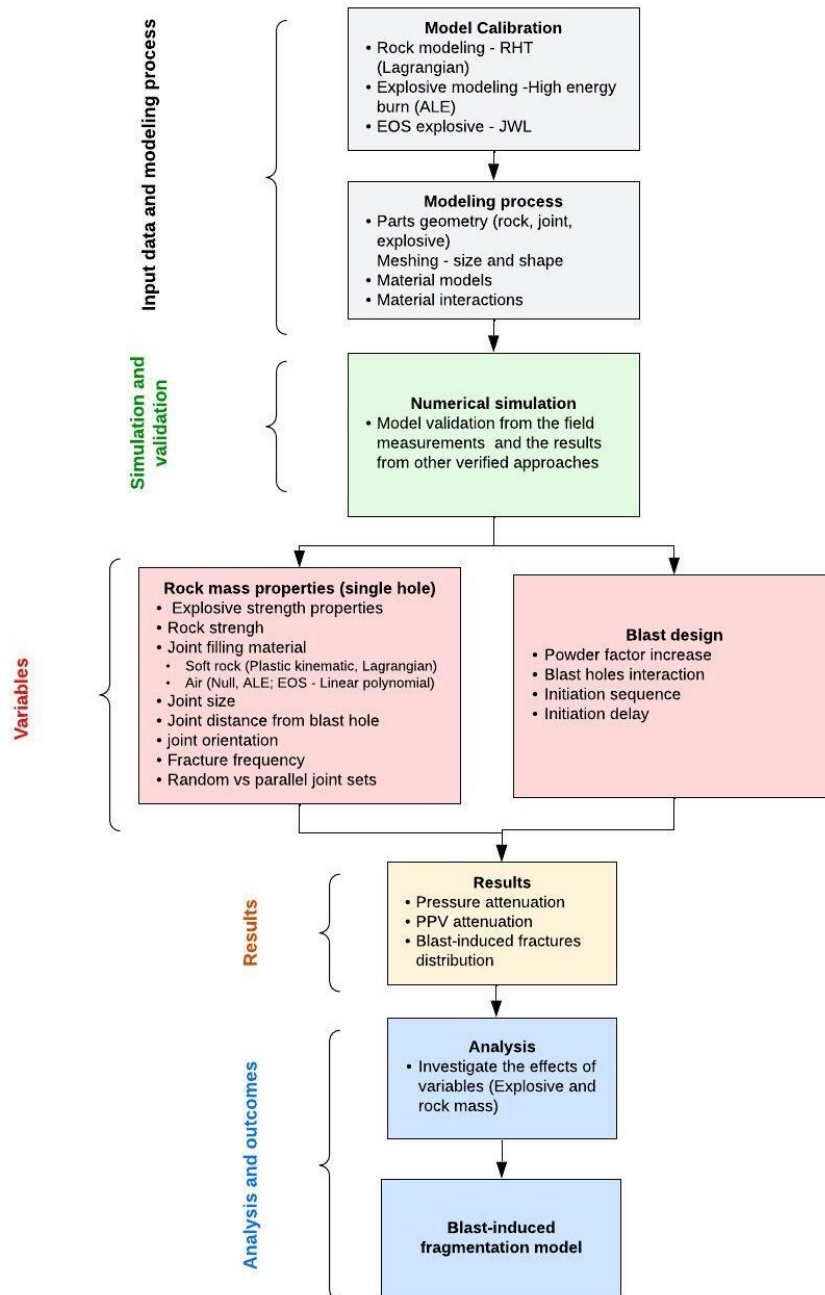


Figure 3-2: Numerical simulation flowchart

3.6 Summary and Conclusion

This chapter presents the analytical approach and finite element modelling to be implemented to estimate damage zones around the blasthole and investigate the influence of explosive and rock mass properties, and design parameters on the blast outcomes. The approaches aim at modelling blast-induced fragmentation. Explosive energy is the function of the explosive type, density, and detonation efficiency which is monitored by measuring VOD. The rock mass is made up of rock and structures, which influence the distribution of explosive energy and fractures.

The analytical approach is simple to use and can easily accommodate the dynamic strength of the rock in the estimation of damage zones but it is limited in evaluating the influence of various rock mass properties. The numerical modelling takes care of both the dynamic strength and the effect of rock mass properties. These approaches are used to study stress wave propagation, fracture mechanisms, and crack propagation. The models are created based on the field data, and results are compared with the measurements from field blasts and estimations using other approaches.

The analysis is used to suggest a blast-induced fragmentation model based on balancing explosive energy produced with rock-specific surface energy, and stress wave transfer efficiency function of encountered rock and structural properties. From these, decisions on explosive selection, the powder factor, geometric design, firing sequence, and delays can be made as illustrated by Figure 3-3.

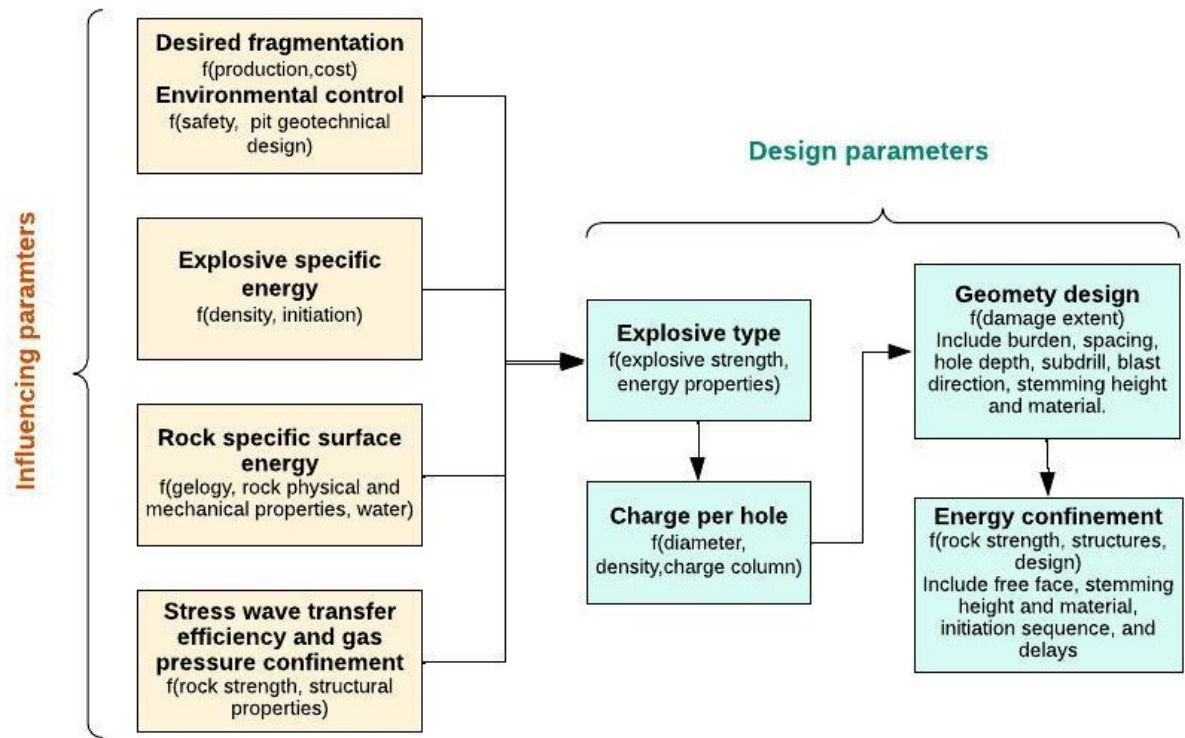


Figure 3-3: Consideration factors and design parameters in the blast-induced fragmentation model

CHAPTER 4

ANALYTICAL APPROACH AND FINITE ELEMENT MODELLING OF DAMAGE ZONES

This chapter details data collection and estimation of input parameters to analytical and numerical models. It also covers the estimation of damage zones using these approaches and the results verification and validation.

A version of this chapter was published as:

Dotto, MS., Pourrahimian, Y., Joseph, T., and Apel, D. (2022), "Assessment of blast energy usage and induced rock damage in hard rock surface mines", CIM Journal, 13(4), 166-80.
<https://doi.org/10.1080/19236026.2022.2126924> .

4.1 Introduction

For decades, explosives have been the primary method for rock breakage in mining and quarry operations. While alternative techniques exist, blasting remains the most practical and cost-effective means of rock fragmentation. The blasting process is influenced by several factors, particularly the properties of the explosives and the rock mass. An understanding of how explosive energy interacts with the rock mass is essential for optimizing blast design and achieving desired outcomes. This involves analyzing how stress waves and expanding gases generated during explosive detonation interact with the rock. Key factors in this process include the chemical and mechanical properties of the explosives which determine the energy release, and the characteristics of the rock mass, which govern the extent of fracturing and damage.

4.2 Blast parameters

A series of tests and measurements were conducted both in the field and in the university's rock mechanics lab to obtain the properties of explosives and the physical and mechanical properties of the rocks, as well as to gain insights into rock fracturing mechanics. Pit wall mapping was performed to characterize the rock mass. This data was then applied in the analytical approach and finite element simulation to estimate the damage zones around the blasthole.

4.2.1 Rock's physical and mechanical properties

This study is based on data collected from Geita Gold Mine (GGM), Nyankanga Pit in Tanzania. Nyankanga Geology comprises a banded iron formation (BIF) and diorite as host rocks. Mineralization is controlled by tectonic structures within fault zones passing through the host rock. The banded iron formation is of sedimentary origin, consisting of cyclic deposition of iron-rich sediments and chert. The diorite is an intrusive igneous rock with variable mineral composition and grain size, defining the Nyankanga Intrusive Complex. The principal composition

of the Nyankanga diorite is plagioclase-rich diorite (DPH) and hornblende-rich diorite (DHP). Porphyry intrusions within the fault zones are the youngest Nyankanga geology. The intrusions are mainly feldspar porphyry (FP) and Quartz feldspar porphyry (QFP) dykes. Figure 4-1 and Figure 4-2 show the location of the bench studied and the lithology distribution, respectively. The rock quality designation (RQD) was estimated using the Deere and Deere (1988) approach on core samples of sizes NQ (47.6 mm) and HQ (63.5 mm) from exploration drilling. The orientation of drill holes ranged from 52 to 79° dip and 178 to 196° azimuth. The Nyankanga rock mass rock is within the “good” range which is RQD ranging from 75% to 90% as shown in Figure 4-2.

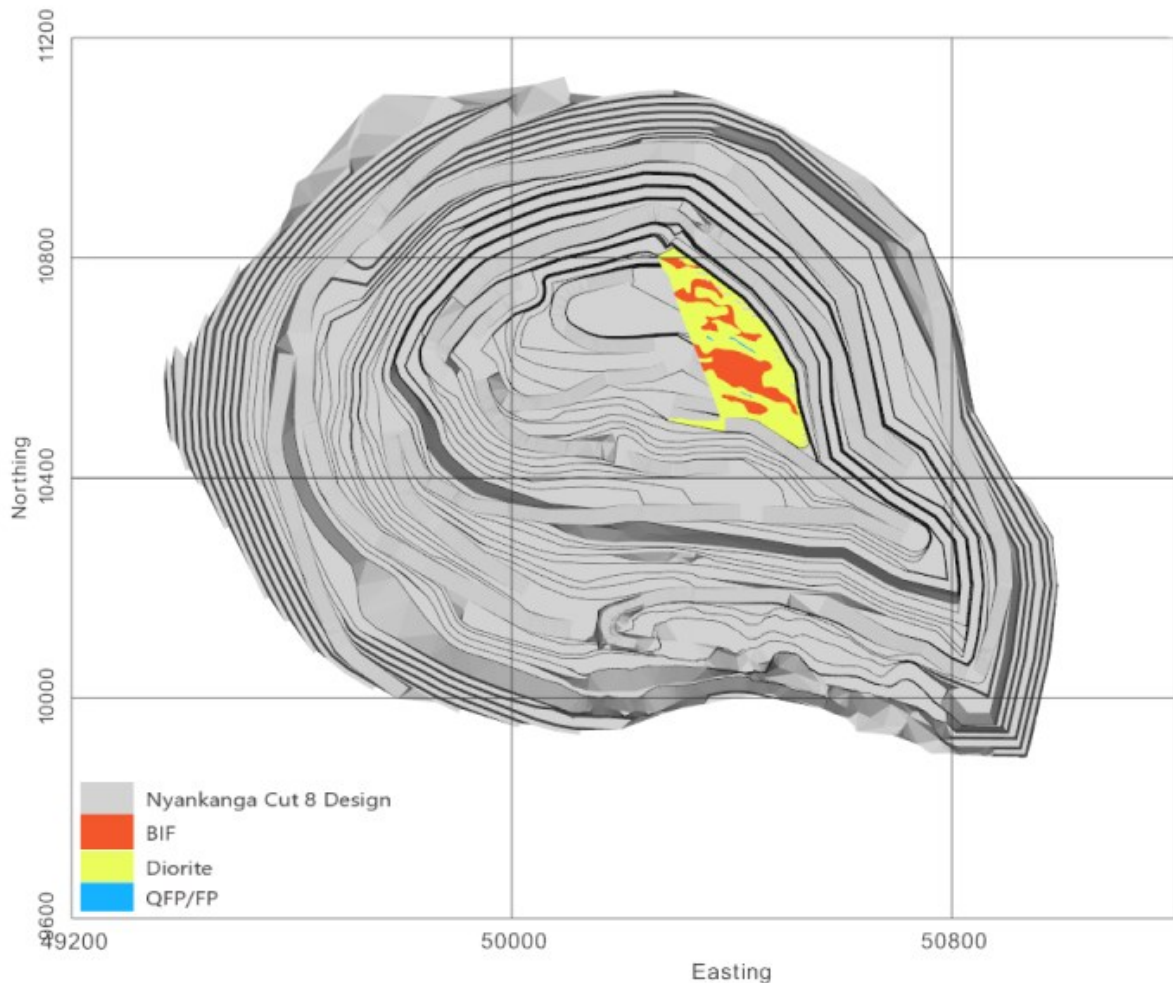


Figure 4-1: Nyankanga pit pushback 8 design showing the study bench

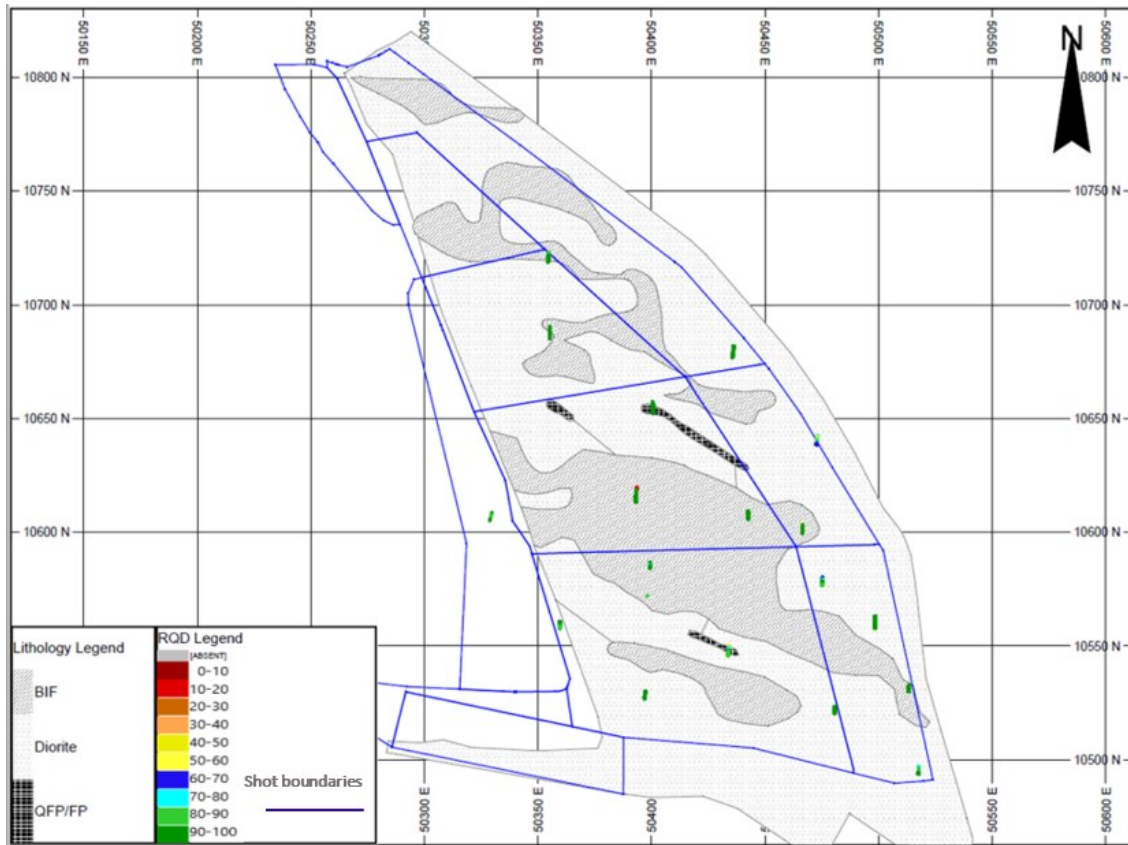


Figure 4-2: Nyankanga Pit Cut 8 Bench 920_910 lithology distribution.

BIF: banded iron formation; QFP: quartz feldspar porphyry; FP: feldspar porphyry; RQD: rock quality designation

Physical measurements and rock tests are conducted to gather the physical and mechanical properties of the rock. Intact rock strength can be obtained through rock tests such as the uniaxial compressive strength test and the Brazilian tensile strength test. Sonic logging measures the travel time of an elastic wave in the rock. Sonic logging is conducted using handheld equipment UK1401 p-wave tester which sends pressure wave into the sample from the transmitter probe and records the time it takes the wave to reach the receiver probe. The distance between the probes and the time taken are used to calculate wave velocity. Wave speed in the rock is affected by porosity, permeability, and mineralogical composition; therefore, it indicates a change in lithology or the presence of rock structures. For the four rock types, the P-wave velocities are summarized in Table 4-1.

Table 4-1: P-wave speed measurements

Rock type	BIF	DHP	DPH	FP/QFP
Maximum V_p , (m/s)	5880	6200	6300	5960
Mean V_p , (m/s)	4369	5089	4683	4481
V_p standard deviation	1466	1278	1453	1685
Number of samples	34	61	65	27

DPH: plagioclase-rich diorite; DHP: hornblende-rich diorite; BIF: banded iron formation; QFP: quartz-rich porphyry; FP: felsic porphyry

The Brazilian tensile strength test is a simple indirect test method to obtain the tensile strength of materials such as rock, concrete, etc. The nature of the stress field applied to the rock is dependent on the geometry of the loading plate and the orientation of the rock sample. Brazilian tensile strength tests were conducted to determine the tensile strength of different rock samples following the ASTM standards (ASTM, 2008). Tensile strength varies depending on the rock type. A CMTmulti tester – 178 digital multi-testing machine was used under UCS testing settings for these tests. Drop-down speed varied from 0.05 mm/min to 0.5 mm/min. Core samples were cut in a way that the thickness was half the core diameter i.e.; 24 mm thick for 48 mm diameter samples.

The test specimens were placed between loading platens aligned with the loading axis of the testing machine. Pre-loading was applied slowly until the top plate touched the sample with little or no load on it. A continuously increased load was applied by moving the top plate at a rate set to provide constant loading until the sample failed. It is recommended that, for static tensile strength, failure should occur within 1 to 10 minutes of applying, where the loading rate is between 0.05 and 0.35MPa/s. The recorded maximum sustained load was used to calculate tangential strength from equation (3.1).

$$\sigma_t = \frac{2P}{\pi tD} \quad (3.1)$$

Where σ_t is tensile strength in MPa, P is the maximum applied load in N, D is sample diameter in mm and t is sample thickness in mm. The results obtained are summarized in Table 4-2.

Table 4-2: Brazilian tensile strength test results

Sample serial number	Rock type	Loading rate (mm/min)	Max Load (N)	Tensile strength (MPa)	Average Tensile strength (MPa)
3	DHP	0.50	24,839	13.73	15.21
4			34,422	19.02	
6		0.20	33,077	18.28	
7			17,761	9.82	
2	BIF	0.5	26,503	14.65	14.16
8		0.20	31,815	17.58	
9			18,564	10.26	

DHP: hornblende-rich diorite; BIF: banded iron formation

The Uniaxial compressive strength tests were conducted following ISRM standards (ISRM, 2007). Density measurements were also taken from the same samples. The tests were conducted using CMT testing compression machine model CT380. Figure 4-3 shows the UCS experiment setup with a crushed sample. Samples were cut in a way that the length is around 2.1 times the diameter; the length was 100 mm for a 48 mm diameter core. The applied loading rate was 10 KN/s (equal to $7.2 \times 10^{-5} \text{ s}^{-1}$ strain rate). The UCS is calculated from the maximum load applied (P_{\max}) using equation (3.2); A is the initial cross-section area of the sample. Table 4-3 shows the UCS and density values obtained for various rock types.



Figure 4-3: Uniaxial compressive strength test setup

$$UCS = \frac{P_{\max}}{A} \quad (3.2)$$

Elastic constants, Young's modulus, (E), and Poisson's ratio (ν) were also estimated from these tests. The E is calculated from the ratio of axial stress and axial strain [$E = \Delta\sigma / \Delta\varepsilon_a$; $\varepsilon_a = \Delta l / l_0$] l_0 is the original length and Δl is a change in axial length measured as the difference in the distance between the loading plates before loading (when the plates are in contact with the sample and the load is zero) and after failure. The Poisson's ratio is the ratio of diametric strain to axial strain [$\nu = \varepsilon_d / \varepsilon_a$; $\varepsilon_a = \Delta_d / D$]. Here Δ_d is a change in diameter, and D is the initial diameter. The change in diameter Δ_d was measured by the difference (in the diameter) of the wrapped copper wire around the sample before and after failure. Both measurements were compared with results obtained from previous assessments of the same rock types, as recorded in the mine's Geotech database. This cross-referencing provided confidence in the accuracy and consistency of the current measurements. With E and ν values, bulk modulus (K_m) and shear modulus (G_m) can be estimated from equations (3.3) and (3.4), respectively.

$$K_m = \frac{E}{3(1-2\nu)} \quad (3.3)$$

$$G_m = \frac{E}{2(1+\nu)} \quad (3.4)$$

The tested samples' results are shown in Table 4-4. Studies have shown that the compressive strength of most rocks is 8 to 10 times the tensile strength (Cai, 2010, Sheorey, 1997). From the tests, the ratios of UCS to tensile strength are 8.9 and 7.3 for BIF and DHP, respectively. When the loading rate was varied from 5KN/s to 20 KN/s for the DPH rock it was observed that the UCS increased with the loading rate as seen in Figure 4-4.

Table 4-3: UCS and density for rock types

Sample	Rock type	Density (t/m ³)	Average density (t/m ³)	Max Load, P _{max} (KN)	UCS (MPa)	average UCS (MPa)
1	DHP	2.62	2.62	210	115.83	110.39
2		2.62		190	104.83	
3	BIF	2.81	2.68	224	123.9	126.02±8.03
4		2.51		146	80.74	
5		3.08		165	91.18	
6		2.64		246	135.86	
7		2.48		213	117.76	
8		2.56		186	102.51	
9		2.69		271	149.82	
10	DPH	2.67	2.67	61	33.93	46.36±5.22
11		2.64		76	41.72	
12		2.7		96	52.94	
13		2.66		103	56.75	

DPH: plagioclase-rich diorite; DHP: hornblende-rich diorite; BIF: banded iron formation

Table 4-4: Poisson's ratio and Young's modulus for rock types

Rock type	DPH	BIF	DHP
Young's modulus (GPa)	76.73	90.83	-
Poisson's ratio	0.25	0.24	-
UCS to tensile strength ratio	-	8.90	7.30

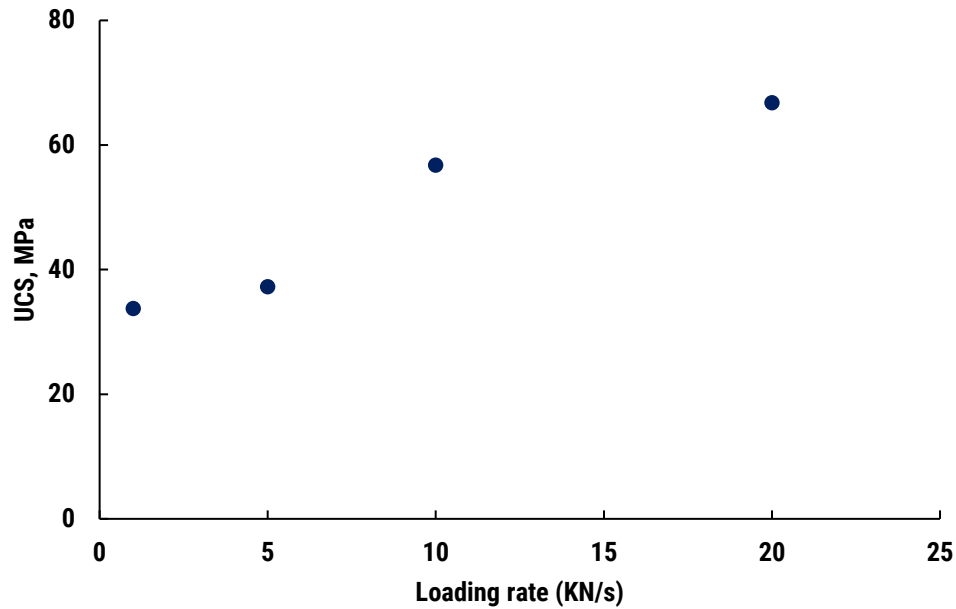


Figure 4-4: Loading rate effect on UCS for DHP rock

4.2.2 Structural mapping

A combination of Sirovision and scanline mapping was done on the Nyankanga cut 8 on eastern pit wall bench 920_910 to define the main wall structures where prominent structures were identified and mapped. The mapping revealed that most of the structures in the Nyankanga Pit dip between 50° and 70° , with a dip direction ranging from 320° to 350° . A stereonet summary of this mapping data is presented in Figure 4-5 while the joint sets summary is outlined in Table 4-5. The joints are spaced 0.2–0.42 m along the scanline, the surfaces are slightly rough, and joint apertures are mostly less than 5 mm filled with clay or calcite. The groundwater condition is generally moist, with water dripping in a few areas. The mapping results are presented in APPENDIX A.

Mapping data	Dip direction	Dip angle
Count	134	134
Minimum	8	17
Maximum	353.8	90
Average	227.39	57.4
Median	239.7	58.5
StDev	97.49	19.65
CoefOfVar	0.43	0.34
Perc25	135	42.75
Perc50	239.7	58.5
Perc75	321.4	72.38
Perc95	350	88

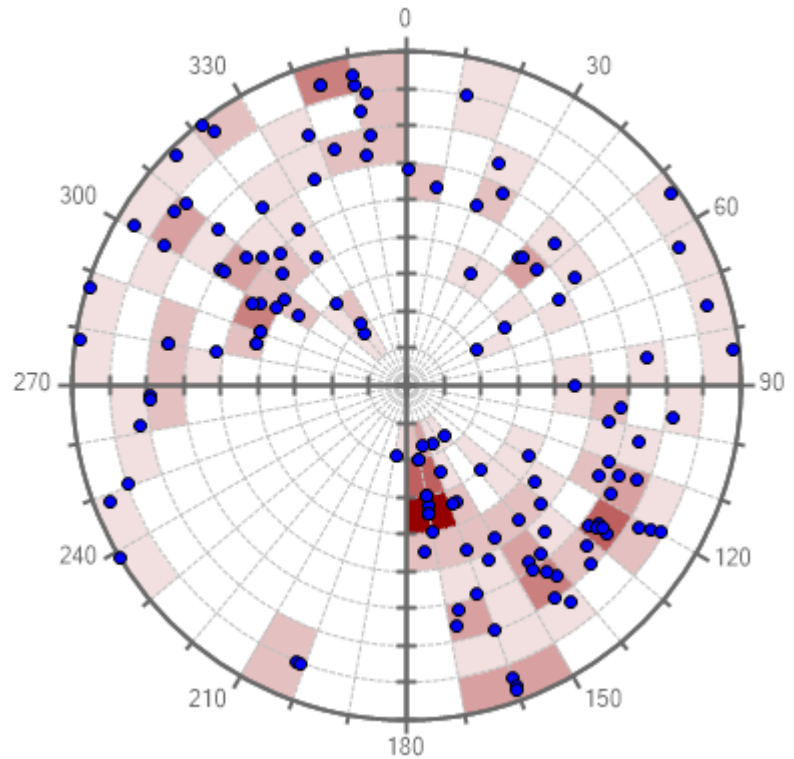


Figure 4-5: The stereonet of the mapped structures

Table 4-5: The joint sets summary

Joint Set	Average Dip (°)	Average Dip Direction (°)	Size Range (mm)	Number of joints
Set 1	65-75	320-350	3-10	52
Set 2	60-70	120-140	2-10	26
Set 3	80-90	170-190	5-10	20

4.2.3 Point load test

Point load tests are widely used on cylindrical cores or irregular specimens in rock engineering to determine the point load strength index, I_s (PLSI). These tests are simple to perform with little or no specimen preparation required and can be done in the field using simple tools or in the laboratory using testing machines. PLSI is used as a quicker way to estimate the UCS of rock

samples. In mine sites, cores are usually cut into two equal parts, and one is sent to the laboratory for geochemical analysis. While estimating PLSI using ISRM standardized methods (Franklin, 1985) from full-core or irregular lumps is easy, it is not a straightforward approach to the half-core samples.

I_s is determined from a rock specimen of any shape or size, and by applying correction to a standard 50mm sample, the standardized PLSI, ($I_{s(50)}$) is obtained. The standard requirements for the test sample for estimation of I_s are as shown in Figure 4-6. The I_s is estimated from the equation (3.5) where P is the failure load in kN and D_e is the equivalent diameter in mm.

$$I_s = \frac{P}{D_e^2} \quad (3.5)$$

If the specimen is loaded diametrically (Figure 4-6 (a)), D_e equals the diameter of the sample and the distance between the loading plates. For an irregular lump loaded axially (Figure 4-6(b)), D_e is defined from equation(3.6).

$$D_e = \left(\frac{4WD}{\pi} \right)^{0.5} \quad \text{and} \quad W = \frac{W_1 + W_2}{2} \quad (3.6)$$

The ratio D/W is at least 1/3 and the sample length is at least 0.5W.

For half a core sample the area is given by $A_{half} = \frac{\pi D^2}{8}$; the equivalent diameter D_e can be estimated from equation (3.7).

$$D_e^2 = \frac{4A_{half}}{\pi} \quad (3.7)$$

Correcting I_s to a standard sample size of 50 mm, $I_{s(50)}$ ISRM suggests a correction factor CF in equation (3.8).

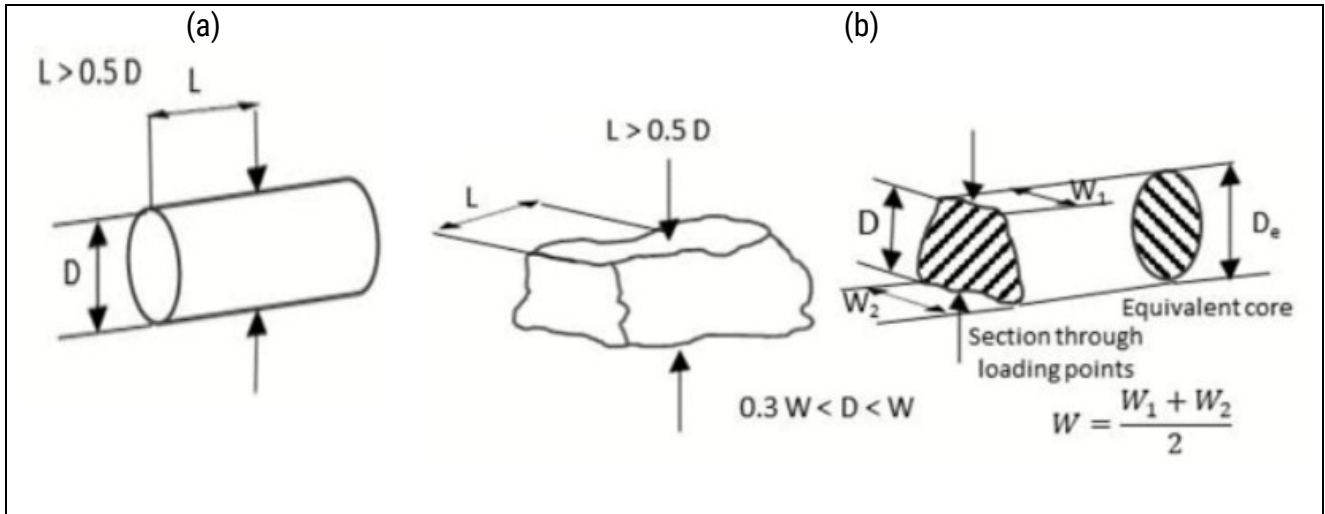


Figure 4-6: Specimen shapes suggested by ISRM 1985

$$I_{s(50)} = I_s \times CF \quad \text{where} \quad CF = \left(\frac{D_e}{50} \right)^{0.45} \quad (3.8)$$

Given the importance of UCS in rock engineering design and analysis projects, several studies have been conducted to estimate UCS from simpler tests such as PLSI. The tests conducted by Yin et al. (2017) on granitic rock samples determined that the ratio of UCS to PLSI is around 22.3. Similar tests done by Şahin et al. (2020) on half-core samples from 12 different rock samples determined that the UCS ranges from 12.3 to 14.9 times the PLSI.

Point Load Strength Index (PLSI) tests were conducted in the field to establish the correlation between Uniaxial Compressive Strength (UCS) and PLSI for the three rock types under study: plagioclase-rich diorite (DPH), hornblende-rich diorite (DHP), and banded iron formation (BIF). Half-core samples were used. Sample preparations and test procedures followed the ISRM standards (Franklin, 1985) and calculations of PLSI, ($I_{s(50)}$) using the relationships suggested by Şahin et al. (2020). Portable equipment; Point Load Tester model 6510 in Figure 4-7 was used to crush the sample and obtain the failure load (P). Relationships in equations (3.5), (3.7), and (3.8) were used to calculate $I_{s(50)}$. The test results are presented in Table 4-6.

Table 4-6: Relationship between UCS and $I_{s(50)}$

Rock type	UCS (MPa) Mean±STD	Number of samples	PLSI (MPa) Mean±STD	Number of samples	UCS to $I_{s(50)}$ ratio
DHP	110.39	2	6.78±1.58	20	8.58
BIF	126.02±8.03	7	6.11±2.57	13	18.60
DPH	46.36±5.22	4	5.40±1.13	12	18.06



Figure 4-7: Point Load Strength index test setup

4.2.3.1 Dynamic properties of the rock

The fracture behavior of rocks depends on mechanical properties and rock structural features such as composition, grain size, shape, and microstructure as discussed in section 2.4.3. Grain

shape and size significantly influence the material's response to static and dynamic loading. Smaller, equidimensional grains offer greater resistance to fracturing under static loading by minimizing stress concentration. In dynamic loading, the smaller, equidimensional grains are better at absorbing and dissipating energy, thereby reducing the likelihood of failure compared to larger or elongated grains.

The mechanical testing performed in this study occurred under quasi-static stress with the strain curve defined by the constant strain rate ranging from 10^{-5} to 10^{-3} s^{-1} . Blast wave loading is a high strain rate phase estimated to occur between 10^1 to 10^4 s^{-1} (Chitombo et al., 1999, Fleetwood et al., 2009, Zhang and Zhao, 2014, Sun, 2013). In this range, a significant increase in rock strength has been observed. From equations (2.39) and (2.42) the dynamic UCS and tensile strength can be estimated for strain rates higher than 10 s^{-1} . Assuming that the crushing zone forms at a strain rate ranging from 100 to 1000 s^{-1} and the fracture zone between 10 and 100 s^{-1} the values for dynamic compressive strength and dynamic tensile strength for BIF are estimated from static values as seen in Table 4-7.

The dynamic Young's modulus was estimated using equation (2.45). The known static Poisson's ratio is used in a position of dynamic Poisson's ratio in this study. The formula to estimate the dynamic Poisson ratio from P-wave velocity (V_p) and S-wave velocity (V_s) in equation (2.46) is shown to be suitable for low-stress waves (Sun, 2013) which is not the case in high-stress environments such as blasting.

Table 4-7: Estimated rock dynamic properties

Parameter (Unit)	Static value	DIF	Dynamic value
UCS (MPa)	126.02	2 - 4.16	252.16 - 524.24
Tensile strength (MPa)	14.16	1.7 - 3.48	24.10 - 49.28
Young's modulus (GPa)	90.83	-	122.76
Poisson ratio	0.24	-	0.24

4.2.4 Blast design and explosive properties

The arrangement of blasthole rows in a shot includes a pre-split line followed by the two rows of buffer holes for wall control, and then production blastholes which is a bigger portion of the blast shot. Detailed pattern parameters are presented in Figure 4-8 and Table 4-8. The blastholes are drilled vertically in a staggered pattern and charged with a specially manufactured emulsion by ORICA; Fortis extra with properties summarized in Table 4-9 (ORICA, 2018). The detonation method used is a bottom-up approach, with the booster and detonator positioned 1.5 meters from the bottom of the blasthole.

VOD measurements were conducted in the field to determine the efficiency of explosive detonation using MREL's Micro-Trap Data Recorder. The equipment operates under the constant resistance wire theory described in section 2.2.2. Figure 4-9 shows a sample of VOD measurements. Cup density measurements were also completed to monitor explosive gassing and obtain the final explosive density. Table 4-10 presents details of measured VOD and explosive density. The blasthole depths do not match the design precisely due to an uneven bench floor and operational errors.

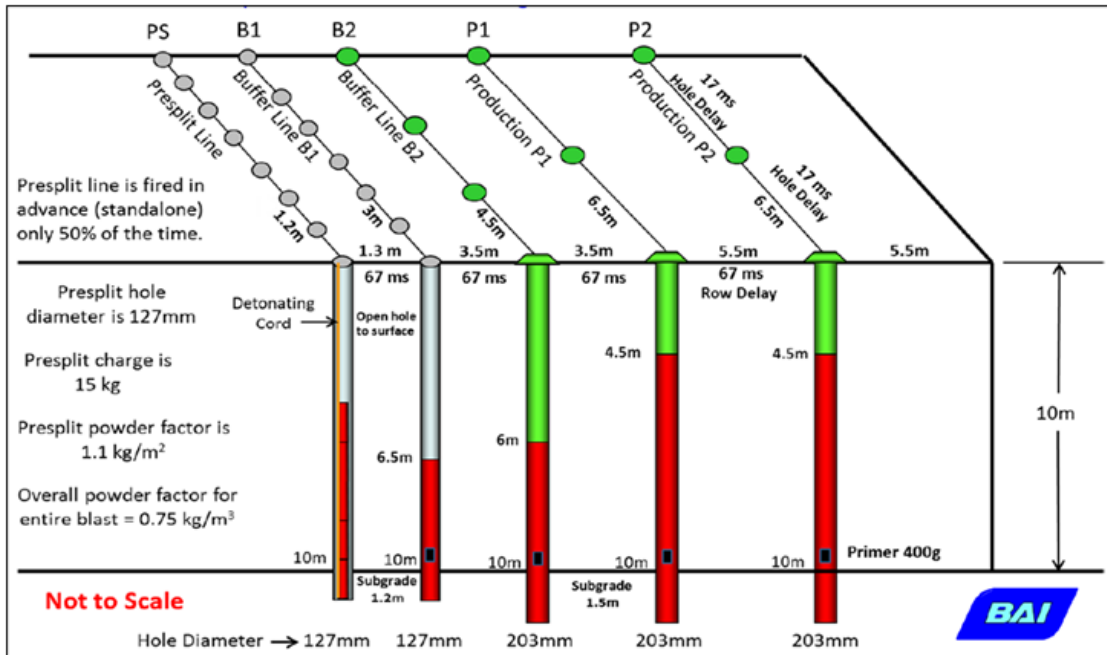


Figure 4-8: Blast design layout

Table 4-8: Blast design parameters

Parameter (unit)	Symbol	Pre-split	Buffer 1	Buffer 2	Production
Hole diameter (mm)	D	127	127	203	203
Burden (m)	B	1.3	3.5	3.5	5.5
Spacing (m)	S	1.2	3	4.5	6.5
Bench Height (m)	H	10	10	10	10
Sub-drilling (m)	S _d	1.2	1.2	1.5	1.5
Hole depth (m)	H _d	11.2	11.2	11.5	11.5
Stemming length	S _l	-	6.5	6	4.5
Explosive density(kg/m ³)	ρ _e	-	1,207	1,207	1,207
Maximum instantaneous charge (kg)	W	15	73	210	267
Powder factor (kg/m ³)	PF	-	0.70	-	0.75

Table 4-9: Explosive properties

Explosive property (units)	Value
Density (g/cm ³)	1.10 – 1.25
Minimum diameter (mm)	64
VOD (km/s)	4.1 – 6.7
Relative Effective Energy (REE), (%)	151 - 189
Bulk Energy (MJ/kg)	3.47 – 4.35
Priming	Electronic detonators (I-kon)
Booster	Trojan 400 g boosters
Hole-to-hole delay (ms)	2 - 8
Row-to-row delay (ms)	100

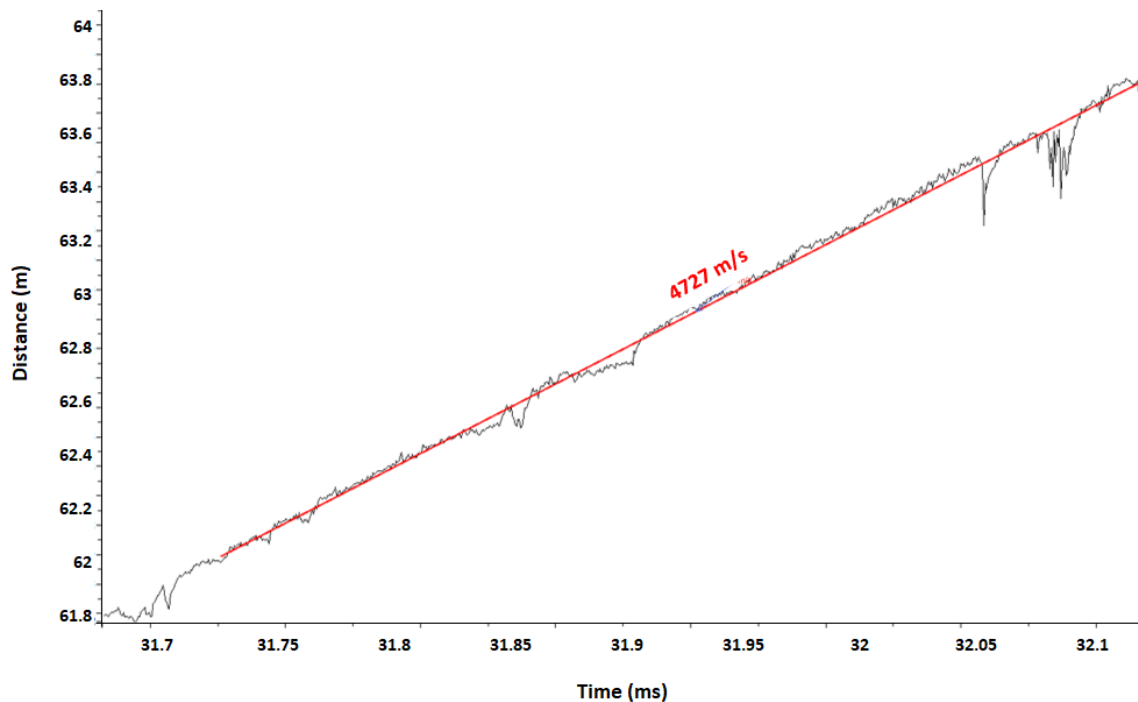


Figure 4-9: VOD measurement from blasthole EC3

Table 4-10: VOD and explosive density measurements

Pit/Lavel/Shot	Hole ID	Rock properties	Hole depth (m)	Initial density (kg/m ³)	Final density (kg/m ³)	VOD (m/s)
Nyankanga 8/910/ 6	K02	Hard, less fractured	12.8	1250	1180	4401.5
Nyamulilima 1/1460/3&4	EC1	Sub-soil	10	1265	1217	4694.0
Nyamulilima 1/1460/3&4	EC2	Transitional rock	9.8	1265	1217	5334.0
Nyamulilima 1/1460/3&4	EC3	Sub-soil	9.4	1265	1217	4727.0

4.3 Blast monitoring

Blast monitoring involved measurements of ground vibrations and visual observations. InstanTel Micromate, commonly used in far-field monitoring was used to monitor vibration and air overpressure. The geophone was positioned at different locations for various blast shots, and the monitoring distance was calculated as the distance from the geophone to the specific blasthole that detonated at the corresponding delay, following the designed initiation sequence. Data recorded over five production shots indicated wave perpendicular velocity components in longitudinal (Long), transverse (Trans), and vertical (Vert) directions measured in mm/s. The sampling frequency was set to 2,048 samples per second, with a lower trigger level of 5 mm/s, which activates the geophone to collect vibration data when the shot is initiated. The seismograph also recorded wave frequencies or duration of vibration, peak accelerations (g), and air overpressure level (Pa) for each event. The geophone recording range is limited to 254 mm/s and the air overpressure (air blast) microphone is limited to 500 Pa.

Based on the Office of Surface Mining, (OSM), among the measured particle orthogonal velocities, the component with the greatest amplitude is reported as the peak particle velocity (PPV). In this case, as far as blast damage is concerned, the peak particle velocity is considered the peak vector sum (PVS) of the three components. Figure 4-10 shows a sample vibration monitoring setup and the calculated PVS for the same shot are shown in Figure 4-11.

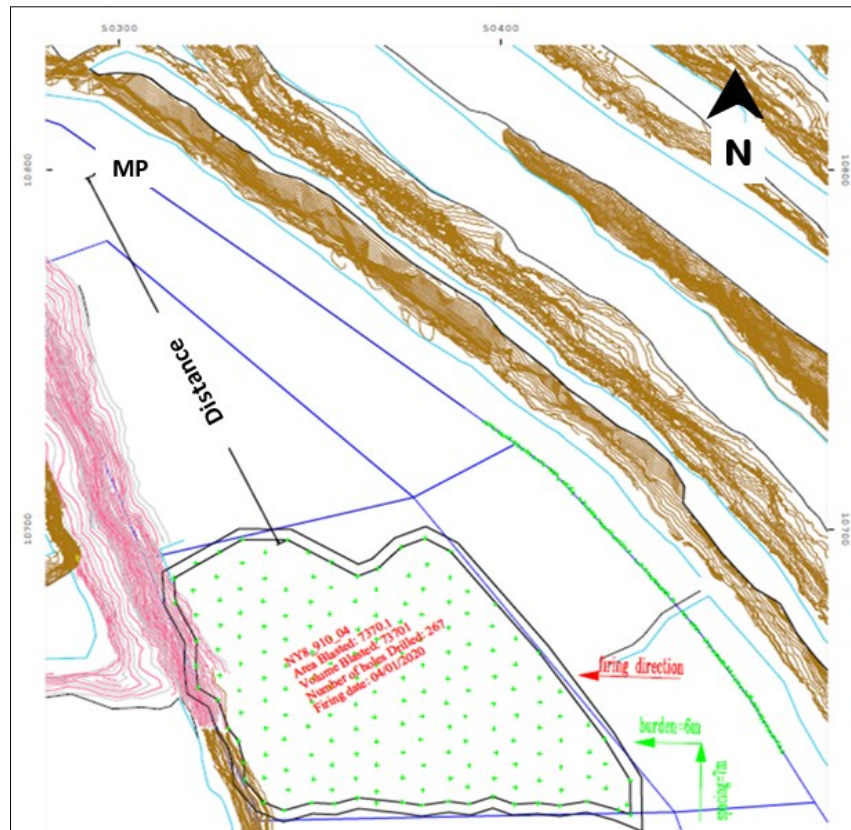


Figure 4-10: Vibration monitoring shot NY8_910_04

The data obtained was filtered, and a relationship between the scaled distance (SD_2) and particle velocity was derived using equation (2.49) as seen in Table 4-11 and Figure 4-12. The correlation coefficient of 0.86 indicates a strong relationship between PPV and scaled distance, suggesting that the model fits the data well. However, this conclusion is based on a small sample size, which may not fully capture the variability in the data. For critical applications, it is essential to increase

the sample size to ensure that the results are reliable and can be confidently applied to predict outcomes in similar scenarios.

Although frequency is a crucial factor in estimating damage during blasting operations, it was not analyzed in this study. The Micromate analyzes frequencies ranging from 2 to 250 Hz. The dominant frequency is defined as the frequency with the maximum amplitude over the whole frequency range. The Fast Fourier Transform (FFT) frequency recorded for each channel ranged from 19 to 55 Hz at a distance range of 122 to 225m. The waveforms for shot 910_3 and shot 920_6 were not calculated. According to InstanTel (2015), this can be caused by the complex nature of the waveforms or large offset values. From the visual observation during and after blasting, there was no indication of premature escape of explosive energy or explosive malfunction in the form of stemming ejection, excessive fumes, or misfires.

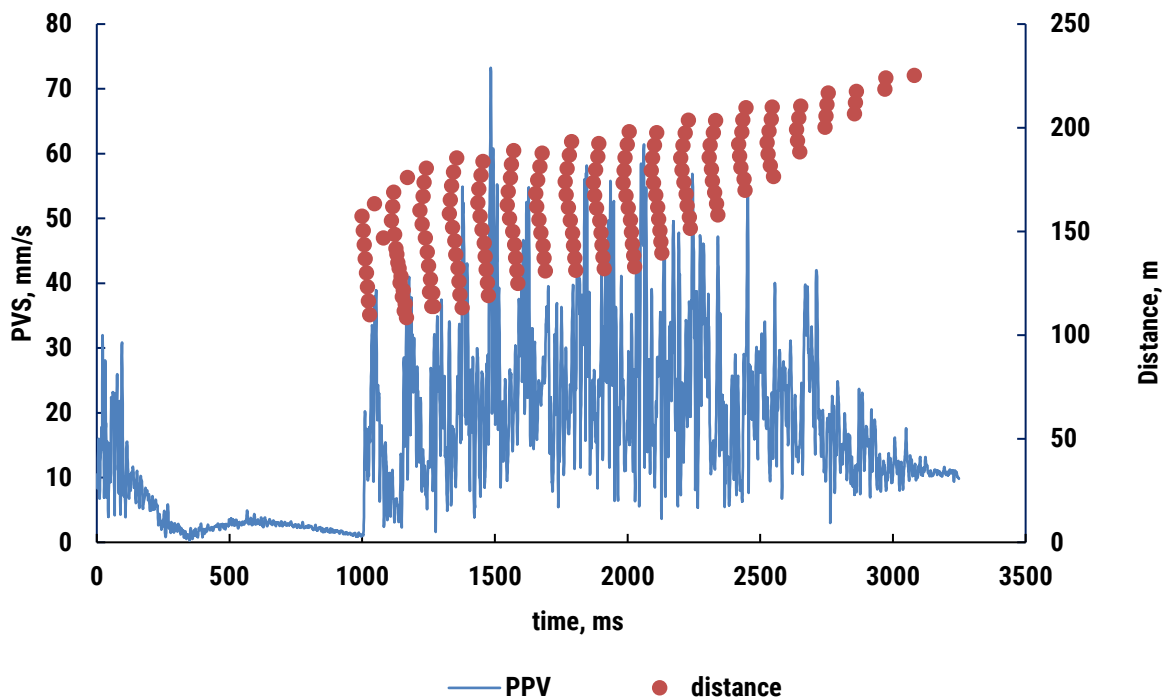


Figure 4-11: Resultant peak particle velocity on Shot 910#4

Table 4-11: Vibration monitoring

Shot number	Distance (m)	Charge size (kg) (in 8ms delay)	SD ₂ (m/kg ^{0.5})	PVS (mm/s)	Overpressure (Pa)
910_3	82.82	553	3.52	110.20	> 500
910_4	122.13	553	5.19	71.77	> 500
910_5	206.93	553	8.80	47.03	219.4
910_6	225.26	1,106	6.77	21.48	493.8
920_6	550.49	277	33.11	8.52	365.6

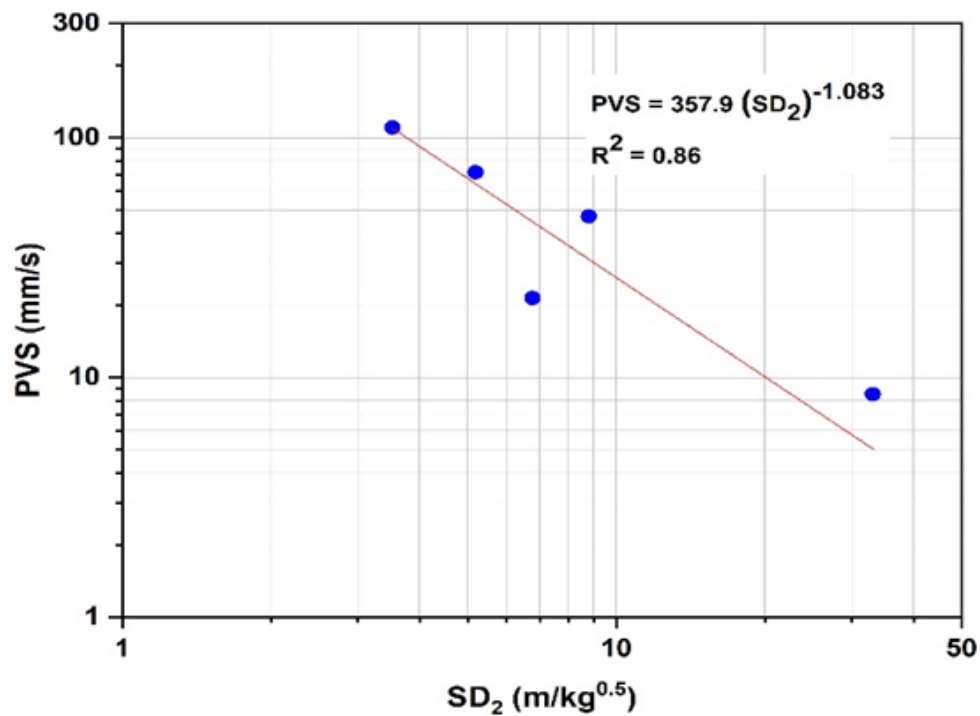


Figure 4-12: Particle velocity attenuation with scaled distance

4.4 Analytical approach to estimating damage zones

Several methodologies have been presented to estimate and assess damage zones around the blastholes. Due to the complexity and uncertainty of the input parameters especially the rock

mass, assumptions are made which limit the applications of these models. The empirical formulations, for example, are often applicable to the environment similar to those used to develop them. To apply the model in a different environment, it is crucial to understand the formulation process and the assumptions that were made. Necessary modifications should be made to account for variabilities, such as changes in geology or structural properties. As they stand, these models are vital for providing insights into rock fragmentation and can serve as foundational models for estimating damage zones in a more uniform rock mass.

The analytical approach to blast damage prediction is based on the calculations of the magnitude of the stress wave produced by explosive detonation and the radial attenuation in the rock mass. Parameters such as the borehole pressure or PPV are calculated. The size of damage zones is estimated from the critical values for the fracture mechanisms. This study uses a combination of theoretical and empirical formulas discussed in section 2.5.1 and a series of steps presented in section 3.4 to calculate these parameters, determine the critical values, and estimate the damage zones.

4.4.1 Crushed zone estimation

Borehole pressure is a common parameter in blast damage estimation, especially in the crushed zone. Crack initiation and propagation from blasting in the vicinity of the blasthole is caused by the shock wave from the explosion gases pushing out the walls of the blasthole and causing crushing of the surrounding rock. The intensity of the stress wave and the size of the crushing zone depend on the properties of the rock and the explosive. The dynamic compressive strength of the rock and the borehole pressure are the main influencing factors in crushing zone formation.

Table 4-12 presents the parameters used to estimate the damage zones. These parameters were measured and/or estimated from the tests discussed in section 4.2.1.

Using equations (2.43) to (2.45), the radius of the crushed zone, r_c is estimated to be 168.87 mm which is 1.7 times the blasthole radius. The PPV (u_e) at the limit of the crushed zone is estimated from the experienced pressure at the end of the crushed zone using equations (2.47) and (2.48) as 74.23 m/s. The critical peak particle velocity is assumed to occur at the mid-point of the charge and is thus independent of charge length. The pressure at the limit of the crushed zone, P_e is calculated from the estimated peak pressure attenuation function and is obtained to be 1,543.27 MPa. Other estimated values are shown in Table 4-13.

Table 4-12: Input parameters to damage zone prediction

Parameter (units)	Value
VOD (m/s)	4,789
ρ_e (kg/m ³)	1,208
E_s (GPa)	90.83
v	0.24
V_p (m/s)	4,369
ρ_r (kg/m ³)	2,680
UCS (MPa)	126.02
r_o (mm)	101.5
σ_T (MPa)	14.16

The obtained crushed zone radius and PPV at the end of the crushed zone are compared with results from the Hugoniot Elastic Limit (HEL) in equation (2.19), the shock wave transfer (SWT) approach by Sun (2013) in equation (3.9), and the site monitoring as shown in Table 4-14. UCS_{confd} is the dynamic confined compressive strength of the rock approximated to 2.5 to 5 times the

static UCS, in this case, DIF of 5 was used to calculate the radius of the crushed zone using the SWT approach.

Table 4-13: Damage zones estimated

Parameter (units)	Value
P_d (MPa)	6,925.15
P_b (MPa)	3,462.58
E_d (GPa)	122.76
K (MPa)	98,998
CZI	26.41
r_c (mm)	168.87
Φ	-1.59
P_e (MPa)	1,543.27
u_e (m/s)	74.23
U_{cr} (m/s)	1.25
u_s (m/s)	0.70

$$r_c = \left(\frac{P_b}{UCS_{confd}} \right)^{\frac{1-\nu}{2}} r_0 \quad (3.9)$$

It is observed that the results obtained offer a good comparison with the other approaches with the percentage error within 15 % for the crushed zone radius and 7.0% for the PPV at the end of the crushed zone. It is further observed that far-field monitoring underestimates PPV close to the charge. Beyond one metre from the blasthole, far-field measurements offer a good comparison with SWT as seen in Figure 4-13. This agrees with the observations made by Blair and Minchinton (1997) that the PPV estimated from the far-field monitoring is valid for distances ten times the blasthole radius.

Since PPV and pressure could not be monitored on-site in the near field for direct comparison with the results, the SWT approach and HEL equation were used as alternatives. Although these methods show consistency, they may not be entirely reliable for validating the results. For critical operations, comparison with real-world data is recommended.

Table 4-14: Crushed zone parameters comparison

Approach	r_c (m)	P_e (MPa)	PPV (m/s)
Study approach	0.169	1,543.27	74.23
SWT	0.194	1,353.70	79.39
HEL	0.164	1473.47	76.37
Far-field monitoring	0.169*	592.82	50.63

4.4.2 Fracture zone estimation

Vibration monitoring data and the rock's dynamic tensile strength were used to estimate the damage beyond the crushed zone limit, (CZL). From the range calculated from equations (2.40) and (2.42) dynamic tensile strength of 2.5 times the static tensile strength was used to estimate the fractured zone limit (FZL). Using Forsyth expression in equation (2.50) with the input parameters in Table 4-12 the critical peak particle velocity in the dynamic tensile fracture zone, u_{cr} was calculated to be 1.25 m/s. This value corresponds to a burden distance of 5.25 m. Further cracking from this point can be caused by the spalling effect when the compressive wave reflects at the free face and transforms into a tensile wave. If the intensity of this wave exceeds the tensile strength of the rock, it induces additional fractures.

Interaction from neighbouring blastholes can also influence the extent of fracturing. In the absence of such interactions, the influenced zone is formed beyond the fracture zone, where no

fracturing relevant to fragmentation occurs; the wave induces incipient damage and swelling and is later lost as ground vibrations. The limits of damage zones relevant to fragmentation are illustrated in Figure 4-13. The site PPV was estimated from the relationship in Figure 4-12. SWT PPV was estimated from the relationships presented by Sun (2013) which track shock wave attenuation in the rock mass and estimate the damage zones.

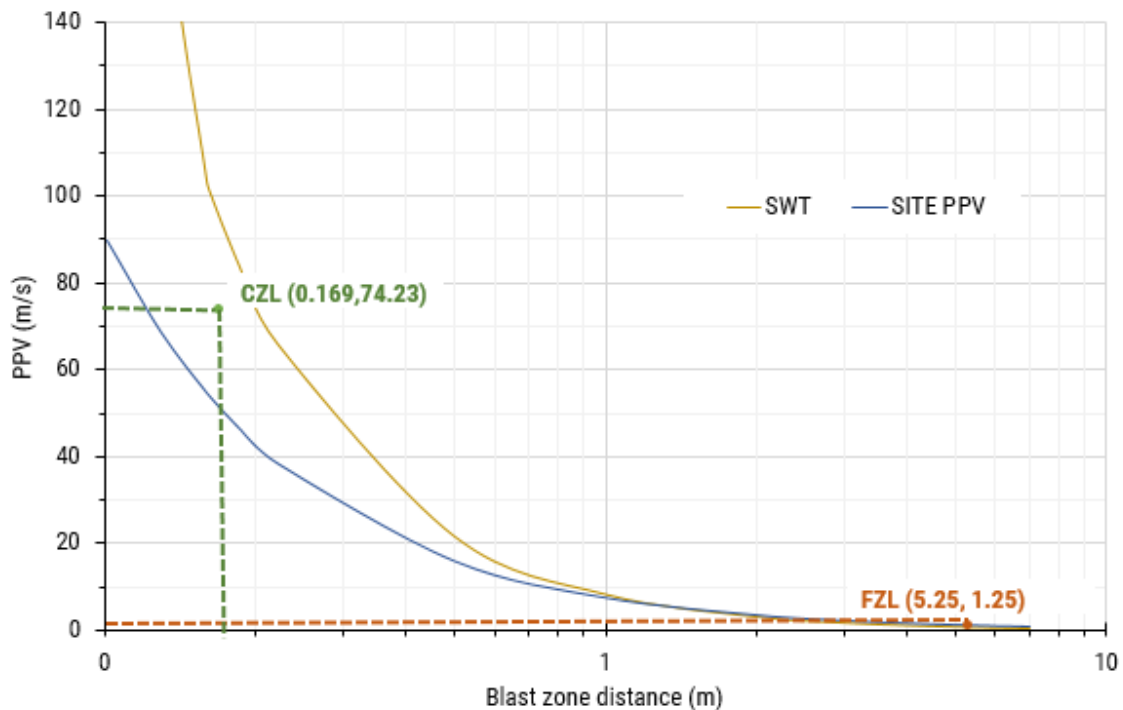


Figure 4-13: Damage zones estimated using the analytical approach

4.5 Finite element modelling of blast-induced fragmentation

Based on the blast design for production blast shots in Table 4-8, the rock and explosive properties, the simulation model was created and executed in LS-DYNA. Figure 4-14 illustrates the full-size single blasthole model for the intact rock. The model dimensions follow the size of the blast pattern, where the burden is 5.5 m, and the spacing is 6.5 m. The bench height is 10 m with a 1.5 m sub drill, a charge column is 7 m, and a stemming height of 4.5 m. Gravel was used as a stemming in the model and is represented by the soil material model (MAT_SOIL_AND_FOAM)

with properties adopted from Wang et al. (2013) in Table 4-15. A 2 m depth is added below the bench to analyze pit floor formation. The radius of the blasthole is 0.1015 m, and a coupled charge was used where the diameter of the charge is the same as that of the blasthole. The detonation takes place 1.5 m from the bottom of the blasthole. Two free boundaries are introduced on top of the bench and along the burden, where the stress wave is reflected to the rock mass. Non-reflecting boundary conditions are set on the remaining sides, allowing the stress wave to transmit.

Table 4-15: Stemming parameters for soil material model

Material	Density (Kg/m ³)	Shear Modulus (MPa)	Bulk modulus (GPa)	Pc (KN)	a_0 (MPa ²)	a_1 (MPa ²)	a_2 (MPa ²)
Gravel	2500	30	0.4	-6.9	3.4×10^{-13}	7.033×10^{-7}	3

Mesh shape and type selection are critical to the outcomes of the simulation. Hexahedron meshes are chosen for their efficiency and accuracy in blocky and simple geometries like a bench layout. These meshes provide computational advantages by requiring fewer elements than tetrahedron meshes for equivalent accuracy, translating to better computation time and less storage requirements. Near the blasthole, where small fragmentation is prevalent, a fine mesh is selected to capture the details accurately. A coarser mesh is used as the distance from the blasthole increases and the fragmentation size grows larger. Simulations were conducted for mesh size sensitivity analysis using various mesh sizes (ranging from 2 cm to 5 cm, 3 cm to 10 cm, and 3 cm to 8 cm), and it was determined that a 3 cm mesh size was optimal near the charge. This mesh size was then gradually increased to a maximum of 8 cm beyond half a meter from the blasthole.

The rock is modelled using the RHT material model, while the explosive is represented by the High Explosive Burn material model. To prevent mesh distortion, the Arbitrary-Lagrange-Eulerian (ALE) algorithm is applied to the explosive, and fluid-structure interaction (FSI) coupling is implemented between the explosive products and the rock, which is a Lagrangian part.

4.5.1 Determination of RHT model parameters

The RHT model has 39 parameters, 18 of which are obtained or estimated from the rock's physical and mechanical properties. Properties like the density, UCS, tensile strengths, and bulk and elastic shear moduli were obtained from the lab measurements, tests, and derivatives. Other parameters such as the Hugoniot polynomial coefficients A_1 , A_2 , and A_3 , the pore crush pressure (P_{crush}), compressive and tensile strain rate dependence exponents, etc. were estimated based on the rock's physical and mechanical properties. Additional parameters, such as the yield surface parameters (G_c^* and G_t^*), and others that are insensitive to simulation results, were adopted from the literature (Borrvall and Riedel, 2011). The RHT model parameters were estimated from BIF's physical and mechanical properties in Table 4-13. These properties were obtained from the laboratory tests and equations in Section 4.2.1.

4.5.1.1 Strain rate dependence

The strain rate dependence of the rock strength for the model is defined in equation (2.65) where, the reference strains are $3 \times 10^{-5} \text{ s}^{-1}$ and $3 \times 10^{-6} \text{ s}^{-1}$ in compression and tension, respectively. These reference strains were adopted from the original model (Borrvall and Riedel, 2011). The quasistatic tests are conducted at strain rates 0.001 and 0.01 s^{-1} . As discussed in APPENDIX B section 8.1 the change in strain rate below 0.01 s^{-1} has an insignificant change in the rock strength, meaning the same strengths can be used with the reference strains without affecting the results.

The material constants in compression and tension β_c and β_t are calculated from equations (2.66) and (2.67) as 0.01 and 0.013, respectively.

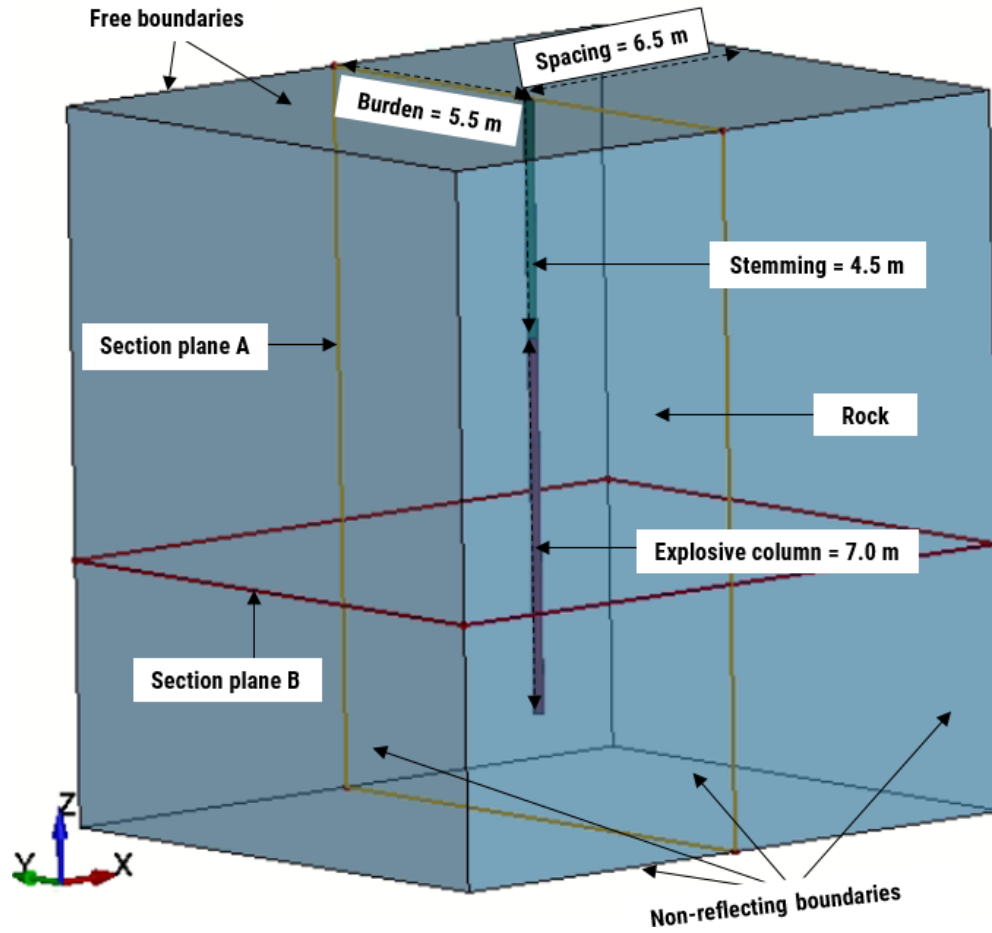


Figure 4-14: Full-size simulation model of an intact rock

4.5.1.2 Failure surface parameters

Under quasi-static load, the failure strength of the rock is obtained from the tri-axial compressive tests, and the dynamic strength is estimated from the static values comparable to variable confining pressures. For example in this case the strain rate of up to 1000s^{-1} is within 0 to 100 MPa confining pressure. Hoek-Brown failure criterion relationship can estimate the tri-axial compressive strength under confining pressure. The formula for intact rock is presented in

equation (3.10). σ_1 and σ_3 are maximum and minimum effective stresses at failure, σ_{ci} is the uniaxial compressive strength, mi is the intact rock constant and s is the degree of fracturing of rock mass; for intact rock $s=1$. From the triaxial compressive strength tests conducted on BIF, the constant mi is 7.78 (obtained from mine's Geotech database). Fitting in the values of σ_{ci} , s , and mi , the equation for BIF is simplified as seen in equation (3.11).

$$\sigma_1 = \sigma_3 + \sigma_{ci} \left(m_i \frac{\sigma_3}{\sigma_{ci}} + s \right)^{0.5} \quad (3.10)$$

$$\sigma_1 = \sigma_3 + 126.02 \left(7.78 \frac{\sigma_3}{126.02} + 1 \right)^{0.5} \quad (3.11)$$

From equations (3.11), (2.63), and (2.64), the normalized strength (σ_f^*) and normalized pressure (P_0^*) are presented in Table 4-16. The failure parameters A and N are determined to satisfy the condition $3P_0^* \geq F_r$ (the dynamic strain rate increase factor) in equation (2.68). For the quasi-static state, the value of F_r is 1. If the values of P_0^* and σ_f^* are substituted corresponding to the confining pressure from 0 to 100 MPa, the values of A and N are obtained as 1.95 and 0.6, respectively. The values of Q_0 and B ; 0.68 and 0.105, respectively, are adopted from the literature (Borrvall and Riedel, 2011).

Table 4-16: Mechanical properties under various confining pressure

σ_3 (MPa)	σ_1 (MPa)	P (MPa)	σ_f (MPa)	P_0^*	σ_f^*
0	126.02	42.01	126.02	0.33	1.00
5	149.16	53.05	144.16	0.42	1.15
10	170.27	63.42	160.27	0.50	1.28
20	208.39	82.80	188.39	0.66	1.51
40	274.73	118.24	234.73	0.94	1.87
60	333.33	151.11	273.33	1.20	2.17
80	387.11	182.37	307.11	1.45	2.43
100	437.53	212.51	337.53	1.69	2.66

4.5.1.3 Equation of state

The pressure within the rock is described by the p- α equation of state for non-linear compression in equation (2.57). Since the BIF rock has lower porosity, a_0 is set to 1. Based on equation (2.60) taking the value of S as 1.2; T1, = A1 = 58.22 GPa, A2 is 81.51 GPa, and A3 is 30.28 GPa. Beyond the pore crush, inelastic deformation of rock occurs. Pore crush pressure (Pcrush) is 84.01 MPa, which is $2f_s/3$. The material constants B0 and B1 are taken from the reference values provided by Borrvall and Riedel (2011), where B0 = B1 = 1.22. Other parameters that could not be estimated from the tests such as residual parameters A_f and N_f and yield surface parameters G_c^* and G_t^* , relative shear strength F_s^* , reduction factor in shear modulus XI , and the minimum damaged residual strain ϵ_p^m are obtained from the reference values suggested by (Borrvall and Riedel 2011) and from other similar literature. Table 4-17 summarizes the RHT model parameters used for BIF rock blasting simulation.

Table 4-17: RHT model parameters for BIF rock

Parameter (unit)	Value	Parameter (unit)	Value
Density, RO (kg/m ³)	2,680	Compressive strain rate dependence exponent, β_c	0.0104
Elastic shear modulus, SHEAR (GPa)	38.62	Tensile strain rate dependence exponent, β_t	0.0137
Unit conversion factor, ONEMPA	0	Pressure influence on plastic flow in tension, PTF	0.001
Eroding plastic strain, EPSF	2	Compressive yield surface parameter, G_c^*	0.53
Polynomial EOS parameter (Pore crush), B ₀	1.22	Tensile yield surface parameter, G_t^*	0.7
Polynomial EOS parameter (Pore crush) , B ₁	1.22	Shear modulus reduction factor, XI	0.5
Polynomial EOS parameter, (Bulk modulus) T ₁ (GPa)	58.22	Damage parameter, D ₁	0.04
Failure surface parameter, A	1.95	Damage parameter, D ₂	1
Failure surface parameter, N	0.6	Minimum damage residual strain, ε_p^m	0.015
Compressive strength, f_c (MPa)	126.02	Residual surface parameter, A _f	0.61
Relative shear strength, F_t^*	0.18	Residual surface parameter, N _f	1.6
Relative tensile strength, F_s^*	0.11	Gruneisen gamma, Γ	0
Lode angle dependency factor, Q ₀	0.68	Hugoniot polynomial coefficient, A ₁ (GPa)	58.22
Lode angle dependency factor, B	0.0105	Hugoniot polynomial coefficient, A ₂ (GPa)	81.51
Parameter for poly EOS, (Bulk modulus) T ₂ (GPa)	0	Hugoniot polynomial coefficient, A ₃ (GPa)	30.28
Reference compressive strain rate, ε_0^c	3×10 ⁻⁵	Crush pressure, P _{crush} (MPa)	84.01
Reference Tensile strain rate, ε_0^t	3×10 ⁻⁶	Compaction pressure, P _{comp} (GPa)	6
Break compressive strain rate, ε_c^*	3×10 ²⁵	Porosity exponent, NP, γ	3
Break tensile strain rate, ε_t^*	3×10 ²⁵	Initial porosity, α_0	1

4.5.2 Explosive parameters

The high explosive burn material and Jones-Wilkins-Lee equation of state (JWL EOS) are commonly used to model explosive charge detonation as explained in Section 2.5.2.2. The actual field measurements were performed to determine the explosive VOD and density, and estimate P_{cj} . Based on the similar ranges of the VOD and E_0 , the JWL model constants for emulsion were adopted from a similar emulsion explosive E682 calibrated by Hansson (2009) from the cylinder expansion test as seen in Table 4-18.

Table 4-18: High explosive material model parameters and JWL constants for Fortis extra

Explosive Type	Density (kg/m ³)	VOD (m/s)	P_{cj} (GPa)	A (GPa)	B (GPa)	R_1	R_2	ω	E_0 (kJ/cm ³)	v_0
E682	1,207	4,789	6.926	276.2	8.44	5.2	2.1	0.5	3.87	0

4.5.3 Damage mechanisms on the intact rock and model verification

As described in section 2.4, the numerical simulation shows three main mechanisms of rock fracturing from explosive detonation in the blasthole resulting in three distinctive damage zones. The overall fracture and damage distribution in a bench along Section A and Section B from Figure 4-14 are shown in Figure 4-15. The action of high shock waves pulverizes the area around the charge, forming a crushed zone (r_c) represented by the red region (damage =1) in Figure 4-15(a) and (b). The shock wave quickly decays into a high-amplitude stress wave, creating a highly fractured zone followed by extended fractures in a fractured zone. This region terminates at around a 5 m radius (r_f) along burden, as seen in Figure 4-15(b). When encountering a free surface, the stress wave is reflected, causing spalling where its intensity exceeds the rock's tensile strength, as seen on the upper and the left areas of part (a) and the upper area of part (b) in Figure 4-15.

Upon explosive detonation, the blasthole expands due to gas expansion from a radius of 101.5 mm to 132.4 mm (the initial blasthole boundaries are traced white in Figure 4-15(a)). The crushed zone radius is initially 0.184 mm at 0.6 ms, which is 1.8 times the blasthole radius, and later extends to 0.33 mm at 2.5 ms. Some studies suggest that further damage is caused by the rapid expansion of the explosion gases into the cracks (Ding et al., 2022). The damage decreases with increased distance in the fractured zone with the pattern crossing near the blasthole and extending radially away from the blasthole, extending to 5 m along the burden. Spalling is observed on the top of the bench and extends beyond 5 meters along the burden on the free-face side. In numerical modelling, spalling is distinguished from radial cracks by the different mechanisms that create them and the directions in which they propagate. This is also observed in field blasting, where fragmentation increases significantly when the blast shot is free-faced. Therefore, along the spacing, fracturing stops when the pressure drops below the dynamic tensile strength of the rock, while along burden spalling can occur until the reflected wave falls below the rock's dynamic tensile strength. This concept is investigated further in section 4.6.

From the discussion above, the simulation model is verified since it works the expected way, including the formation of damaged zones around the charge, attenuations, and stress wave reflection at the free face, with similar outcomes as observed in an actual blast.

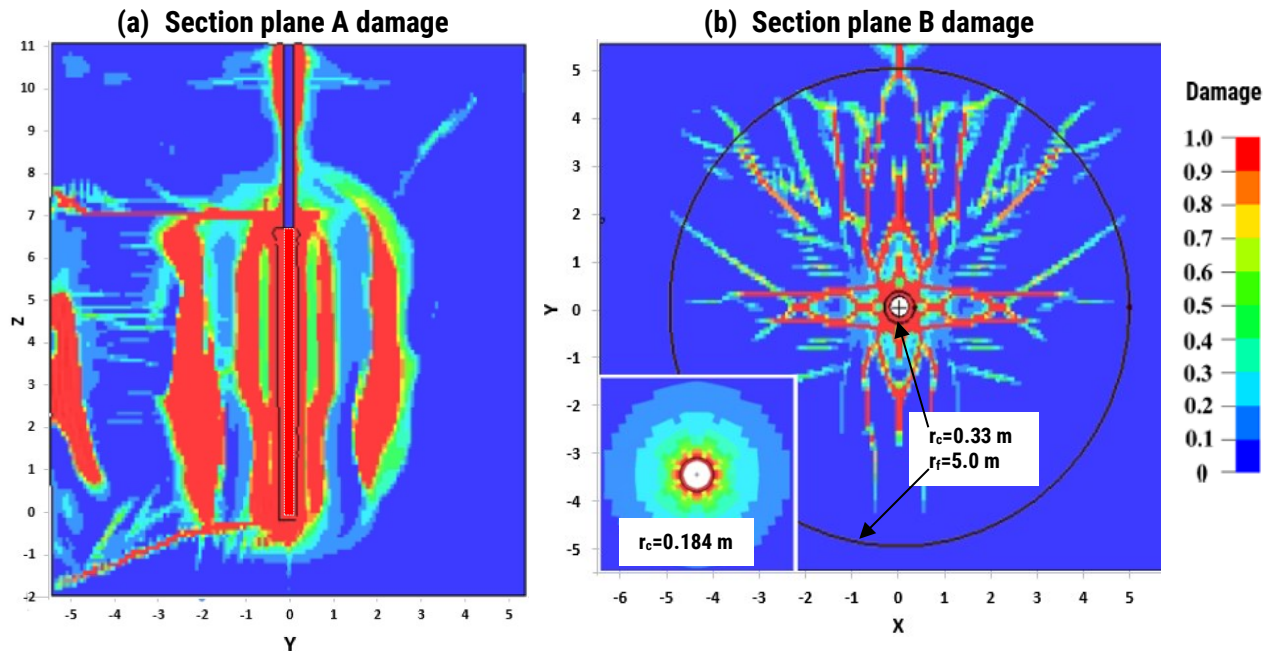


Figure 4-15: Damage distribution from the simulation of single blasthole blasting

4.5.4 Model validation

The maximum pressure and PPV recorded at the blasthole wall are 2640 MPa and 202 m/s, respectively. Rapid attenuation occurs from pulverization of the blasthole wall and the surrounding rock causing a drop in pressure and PPV at the end of the crushed zone to 1280 MPa and 95.2 m/s, respectively. Gentle attenuation occurs in the fractured zone from spreading and the propagation of the stress wave and fractures. The pressure and PPV at the boundaries of the model which is also the limit of the fractured zone are 15.7 MPa and 1.9 m/s, respectively.

Figure 4-16 compares the field measurements (vibration monitoring) in Figure 4-13 to the pressure and PPV curves obtained from the simulation. The field PPV and pressure values near the blasthole (within 1 meter) were estimated using the SWT method. The figure shows that the simulation results compare reasonably well with the field measurements. The comparison between the fitted curves for simulation pressure (P_s) and field pressure (P_f), along with their respective particle velocities (PPV_s and PPV_f), shows reasonable similarity. However, some

differences arise due to field conditions, such as the effects of rock structures, which were not accounted for in the simulation model.

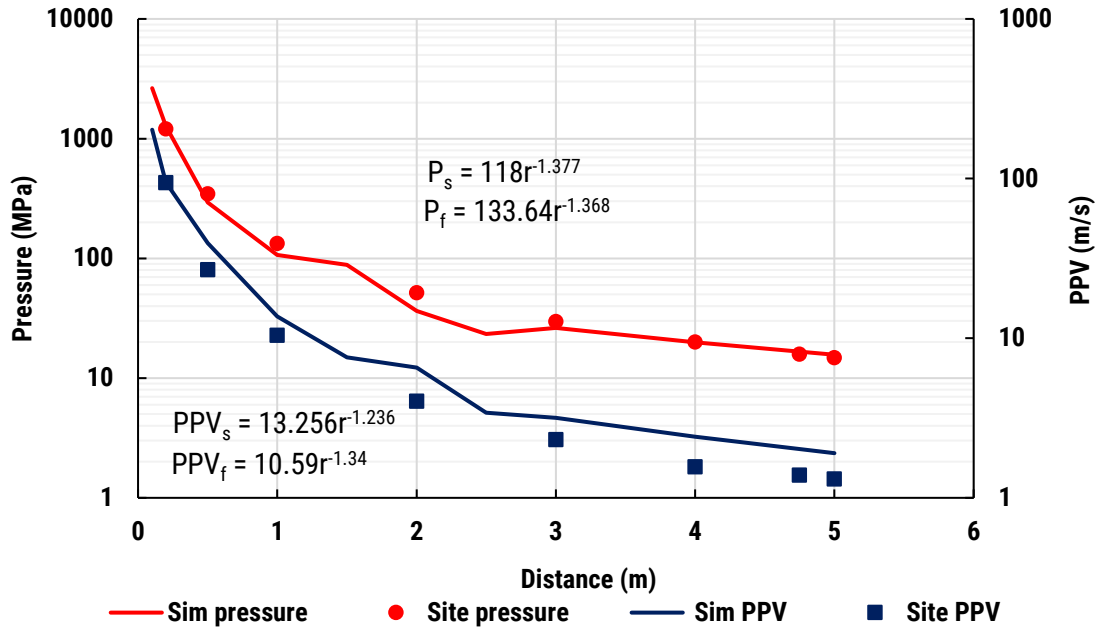


Figure 4-16: Comparison of the simulated pressure and PPV curves with field measurements

In section 4.4 the analytical approach, field measurements, and other approaches were used to estimate the damage zones around the charge using the same data. The standard error (SE) was calculated using equation (4.12) to assess the variability or consistency between the results as presented in Table 4-19. SD is the standard deviation of the sample and n is the sample size. The results show some variability in the crushed zone parameters and a better consistency in the fractured zone. The overall observation indicates that the simulation results compare reasonably well to other approaches except for the far-field monitoring close to the blasthole as explained in section 4.4.1. From this comparison and the comparison of the curves in Figure 4-16, there is a reasonable indication that the simulation results are feasible.

$$SE = \frac{SD}{\sqrt{n}} \quad (3.12)$$

Table 4-19: Results comparison with field measurements and estimations

Approach	r_c (m)	P_e (MPa)	u_e (m/s)	r_f (m)	P_f (MPa)	u_f (m/s)
Analytical approach	0.169	1,543	74.23	5.25	14.69	1.25
SWT	0.194	1,261	98.24	4.75	15.85	1.23
HEL	0.173	1,474	114.84	-	-	-
Far-field monitoring	0.169*	593	50.63	5.25	13.82	1.25
Numerical modelling	0.184	1,280	95.21	5.00	15.67	1.90
Standard deviation (SD)	0.011	141	16.67	0.24	0.94	0.33
Standard error (SE)	0.006	70.24	8.34	0.11	0.42	0.15

4.6 Full-scale model to 2D model comparison

A 2D model is constructed along an x-y plane with the same dimensions as the full-scale model in the same plane using the same mesh size. Similar boundary conditions to the full-scale model were applied with additional constraints to restrict elements' movement in the z direction to mimic bench blasting. The stress wave pulse monitored at the blasthole wall is shown in Figure 4-17(a) for a full-scale 3 m from the bottom of the blasthole and the 2D model. From the figure, the pressure of the shock wave at the blasthole wall is 2,750 MPa on a 2D model and 2,640 MPa on a full-scale model. The stress wave pulse is observed to diminish at 1 ms with a faster rate on the full-scale model.

The stress wave monitoring mid bench ($x, y = 3.25$ mm, 2.75 m) Figure 4-17(b), indicates that the wave arrives at 0.6 ms after the detonation in both models. A higher spike is observed on a 2D model, and a second spike is caused by the wave reflection at the free face. The average stress is the same in both models. The comparison of damage intensity indicates more damage on a 2D

model, while the fracture pattern and extent are more or less the same as described in Figure 4-18. 2D models are used for analysis in Chapter 5 due to their ease of implementation and analysis and reduced computational time on the plane of interest i.e. along the burden and spacing.

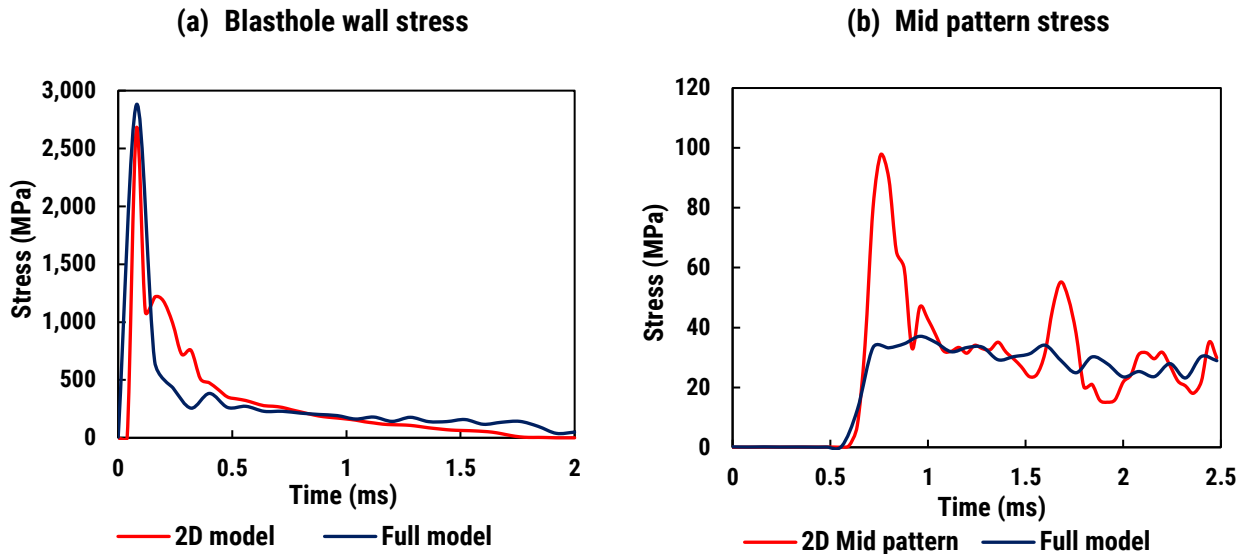


Figure 4-17: Stress wave comparison in full-scale and 2D simulation models

In both models, the role of the free face in enhancing fracturing is observed with pronounced effects on a 2D model due to differences in how waves propagate and interact with boundaries in two versus three dimensions. A 2D model confines the wave energy to a plane, resulting in less dispersion and, hence higher intensity of the reflected wave from the boundaries.

Radial fractures seize when the stress drops below dynamic tensile strength which, from the full-scale model is 3.8 m along spacing where the peak pressure of the stress wave is around 21 MPa and 5 m along burden where the peak pressure is 16 MPa, see Figure 4-19(a). Along the free surface, spalling occurs, propagating towards the blasthole and seizing when the stress wave is below the tensile strength of the rock as seen in Figure 4-19(b). The spalling effect seizes at

approximately 1 m from the free face. The negative pressure is a tensile stress wave formed by the compressive stress wave reflection at the free face.

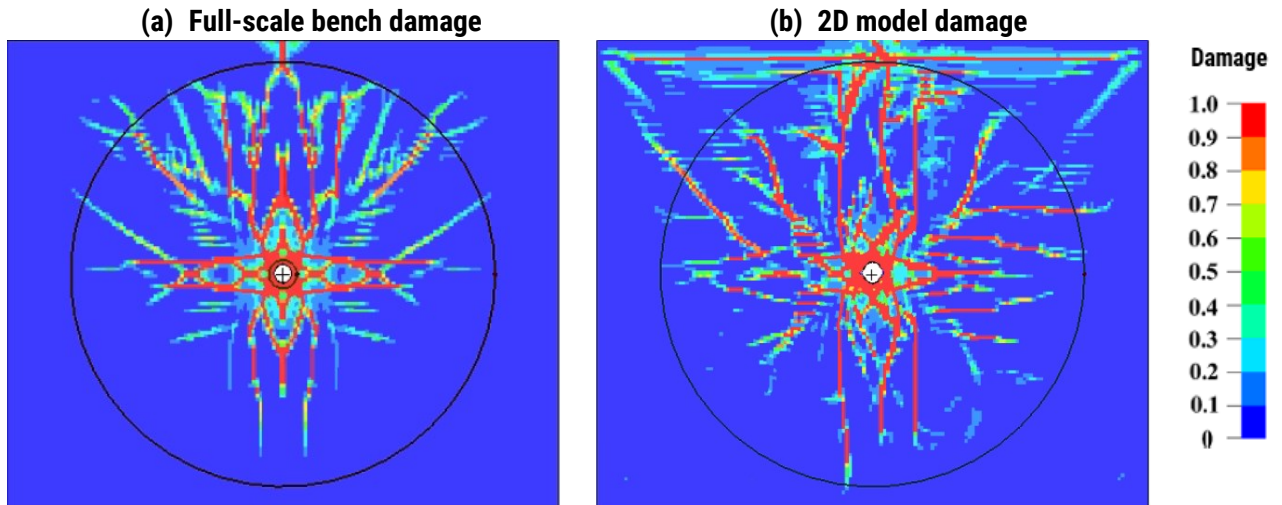


Figure 4-18: Damage distribution comparison for 3D and 2D simulation models

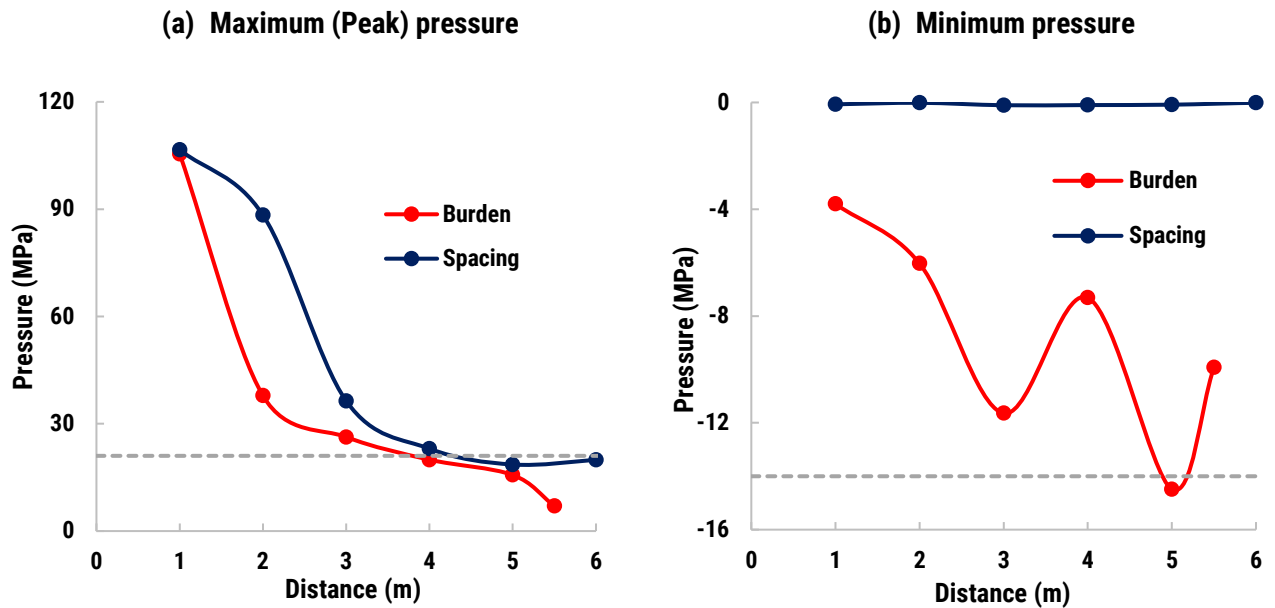


Figure 4-19: Pressure of stress wave at the free-face along burden and spacing

4.7 Summary and Conclusion

Chapter 4 discusses the use of both analytical approaches and finite element simulations to study the blasting process and mechanisms, as well as to estimate damage zones around the blasthole.

The chapter delves into the types of data required for these approaches and explains how this data is obtained or estimated through laboratory and field measurements. It includes detailed descriptions of the measurements and experiments conducted to determine the properties of the explosives and the physical, mechanical, and structural properties of the rock. Additionally, the chapter addresses the estimation of parameters that could not be directly measured in the field.

The analytical approach uses the rock and explosive properties to estimate the damage zones from the existing empirical formulas with some modifications to account for the strength increase in dynamic fracturing. Finite element numerical modelling is performed in the LS-DYNA program to study blast wave propagation, fracture distribution, and estimate damage zones. For the numerical simulations, the parameters for the RHT material model and the JWL EOS needed to be estimated; the calculations and assumptions are covered in this chapter.

From the rock and explosive properties, it is shown that the crushed zone extends to around 0.2 m radius, and the fractured zone extends up to 5 m with extra fracturing occurring near the free face. The results from these two approaches were compared with results from other approaches such as SWT, HEL, and far-field monitoring. The results show that these models have relatively similar results except for the far-field monitoring estimations close to the blasthole. The established relationships between pressure and PPV with the distance from the blasthole, derived from the fitted curves, can be used to estimate the parameter value at any distance and determine the extent of damage based on rock strength. However, as shown in Figure 4-16 the results are not precisely the same. The variation can be attributed to the influence of rock mass properties, which were not accounted for in the numerical simulation.

CHAPTER 5

THE INFLUENCE OF ROCK PROPERTIES AND EXPLOSIVE PROPERTIES ON BLAST-INDUCED FRAGMENTATION

This chapter covers the analysis of explosive strength properties, rock mass strength, and structural properties on stress wave propagation and crack development. It examines the influence of contacts between soft and hard rock, as well as discontinuity parameters, including infill material, width, continuity, distance from the charge, and the presence of single and multiple discontinuities at various orientations. The results are compared with fragmentation analysis for validation and provide valuable inputs to blast design and the improvement of blast-induced fragmentation prediction models, which will be covered in Chapter 6.

Two sections of this chapter were published as:

1. Dotto, MS., Apel, D., and Pourrahimian, Y. (2024), "Investigating the influence of discontinuity parameters on blast-induced fragmentation", *International Journal of Mining, Reclamation, and Environment*, 1-25. <https://doi.org/10.1080/17480930.2024.2347128>
2. Dotto, MS. and Pourrahimian, Y. (2024), "The Influence of Explosive and Rock Mass Properties on Blast Damage in a Single-Hole Blasting". *Mining*, 4(1), 168-88. <https://doi.org/10.3390/mining4010011>.

5.1 Introduction

Several factors affect fragmentation from blasting. Extensive studies have been done over several decades to understand the influence of blast input parameters on improving blast outcomes. The numerical study on the burden size conducted by Saadatmand Hashemi and Katsabanis (2020) showed that the extent of damage decreases with the increase in burden size. They suggested that an optimum burden is the one that allows the reflected tensile cracks to be formed from the wave reflection within the influenced zone. Regarding the specific charge, the study conducted by Rustan (2013) showed that increasing specific charges improves fragmentation, but larger specific charges result in higher over-breaks. The spacing between blastholes plays an important role in rock fragmentation, similar to initiation delay by allowing enough time for the cracks to grow between the blastholes with minimum interference from each other. Larger spacing leads to poor fragmentation and increased burden for the subsequent rows.

The rock mass's physical, mechanical, and structural properties determine the extent of the area influenced by the stress wave propagation. The influence of structural properties on blast-induced fragmentation studied by several researchers for various applications (Chen and Zhao, 1998, Ismail and Gozon, 1987, Wang et al., 2019, Yang et al., 2018, Jiang et al., 2023, Zhu, 2011, Chen et al., 2022) indicate that the presence of interfaces as rock contacts, fractures, joints, etc. may result in partial propagation, reflection, or total arrest of the stress waves and cracks in variable proportions depending on the properties of structures and strength of the stress wave. This complicates the blasting process and blast outcomes and is worth investigating.

Wei et al. (2024) used 3D finite element simulation to reconstruct bench blasting in jointed rock masses. Their comparison of simulation results to field fragmentation demonstrated that

simulation is an effective tool for modelling bench blasting, with an error margin of only 12.8%. Similarly, Wang et al. (2018) observed through lab tests and numerical simulations that joints with lower yield strength hinder wave propagation across the joint and can highly affect the fracturing of the rock mass. Ding et al. (2022) studied stress wave transmission and crack propagation in soft and hard composite rocks, noting an increase in fragmentation in hard rock when the wave travels from hard to soft rock. These studies provide valuable insights into the application of finite element simulation in blasting problems, highlighting some factors that influence blast outcomes, although they are not exhaustive.

This chapter investigates the explosive strength properties, as well as the rock's strength and structural properties, and their influence on blast energy distribution and crack propagation. The analysis outcomes offer a deeper understanding of the blasting process with variable input parameters and can be used to enhance blast fragmentation prediction models and provide guidance for optimizing blast designs.

5.2 Explosive properties

ANFO and emulsion are the commonly used commercial explosives in civil and mining applications. The choice of one over the other depends on the energy requirements from the rock properties and the presence of water/moisture in the blastholes. The EOS parameters for emulsion are presented in Table 4-18. Similar parameters for ANFO have been adopted from Sanchidrián et al. (2015) as seen in Table 5-1.

Explosive properties and rock properties govern the formation of damage zones and crack distribution around the charge. Four scenarios are evaluated on the influence of explosive strength properties (VOD, density, and detonation pressure) on the formation of damage zones in hard and

soft rocks. Using the criteria above, an emulsion in this study is termed a high-strength explosive, and ANFO is a low-strength explosive.

Table 5-1: High explosive material model parameters and JWL constants for ANFO explosive

Explosive Type	Density (kg/m³)	VOD (m/s)	P_{cj} (GPa)	A (GPa)	B (GPa)	R_1	R_2	ω	E_o (GPa)	ν_o
ANFO	902	4,426	4.503	207.79	2.91	5.91	1.08	0.4	2.29	0

Rock strengths are categorized by their UCS, tensile strength, Young's modulus, and Poisson ratio. The estimated RHT material properties for BIF in Table 4-17 are used for hard rock simulation, and the sandstone RHT properties are estimated from the properties adopted from Jeong and Jeon (2018) in Table 5-2. The estimated RHT material properties for soft rock simulation are shown in Table 5-3.

A single blasthole 2D model is used in the simulation with a blasthole diameter of 203 mm and a square pattern of 5.5 m by 5.5 m. The same mesh sizes as the previous chapter (3 cm to 8 cm hexahedral) were used. The elements were constrained with fixed boundaries on three sides, with no movement on the z-axis; the top boundary and the burden side were left as free boundaries.

Table 5-2: Sandstone physical and mechanical properties

Density (kg/m³)	UCS (MPa)	Tensile strength (MPa)	Young modulus (GPa)	Poisson ratio	P-wave velocity (m/s)
2400	88	0.1×UCS	25	0.3	2589

A single blasthole 2D model is used in the simulation with a blasthole diameter of 203 mm and a square pattern of 5.5 m by 5.5 m. The same mesh sizes as the previous chapter (3 cm to 8 cm

hexahedral) were used. The elements were constrained with fixed boundaries on three sides, with no movement on the z-axis; the top boundary and the burden side were left as free boundaries.

Table 5-3: Sandstone RHT material model parameters

Density, RO (kg/m ³)	2,400	Comp. strain rate exp., BETAC	0.026
Elastic shear modulus, SHEAR (GPa)	9.8	Tens. strain rate exp., BETAT	0.007
Unit conversion factor, ONEMPA	0	Pressure influence in tension, PTF	0.001
Eroding plastic strain, EPSF ()	2	Comp. yield surface par, GC	0.53
Par for polynomial EOS (Pore crush), B0	1.2	Tensile yield surface par, GT	0.7
Par for polynomial EOS (Pore crush), B1	1.2	Shear modulus reduction factor, XI	0.5
Par for polynomial EOS, (Bulk mod) T1 (GPa)	12.87	Damage parameter, D1	0.04
Failure surface parameter, A	1.6	Damage parameter, D2	1
Failure surface parameter, N	0.6	Min damage residual strain, EPM	0.015
Compressive strength, FC (MPa)	88	Residual surface parameter, AF	0.61
Relative shear strength, FS	0.1	Residual surface parameter, NF	1.6
Relative tensile strength, FT	0.1	Gruneisen gamma, GAMMA	0
Lode angle dependency factor, Q0	0.68	Hug. polynomial coefficient, A1 (GPa)	12.87
Lode angle dependency factor, B	0.05	Hug. polynomial coefficient, A2 (GPa)	18.02
Par for polynomial EOS, (Bulk mod) T2 (GPa)	0	Hug polynomial coefficient, A3 (GPa)	6.69
Reference compressive strain rate, EOC	3×10^{-5}	Crush pressure, PEL (MPa)	58.67
Reference Tensile strain rate, EOT	3×10^{-6}	Compaction pressure, PCO (GPa)	6
Break compressive strain rate, EC	3×10^{25}	Porosity exponent, NP	3
Break tensile strain rate, ET	3×10^{25}	Initial porosity, ALPHA	1

Figure 5-1 shows the peak pressure and PPV monitored at locations 0.2 m, 0.5 m, 1 m, 2 m, and 3 m from the charge. Hard rock with a high-energy explosive (emulsion) experiences high pressure and low PPV, unlike soft rock. The pressure attenuates faster in soft rock. Due to higher strength

the size of the crushed zone formed around the hard rock is relatively small (0.33 m radius) and with a good energy confinement associated with rock hardness (also indicated by low PPV) a larger fractured zone is formed, extending to 5 m at 2.5 ms simulation time. On the contrary, a bigger crushed zone is formed around the soft rock (0.54 m radius) with a reduced fractured zone (4.0 m) as demonstrated by Figure 5-2. Further cracking is observed along the free face with different shapes for the two rock types used.

With ANFO the peak pressures recorded are relatively lower for both rock types with much lower values in hard rock. Considerable stress wave energy is used up in forming the crushed zone (0.3 m radius) slightly less than the emulsion and the fractured zone is reduced to 4.5 m. Burden fracturing is significantly reduced and much less energy is reflected on the free face. On the soft rock, the sizes of damage zones are the same: 0.54 m crushed zone and 4 m fracture zone. The overall energy distribution is improved with ANFO explosives, as demonstrated in Figure 5-2, but higher damage extents are achieved by emulsion, as seen in Figure 5-3. Similar results on stress wave decay and crack formation were obtained by Ding et al. (2022) from the numerical simulation and empirical formula.

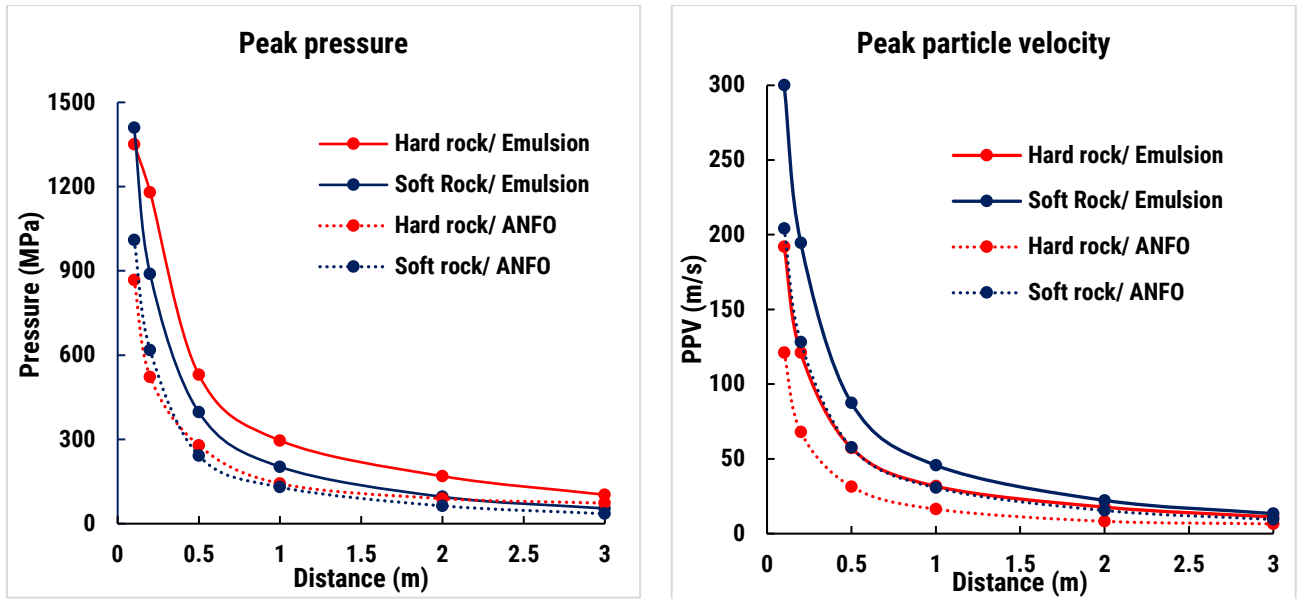


Figure 5-1: Pressure and PPV attenuations in soft and hard rock

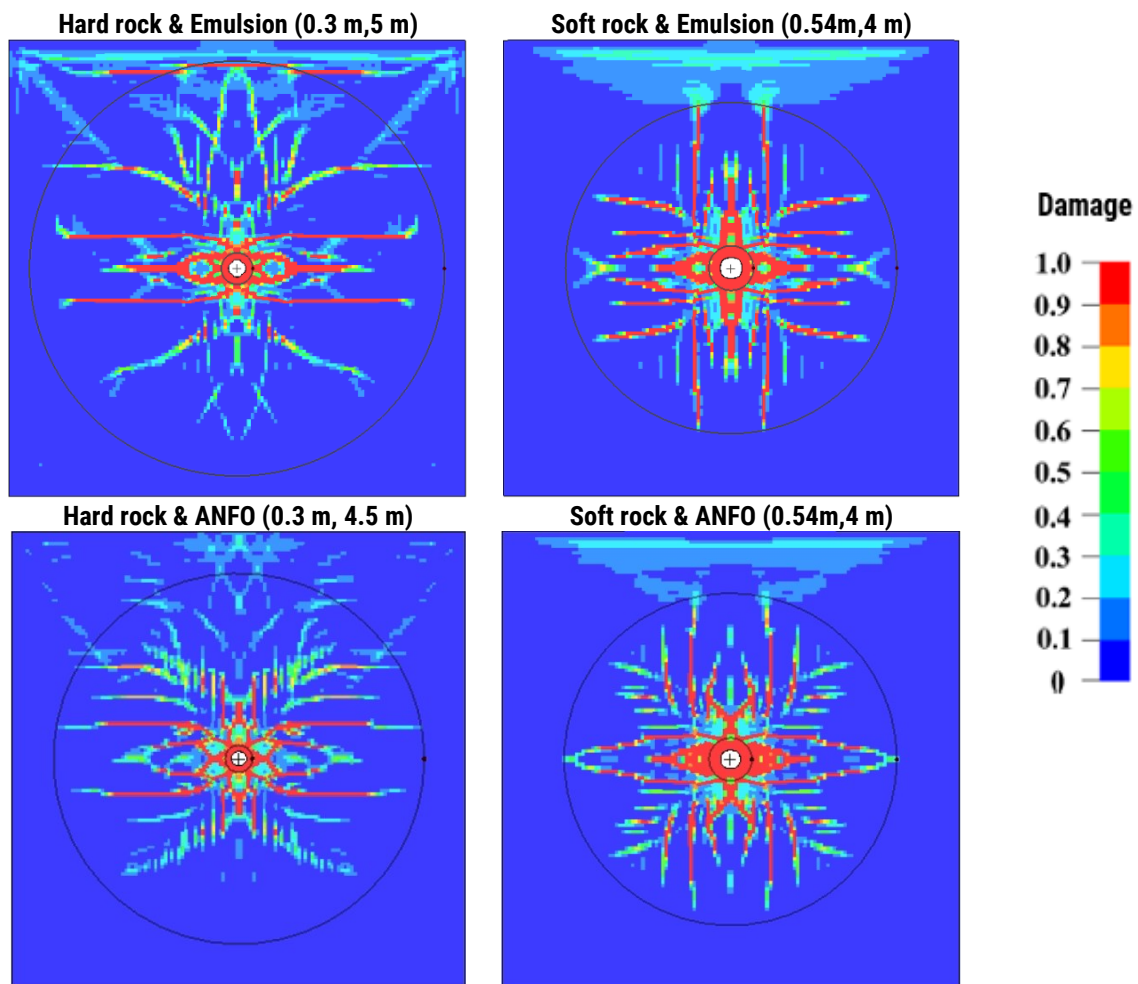


Figure 5-2: Damage zone extents in soft and hard rock

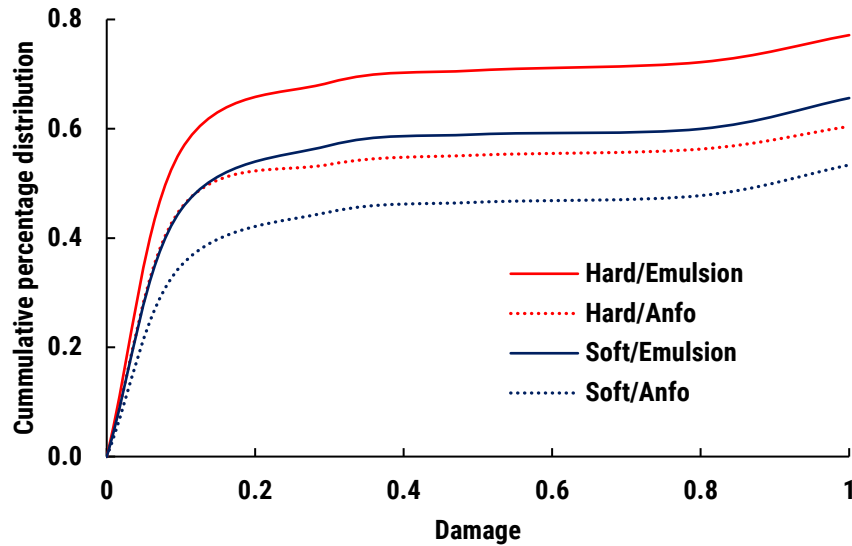


Figure 5-3: Damage percentage distributions for various explosives and rocks

5.3 Explosive energy transmission through rock contacts

The natural rock mass is heterogeneous and usually consists of layers with different rock compositions, properties, thicknesses, etc., making their mechanical properties different from a homogeneous rock mass. Such responses need to be addressed in engineering designs, such as blast design. Contacts between different rock types are commonly formed from magma intrusion, faulting, or deformation of bedding rocks. The contact between soft rock and hard rock in blasting results in variable energy dissipation at the interface and hence variable stress wave attenuations. Studies on the behavior of the transmitted wave through interfaces with different impedances show that the wave can either be attenuated or enhanced depending on the direction of wave travel. The presence of interfaces may cause partial propagation, reflection, or total arrest of the stress waves and cracks in variable proportions, depending on the properties of structures and the strength of the incident wave.

This study investigates two rock contact scenarios in 2D models of square patterns 5.5 m by 5.5 m with a single blasthole 203 mm diameter charged with emulsion. The first scenario is the

contact between “hard-to-soft” and “soft-to-hard” with the interface at 1.5 m from the blasthole. The second scenario is “hard-soft-hard” and “soft-hard-soft” with interfaces at 1.5 and 2.5 m from the blasthole and monitoring points at 1, 2, and 3 m distances (M_1 , M_2 , and M_3) as demonstrated in Figure 5-4 for pressure and PPV monitoring.

Comparing the intact soft rock, the stress wave attenuates when passing through the interface from “hard-to-soft” rock as seen in Figure 5-5 (a) and (c), and is enhanced through the “soft-to-hard” interface, as seen in Figure 5-5 (b) and (d). This was also observed by Ding et al. (2022) and Fan et al. (2018). The pressure is reflected in the “hard-to-soft” interface, resulting in double peaks on the incident side. The PPV is enhanced through “hard-to-soft” contact, as seen in Figure 5-6 (a) and (b), and attenuates through “soft-to-hard” contact, as seen in Figure 5-6 (b) and (d).

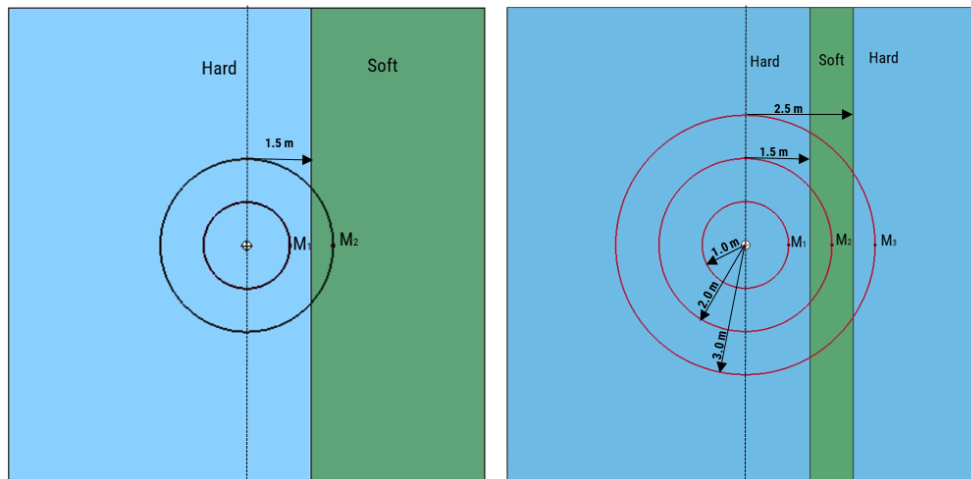


Figure 5-4: General models for the simulation of contacts between soft and hard rock

On multiple contacts, energy transmission and reflection across the contacts follow the same trend, although depending on the interface, for example, on “hard-to-soft-to-hard” (HSH) in Figure 5-5 (e) and (c), the pressure on the soft rock at 2 m increases due to increase in confinement causing increase in the pressure transmitted to the hard rock at 3 m distance. The opposite to this

is observed on “soft-to-hard-to soft” (SHS) in Figure 5-5 (d) and (f). As demonstrated in Figure 5-6(e) and (f), the PPV decreases on HSH contacts and increases on SHS contacts.

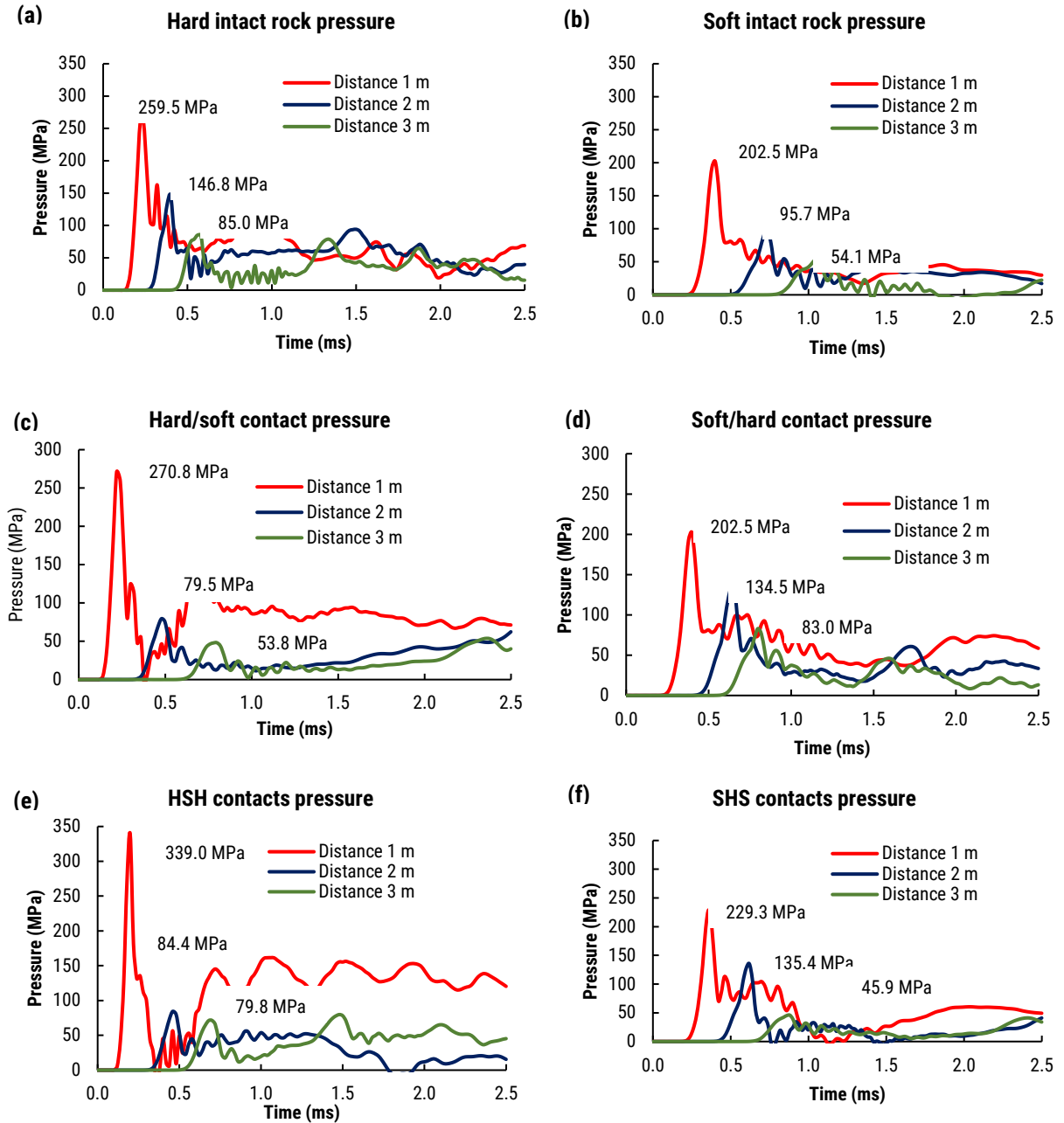


Figure 5-5: Pressure curves across the interfaces of soft and hard rock

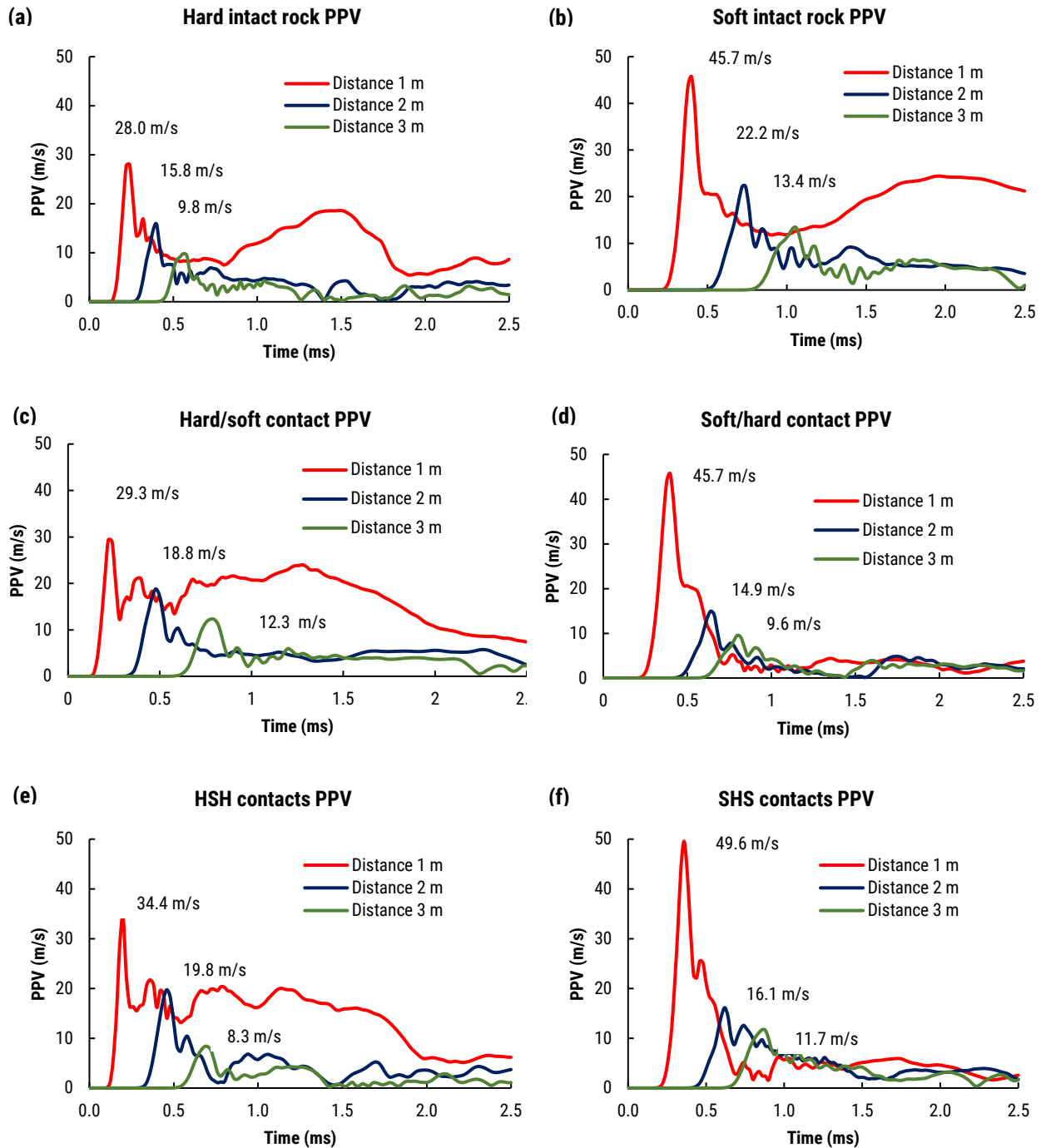


Figure 5-6: PPV curves across the interface of soft and hard rock

Although the pressure is enhanced on “soft-to-hard” contact due to higher attenuation in the soft rock, the stress wave barely exceeds the dynamic strength of the hard rock, causing the cracks to terminate at the contact, as demonstrated in Figure 5-7(b). Near the free face, the reflected stress

wave is higher than the rock's tensile strength, causing further fracturing. On the contrary, on the "hard-to-soft" interface, the stress is attenuated but still above the soft rock strength and therefore, the cracks propagate as seen in Figure 5-7 (a). Additional burden fracturing is observed on HSH contact from the stress wave reflection at the free face. Similarly, new cracks are observed mid-bench on the hard section of SHS contacts due to stress wave reflection on the second interface. Generally, cracks are likely to be terminated on the "soft-to-hard" interface and propagated on the "hard-to-soft" interface.

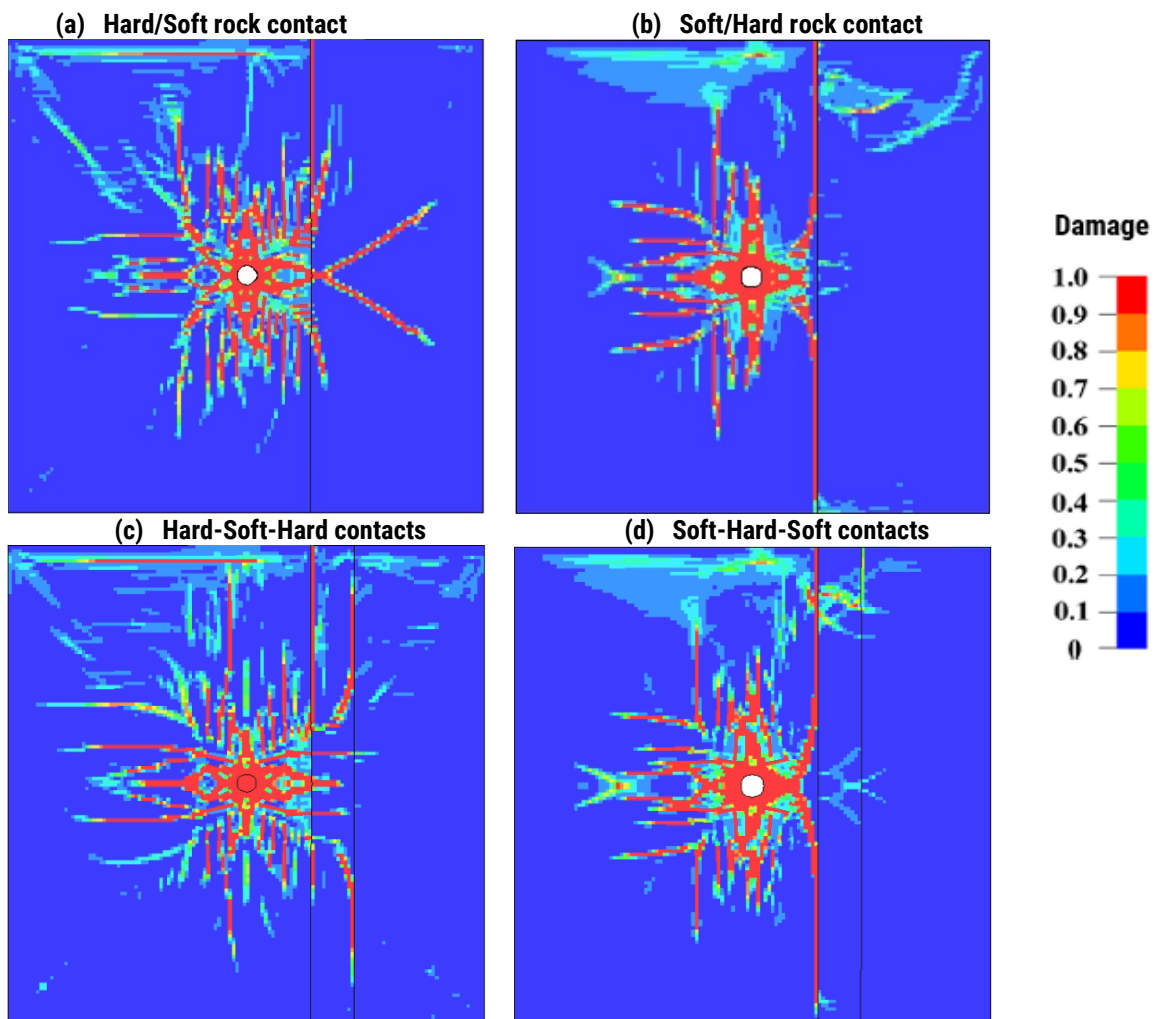


Figure 5-7: Damage propagation beyond the contacts between soft and hard rock

5.4 The effects of joint parameters on blast fragmentation

The most common feature encountered in the rock mass is the joints formed from brittle rock fracture, usually by tensile stress acting on a solid rock. The joints can be empty or filled with various materials such as clay, sand, etc. When the rock fractures and somehow gets displaced, it forms a fault. The joints and their properties influence overall rock strength, the interaction of explosive energy with the rock, and the subsequent fragmentation during blasting. Understanding the influences of joints' properties is important in enhancing blast designs.

5.4.1 Joint infill material

The infill material influences energy distribution in blasting. Depending on the properties of the infill material, the joint can absorb, reflect, or propagate explosive energy at various proportions, leading to various outcomes. The effect of infill material is analyzed through simulations of empty joints (air-filled joints) and joints filled with clay material. Air is modelled as NULL material and ALE part with properties described in Table 5-4, while the clay infill is modelled using the plastic kinematic material model as a Lagrangian part with properties detailed in Table 5-5. A 2D model consisting of a single blasthole 203 mm in diameter and a square pattern 5.5 by 5.5 m is used in the simulation with a 3 cm joint wide 1 m from the blasthole. The same model size and blasthole size is used for the analysis of the remaining joint parameters.

Table 5-4: Air material parameters

Density (kg/m ³)	C4	C5	C6	E _o (MPa)	Vo
1.29	0.4	0.4	0	0.5	1

Table 5-5: Clay material parameters

Density (kg/m ³)	Young's Modulus (GPa)	Poisson's ratio	Yield stress, (MPa)	Tangent Modulus, (GPa)	Hardening parameter	Failure strain, FS
1,600	5	0.35	0.4	4	0	0.5

When the stress wave encounters the joint, partial or complete reflection and transmission occur with energy re-distribution depending on the material type. In this case, as demonstrated in Figure 5-8 (a) reflection at the joint/rock boundary is observed on the pressure contours at 0.7 ms. More energy is reflected on air-infill joints leading to excessive failure on the incident side around the charge and less fracturing on the opposite side as illustrated by Figure 5-8 (b) and Figure 5-9. The number of damaged elements when the joint infill material is clay (see the dotted graphs in Figure 5-9) is higher than in the air-infill joint model, except for higher damage levels between 0.8 and 1. This is contributed by the elements on the incident side of the air-filled joint as seen in Figure 5-8 (b). The peak pressure from the blasthole was monitored at various intervals. Figure 5-10 illustrates the relationship between pressure and distance from the two infill materials. The stress waves closer to the blasthole are lower when joints are present with a much lower value in the air-filled joint. Pressure at 1 m is higher for the air-infill joint due to wave reflection at the joint; the pressure drops and falls below the clay curve beyond 2.5 m. Changing the properties of the clay will lead to different results depending on the material's yield strength (Wang et al., 2018). The transmission of wave energy also depends on factors such as the angle at which the wave meets the interface. Further analysis of joint angles and their impact will be discussed in Section 5.4.4.

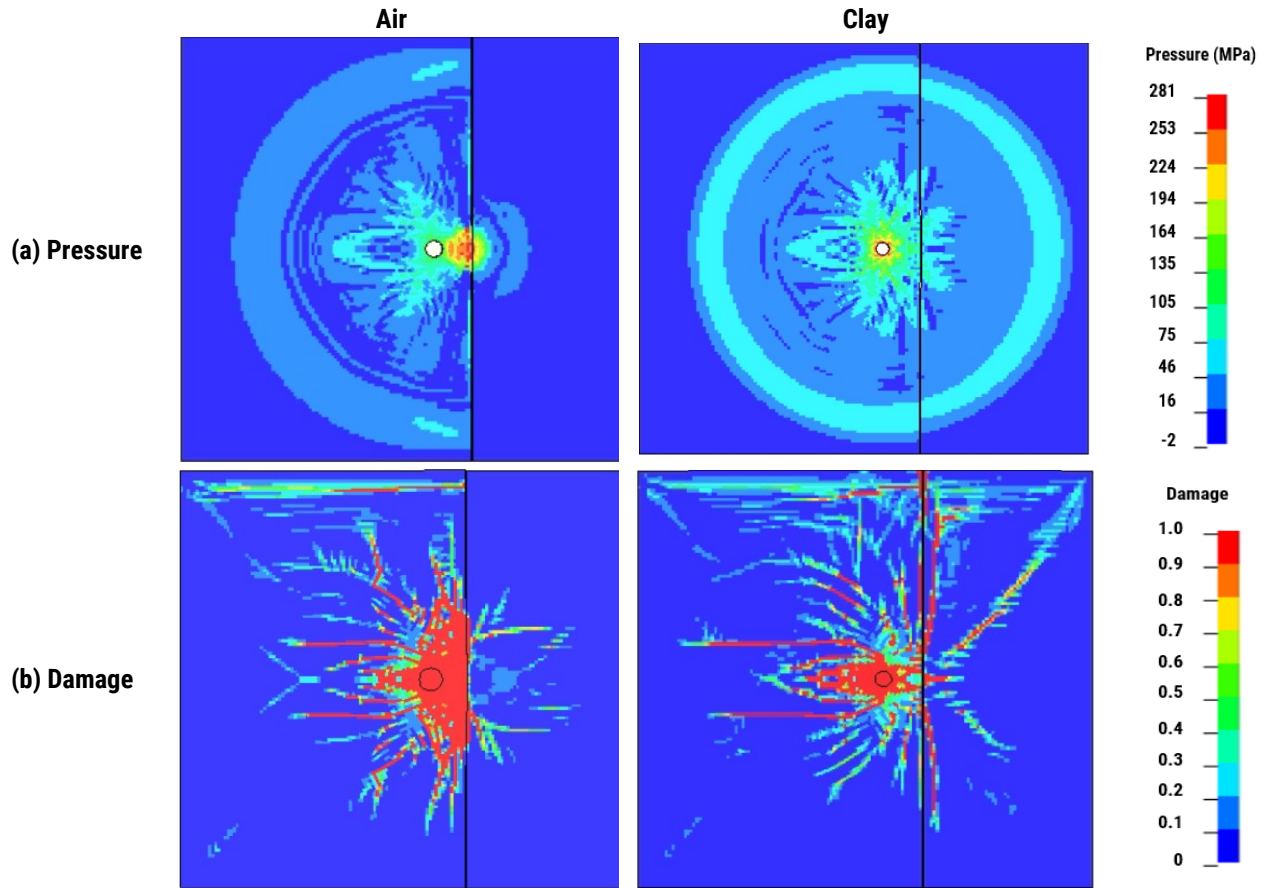


Figure 5-8: The effect of empty joint and clay as joint infill material on the extent of damage

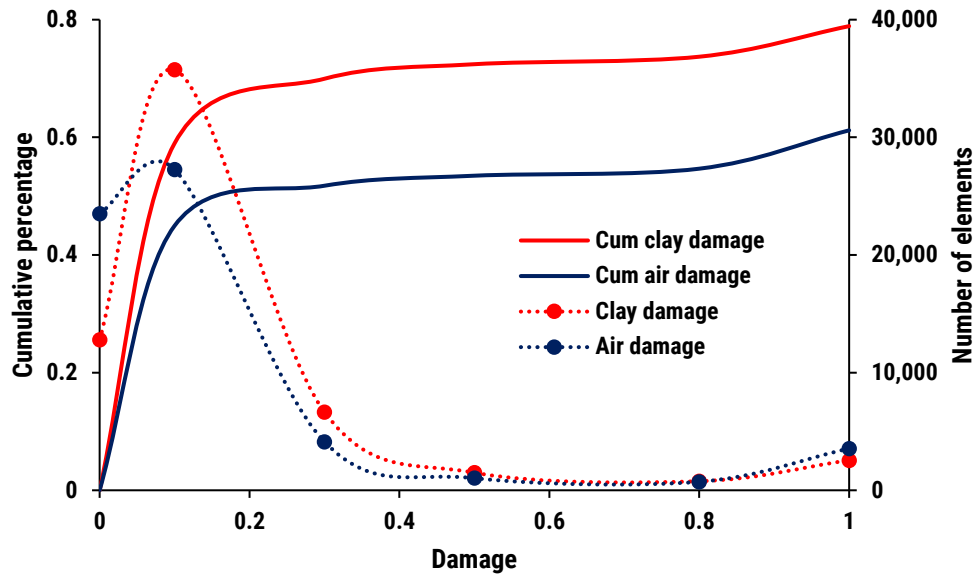


Figure 5-9: Cumulative damage distribution for empty joint and clay as infill material

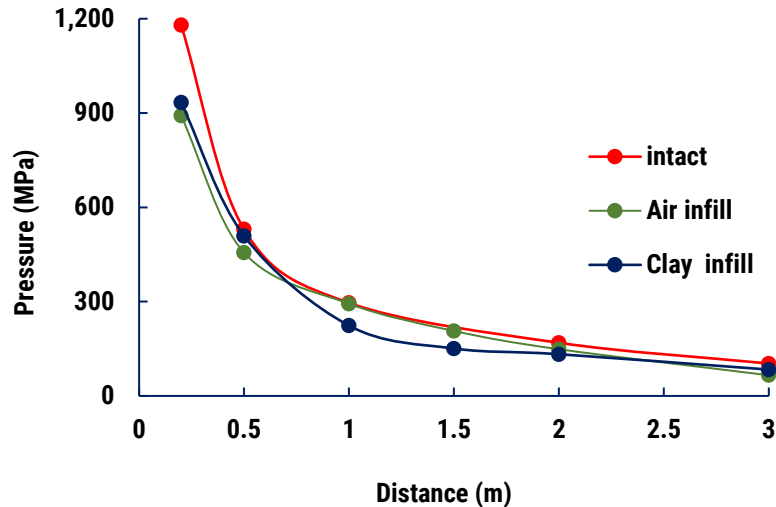


Figure 5-10: Pressure across a 3 mm joint with clay and air-infill materials

5.4.2 Joint width and persistence

For the same type of infill material, various outcomes can be expected from various joint widths and persistence. Two cases are presented with joint widths set at 3 cm and 10 cm for the same pattern size and explosive. Clay material is used as a filling in the joints. Comparing the two cases, the damage on the opposite side of the joints decreases significantly as the width increases. From Figure 5-11(a), several cracks are observed on the opposite side of the joint on a 3 cm wide joint. When the joint width is 10 cm, the explosive energy attenuates significantly with the least fracturing on the opposite side of the joint.

When the stress wave reaches the interface, the stiffness of the joint increases at a rate that depends on the joint's thickness and the normal stress. For the same infill material and normal stress, smaller joints have higher specific stiffness growth than wider joints. An increase in joint stiffness increases the joint's transmission coefficient.

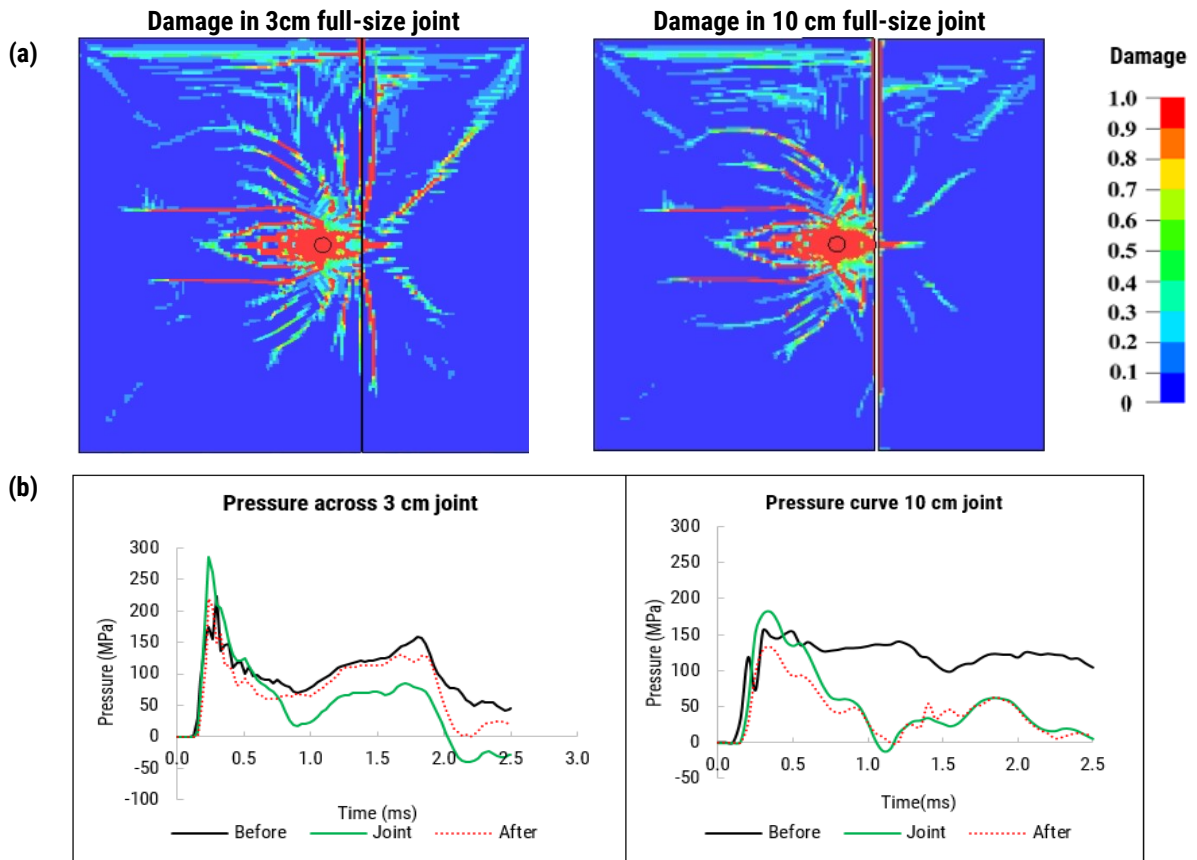


Figure 5-11: Damage distribution and pressure curves for 3 cm and 10 cm joint widths

Figure 5-11(b) describes the pressure history for both cases before, within, and after the joint. The double peaks are observed on the pressure curves before the joint from the wave reflection at the joint; more energy is absorbed on a wider joint. The pressure inside the joint is higher than the incident pressure in both cases; lower peaks are observed in the wider joint due to higher joint compressibility. The transmitted stress wave on a wider joint is much lower due to joint deformation under the stress wave, which is also seen at the rock/joint interface in Figure 5-11(a); extra energy absorption causes a further decrease in the energy transferred across the joint.

Joint persistence refers to the continuity of the joint in the rock mass. For the same joint properties and orientation, fracturing is favoured by discontinuous joints by the formation of new fractures from stress concentration on the cracks/joint tips and uninterrupted energy

transmission on the rock bridges as illustrated in by the damage and pressure contours in Figure 5-12(a) and (b). Similar outcomes were observed by Jayasinghe et al. (2019).

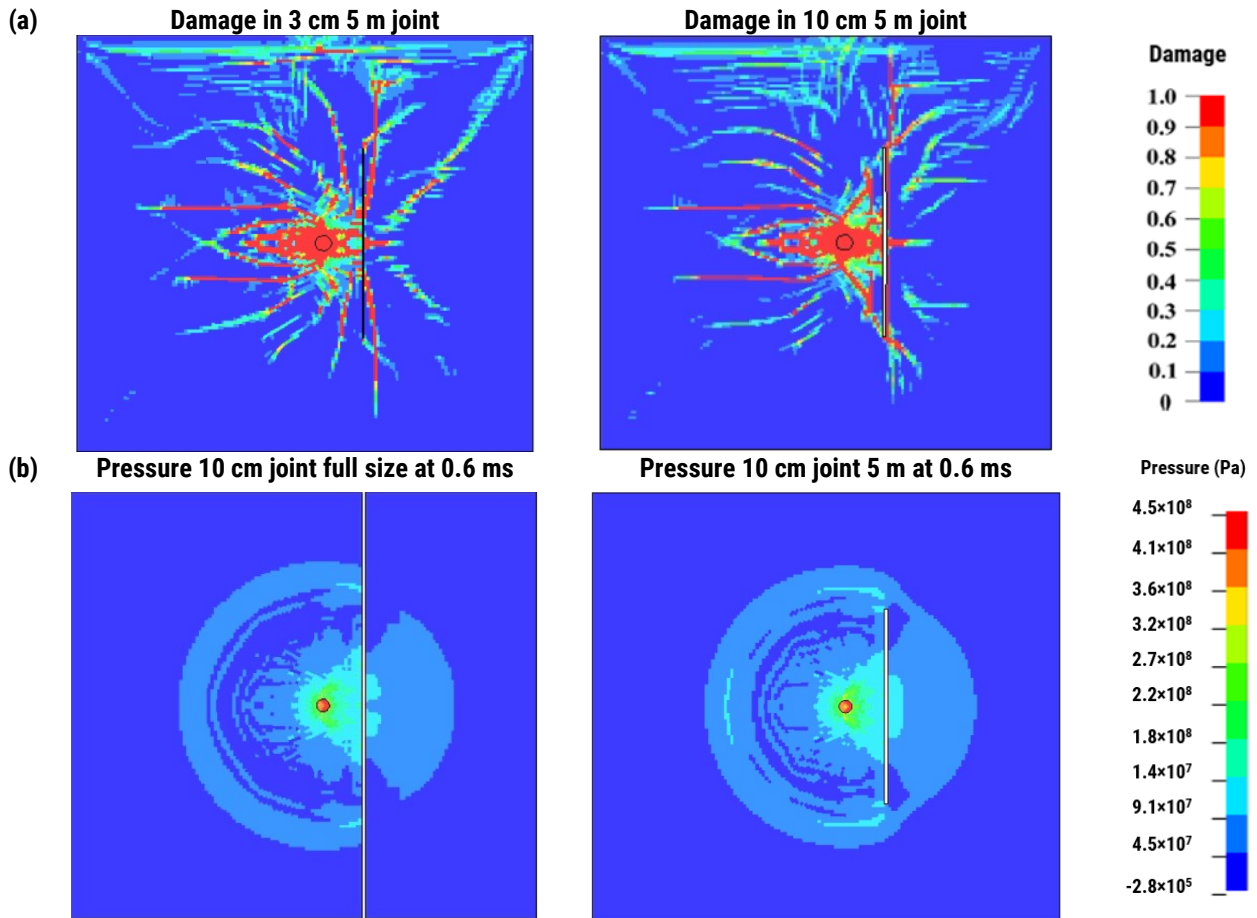


Figure 5-12: Variability in stress and damage distribution with joint continuity

5.4.3 Joint distance from the blasthole

During blasting, the stress wave encounters joints in the rock mass at various distances. The strength of the transmitted wave and, hence, fracture distribution beyond the joint depend on the properties of the joint and the distance the joint has been encountered, which, in light of attenuation, define the intensity of the incident wave. Four scenarios are presented with a joint at 0.5, 1, 2, and 3.25 m; with the same joint properties and orientation. The analysis of the fracture pattern generated in the four cases indicates that the closer the joint is to the blasthole; the more

energy is reflected and used up on joint deformation, causing less fracturing on the opposite side as is the case with the 0.5 and 1 m distance joints in Figure 5-13.

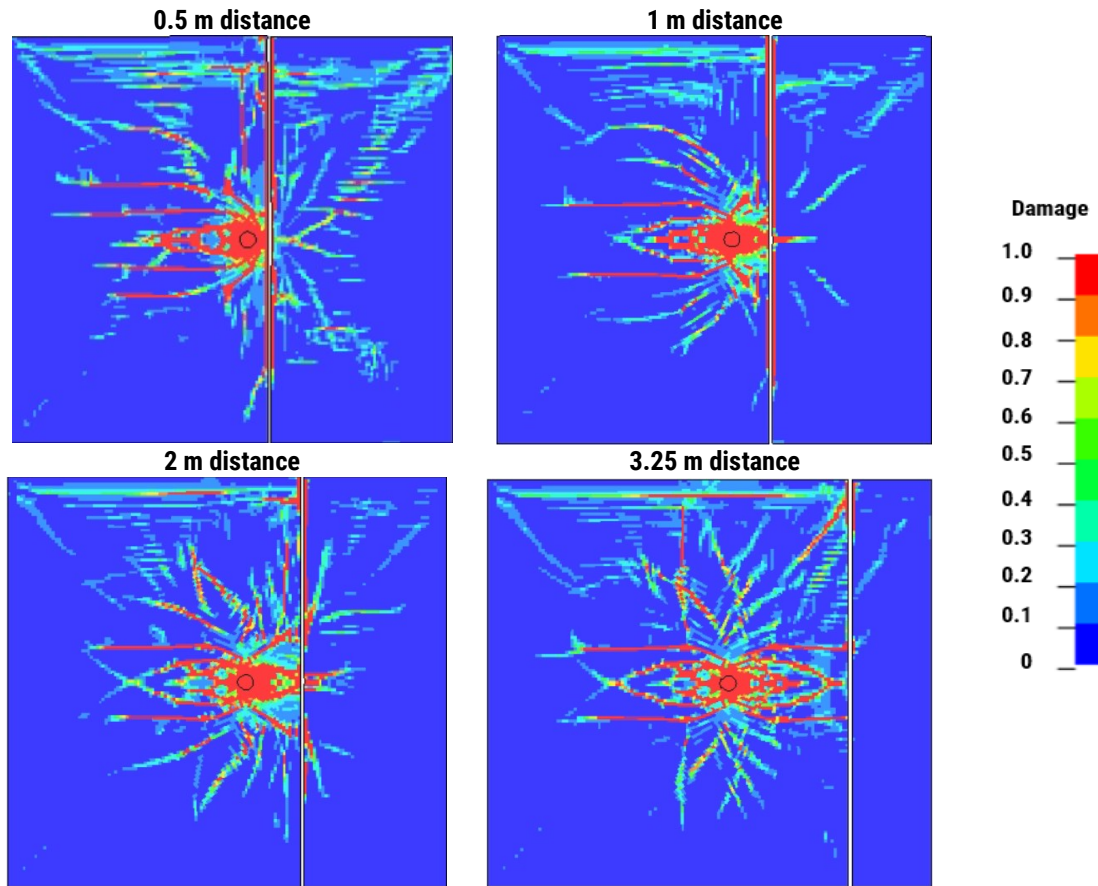


Figure 5-13: Damage distribution for variable joint distances from the blasthole

Unlike the 1 m distance joint, when the joint is at 0.5 m distance, the high-stress wave energy associated with proximity to the blast influences the transmission of adequate energy across the joint to continue fracturing with additional enhancement from the wave reflection at the free face. At 1 m, the stress wave has slightly attenuated. With a substantial amount being used in joint deformation, the stress wave is weakened, causing less fracture on the opposite side. As distance increases, wave energy reflection and joint deformation decrease; hence, with increased stiffness at 2 m distance, the joint transmission improves along with fracturing on the opposite side of the

joint. At 3.25 m, the stress wave has attenuated, and way less energy is transmitted across the joint, resulting in little to no cracking on the opposite side of the joint.

5.4.4 Joint orientation angle

The dipping angle and orientation of the joints relative to the free face influence the propagation of the stress wave and distribution of fractures. Six scenarios for various joint orientations were analyzed, including a joint at 0, 15, 30, 45, 60, and 90 degrees relative to the free face. The joints are 3 cm wide with clay as the infill material and are 2 m from the blasthole. The general view of the models and the damage distribution for variable orientations and the intact rock are illustrated in Figure 5-14.

The orientation of the joints influences the direction and propagation of cracks. Cracks propagation beyond the joint depends on the angle at which the stress wave strikes the joint interface. Regardless of the joint orientation, in the areas where the joints are hit perpendicularly or near perpendicular, sufficient energy is transmitted and cracks propagate across the joint. This was also observed by Fakhimi and Lanari (2014). Better crack propagation beyond the joints is observed on angled joints i.e. the 30 and 45 degrees joints.

When the stress wave meets the discontinuity at an angle, it is reflected and causes tensile fractures on the incident side if it is higher than the tensile strength of the rock as seen in Figure 5-14 (60° scenario). Further burden fracturing depends on the wave reflection at the free face. Energy reflection is limited to the area close to the free face when the joint is near or perpendicular to the free face as for 60° and 90° joints. Since the joints' orientations do not favor further cracking from wave reflection at the free face, fragmentation on the opposite side of the joint is reduced significantly.

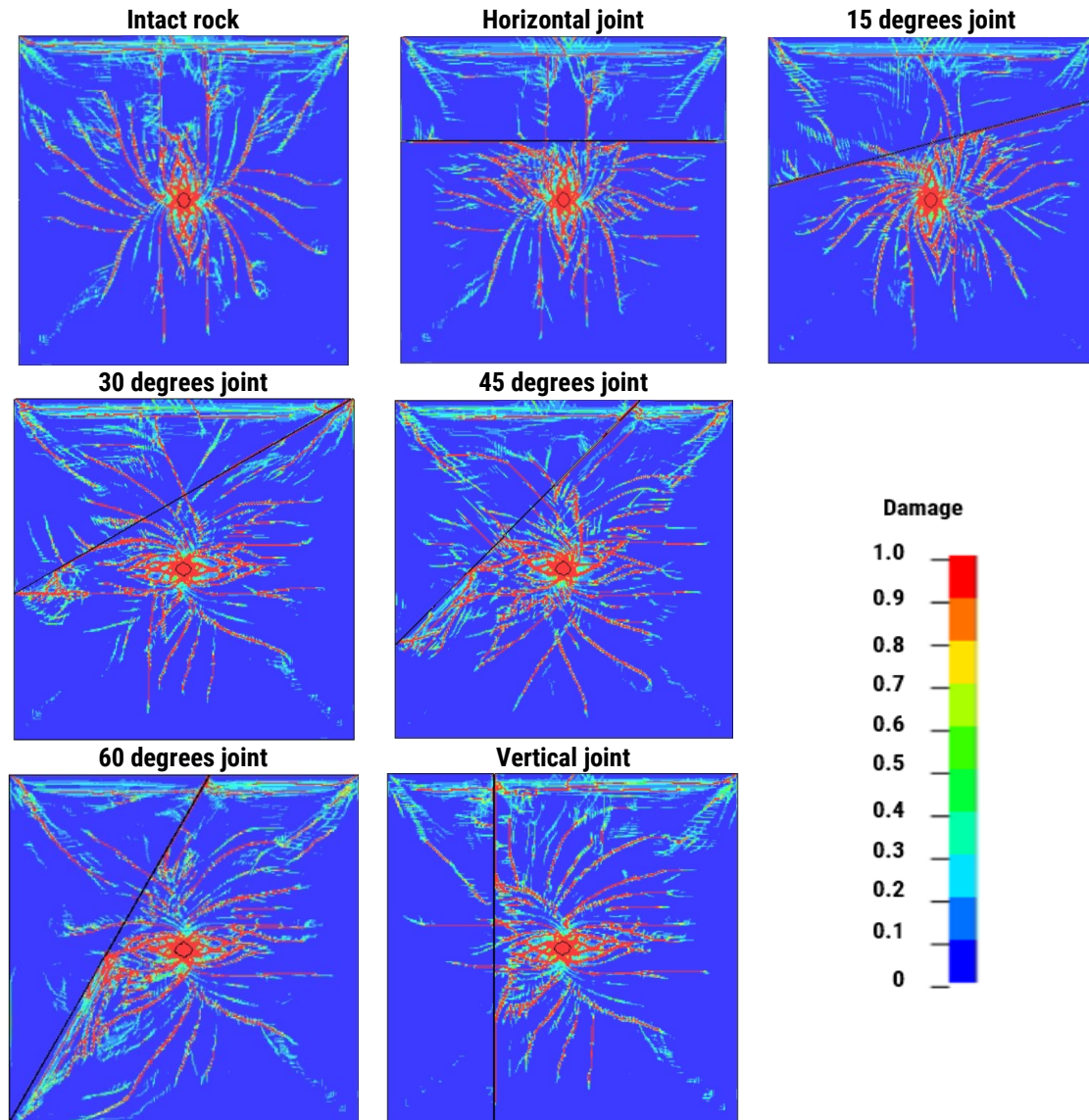


Figure 5-14: Influence of joint orientations on damage distribution

Joint dipping direction influences blast fracturing, as described in Figure 5-15. The joint is 8 cm wide with clay as the infill material and is at an average distance of 2.7 m from the blasthole. When the joint is dipping towards the blasthole, fractures propagate more easily along the joint planes, enhancing fracturing on the opposite side. Conversely, when the joint is dipping away from the blasthole, less stress wave energy propagates along the joints, reducing the extent of fracturing.

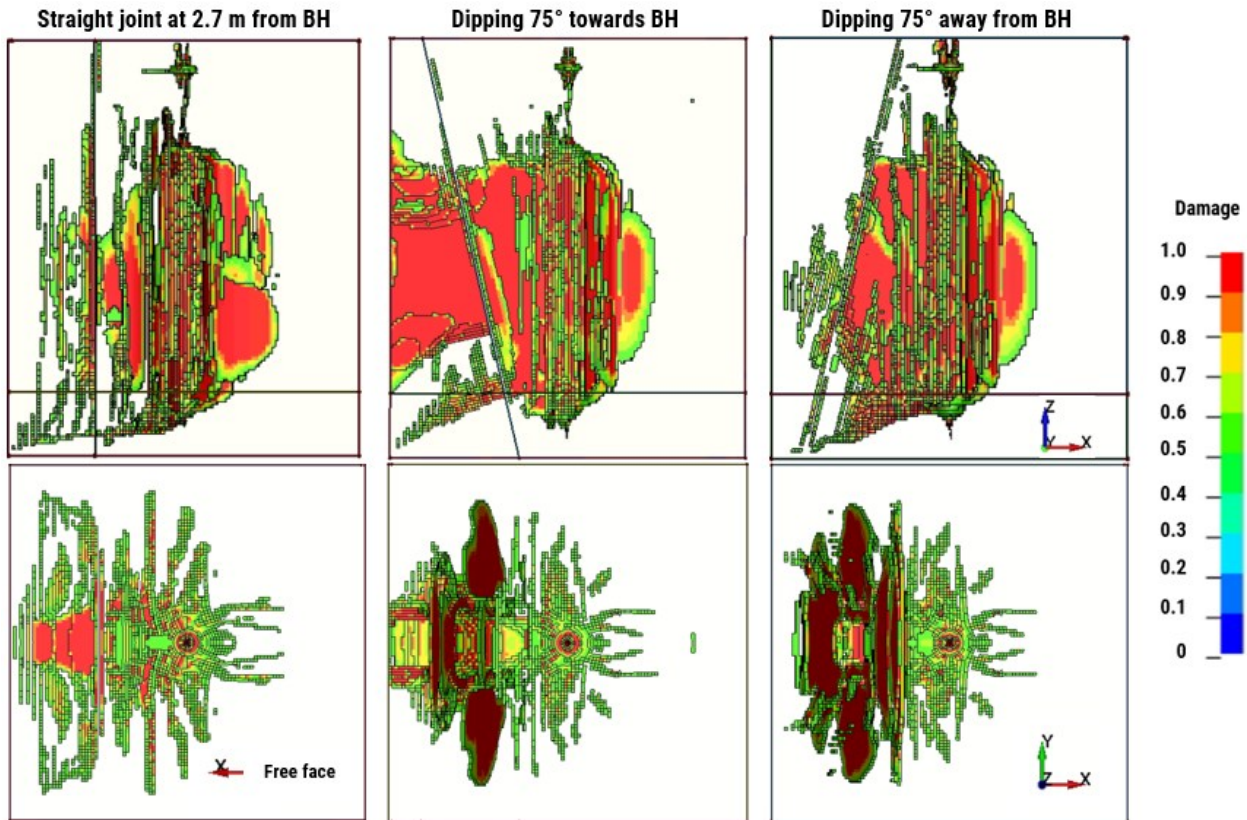


Figure 5-15: Joint dipping angle and its effect on fracturing

5.4.5 Joint spacing (fracture frequency)

The presence of joints interrupts energy transmission in the rock mass as discussed in sections above. Joints usually occur in multiples, evenly spaced, with the same orientation and physical properties forming a joint set. When two or more joint sets intersect, they create a joint system, a common feature of rock mass. The spacing between the joints (fracture frequency), orientations, and intersections affect the fracture distribution from blasting. For the joint sets, three scenarios are investigated for the influence of fracture frequency with 2, 3, and 4 joints per meter.

The simulation results show that the increase in joint frequency reduces the burden cracking as illustrated in Figure 5-16(a). With the increase in joint frequency, the wave goes through multiple partial reflections and transmissions, weakening the strength of the wave. The stress wave is also

weakened by joint deformation, which is more significant with the increase in the number of joints. Stress concentration between adjacent joints also alters stress distribution and rock strengthening as also observed by Wei et al. (2024).

The analysis of the joint system (randomness) with three parallel joints and three intersecting joints, all within 3 m width in Figure 5-16(b), shows better energy transfer in parallel than random joints, indicated by the least fracturing on the opposite side of the joints. This is caused by multiple reflections, refractions, and scattering at the joint interfaces, increasing the wave's attenuation.

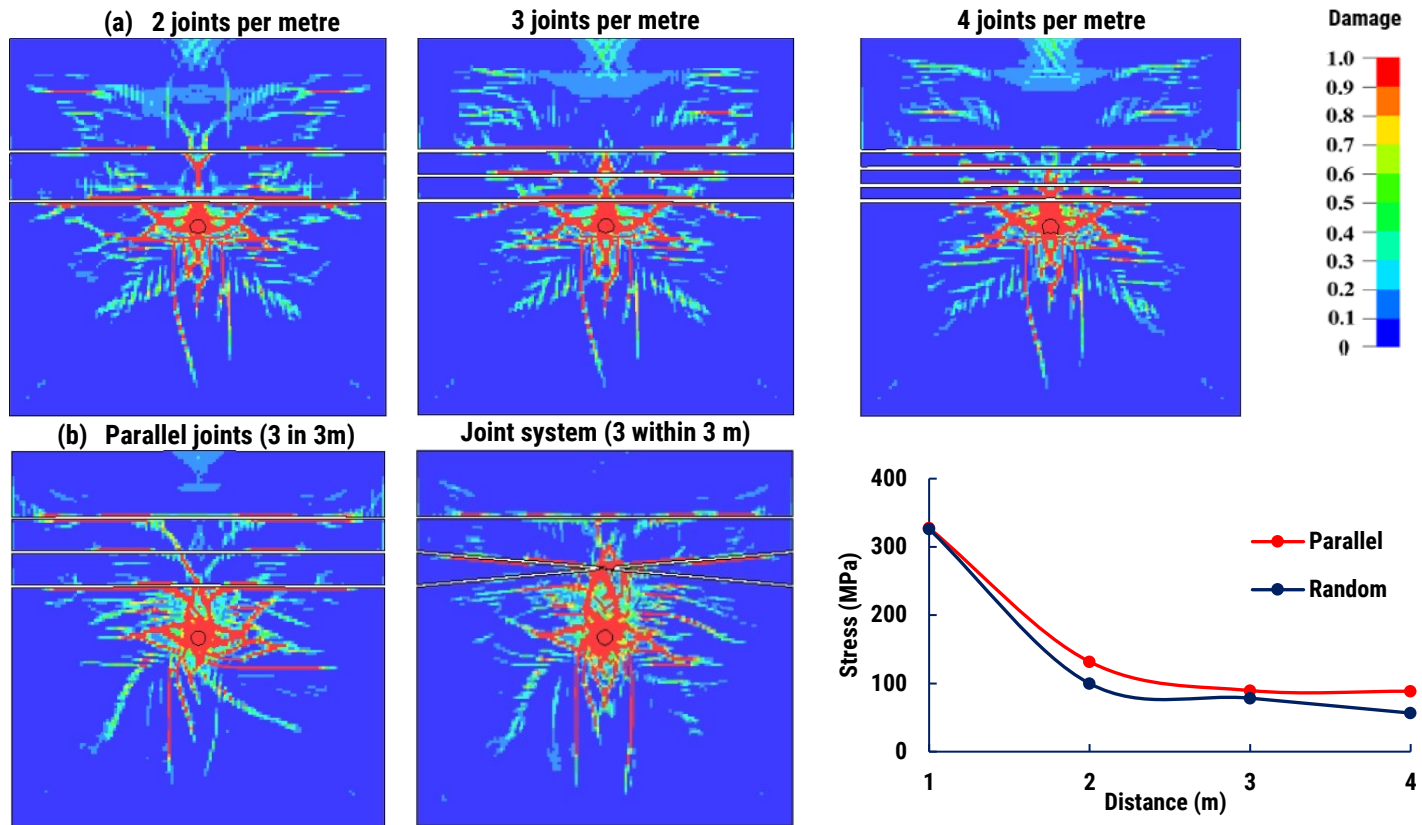


Figure 5-16: Fracture frequency and joints randomness influence on rock mass fracturing

5.5 Summary of the analysis

Sections 5.2 to 5.4 cover the analysis of several factors influencing blast outcomes. The analysis of explosive energy and rock strength indicates that high-energy explosives offer a greater extent of fracturing, while low-energy explosives offer a better energy distribution. However, the extent of fracturing in soft rock does not improve with increasing explosive energy due to less confinement associated with the low strength and higher deformations.

Regarding the influence of structural properties, the contacts between soft and hard can enhance or attenuate the stress wave depending on the direction of the wave. The intensity of the transmitted wave, hence its ability to cause fracturing, depends on the incident wave's strength and the associated rocks' impedance difference.

The joint parameters affect explosive energy and fragmentation differently depending on the size (width) of the joint and the type of infill material. Other factors such as the orientation, continuity, fracture frequency, and distance from the charge intensify the effects. The influences of these parameters on the damage extent are summarized in Figure 5-17.

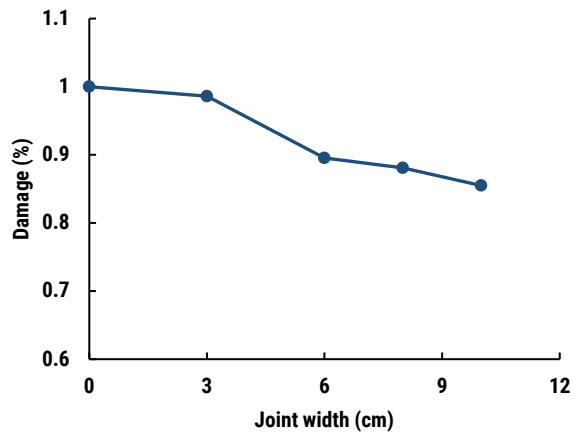
The type of joint infill material and the width influence the transmission of the energy and crack propagation across the joint depending on the rock/joint material impedance difference and joint stiffness. Empty joints reflect most energy, while wider joints lower the transmitted wave energy from partial reflection and energy absorption in joint deformation. The analysis indicated reduced overall damage by 13% by increasing joint width from 3 cm to 10 cm. Joint persistence determines the surface area in which the joint affects the wave. Discontinuous joints favour more fragmentation by offering rock bridges for stress wave and crack propagation and by the stress concentration points on the joints' tips where fractures are initiated.

Stress energy and cracks can easily propagate in the areas where the stress wave strikes the interface perpendicularly or near perpendicular; more energy is reflected when the wave hits the interface at an angle, making the angled joints (in this case 30 and 45 degrees) favourable in energy and cracks propagation; see Figure 5-14. Fracturing on the opposite side of the joint can occur due to stress wave reflection at the free face. However, in the case of perpendicular joints to the free face, the limited exposure limits the improvements in fracturing from stress wave reflection.

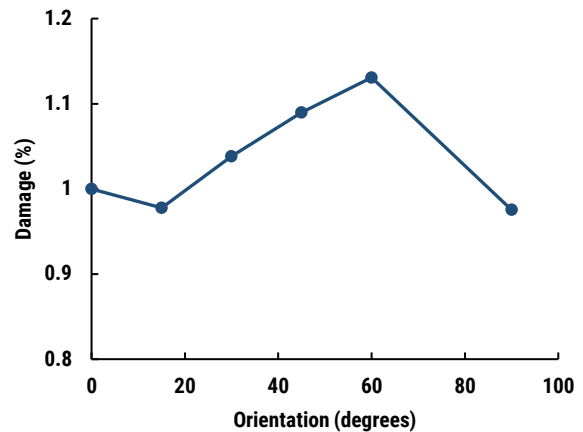
While there is consistent attenuation of energy and formation of cracks with an increase in fracture frequency, the increase in distance from the charge does not necessarily dictate stress wave and crack propagation. When the joint is very close to the blasthole, the stress wave is strong, allowing transmission of a strong enough stress wave across the joint. As the distance increases, from the high-intensity zone, most of the energy is either used in joint deformation or gets reflected on the interface, resulting in minimal fracturing on the opposite side. Further increase in distance enhances joint stiffness, and with less energy being used up on joint deformation, improvements in fracturing are observed. When the joint is the furthest, most of the fracturing occurs before the joint, and the stress wave weakens, resulting in less energy transmission and less fracturing on the opposite side.

Joints usually occur in families with similar properties and orientations, forming joint sets or systems. Analysis shows that increased fracture frequency leads to a consistent decrease in radial crack formation on the opposite side of joints while enhancing tangential cracks. Overall damage reduces by 9% when fracture frequency increases from one to four. Parallel joints

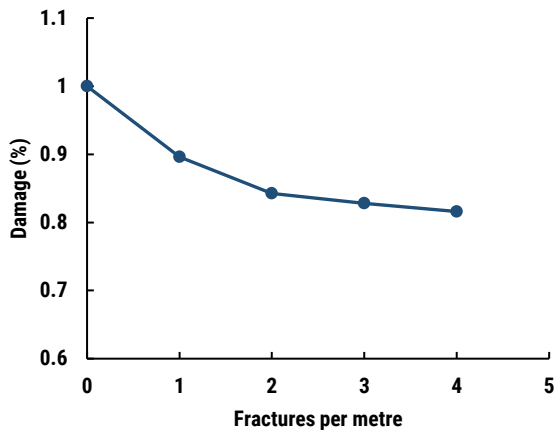
transmit energy more effectively than randomly oriented (intersecting) joints, primarily because random joints cause changes in stress wave direction, reducing energy transmission.



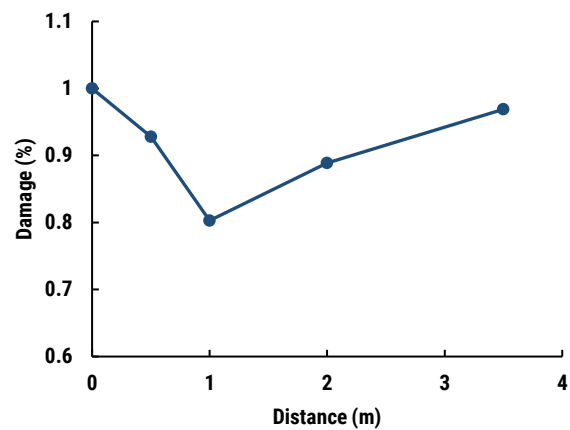
(a) Damage for various joint widths compared to intact rock



(b) Damage at various orientations compared to horizontal joint



(c) Damage for various fracture frequencies compared to intact rock



(d) Damage at various distances compared to intact rock

Figure 5-17: Summary of the effect of joint parameters on rock mass fracturing

5.6 Comparison of results with fragmentation analysis

Fragmentation size analysis was done using Wip-frag software (WipWare, 2021) from the pictures taken from the blasted muckpile. The pictures were taken from a single point at the top of the muckpile. Usually, the oversize fragmentation on top of the muckpile can be expected due to

excessive stemming or toe problem from the upper bench, which was not the case in the study area. Blast movement observed from the tie-up plan in Figure 5-18 indicates material movement perpendicular to the pit wall, making a comparison between intact block size and resulting fragmentation size straight ahead justifiable.

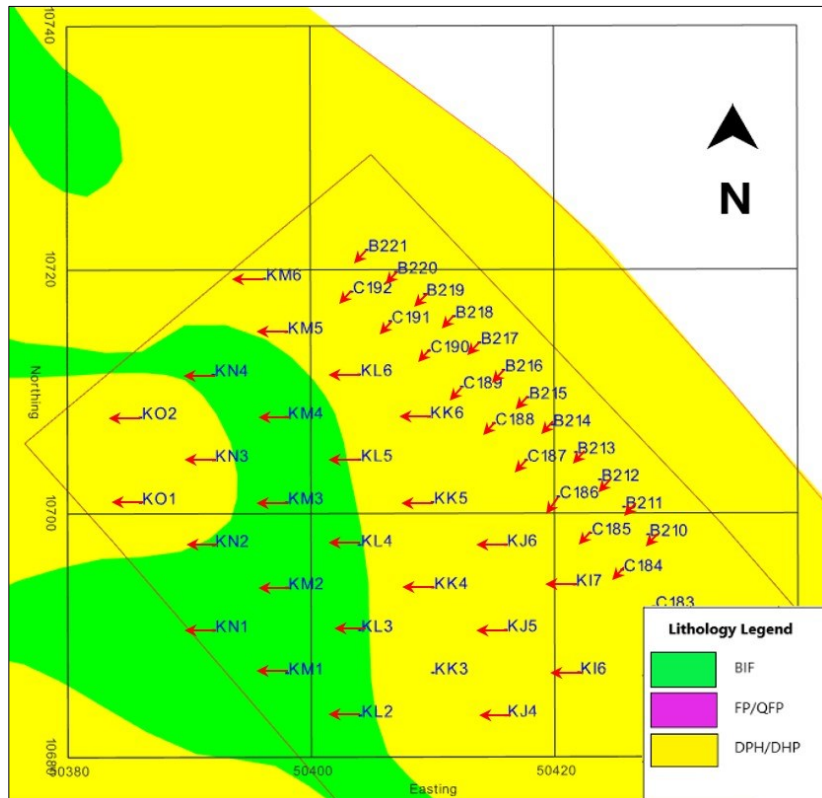


Figure 5-18: Blast movement from tie-up plan

Figure 5-19 shows all mapped structures. Seven pairs of data for in-situ block size and resulting fragmentation were taken from the locations shown in Figure 5-20 and analyzed. The fragmentation images captured areas approximately 3 to 4 m wide by 4 m high at a perpendicular distance to the wall point as described in the figure. It should be noted that Figure 5-20 displays only the structures surrounding blastholes studies that could influence fragmentation around the fragmentation analysis point. Mapping was done by combining stereo photograph analysis

(sirovision) with scanline mapping. Figure 5-21 shows a sample set analysis from the pit wall structures in location 7 to fragmentation distribution in location 8.

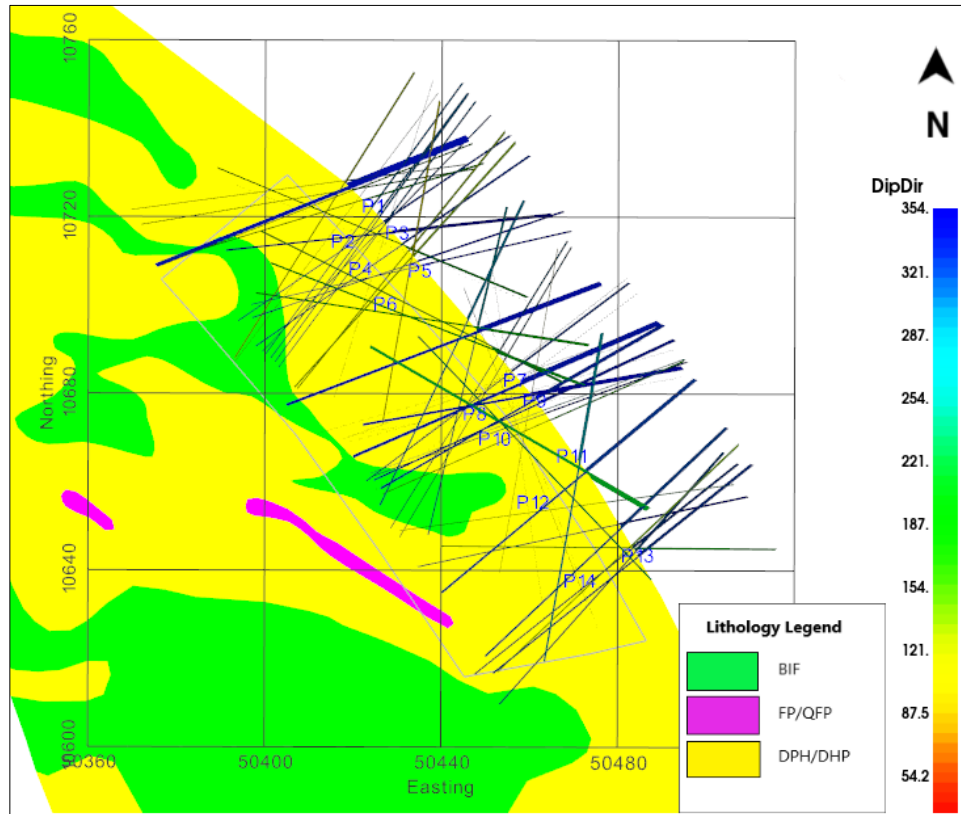


Figure 5-19: Mapped structures on Shot 910_6

The average in-situ block size (B50) was estimated using Wang's equation method (Wang et al., 1990, Latham et al., 2006) based on the characteristics of joint sets. The in-situ block size is the intact rock fragment between joints and is influenced by joint sets' orientation, spacing, and persistence. Mapping is conducted to define the discontinuity sets (Set A, B, and C), the average spacing between joints in a set (S_A , S_B , and S_C), and their average orientations (α , β , and θ) relative to the scanline orientation. From histogram plots of frequency versus joint spacing, the coefficient of spacing distribution for a particular percentage passing value (C_{ip}) is selected based on the coefficients suggested by Wang et al. (1990). In this case, the 50% coefficient C_{50} is used to

calculate B50. The Wang Equation for estimating the in-situ block volume (V_{50}) is shown in equation (5.1). B50 is calculated as the cube root of V_{50} .

$$V_{50} = C_{50} \left(\frac{P_A \times P_B \times P_C}{\cos \alpha \times \cos \beta \times \cos \theta} \right) \quad 5.1$$

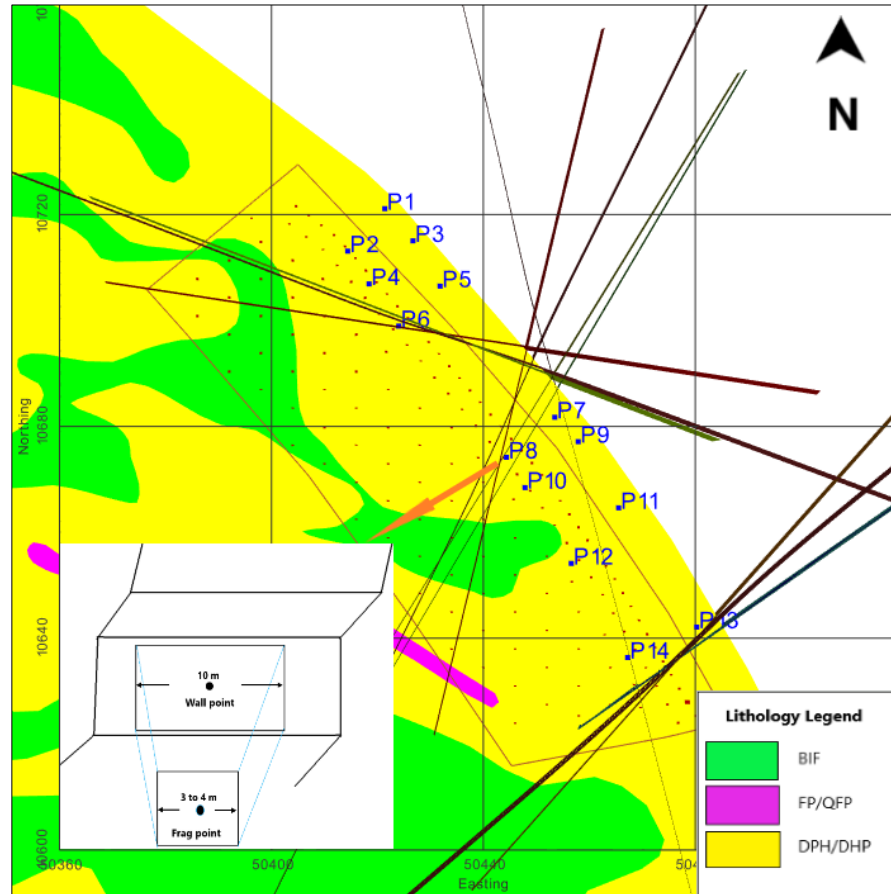


Figure 5-20: Locations for fragmentation analysis with associated structures

From the fragmentation analysis, P50 is the average fragment size. The ratio of intact block size to muck-pile fragment size (B_{50}/P_{50}) is presented as a block reduction factor (BRF). Variation of P50 along the burden is illustrated in Figure 5-22 from the computations in Table 5-6. The analysis excludes P2 and P4 because these are buffer holes with different charge sizes.

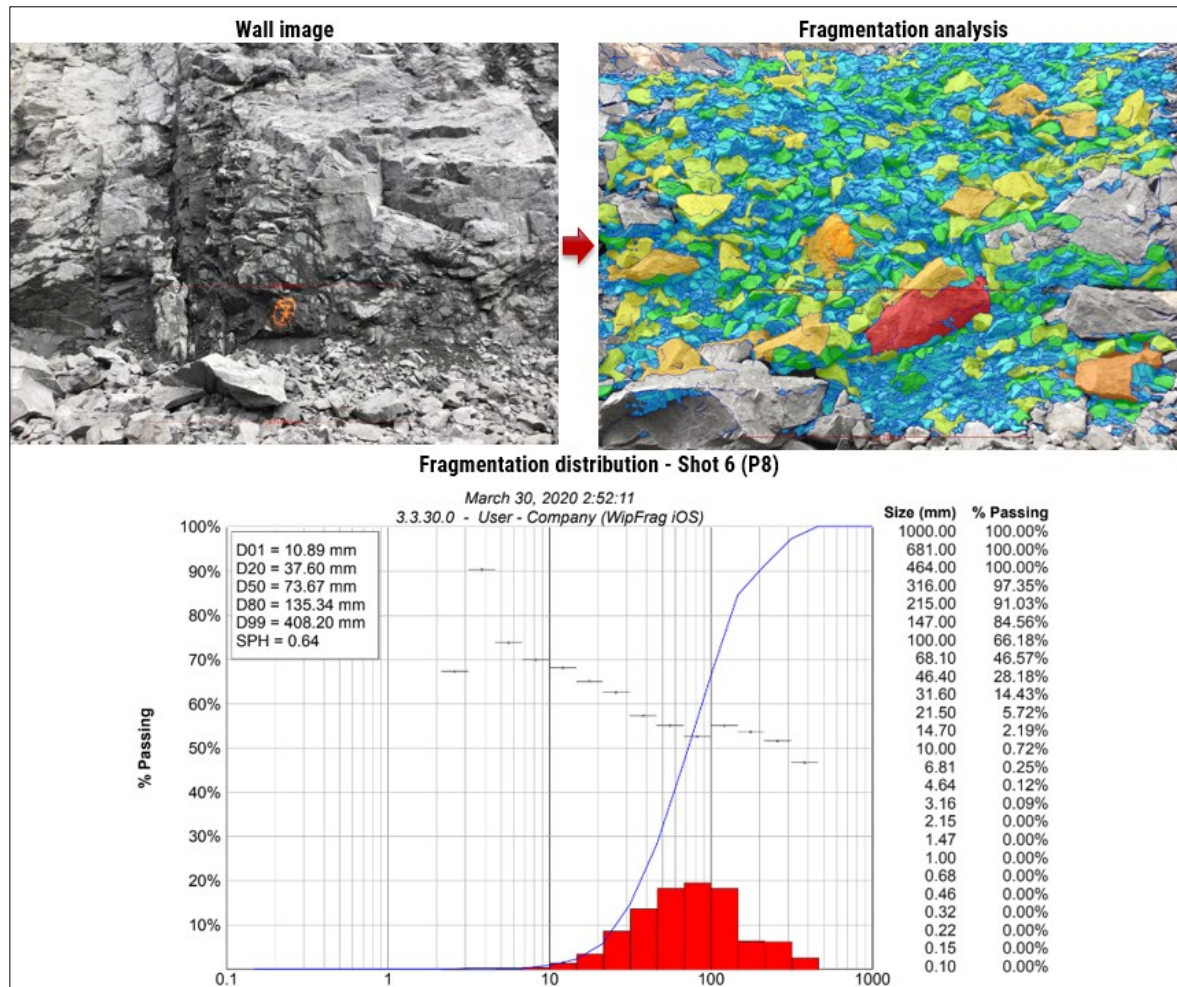


Figure 5-21: Fragmentation sample set analysis

Based on the fragmentation analysis, P8 has the smallest fragmentation size and is the closest to the blasthole. Although multiple random joints cross the burden (see Figure 5-20) they are very close to the blasthole. The monitoring location is also close to the blasthole (within 0.8 m) within the high-intensity stress wave zone, similar to the analysis results in Figure 5-13. P6 is the furthest from the blasthole and has several joints at random orientations crossing the burden, forming coarser fragmentation similar to the scenario in Figure 5-16 (b).

Table 5-6: Block reduction factor estimations

Muckpile Point	Distance from BH (m)	Intact rock size (B50) (m)	Charge (kg)	SD (m/kg ^{0.5})	PPV (m/s)	Average frag. (P50, mm)	BRF (B50/P50)
P2	2.48	1.04	73.24	0.29	1.37	129.14	8.09
P4	2.17	1.68	73.24	0.25	1.58	237.42	7.07
P8	0.8	0.67	210	0.06	8.25	73.67	9.12
P6	2.8	2.38	210	0.19	2.12	267.09	8.89
P10	1.27	2.26	210	0.09	5.00	103.97	21.72
P12	1.65	1.42	210	0.11	3.76	87.98	16.16
P14	1.99	1.30	210	0.14	3.07	184.40	7.07

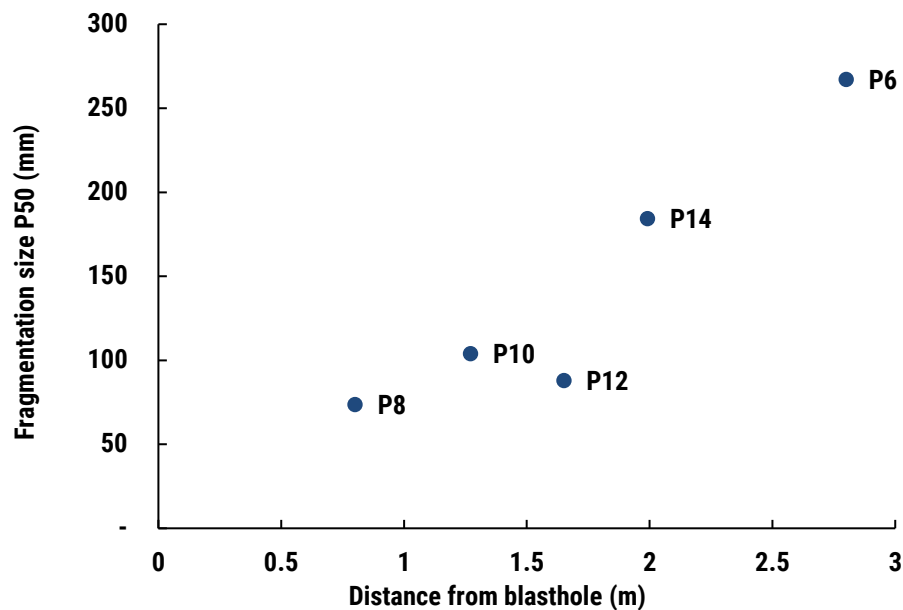


Figure 5-22: Fragmentation along burden in various monitoring locations

P10 and P12 are almost a quarter burden from the blasthole, with no significant joints between the blasthole and the monitoring point. A medium-size fragmentation is observed in both cases with the highest block reduction factor; the BRF for P10 and P12 are 22 and 16, respectively. The similarity between simulation and the blasting fragmentation on the increase of the fragmentation

size (reduced damage) with the distance and the role of joints on the redistribution of stress waves and fractures indicate that the simulation results are feasible.

5.7 Chapter summary and conclusion

Chapter 5 covers the analysis of the various factors that affect blast outcomes and the comparison of the outcomes with the resulting field blast fragmentation. The analysis shows that the explosive properties, rock strength, and structural properties influence the blast outcomes. When blasting an intact hard rock with a strong explosive, the size of the crushed zone formed is relatively small, followed by the longer widely spaced fractures. Using a less strong explosive on the same rock reduces the length of fractures significantly with better fracture distribution. On the other hand, when blasting a soft rock with a strong explosive, the size of the crushed zone formed is relatively bigger (from 0.33 to 0.54 cm) but the extent of fractures is reduced from 5 to 4.5 m: the intensity of damage increases significantly. Using less strong explosives on a soft rock achieves the same damage zone extents with a better distribution of fractures.

The natural rock mass is heterogeneous, with various structures that cross-cut the mass. Such fractures affect the distribution of explosive energy and blast outcomes. The analysis of the structural properties shows the similarity in the behaviour of the stress wave and crack propagation at the interface from the impedance difference of materials and the intensity and direction of the stress wave. When the stress wave travels from the soft to hard rock, it is enhanced and attenuated when it travels in the opposite direction, similar to the cracks. The same is observed in multiple interfaces, although the outcomes may vary depending on the thickness of rock layers.

The presence of joints influences the stress wave and fracture propagation differently depending on the properties of the infill material, the width, and the continuity of the discontinuities. The distance from charge, the number of joints within the designed geometric boundaries, and their orientations intensify the effects. Regardless of the case, to ensure fracturing on the opposite side of the discontinuity, the stress wave has to be stronger than the rock strength; this also applies to the wave reflected on the free face.

From this analysis, it is clear that several factors influence blast outcomes; therefore, no one design fits all sets of desired outcomes. Since the geology, rock, and structural properties cannot be altered, the blast design can be adjusted to mitigate their influence and improve the outcomes.

CHAPTER 6

BLAST FRAGMENTATION MODELLING AND THE INFLUENCE OF DESIGN PARAMETERS ON BLAST-INDUCED FRAGMENTATION

This chapter is the continuation of the work done in Chapter 5. The chapter covers blast-induced fragmentation modelling, including considerations for blast design to improve fragmentation in a discontinuous rock mass. Rock mass considerations are limited to intact hard and soft rocks, contacts between soft/hard rock, and a jointed rock mass.

6.1 Introduction

The fragmentation size and size distribution affect the productivity and production costs of a hard rock mine. Blast-induced fragmentation is influenced by the encountered rock mass as discussed in Chapter 5. The rock mass encountered cannot be modified; therefore, blasting improvements depend solely on the blast design, which includes explosive selection, pattern design, and initiation sequencing and delays. Blast-induced fragmentation modelling as seen in Chapter 5, can be used to effectively predict blast outcomes from the explosives, rock mass properties, and the blast design.

A high level of uncertainty in blast outcomes is caused by geological conditions, which vary from location to location. This and other factors, such as the strength of the explosive and interaction between neighbouring charges, make blasting design a complex task. There can not be one general design, and trial and error can be expensive and time-consuming; blast-induced fragmentation modelling is therefore instrumental in optimizing blast designs.

Several methods are available to predict fragmentation from blasting. Regardless of the method used, it is essential to ensure that the results are feasible by comparing them to the laboratory and/or field measurements. This study used analytical and numerical modelling and covered the validation process in Chapters 4 and 5.

The analysis shows that the rock and explosive strength properties govern the blast outcomes in the intact rock. In the actual blasts where various structures, such as rock contacts and joints are encountered, a layer of complexity is added to the blast process and the outcomes. In production blasts involving the detonation of multiple blastholes, the interaction between the blasts plays a crucial role in determining overall fragmentation. This chapter covers blast-induced fragmentation

modelling, including the role of blast design and the interaction of blastholes in improving fragmentation in different rock masses. A summary of the modelling process is presented in Figure 3-3.

6.2 Blast-induced fragmentation modelling

6.2.1 Energy balance

Fragmentation prediction models are based on the powder factor to determine the explosive charge required to fragment rock within the geometric boundaries based on the explosive strength and rock blastability (the strength and brittleness of material). The two important outcomes of blasting are the fragmentation size distribution and the average size of the fragments. The energy used up in fragmentation to generate rock fragments or create new surface areas is termed fracture energy (G_c) and it is calculated from the density, fracture toughness (K_{Ic}), Young's modulus, and the yield strength of the rock minerals. Equation (5.1) shows an expression used to estimate energy absorbed in creating a new fracture considering fracture toughness. Fracture toughness is a rock property indicating resistance to crack propagation and can be obtained through fracture toughness tests (Grady and Kipp, 1980). Experiments have shown that fracture toughness is controlled by critical stress; mostly the tensile stress. The regression analysis conducted Whittaker et al. (1992) shows that the relationship between the fracture toughness with tensile and uniaxial compressive strength is linear and can be estimated from equations (5.2) and (5.3) for tensile and uniaxial compressive strength, respectively. Like other rock properties, fracture toughness increases with the loading rate and should be considered in the prediction of blast-induced fragmentation.

$$G_c = \frac{K_{Ic}^2}{2E} \quad (5.1)$$

$$K_{Ic_t} = 0.27 + 0.107\sigma_t \quad (5.2)$$

$$K_{Ic_c} = 0.708 + 0.006\sigma_c \quad (5.3)$$

In 1985, Berta presented a relationship to estimate powder factor (PF) required to achieve an average fragmentation from blasting based on the energy balance in equation (5.4); e_r is rock specific energy (kJ/m²), E_o is explosive specific energy (kJ/kg), and η_e account for energy transfer efficiency due to impedance difference between explosive and rock, the coupling ratio, and a fraction of energy used in actual fragmentation (Tomi et al., 2011). Experiments show that the energy absorbed by the rock in dynamic rock fracturing is around 11 to 18% of the total explosive energy; the rest is lost as seismic energy, and used up in other forms of energy like heat, translational and rotational energies of the fragments, etc. (Zhang, 2016, Sanchidrián et al., 2007, Hamdi et al., 2008). Other studies have suggested this value to be as low as 0.1-1% of the total energy (Calnan, 2015, Ouchterlony et al., 2003). It should be noted that these studies ignored the effect of higher strain energy in rock fracturing which is significant in blasting loads.

$$PF = \frac{P_{50} \times e_r}{\eta_e \times E_o} \quad (5.4)$$

The geometric parameters such as the burden, spacing, sub-drill, and stemming height can be estimated by the rule of thumb from the known blasthole diameter and the specific charge and later be modified depending on the properties of the rock mass.

From the case study, the pattern is 5.5 m by 6.5 m by 10 m bench height. Targeting the average fragment size of 5 mm around the blasthole within 0.3 m and 200 mm on the rest and the fracture energy as 18% of the total energy, the powder factor is obtained as 0.76 kg/m³ estimated from equation(5.4). The fracture toughness is considered to increase with dynamic loading from 1.78

to $3.18 \text{ MPam}^{0.5}$ in tension and from 1.46 to $2.57 \text{ MPa m}^{0.5}$ in compression estimated from the equation (5.2) and (5.3), respectively. The total fracture energy requirement of 0.475 MJ/m^3 . Sample calculations are presented in APPENDIX C1.

6.2.2 Influence of rock mass properties

When the powder factor is decided, along with the initial geometrical design, the interaction between the energy produced with the encountered rock mass is important to inform further design modifications, including the decision on the firing sequence and delays. From the explosive detonation, high shock waves are transmitted to the blasthole walls at a pressure termed borehole pressure. This pressure is estimated to be half the detonation pressure, but from the thermodynamic calculations presented in APPENDIX C2, it can be as low as 20%. Simulation results show that the maximum recorded borehole pressure is 2.64 GPa for hard rock and 1.99 GPa for soft rock, which is around 40% and 30% of the detonation pressure.

The attenuation depends on rock properties such as strength and structural properties. Full-size models for hard rock and soft rock were created to analyze the attenuations in various rock properties. Fitting the curve from the peak pressures obtained from monitoring points 5 m from the bottom of the blasthole, the attenuations on the hard rock in the crushed zone up to 1 m distance, (P_{hc}) and fractured zone (P_{hf}), and on the soft rock (P_s) are as indicated in Figure 6-1; where r is blasthole radius, R is the distance from the blasthole, and the exponents are the attenuation constants. On the hard rock, the attenuation close to the charge is significantly rapid and gentle beyond 1 m; separate expressions are used to describe attenuations in these zones.

This was similarly observed by Sun (2013). On the soft rock, the peak pressure increases from the blasthole until the maximum is achieved at a 0.5 m distance, followed by constant attenuations. This can be caused by material compressibility; further studies on this theory are recommended.

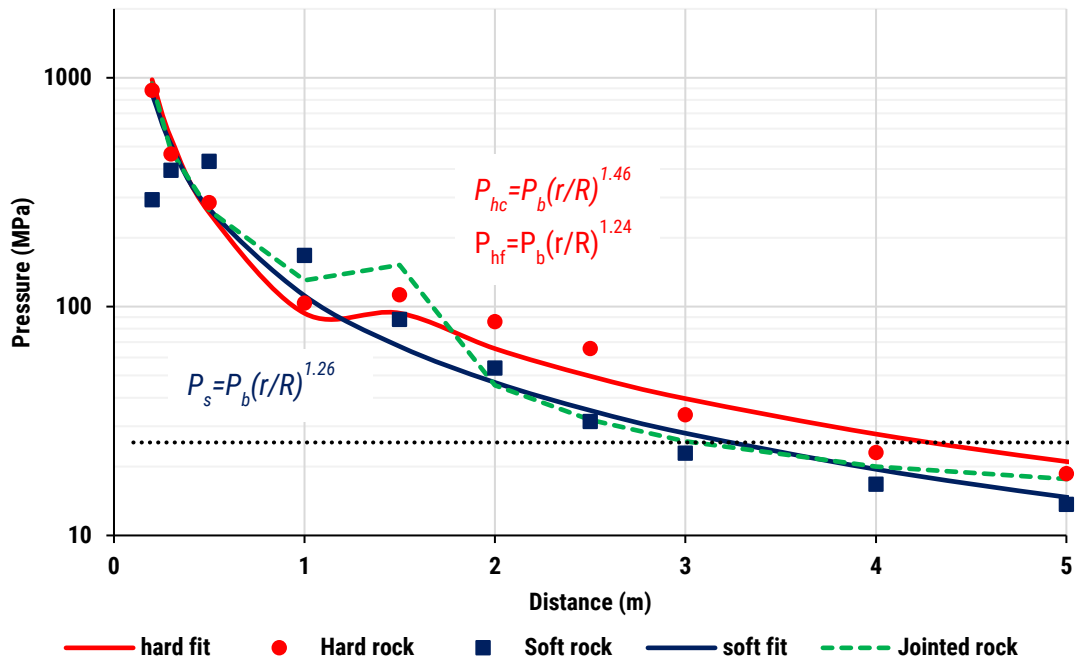


Figure 6-1: Pressure attenuation comparison for various rock masses

These equations can be used to estimate the pressure/stress experienced at any distance from the blasthole. When the stress is compared to the rock strength, the burden, and spacing distances can be determined. In the simulated cases, the cracks extend up to 5 m in hard rock along the burden with the cut-off pressure of 16 MPa and 4.5 m in soft rock at 15.3 MPa, spalling can occur along the burden beyond this point. Crack propagation along spacing occurs when the stress wave pressure (Peak P_s) is higher or equal to 25.6 MPa (black dotted line in Figure 6-1) which is 1.8 times the rock's tensile strength in hard rock and 19.7 MPa in the soft rock, which is 2.2 times the soft rock's tensile strength.

When a 5 cm clay-filled joint is introduced in a hard rock 1.5 m from the blasthole perpendicular to the free face, the results indicate a drastic increase in peak pressure before the joint and a decrease after the joint below the intact hard rock peak pressure (see Figure 6-1). In this case, the stress wave falls below 25.6 MPa earlier, and the crack extents range from 3.2 m to 4.5 along spacing as illustrated in Figure 6-2.

The formed crater depth also depends on rock mass properties as summarized in Figure 6-2. General observations indicate a decrease in crater depth with increasing in rock strength. The depth also increases on the incident side of the jointed rock mass from the energy reflection at the joint.

If we assume that the cracks in an intact rock can extend up to 3.7 m along spacing referencing Figure 6-2, there is hardly any interaction between the cracks in these adjacent holes if cracks from the opposite side of the joint can extend to 3.2 m on a 6.5 m spacing. In such cases, design modification can be necessary to achieve a better distribution of fractures between blastholes. In the presence of structures, the expression to estimate peak pressure in Figure 6-1 is modified as suggested in equation (5.5).

$$P = P_b \eta_t \left(\frac{r}{R_1 + R_2} \right)^\beta \quad (5.5)$$

R_1 and R_2 are distances before and after the structure, respectively and η_t is the structure's transmission coefficient, and β the attenuation constant. From the discussion in Chapter 5, the transmission coefficient varies with the properties of the structure mainly the width and the type of infill material.

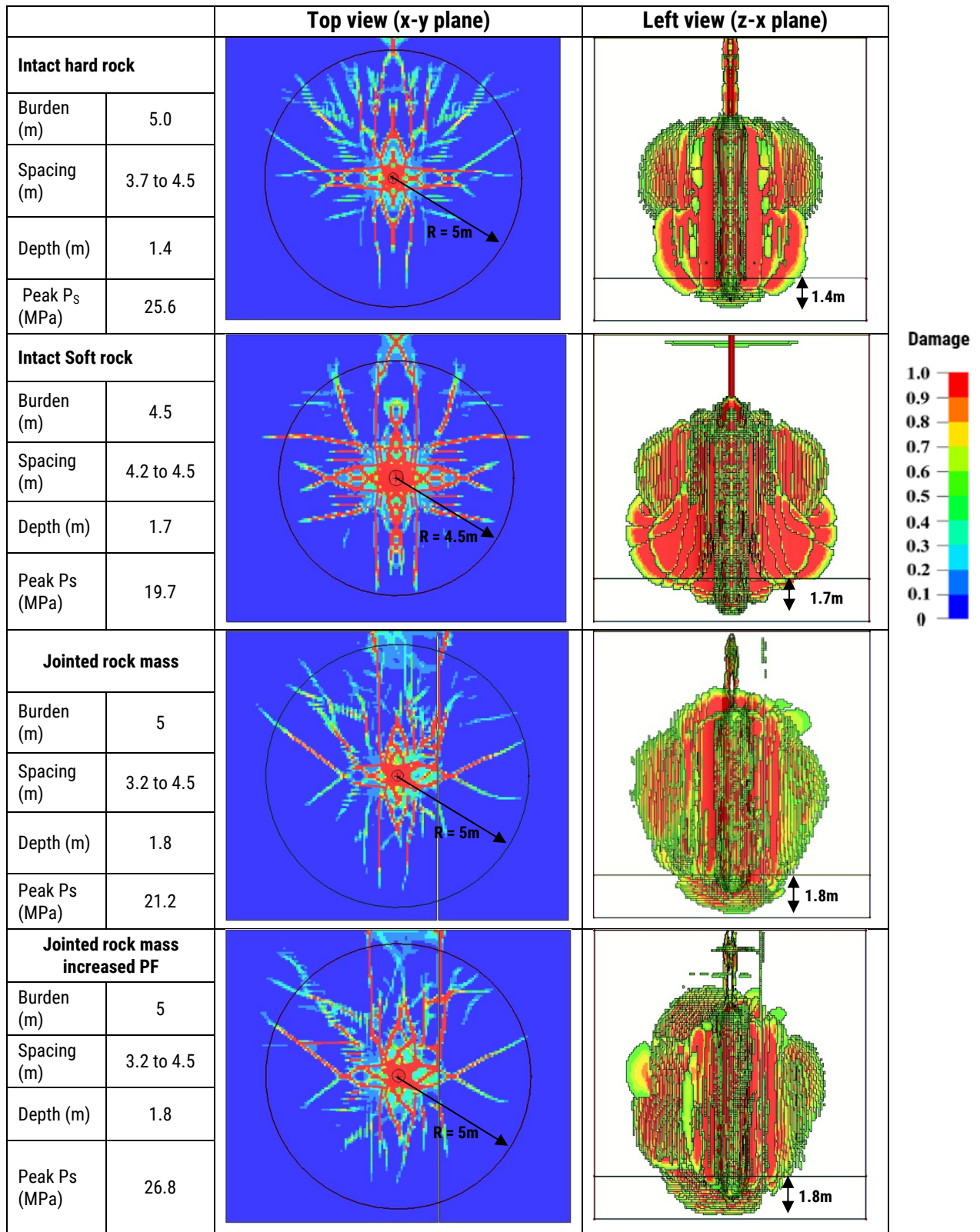


Figure 6-2: Damage distribution on various rock mass properties and the effect of powder factor increase

Some of the common design modifications to improve fracturing include changing the explosives' strength properties and varying the powder factor by changing the hole diameter or changing the dimensions of the geometric design like the burden and spacing. The change in bench height seldom occurs because that affects the pit wall and structure stability as well as the productivity of excavating equipment. When the powder factor was increased from 0.75 kg/m^3 to 1.07 kg/m^3 by changing the charge diameter from 203 mm to 240 mm on the jointed rock mass, the extent of the fractures did not significantly improve as seen in Figure 6-2. Other options, such as varying the pattern size or maximizing fracturing through the interaction between the blastholes can be explored. The latter is discussed in detail in the next section.

6.3 Initiation delays and sequencing

In mining production, surface or underground, several holes are initiated in the blast shots. The total number of blastholes, their arrangement, and the initiation pattern and delays are critical in the fragmentation, safety, and stability of the remaining rock and structures. From small-scale experiments, Katsabanis et al. (2006) determined that simultaneous initiation results in coarser fragmentation and higher disturbances on the pit wall and structures. In their study, Rossmannith (2002) and Vanbrabant and Espinosa (2006) noted that shorter delays are favourable for improving fragmentation since the tensile tail of the stress wave is enhanced by stress wave interaction between the holes. This was debated by Yi et al. (2017) from the theoretical and numerical investigation, which concluded that it is impossible to improve fragmentation from wave superposition when the stress waves interact between the blastholes because the increase in tensile stress occurs in a very small area around the collision zone.

Stagg and Rholl (1987) observed that better fragmentation is achieved when the subsequent hole is initiated after the failure process in the prior is completed. This is in line with the observations by Saadatmand Hashemi and Katsabanis (2020), who recommended the optimum delay as the time that allows cracks to grow and precondition the surrounding rock for subsequent blasthole.

These studies provide important insight into the interaction between stress waves from adjacent blastholes. The theories presented are contradictory on the use of delays and their duration, and none of them offer insight into the influence of non-uniform rock mass on the blast process and how it would impact the interaction of stress waves between blastholes, the initiation sequencing, or delays.

To evaluate the effect of initiation delays and sequencing on blast-induced fragmentation for various rock masses, three scenarios with two blastholes are modelled in a 2D axisymmetric model with a burden of 5.5 m and spacing of 6.5 m. The scenarios involve the intact rock (BIF), the contact between a soft and hard rock (BIF/Sandstone contact 1.5 m from the first blasthole), and a jointed rock mass (BIF as host rock and a 10 cm clay-filled and an empty joint 1.5 m from the first blasthole). In all cases, the emulsion is used for the explosive in 203 mm diameter blasthole. The initiation delays between the holes vary from 0 to 1.5 ms and since no further fracturing is observed beyond 2 ms of the last hole initiation, all models are run for 4.2 ms. Damage intensity for each delay is examined and compared to simultaneous initiation to investigate the effect on delay timing in blast-induced fragmentation. Switching the initiation sequencing by firing the further hole from the structure first is used to evaluate the effect of initiation sequencing on the overall damage.

6.3.1 Intact rock delays analysis

The results for the damage intensity as a function of initiation delay in the intact rock are illustrated in Figure 6-3. From the figure, it is evident that in the absence of a free face, fracturing reduces significantly. When adjacent blastholes are fired simultaneously, the damage is concentrated directly along the blastholes axis, where the stress wave is intense and is mainly compressional. A wider area of the burden (diagonal) between the blastholes remains unfractured. This is caused by destructive interference of the stress wave as illustrated by the elements velocity vectors in Figure 6-4 and the stress curve plots at the mid burden/spacing ($x, y = 3.25 \text{ m}, 2.75 \text{ m}$) in Figure 6-5. When a 0.5 ms delay is used on the second hole, the damage around the first blasthole increases, and with increased delay the interference moves closer to the second hole, causing less damage around it as seen in Figure 6-3(c).

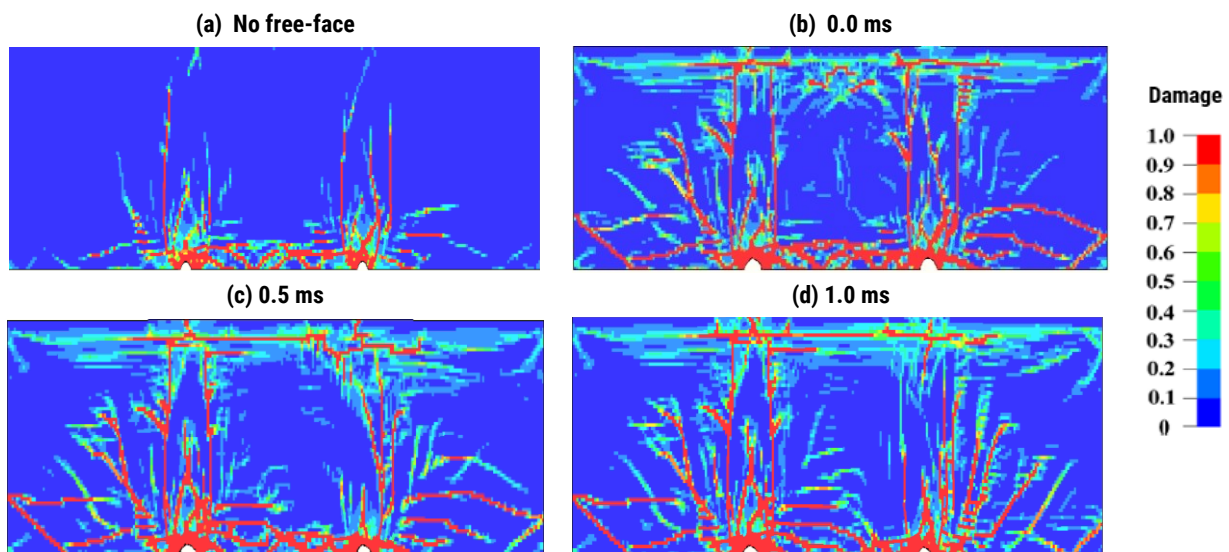


Figure 6-3: Damage intensity with delays for the intact rock

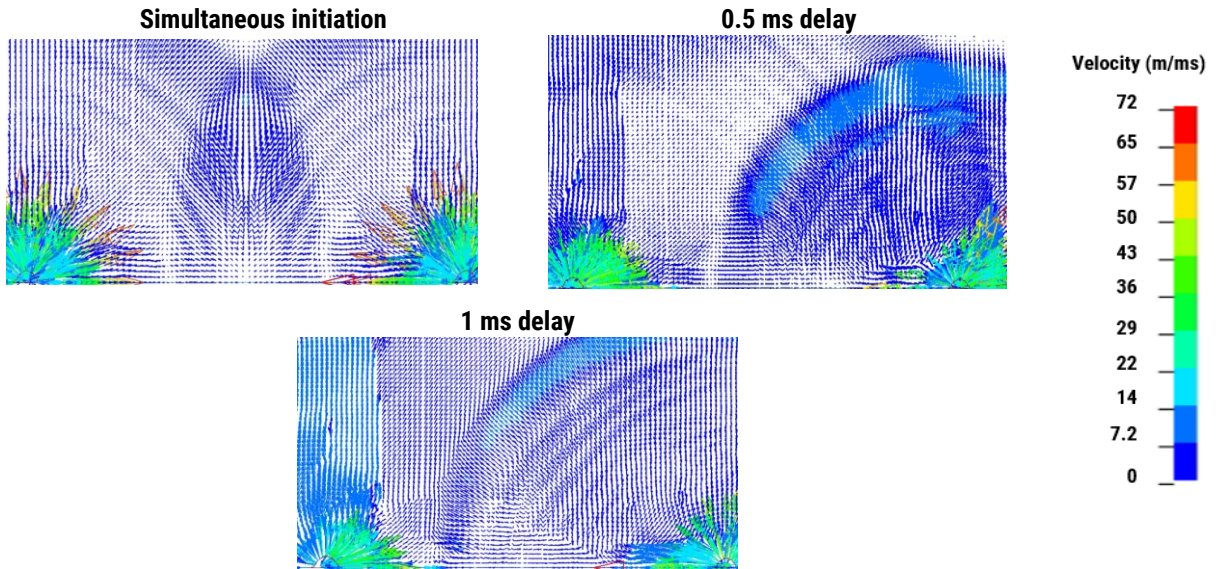


Figure 6-4: Velocity vectors between blastholes for various initiation delays

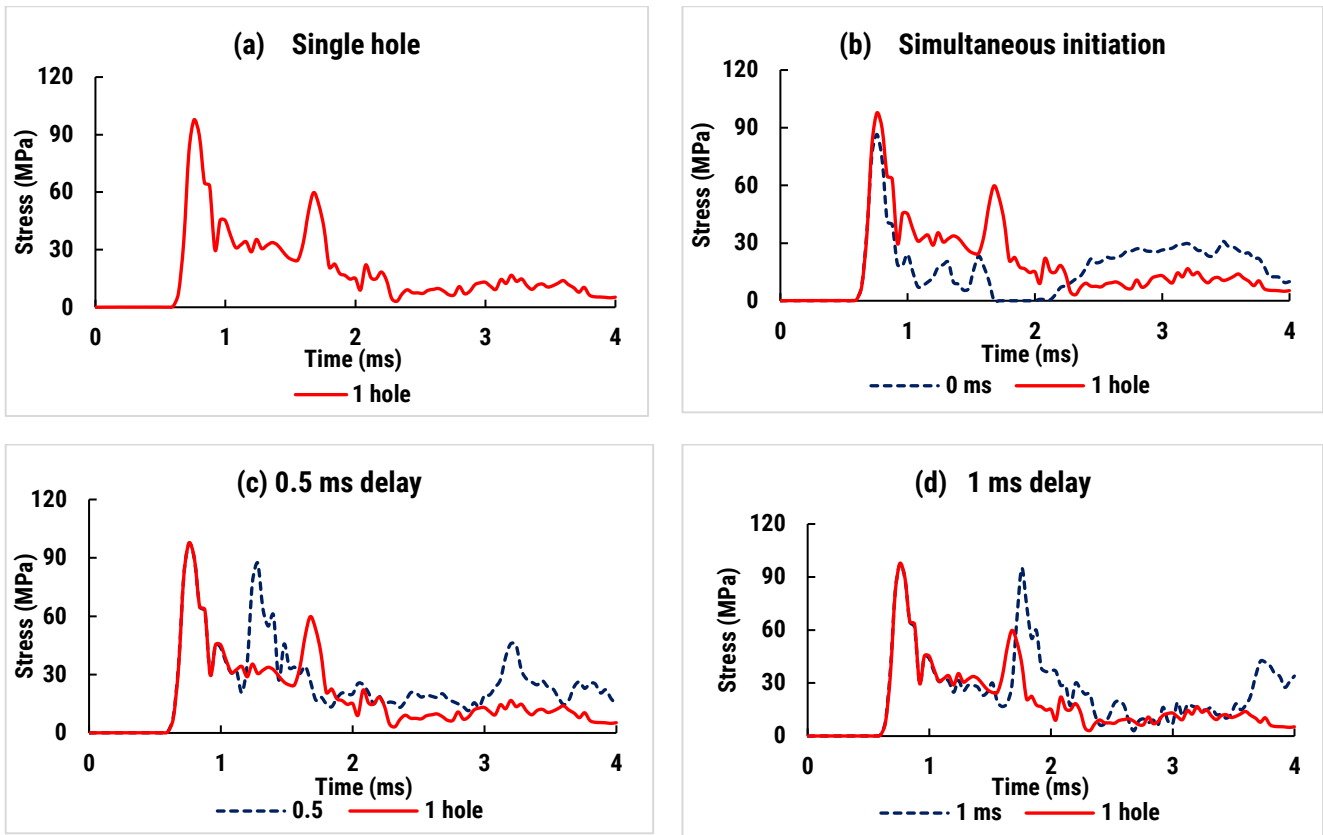


Figure 6-5: Stress curves mid-bench for various initiation delays

Further delay increase to 1 ms allows better fracturing around the first hole with minimum interference on the second since the stress wave from the first is attenuated significantly when

the second detonates. Constructive interference occurs mid-bench, as observed in Figure 6-5d causing the increase in the wave pulse, fracturing between the blastholes, and overall damage, as seen in Figure 6-3d.

Additional observations from Figure 6-5 are: when blastholes are fired simultaneously, the second peak of the stress wave diminishes to almost zero once the waves interact, shortening the wave pulse. When the delay is 0.5 ms, the second peak appears much quicker and is short-lived. At a 1 ms delay, the stress wave is in phase with one blasthole, which is equivalent to the first blasthole; the wave is therefore enhanced, and the pulse is increased/extended.

Shorter delays in addition to causing destructive interference between the blastholes, also influence stress concentration around the succeeding blasthole, as demonstrated in Figure 6-6.

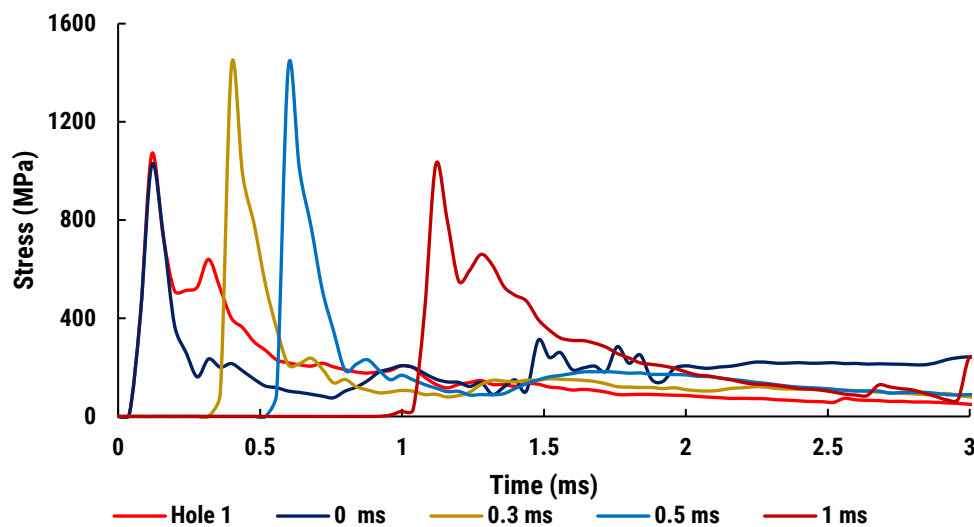


Figure 6-6: Stress curves around the blastholes for various initiation delays

When the blastholes are initiated simultaneously, the stress around the first and the second blasthole is 1,070 MPa and 1,020 MPa, respectively; there is no influence on the second hole. The stress around the first hole remains the same throughout the delays. The stress on the second

blasthole increases to 1,420 MPa when the delay is 0.3 and 0.5 ms and falls back to 1020 MPa with a similar shape as the first hole at 1 ms.

The overall observation suggests that an optimum delay is a delay that allows enough time for the fractures to form around the preceding hole and its stress wave to attenuate and cause less interference with the detonation and fracturing of the succeeding holes. If these conditions are achieved, fragmentation is improved, as illustrated in Figure 6-7a. From the stress wave monitoring between holes at various distances, the optimum delay forms a smooth peak stress curve as seen in Figure 6-7(b). For the intact rock, the optimum delay is 1 ms, causing a 10% improvement in fracturing. No improvement in fracturing is observed with a further increase in delay timing as also observed by Saadatmand Hashemi and Katsabanis (2020). Initiation sequencing does not affect intact rock fracturing unless there is a limitation on the direction of the free face.

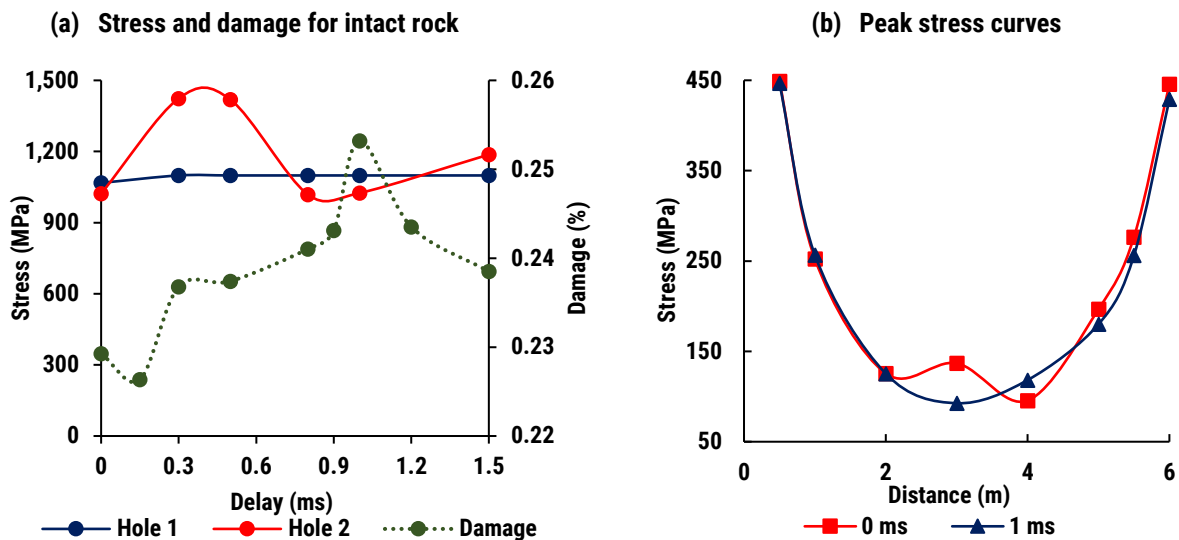


Figure 6-7: Damage extents and interference illustration for various initiation delays

6.3.2 Stress wave interaction and delays across rock contacts

The stress wave is enhanced across from soft rock to hard rock, and it attenuates in the opposite direction, as discussed in section 5.3. This section investigates the role of initiation delays and initiation sequences in enhancing fracturing through contacts of soft and hard rocks. The general analysis model is illustrated in Figure 6-8.



Figure 6-8: General model for rock contacts analysis

In the first case, the sequence is from 'hard to soft' (H-S), where the second hole (on soft rock) is fired at variable delays. With increasing delays, the damage to the soft rock declines, as illustrated in Figure 6-9. The stress wave from the first blasthole influences detonation on the second with shorter delays, as seen in 0.3 and 0.5 ms delays in Figure 6-10.

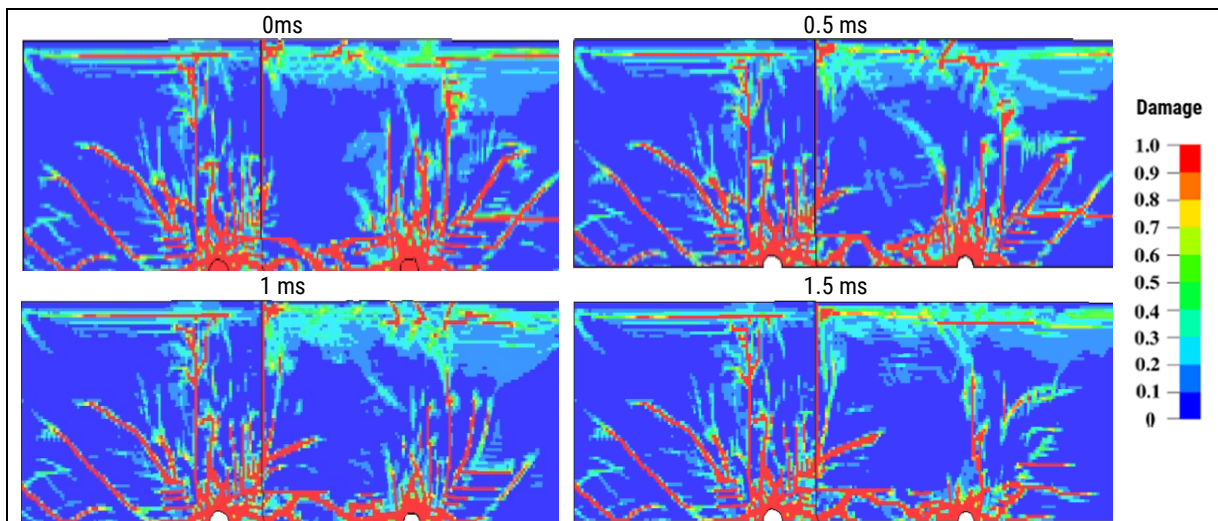


Figure 6-9: Damage distribution when firing from hard rock to soft rock at various delays

High damage formed around the first blasthole is from wave reflection at the interface. The transmitted wave through the interface increases confinement on the soft rock, which moves towards the second blasthole as the delay increases. The increased delay allows more fractures to form across the contact from the first hole, while the development of fractures around the second is significantly halted by the increased confinement, as seen in Figure 6-9.

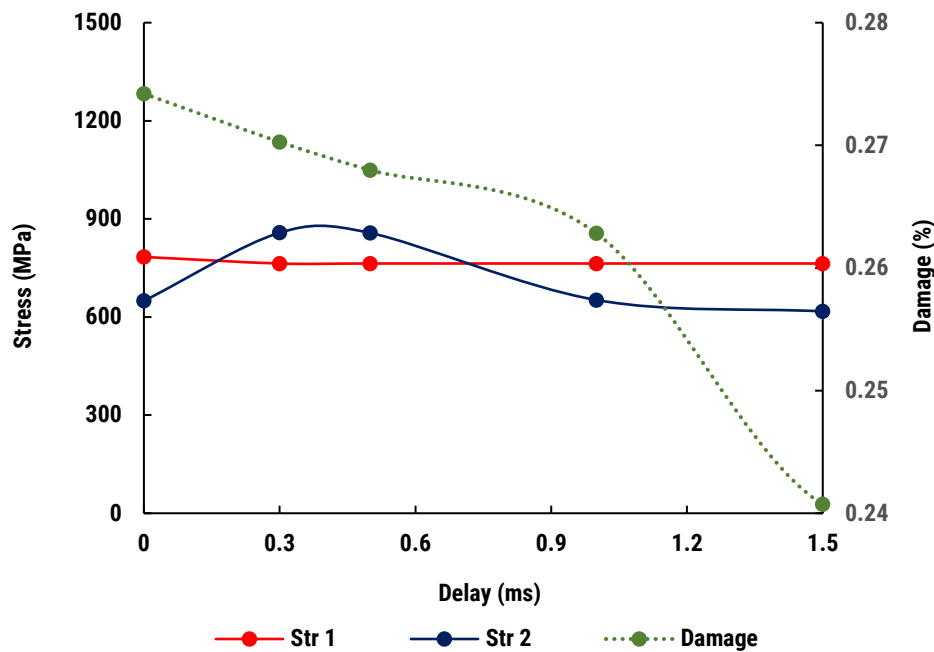


Figure 6-10: Borehole peak stresses and overall damage for hard to soft initiation sequence

In the second case, the rock types are switched, and the interface is closer to the blasthole in the soft rock, and the firing sequence is from 'soft to hard (S-H) with the blasthole on a hard rock fired at various delays. The highest damage occurs at a 0.3 ms delay with damage improvement of 5% as seen in Figure 6-11 and Figure 6-12. Extra damage is observed on the soft rock side and slightly beyond the interface. The stress wave is enhanced through the interface but does not affect fracturing on the hard rock side when the delay increases from 0 to 0.3 ms. The enhanced stress

wave at the interface causes the confinement to shift towards the hard rock with a further increase in delay, hindering fracturing around it as observed in the damage contours for 0.5 and 1 ms.

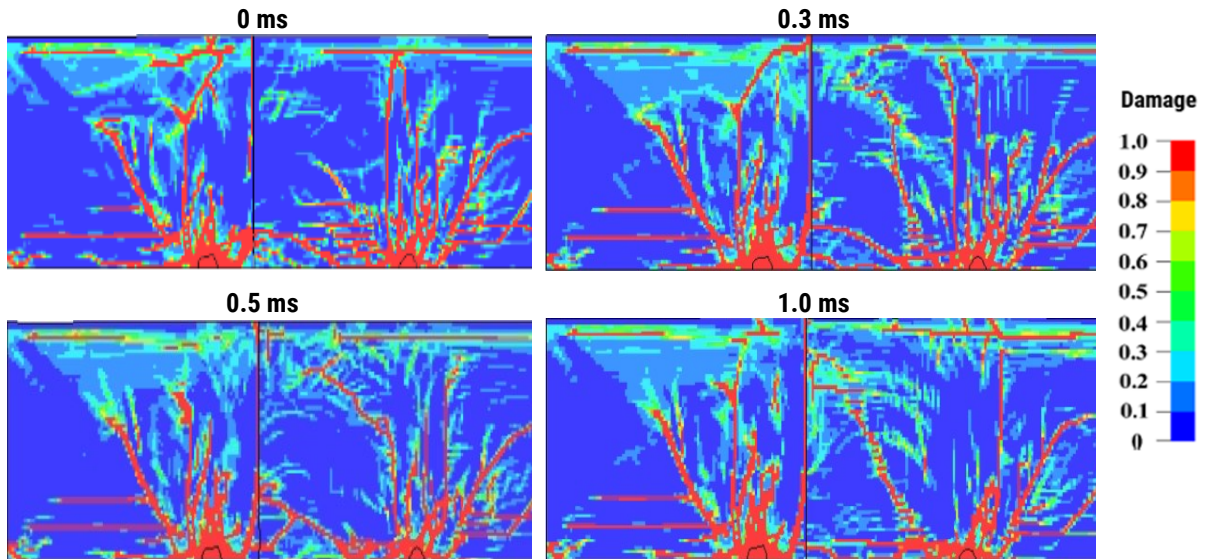


Figure 6-11: Damage distribution with the interface is close to soft rock and firing from soft to hard

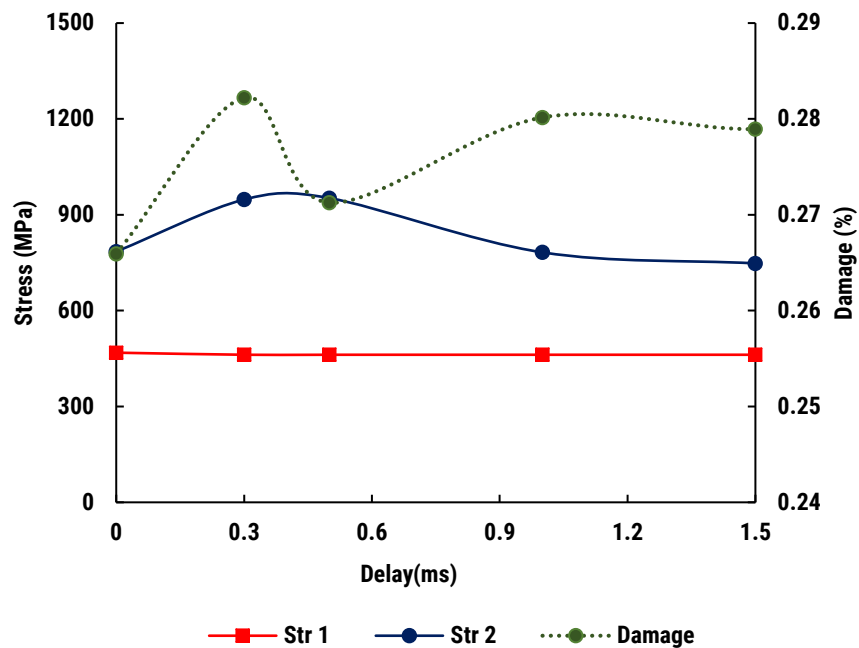


Figure 6-12: Blasthole peak stresses and damage when firing from soft to hard rock

Finally, the interface is moved 5 m from the blasthole on the soft rock (1.5 from the hard rock blasthole) and the firing sequence is from 'soft-to-hard' (S-H) firing the blasthole in hard rock at

various delays. This scenario is the same as the first case, except in this case the soft rock is fired ahead of the hard rock. The results in Figure 6-13 indicate that longer delays are favourable as they allow fractures to form around the first blasthole in the soft rock before the second detonates.

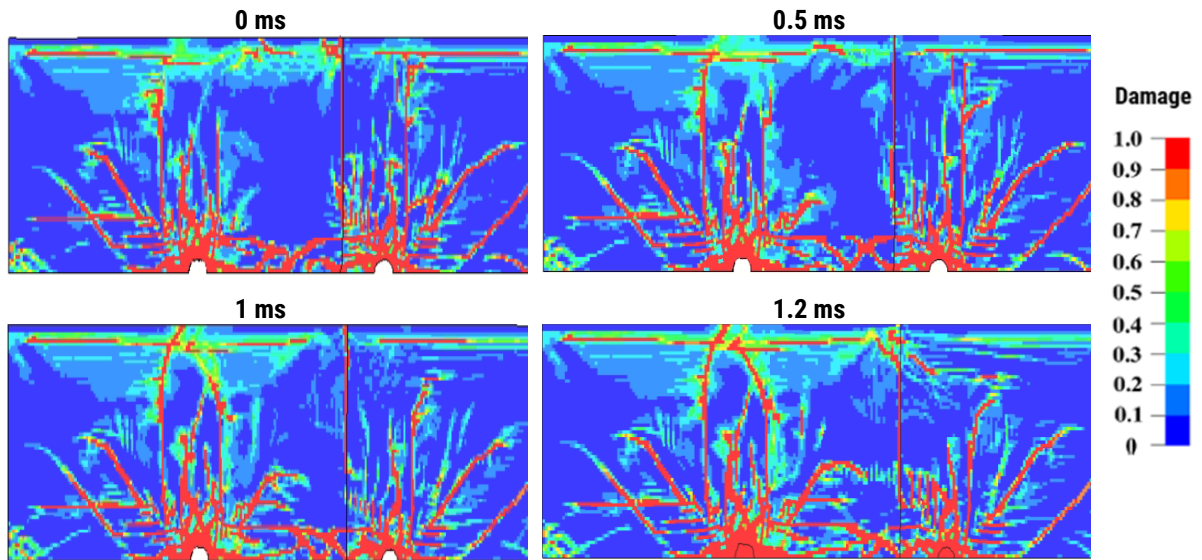


Figure 6-13: Damage distribution when firing from soft to hard rock with a longer interface

Shorter delays permit fracture development beyond the contact from the second charge. This is accompanied by higher confinement that limits fracture development around the interface on the soft rock side. The situation improves with higher delays. The optimum delay is 1.2 ms with a fracture improvement of 7%. Beyond 1.2 ms, no further improvements occur as seen in Figure 6-14.

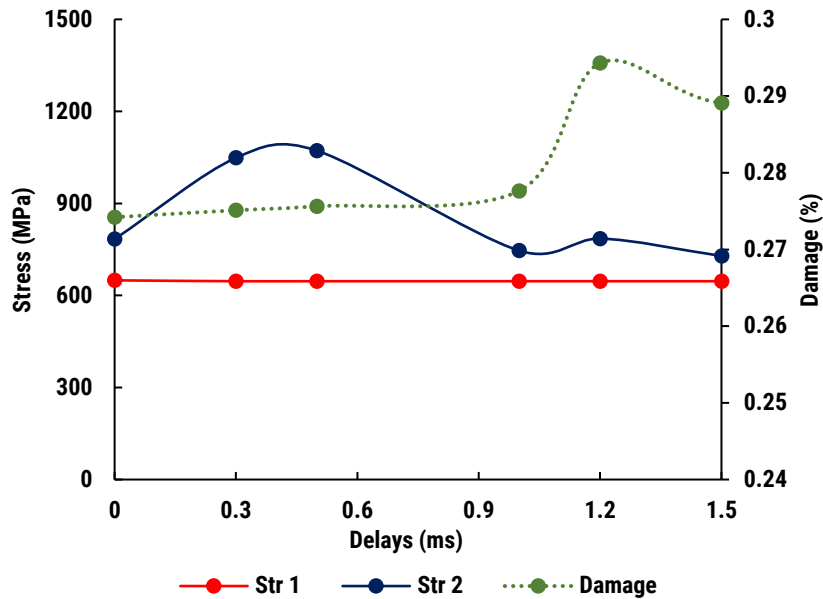


Figure 6-14: Borehole peak stresses and damage on a longer interface firing from soft to hard rock

6.3.3 Stress wave interaction across the joint

6.3.3.1 Clay infill joint

Two cases are studied by varying the firing direction relative to the joint distance from the blasthole. In the first case, the hole close to the joint is fired first and the further hole at various delays. The results indicate that when the closer blasthole is fired first, the fractures develop across the joint with minimum interference between the holes as the delay on the further hole increases. Maximum damage is achieved at a 0.9 ms delay. Further increase in delay interferes with fracture development around the second hole, as observed for 1.2 ms in Figure 6-15. The improvement in fracturing is 14%.

In the 2nd case, where the further hole is fired first, the stress wave attenuates by the time it reaches the joint. With shorter delays, stress wave interaction between the two holes hinders fracturing around the joint on the first charge side. With additional delay, for example, between 0.9 and 1.2 ms fractures from the first charge form with less interference from the second,

improving the fracturing. Beyond the 1.2 ms delay, fracturing around the second hole is halted. Maximum damage is also achieved at a 0.9 ms delay with only a 5% fracturing improvement.

The optimum delay is 0.9 ms regardless of the firing direction, with better results obtained when the charge closer to the joint is fired first, as illustrated in Figure 6-16. Fracturing a jointed rock mass requires a slightly shorter delay (0.9 ms) than the intact rock (1 ms) since the stress waves attenuate at the joint and, therefore, reduce the interference when they meet.

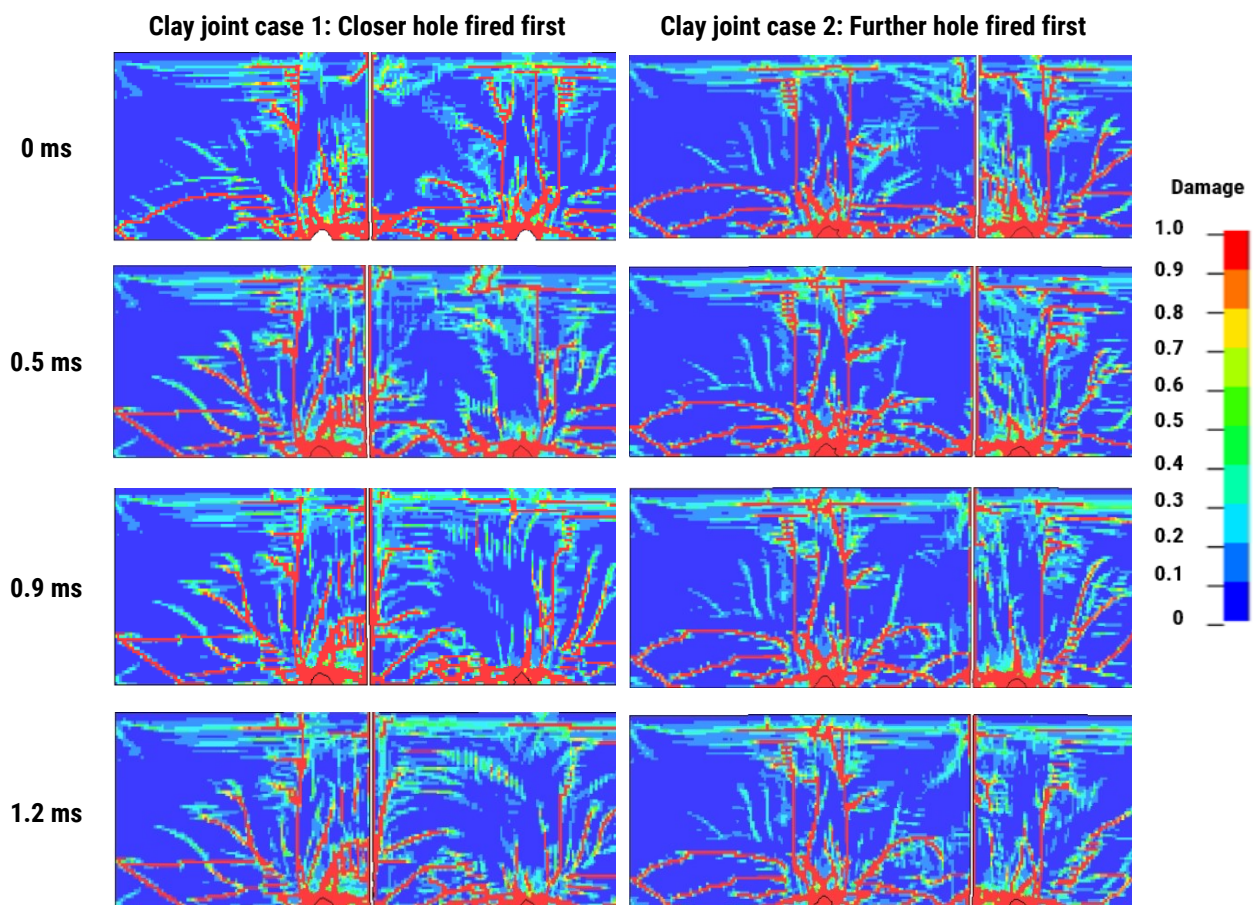


Figure 6-15: Damage extents across the joint for various delays and sequence

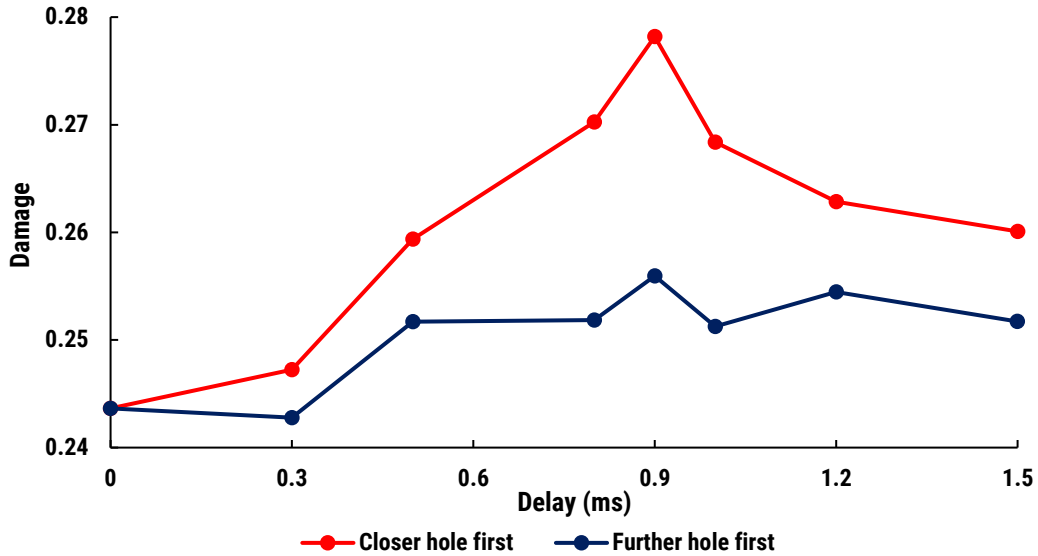


Figure 6-16: Damage extents comparison when changing firing sequence across a clay joint

6.3.3.2 Empty joint

When an empty joint is introduced between the two blastholes, regardless of the sequencing, the two blastholes act as individual charges with the least to no interaction between them. The joint acts as a free face from which most/all the energy is reflected, as observed in Figure 6-17 and Figure 6-18. In this case, maximum fracturing is attained when both charges are fired simultaneously (Figure 6-19).

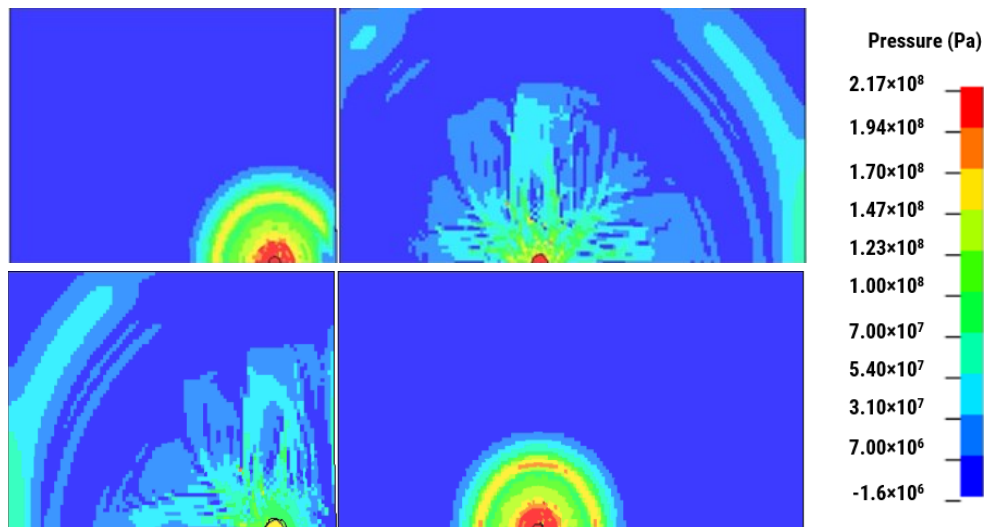


Figure 6-17: Pressure contours for 1 ms delay when changing firing sequence through an empty joint

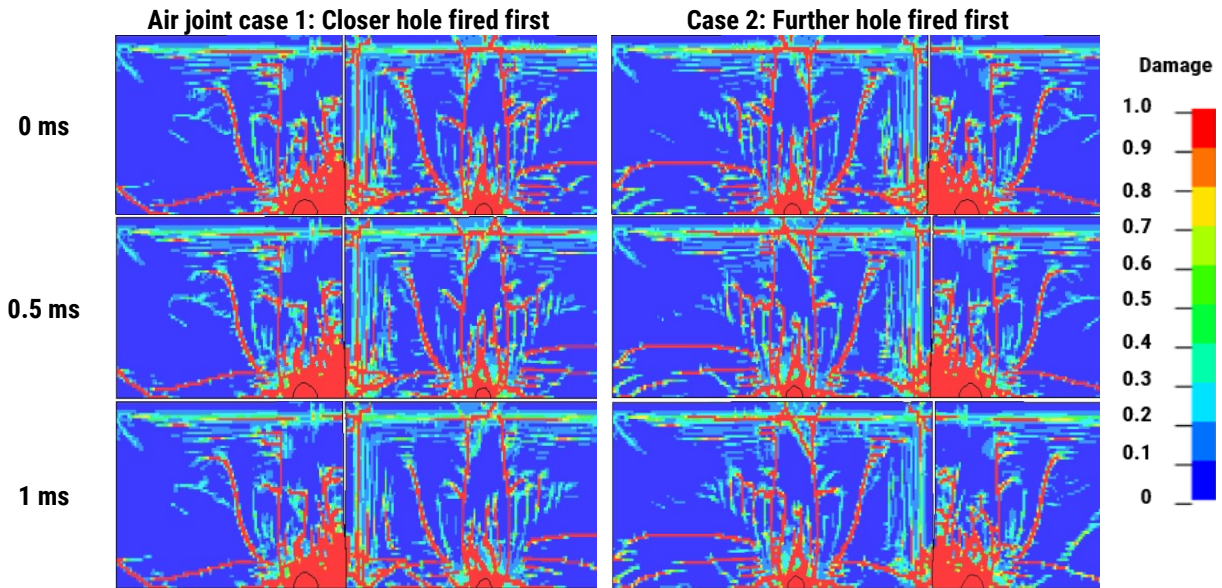


Figure 6-18: Damage extents for various delays and sequences with air joint between adjacent blastholes

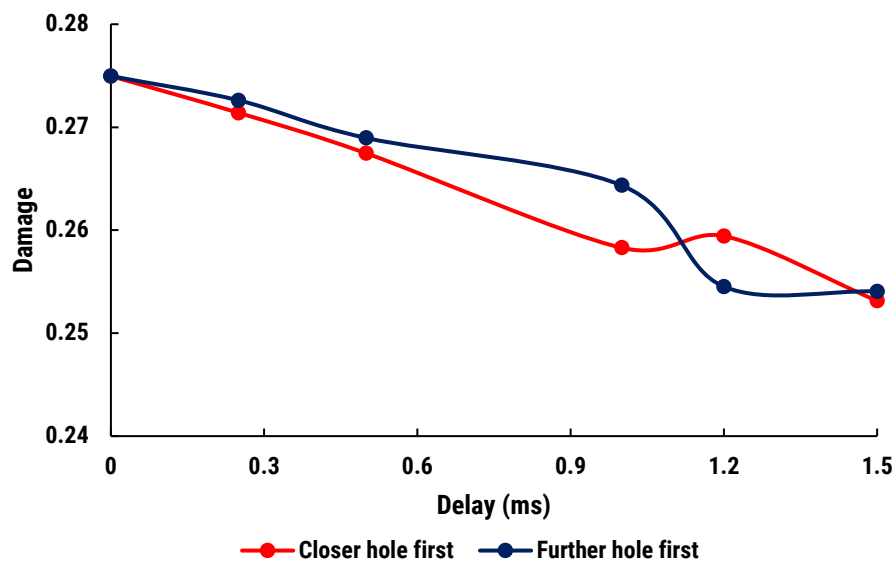


Figure 6-19: Damage across an empty joint in various firing sequences and delays

6.3.4 Initiation delays and sequencing summary

Section 6.3 covered the analysis of stress wave interaction between blastholes on various rock masses. The analysis covered the intact rock, the contact between soft and hard rock, and the hard rock with a joint between blastholes empty on one scenario and filled with clay material on the other. It has been observed that the interaction between blastholes is a significant factor in

the development and distribution of fractures from blasting. Various rock properties influence the interaction differently making the decision on initiation delay and sequencing critical to achieving good fragmentation. Figure 6-20 summarizes the analysis.

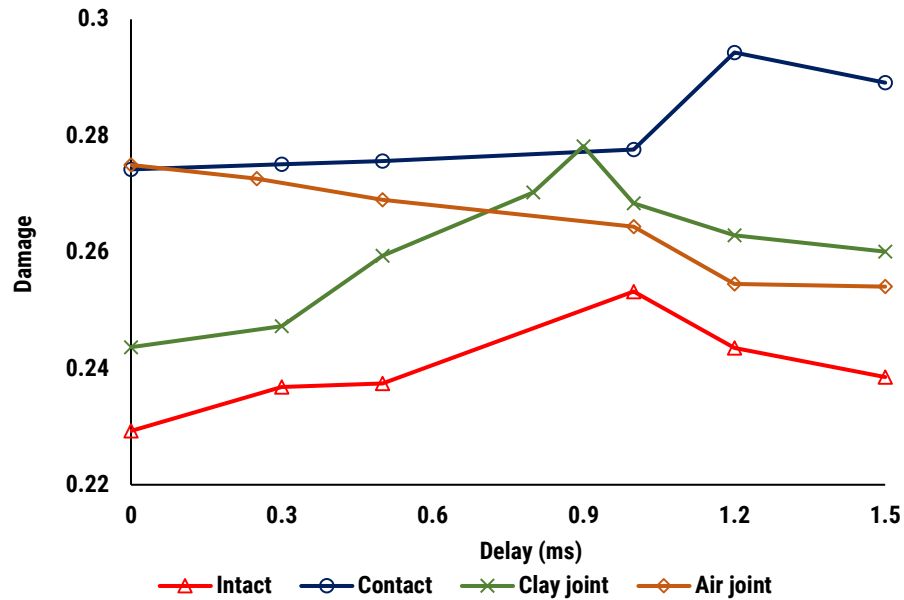


Figure 6-20: Summary of damage variations in variable rock masses for various delays and sequence

Fracturing can be increased by 10% on the intact rock by using a delay between adjacent holes' initiations: firing direction does not influence fracturing. The delay in this case should ensure fractures around the first hole are formed with minimum interference on detonation and fracturing of the succeeding hole. Shorter delays increase destructive interference between the blastholes, causing less fracturing and longer delays hinder fracture development around the succeeding blasthole.

The same concept applies to other rock properties. Firing direction from hard rock to soft rock increases confinement on the soft rock, hindering fracturing regardless of the delay. Firing soft rock first increases fracturing by 7% with the optimum delay, which in this case is 1.2 ms, slightly

higher than 1 ms for the intact hard rock. Additional delay can be explained by the fact that the wave travels slower in the soft rock than in hard rock in addition to disruption at the interface. Overall damage is higher than that of hard rock, partly due to the application of a stronger explosive on a soft (weaker) rock as discussed in Chapter 5.

When a clay-filled joint is introduced between two blastholes, good fracturing is achieved by firing the blasthole closer to the joint first. By allowing enough delay, fractures form around the first blasthole and across the joint. It also allows attenuation of the stress wave and hence lowers destructive interaction between the holes and the succeeding blasthole. The optimum delay is slightly less than the intact rock (0.9 ms) since some of the energy is reflected at the joint reducing the interference during stress wave interaction. The overall damage increases from the interaction of the stress wave with the joint's interface, as discussed in section 5.4.1.

When an empty joint is introduced, the blastholes behave as independent charges with the least to no interaction between them. The joint acts as a free face from which most or all of the energy reflects. Sequential initiation does not improve the fracturing, making simultaneous initiation though attention must be paid to the induced vibrations.

Overall improvements are observed with the use of proper delays and sequence. The simulation shows that the delays range from 0.9 to 1.2 ms, which is relatively small. In selecting appropriate delays, the total amount of explosives detonated from adjacent blastholes within an 8 ms window should be considered to control ground vibrations, following USBM guidelines.

6.4 Chapter summary and conclusion

Chapter 6 covered the blast fragmentation modelling and the overview of steps to design a blast.

The first step in blast design is deciding the powder factor required to fracture the rock to a certain

fragmentation size. One way is through energy balance, which is based on the explosive energy/strength, the rock mass strength, and energy transfer and fracturing efficiencies. When the powder factor is decided on, the geometric design can be estimated by the rule of thumb from the diameter of the blasthole and the bench height. This is a base design, and from the simulation results, it is observed that fracturing can occur within the designed boundaries of the intact rock hard rock.

The rock mass is heterogeneous and anisotropic, with various structures cross-cutting the mass. The analysis has shown that when variability is encountered, the outcomes vary; for example, using the same design on a softer rock reduces the fracture extent with higher fracture intensity. When the joint is introduced on a harder rock, the overall distribution of explosive energy changes, and most of the fractures are terminated at the joint. Design modification is inevitable in ensuring a better distribution of explosive energy and is influenced by the rate of energy attenuation in the rock mass and properties of the encountered structures.

Several design modification options can be applied to ensure better energy distribution within the designed geometry, such as increasing the powder factor by changing the hole diameter within the same pattern size, changing the pattern size for the same blasthole size, changing explosive type, and/or applying the initiation delays and sequencing between adjacent holes. The increase in powder factor did not have any significant improvement in fracturing in this case. Varying initiation sequences and delays have been observed to improve fracturing between blastholes in the intact and jointed rock mass, and through contacts of soft and hard rock.

Although sequencing does not affect fracturing in the intact rock, it is observed to improve the fragmentation through rock contacts of variable strengths and in a jointed rock mass. When

blasting through contact with soft and hard rock, fracturing improves by firing the soft rock ahead of the hard rock with delays depending on the impedance difference between the two rock types.

Fragmentation improves through a jointed rock mass by firing the blasthole closer to the joints first when infill material soft like clay. On empty or less transmitting joints, the joint acts like a free face in which delays and hole sequencing do not affect fracturing. Simultaneous initiation offers better outcomes.

Overall the optimum initiation delay is observed to be the one that allows enough time for the fractures to form around the preceding hole and its stress wave to attenuate enough to cause less interference with the detonation and fracturing of the succeeding holes.

CHAPTER 7

SUMMARY, CONCLUSIONS, AND RECOMMENDATIONS

Chapter 7 contains the summary and conclusion of this thesis. The contributions of this research are emphasized, as well as recommendations for future work.

7.1 Summary and conclusion

This research focused on assessing the distribution and usage of blast energy in hard rock open-pit mines, to understand the extent of blast-induced damage. The research involved both analytical and numerical approaches to evaluate how key factors such as explosive properties, design parameters, and rock mass properties affect stress wave propagation, energy attenuation, and crack formation.

The developed methodology for analysis involved collecting data from existing mines to define rock mass properties, estimate explosive energy, and assess fragmentation after blasting. The study included extensive data collection through laboratory tests and field measurements, along with estimating parameters that could not be directly measured. This data was then applied in a proposed analytical approach and numerical simulation to estimate damage zones around the blasthole.

The results were verified and validated through field measurements, including PPV monitoring and fragmentation analysis, as well as comparisons with estimates from other verified approaches. The comparison demonstrated that both the analytical and numerical models are feasible and effective in predicting blast-induced damage zones, but they have some limitations, as discussed in the next section.

In a blast shot with several blastholes in a complex rock mass, analyzing the influence of individual parameters and their combined effects on blast outcomes is challenging. Numerical modelling is a valuable tool for studying the blasting process, allowing for examining variable inputs in a simplified and controlled environment. This study employs numerical modelling to

investigate explosive and rock mass properties' influence on blast outcomes and explore methods for improving fracturing under different conditions.

Single-hole blast simulation provides valuable insight into the impact of explosive and rock properties on energy and crack distribution within a rock mass, particularly the explosive strength properties, rock strength, and structures, such as contacts between soft and hard rock and joints. However, since a blast shot typically involves multiple blastholes, the interaction between adjacent blastholes is crucial in rock mass fragmentation. To address this, multiple-hole blast simulation was employed to study the interactions between blastholes and to examine the roles of initiation delays and sequencing in enhancing fragmentation. The following observations were made:

- The choice of explosive is a critical aspect of blast design, highly dependent on the rock mass encountered and the desired outcomes. The size of damage zones around the blasthole depends solely on the explosive and rock strengths. Stronger explosives tend to create longer, more extended fractures in hard rock. In soft rock, using stronger explosives does not necessarily extend the fractures further; instead, it intensifies the damage within the same boundaries. Less powerful explosives reduce the extent of fractures in hard rocks but form a more uniform distribution of fractures in both soft and hard rocks.
- The analysis of structural properties reveals similar behaviour in stress wave and crack propagation at rock/structure interfaces, influenced by the impedance difference between them, the intensity of the incident wave, and its direction. When a stress wave travels from hard to soft rock, it is enhanced and attenuated when traveling in the opposite direction. Fractures propagate more easily from hard to soft rock than in the opposite direction

because the stress wave attenuates more rapidly in soft rock, potentially falling below the strength of the hard rock, depending on the interface's distance from the blasthole. This behaviour is also observed with multiple interfaces, though the extent may vary depending on the thickness of the rock layers. Regardless of whether the stress wave is enhanced or weakened, it must be stronger than the rock strength on the opposite side of the interface for fractures to propagate.

- The influence of joints on stress wave and fracture propagation varies significantly depending on the properties of the infill material, joint width, and continuity. Other factors, such as the distance from the charge, the number of joints within the blast pattern boundaries, and their orientations, further intensify these effects. Of all the joint properties evaluated, the type and size of the joint infill material, as well as the fracture frequency, have the most significant influence on fragmentation.

Analysis of empty joints and joints filled with clay revealed that a large proportion of the stress wave is reflected at empty joints. In joints filled with clay, some energy is reflected, some is absorbed in joint deformation, and some is transmitted through the joint. The proportions of energy distribution vary with the width of the joint, where more energy is used up on joint deformation in wider joints. Similar to rock contacts, the stress wave must be stronger than the rock's strength for fractures to propagate on the opposite side of the joint. This principle also applies to the reflected wave at the free face.

- Blast design is the art of balancing strength and confinement. The strength involves matching the explosive energy with the rock strength, while rock mass properties, geometric design parameters, initiation sequencing, and delays typically govern

confinement. This implies that the rock's strength properties determine the decision on the type of explosive while structural properties and the interaction between blastholes dictate the other aspects of the blast design.

- Blast design involves selecting and adjusting key controlled factors, such as explosive type, geometric layout, initiation delays, and sequencing, to account for variations in the rock mass. In intact rock, the size of the burden is primarily determined by the strength of the rock and explosive, which then influences other design parameters and initiation delay. In a structured rock mass, the firing sequence is crucial, whereas in intact rock, it has a lesser impact on fracturing unless there are restrictions on the direction of the free face.
- Variation in rock mass properties necessitates design modifications to improve blasting outcomes. While adjusting the firing sequence and delays can significantly improve fragmentation in blasting, increasing the powder factor for the same burden and spacing may not be effective in a jointed rock mass, as observed in the studied case. Overall, an effective blast design should ensure that the explosive is strong enough to induce fractures within the geometric design boundaries and that the energy is contained long enough to maximize fracturing.

7.1.1 Assumptions of the study

The study covered the analysis of several factors affecting blast outcomes. It came up with valuable conclusions but did not exhaust all influencing factors and techniques as stipulated in section 7.3. Other limitations include;

- The study relies on field measurements and laboratory tests, but certain parameters, such as in-situ rock mass properties under dynamic loading, could not be directly measured; instead, empirical models and estimates were used.
- The application of the analytical approach in variable rock masses averages the effects of rock mass properties based on measured PPV at a distance. This approach is limited in its ability to assess the specific influence of individual rock mass properties on blast outcomes.
- Numerical modelling requires a large dataset, some of which cannot be obtained from common field tests. In this study, for example, the JWL constants, some RHT model parameters, and stemming material parameters were sourced from the literature on similar materials, which may introduce uncertainties in the results. Additionally, fragmentation size could not be directly generated in LS-DYNA; therefore, the analysis relied on estimating damage zones from damage contours to assess fracturing.
- While field measurements were used to validate the results, the validation was limited to far-field vibration monitoring and fragmentation analysis. Far-field monitoring may be inadequate for accurately predicting shock wave pressure and PPV close to the blasthole.
- The results and recommendations are based on the conditions encountered in the studied mine and may not be directly applicable to other mines with different geological settings or blasting conditions without further testing and validation.

7.2 Contributions of the Research

The following is the summary of the contribution of this thesis;

- The research highlights the significant role that rock mass properties play in determining blast outcomes. It provides deeper insights into the mechanisms of blast-induced rock fragmentation, particularly in complex rock masses with varying properties. The study advances the understanding of how factors such as rock strength and structural properties influence explosive energy distribution and the extent and quality of fragmentation. This is particularly valuable for mines with complex geological settings, where blast design modifications may be necessary.
- The study offers practical recommendations for optimizing blast design, particularly in challenging rock masses. The insights gained from analyzing different blast parameters, such as initiation sequence, delay timing, and explosive selection, can help engineers design more effective and efficient blasts.
- The research contributes to the advancement of numerical modelling techniques, particularly in the use of LS-DYNA for blast simulations. It highlights the importance of parameter selection and model calibration, which can guide future studies and applications in rock blasting and related fields.
- The methodologies and findings developed in this study provide a foundation for future research in the field of rock blasting. They can be used to refine predictive models, explore new blasting techniques, or further investigate the interactions between various rock mass properties and blast parameters.

7.3 Recommendations for Future Research

The blasting process is a complex process involving several inputs and mechanisms. This research did not exhaust all the factors that influence blast fragmentation. Further analysis of

the influencing factors and techniques is recommended to increase understanding of the blasting process. Studies on the proportions of shock waves and gas pressure and how they influence fracturing in variable rock masses will be a good extension of this study. Other influencing factors such as water content and techniques such as the use of decoupling charges, explosive decking, etc. can also be investigated.

Laboratory tests are recommended to further explore the influence of explosive properties and rock mass characteristics on the extent of damage in rock blasting. The test design should start with analyzing intact rock and gradually extend to include various rock structural properties, explosive types, and geometric designs. The interaction between blastholes can be investigated by altering the firing sequence and delay times. Pressure and PPV monitoring at different distances should be conducted to capture the impact of various input parameters. The analysis should document the extent of damage mechanisms, the damage zones around the blasthole, and the overall fragmentation size distribution. A complete dataset from these tests can then be used as inputs in equation (5.5) to guide blast designs.

The numerical models used in this study are based on assumptions and simplifications, such as the uniformity of rock properties and idealized boundary conditions. The rock mass is not uniform and continuous as represented in the RHT material model. The simulation of the rock mass could be improved by incorporating algorithms that can model semi-continuous media, which would enhance the accuracy of predictions. Additionally, coupling LS-DYNA with other software could allow for the generation of fragmentation size distributions from the damage plots, enabling comparisons with those obtained from field measurements. This will also improve the reliability of the simulation results.

BIBLIOGRAPHY

1. Ahrens, T., and V. Gregson, (1964) "Shock compression of crustal rocks: Data for quartz, calcite, and plagioclase rocks." *Journal of Geophysical Research* 69:4839-4874.
2. Amoako, Richard, Ankit Jha, and Shuo Zhong, (2022) "Rock Fragmentation Prediction Using an Artificial Neural Network and Support Vector Regression Hybrid Approach." *Mining* 2 (2):233-247.
3. ASTM. (2008). *Standard D3967-08: Standard test method for splitting tensile strength of intact rock core specimens*. West Conshohocken: : ASTM International.
4. Autodyn, N.N. (2005). *Theory Manual*. Vol. Revision 4.3. Horsham, UK: Century Dynamics Limited.
5. Barreto, M. M. M. (2020). "An energy – Fragmentation approach for blasting performance." Master of Science, Department of Civil and Environmental Engineering, University of Alberta.
6. Bhandari, S. (1996). "Changes in fragmentation processes with blasting conditions." In *Fragmentation by blasting*, 301-309. Quebec, Canada: A. A. Balkema.
7. Blair, Dane, and Alan Minchinton, (1997) "On the damage zone surrounding a single blasthole." *Fragblast* 1 (1):59-72. doi: 10.1080/13855149709408390.
8. Borrvall, T, and W Riedel. (2011) "The RHT concrete model in LS-DYNA." 8th European LS-DYNA users conference, Strasbourg, Austria.
9. Brady, B.H.G., and E.T. Brown. (2006). *Rock Mechanics for underground mining*. Third ed. The Netherlands: Springer, Dordrecht.
10. Brinkmann, J. R. (1990). "An Experimental Study of the Effects of Shock and Gas Penetration in Blasting." *Fragblast* 90, Brisbane
11. Brunton, I. , D. Thornton, R. Hodson, and D. Sprott. (2003). "Impact of blast fragmentation on hydraulic excavator dig time." 5th Large Open Pit Conference, Kalgoorlie, WA.
12. Cai, M., (2010) "Practical Estimates of Tensile Strength and Hoek–Brown Strength Parameter m_i of Brittle Rocks." *Rock Mechanics and Rock Engineering* 43:167-184. doi: 10.1007/s00603-009-0053-1.
13. Calnan, J., T. (2015). "Determination of explosive energy partition values in rock blasting through small-scale testing." Doctoral Dissertation, Mining Engineering, University of Kentucky.
14. Chen, Cheng, Renshu Yang, Peng Xu, and Chenxi Ding, (2022) "Experimental study on the interaction between oblique incident blast stress wave and static crack by dynamic

- photoelasticity." *Optics and Lasers in Engineering* 148:106764. doi: <https://doi.org/10.1016/j.optlaseng.2021.106764>.
15. Chen, S. G., and J. Zhao, (1998) "A study of UDEC modelling for blast wave propagation in jointed rock masses." *International Journal of Rock Mechanics and Mining Sciences* 35 (1):93-99. doi: [https://doi.org/10.1016/S0148-9062\(97\)00322-7](https://doi.org/10.1016/S0148-9062(97)00322-7).
 16. Chiappetta, R. Frank, (1998) "Blast monitoring instrumentation and analysis techniques, with an emphasis on field applications." *Fragblast* 2 (1):79-122. doi: 10.1080/13855149809408880.
 17. Chitombo, G. P., A. Guest, Djordjevic, N., and D. M. La Rosa. (1999). "In search of an improved understanding of the fundamentals of rock breakage under controlled dynamic loading." *Fragblast* 1999, Johannesburg, SA.
 18. Cho, Sang Ho, Yuji Ogata, and Katsuhiko Kaneko, (2003) "Strain-rate dependency of the dynamic tensile strength of rock." *International Journal of Rock Mechanics and Mining Sciences* 40 (5):763-777. doi: [https://doi.org/10.1016/S1365-1609\(03\)00072-8](https://doi.org/10.1016/S1365-1609(03)00072-8).
 19. Cook, M.A. (1958). *The Science of High Explosives*. Rheinhold, New York: Krieger Pub Co.
 20. Cooper, P. W. . (1996). *Explosives Engineering*. New York: John Wiley & Sons Inc.
 21. Cottee, Stuart. (2001). "Impact of fragmentation on truck and loader productivity." BSc. in Mining Engineering B.Sc Thesis, Mining, Minerals and Material Engineering, The University of Queensland.
 22. Crosby, W. A., A. W. Bauer, and J. P. F. Warkentin. (1991) "State-of-the-art explosive VOD measurement system." *Proceedings of the Annual Conference on Explosives and Blasting Technique*.
 23. Cunningham, C. (2005) "The kuz-ram fragmentation model - 20 years on." Brighton Conference Proceedings.
 24. Dai, J. (2002). *Dynamic behaviors and blasting theory of rock*. Beijing, China: Metallurgical Industry Press.
 25. Deere, D. U., and D. W. Deere, (1988) "The Rock Quality Designation (ROD) Index in practice, Rock Classification systems for Engineering Purposes." *ASTM STP 98, 4American Society for Testing and Materials, Philadelphia*:91-101.
 26. Dehghan Banadaki, M. M., and B. Mohanty, (2012) "Numerical simulation of stress wave induced fractures in rock." *International Journal of Impact Engineering* 40-41:16-25. doi: <https://doi.org/10.1016/j.ijimpeng.2011.08.010>.
 27. Ding, Xiaohua, Yuqing Yang, Wei Zhou, Wen An, Jinyu Li, and Manda Ebelia, (2022) "The law of blast stress wave propagation and fracture development in soft and hard composite rock." *Scientific Reports* 12 (1):17120. doi: 10.1038/s41598-022-22109-z.

28. Eissa, E. A., and A. Kazi, (1988) "Relation between static and dynamic Young's moduli of rocks." *International Journal of Rock Mechanics and Mining Sciences & Geomechanics Abstracts* 25 (6):479-482. doi: [https://doi.org/10.1016/0148-9062\(88\)90987-4](https://doi.org/10.1016/0148-9062(88)90987-4).
29. Esen, S., I. Onederra, and H. A. Bilgin, (2003) "Modelling the size of the crushed zone around a blasthole." *International Journal of Rock Mechanics and Mining Sciences* 40 (4):485-495. doi: [https://doi.org/10.1016/S1365-1609\(03\)00018-2](https://doi.org/10.1016/S1365-1609(03)00018-2).
30. Evans, W. B., and D. P. Taylor, (1987) "Blended ANFObased explosives." *CIM Bulletin* 80 (905):60-64.
31. Fakhimi, Ali, and Mark Lanari, (2014) "DEM–SPH simulation of rock blasting." *Computers and Geotechnics* 55:158-164. doi: <https://doi.org/10.1016/j.compgeo.2013.08.008>.
32. Fan, L. F., L. J. Wang, and Z. J. Wu, (2018) "Wave transmission across linearly jointed complex rock masses." *International Journal of Rock Mechanics and Mining Sciences* 112:193-200. doi: <https://doi.org/10.1016/j.ijrmms.2018.09.004>.
33. Fleetwood, Kelly, Ernesto Villaescusa, and Jianping Li. (2009) "Limitations of using PPV damage models to predict rock mass damage." Thirty-Fifth Annual Conference on Explosives and Blasting Technique, Denver, CO, USA.
34. Forsyth, W.W., (1993) "A Discussion of Blast-Induced Overbreak in Underground Excavations, Rock." *Fragmentation by Blasting* Rossmannith (ed):161-166.
35. Franklin, J. A., (1985) "Suggested method for determining point load strength." *International Journal of Rock Mechanics and Mining Sciences & Geomechanics Abstracts* 22 (2):51-60. doi: [https://doi.org/10.1016/0148-9062\(85\)92327-7](https://doi.org/10.1016/0148-9062(85)92327-7).
36. Furtney, J., P. Cundall, and G. Chitombo. (2009) "Developments in numerical modeling of blast induced rock fragmentation: updates from the HSBM project." FRAGBLAST 9: 9th International Symposium on Rock Fragmentation by Blasting, Granada, Spain.
37. Gokhale, V.G. . (2011). *Rotary Drilling and Blasting in Large Surface Mines*. London (UK): CRC Press/Balkema.
38. Gong, Fengqiang, Le Zhang, and Shanyong Wang, (2019) "Loading Rate Effect of Rock Material with the Direct Tensile and Three Brazilian Disc Tests." *Advances in Civil Engineering* 2019:8. doi: 10.1155/2019/6260351.
39. Goodman, Richard E. (1976). *Methods of geological engineering in discontinuous rocks / Richard E. Goodman*. St. Paul: West Pub. Co.

40. Grady, D. E., and M. E. Kipp, (1980) "Continuum modelling of explosive fracture in oil shale." *International Journal of Rock Mechanics and Mining Sciences & Geomechanics Abstracts* 17 (3):147-157. doi: [https://doi.org/10.1016/0148-9062\(80\)91361-3](https://doi.org/10.1016/0148-9062(80)91361-3).
41. Hamdi, Essaïeb, Najla Bouden Romdhane, Jean du Mouza, and Jean Michel Le Cleac'h, (2008) "Fragmentation Energy in Rock Blasting." *Geotechnical and Geological Engineering* 26 (2):133-146. doi: 10.1007/s10706-007-9153-4.
42. Hansson, Håkan. (2009). Determination of properties for emulsion explosives using cylinder expansion tests and numerical simulation. Swebrec - Swedish Blasting Research Centre.
43. Henrych, Josef. (1979). *The Dynamics of explosion and its use*. Amsterdam: Elsevier Scientific Publishing Company.
44. Hino, Kumao. (1956) "Fragmentation Of Rock Through Blasting And Shock Wave Theory Of Blasting." The 1st U.S. Symposium on Rock Mechanics (USRMS), Golden, Colorado, 23-25 April 1956.
45. Hogan, James, Lukasz Farbaniec, Nitin Daphalapurkar, and K. T. Ramesh, (2016) "On Compressive Brittle Fragmentation." *Journal of the American Ceramic Society* 99. doi: 10.1111/jace.14171.
46. Holmquist, T. J., G. R. Johnson, and W. H. Cook. (1993) "A Computational Constitutive Model for Concrete Subjected to Large Strains, High Strain Rates and High Pressures." 14th International symposium, Vol 2; Warhead mechanisms, terminal ballistics, Arlington, Quebec; Canada.
47. Hustrulid, W. (1999). *Blasting Principles for Open Pit Mining*. 2 vols. Vol. Volume 2 - Theoretical Foundations A.A.Balkema, Rotterdam.
48. Hustrulid, W. A. (1999). *Blasting Principles for Open Pit Mining*. 2 vols. Vol. Vol. 1 General Design Concepts: CRC Press.
49. Instantel, Inc. (2015). Blastware Operator Manual In 714U0301. Canada.
50. ISEE. (2011). *ISEE blasters' handbook*. Edited by J. F. Stiehr. 18 ed. Cleveland, Ohio: International Society of Explosives Engineers.
51. Ismail, Mostafa A., and Jozsef S. Gozon, (1987) "Effects of discontinuities on fragmentation by blasting." *International Journal of Surface Mining, Reclamation and Environment* 1 (1):21-25. doi: <https://doi.org/10.1080/09208118708944098>.
52. ISRM. (2007). *Suggested Method for Determining the Uniaxial Compressive Strength and Deformability of Rock Materials*. Edited by R. Ulusay and J. Hudson, *The complete ISRM suggested methods for rock characterization, testing and monitoring*. Ankara: Commission on Testing Methods: International Society of Rock Mechanics.

53. Jayasinghe, L. B., Junlong Shang, Zhiye Zhao, and A. T. C. Goh, (2019) "Numerical investigation into the blasting-induced damage characteristics of rocks considering the role of in-situ stresses and discontinuity persistence." *Computers and Geotechnics* 116:103207. doi: <https://doi.org/10.1016/j.compgeo.2019.103207>.
54. Jeong, Hoyoung, and Seokwon Jeon, (2018) "Characteristic of size distribution rock chip produced by rock cutting with a pick cutter." *Geomechanics and Engineering* 15. doi: 10.12989/gae.2018.15.3.811.
55. Jiang, Xudong, Yiguo Xue, Fanmeng Kong, Huimin Gong, Yusong Fu, and Weimeng Zhang, (2023) "Dynamic responses and damage mechanism of rock with discontinuity subjected to confining stresses and blasting loads." *International Journal of Impact Engineering* 172:104404. doi: <https://doi.org/10.1016/j.ijimpeng.2022.104404>.
56. Kanchibotla, Walter Valery, and S. Morrell. (1999) "Modeling fines in blast fragmentation and its impact on crushing and grinding." *Explo'99: A Conference on Rock Breaking*, Kalgoorlie.
57. Katsabanis, P. D., A. Tawadrous, C. Braun, and C. Kennedy, (2006) "Timing effects on the fragmentation of small scale blocks of granodiorite." *Fragblast* 10 (1-2):83-93. doi: 10.1080/13855140600858339.
58. Kimberley, J., K. T. Ramesh, and N. P. Daphalapurkar, (2013) "A scaling law for the dynamic strength of brittle solids." *Acta Materialia* 61 (9):3509-3521. doi: <https://doi.org/10.1016/j.actamat.2013.02.045>.
59. Konya, C. J., and E. J. Walter. (1991). *Rock blasting and overbreak control*. Montville, OH: National Highway Institute
60. Kuznetsov, V. M., (1973) "The mean diameter of the fragments formed by blasting rock." *Soviet Mining* 9 (2):144-148. doi: 10.1007/BF02506177.
61. Lang, L.C., and R.F. Favreau, (1972) "A Modern Approach to Open Pit Blast Design and Analysis." *Can. Inst. Min. Metal Bulletin* 65 (722):37-45.
62. Latham, John-Paul, Jan Van Meulen, and Sebastien Dupray, (2006) "Prediction of in-situ block size distributions with reference to armourstone for breakwaters." *Engineering Geology* 86 (1):18-36. doi: <https://doi.org/10.1016/j.enggeo.2006.04.001>.
63. Lee, E. L., H. C. Hornig, and J. W. Kury. (1968). *Adiabatic Expansion Of High Explosive Detonation Products*. United States.
64. Lee, J., F. W. Sandstrom, B. G. Craig, and P. A. Persson. (1989). "Detonation and shock initiation properties of emulsion explosives." *Ninth International Symposium on Detonation*, Portland, Oregon, USA.

65. Liu, Kai, Qianbing Zhang, and Jian Zhao. (2018) "Dynamic increase factors of rock strength." Proceedings of the 3rd International Conference on Rock Dynamics and Applications, Trondheim, Norway.
66. Liu, Q., and P.D. Katsabanis. (1993). "A Theoretical Approach to the Stress Waves Around a Borehole and Their Effect on Rock Crushing." Proceedings of the Fourth International Symposium on Rock Fragmentation by Blasting-Fragblast-4, Vienna, Austria.
67. Liu, Q., and J.P. Tidman. (1995). Estimation of the Dynamic Pressure Around a Fully Loaded Blasthole. In *report 95-014*. Valda'r Quebec: CANMET/MRL Experimental Mine.
68. Livermore Software Technology Corporation, LSTC. (2018). LS-DYNA Keyword User's Manual R11 Volume II Material Models. 2. Accessed June 15, 2023.
69. Lizotte, Y., and M. Scoble, (1994) "Geological control over blast fragmentation." *CIM Bulletin* 87 (983):57-71.
70. Lopez, J. E., J. C. Lopez, and A. F. Carcedo. (1995). "Initiation sequence and delay timing." In *Drilling and Blasting of Rocks*
71. 281-289. Taylor and Francis.
72. Ma, G. W., and X. M. An, (2008) "Numerical simulation of blasting-induced rock fractures." *International Journal of Rock Mechanics and Mining Sciences* 45 (6):966-975. doi: <https://doi.org/10.1016/j.ijrmms.2007.12.002>.
73. McKee, D.J. (2013). *Understanding mine to mill* Brisbane.
74. Michaux, S., and N. Djordjevic, (2005) "Influence of explosive energy on the strength of the rock fragments and SAG mill throughput." *Minerals Engineering* 18 (4):439-448. doi: <https://doi.org/10.1016/j.mineng.2004.07.003>.
75. Mohanty, B. (1987) "Strength of rock under high strain rate loading conditions applicable to blasting." *Fragblast'87*, Keystone, Colorado.
76. Mojtabai, N., and S. G. Beattie, (1996) "Empirical approach to prediction of damage in bench blasting." *Trans. Inst. Min. and Metall Sect.* 105:75-80.
77. MREL. (2022). *MicroTrap Operations Manual*. Vol. Edition 4.4. Kingston, Ontario.
78. Myer, L R, L J Pyrak-Nolte, and N G.W. Cook. (1990). "Effects of single fractures on seismic wave propagation." Conference: International conference on rock joints, Loen, Norway, 4-6 Jun 1990.
79. Napier-Munn, T. J. (1996). *Mineral comminution circuits : their operation and optimisation*. Indooroopilly, At: Julius Kruttschnitt Mineral Research Centre, The University Of Queensland ;.
80. Nguyen, Thanh Chi, Anh Ngoc Do, Vi Van Pham, and Gospodarikov Alexandr, (2022) "Multiple linear regression analysis model and artificial neural network model to calculate and estimate the blast

- induced area of the tunnel face. A case study Deo Ca tunnel." *Journal of Mining and Earth Sciences* 63 (3):43-52. doi: 10.46326/jmes.2022.63(3).06.
81. Nicholls, H.R., C.F. Johnson, and W.I. Duvall. (1971). *Blasting vibrations and their effects on structures, Bulletin no. 656*. Washington, DC: US Bureau of Mines.
82. Nielsen, K., and T. Malvik, (1999) "Grindability enhancement by blast-induced microcracks." *Powder Technology* 105 (1):52-56. doi: [https://doi.org/10.1016/S0032-5910\(99\)00117-5](https://doi.org/10.1016/S0032-5910(99)00117-5).
83. Ohadi, B. (2018). " Investigation of the influence of heterogeneous and anisotropic nature of rock mass on blast-induced outcomes-a case study at Detour Lake min." Master thesis, University of Toronto.
84. Onederra, Italo A., Jason K. Furtney, Ewan Sellers, and Stephen Iverson, (2013) "Modelling blast induced damage from a fully coupled explosive charge." *International Journal of Rock Mechanics and Mining Sciences* 58:73-84. doi: <https://doi.org/10.1016/j.ijrmms.2012.10.004>.
85. Onederra, Italo, and Sedat Esen, (2004) "An Alternative Approach to Determine the Holmberg–Persson Constants for Modelling Near Field Peak Particle Velocity Attenuation Å." *Fragblast* 8:61-84. doi: 10.1080/13855140412331336151.
86. ORICA, (2018) "Technical data sheet - Fortis Extra System - Africa."
87. Ouchterlony, Finn, (2005) "The Swebrec© function: linking fragmentation by blasting and crushing." *Mining Technology* 114 (1):29-44. doi: 10.1179/037178405X44539.
88. Ouchterlony, Finn, Ulf Nyberg, Mats Olsson, Ingvar Bergquist, Lars Granlund, and Henrik Grind. (2003) "The energy balance of production blasts at Nordkalk's Klinthagen quarry." EFEE World Conference on Explosives and Blasting Technique : 10/09/2003 - 12/09/2003, Rotterdam.
89. Persson, P., (1997) "The relationship between strain energy, rock damage, fragmentation, and throw in rock blasting." *Fragblast* 1 (1):99-110. doi: 10.1080/13855149709408392.
90. Persson, P. A., R. Holmberg, and J. Lee. (1994). *Rock blasting and explosives engineering*: CRC Press.
91. Prasad, Umesh. (2000). "Dynamic Fracture Characteristics of Selected Rocks." PhD dissertation, Department of Mining and Materials Engineering, McGill University.
92. Ramesh, K. T., James D. Hogan, Jamie Kimberley, and Angela Stickle, (2015) "A review of mechanisms and models for dynamic failure, strength, and fragmentation." *Planetary and Space Science* 107:10-23. doi: <https://doi.org/10.1016/j.pss.2014.11.010>.
93. Riedel, W., K. Thoma, S. Hiermaier, and E. Schmolinske. (1999) "Penetration of Reinforced Concrete by BETA-B-500 Numerical Analysis using a New Macroscopic Concrete Model for

- Hydrocodes." 9th international symposium on interaction of the effects of munitions with structures, Berlin, Germany.
94. Rosenberg, Zvi, (1993) "On the relation between the Hugoniot elastic limit and the yield strength of brittle materials." *Journal of Applied Physics* 74:752-753. doi: <https://doi.org/10.1063/1.355247>.
 95. Rossmannith, H. P., (2002) "The Use of Lagrange Diagrams in Precise Initiation Blasting. Part I: Two Interacting Blastholes." *Fragblast* 6 (1):104-136. doi: 10.1076/frag.6.1.104.8854.
 96. Rustan, Agne. (2013). "The dynamics and fragmentation of blasted ore slices in scaled sublevel caving and slab models followed by accuracy analysis of the "Volume weight method" used for determination of ore content at loading." 10th International Symposium on Rock Fragmentation by Blasting, FRAGBLAST 10, 24 November 2012 through 25 November 2012, New Delhi, 2013.
 97. Saadatmand Hashemi, A., and P. Katsabanis, (2020) "The Effect of Stress Wave Interaction and Delay Timing on Blast-Induced Rock Damage and Fragmentation." *Rock Mechanics and Rock Engineering* 53 (5):2327-2346. doi: 10.1007/s00603-019-02043-9.
 98. Şahin, Merve, Resat Ulusay, and Hasan Karakul, (2020) "Point Load Strength Index of Half-Cut Core Specimens and Correlation with Uniaxial Compressive Strength." *Rock Mechanics and Rock Engineering* 53 (8):3745-3760. doi: 10.1007/s00603-020-02137-9.
 99. Sanchidrián, José A., Ricardo Castedo, Lina M. López, Pablo Segarra, and Anastasio P. Santos, (2015) "Determination of the JWL Constants for ANFO and Emulsion Explosives from Cylinder Test Data." *Central European Journal of Energetic Materials* 12:177-194.
 100. Sanchidrián, José A., Pablo Segarra, and Lina M. López, (2007) "Energy components in rock blasting." *International Journal of Rock Mechanics and Mining Sciences* 44 (1):130-147. doi: <https://doi.org/10.1016/j.ijrmms.2006.05.002>.
 101. Scott, A., Seshadri Kanchibotla, and S. Morrell, (1999) "Blasting for mine to mill optimisation." *Explo '99: a Conference On Rock Breaking, Proceedings* 99 (5).
 102. Sheorey, P. R. (1997). *Empirical rock failure criteria*. Rotterdam: A.A. Balkema Rotterdam.
 103. Spathis, AT, (2015) "Report on the 11th international symposium on rock fragmentation by blasting." *Blasting and Fragmentation* 9:73-82.
 104. Stagg, M. S., and S. A. Rholl, (1987) "Effects of accurate delays on fragmentation for single-row blasting in a 6.7 m (22 ft) bench." *Proceedings of the Second International Symposium on Rock Fragmentation by Blasting*:210-223.
 105. Sun, Changshou. (2013). "Damage zone prediction for rock blasting." Ph.D. Thesis, Mining Engineering, University of Utah.

106. Tomi, G., J. Seccatore, M Dempieri, and A. Rezende. (2011) "Blasting Fragmentation Management using Complexity Analysis." 6th Brazilian Congress on Open-Pit Mining, Brazil.
107. Tosun, Abdurrahman, G. Konak, Dogan Karakus, Ahmet Onur, and Tugce Ongen. (2012). *Investigation of the relationship between blasting pile density and loader productivity.*
108. Udy, L., and C. M. Lownds. (1990). "The Partition of Energy in Blasting with Non-Ideal Explosives." FRAGBLAST.
109. Vanbrabant, Frederic, and A. Espinosa, (2006) "Impact of short delays sequence on fragmentation by means of electronic detonators: Theoretical concepts and field validation." *Proc. 8th Int. Symp. on Rock Fragmentation by Blasting- Fragblast* 8:326-331.
110. Vutukuri, V. S. Lama R. D. Saluja S. S. (1978). *Handbook on mechanical properties of rocks : testing techniques and results. 2 2.* Clausthal: Trans Tech Publ.
111. Wang, H., Latham J. P., and Poole A. B. (1990) "In-situ block size assessment from discontinuity spacing data." Proceedings of the 6th Congress of the IAEG, Amsterdam, August 6-10.
112. Wang, Jianxiu, Yao Yin, and Kamran Esmaili, (2018) "Numerical simulations of rock blasting damage based on laboratory-scale experiments." *Journal of Geophysics and Engineering* 15 (6):2399-2417. doi: 10.1088/1742-2140/aac17.
113. Wang, Shu-you, Jian-wei Jiang, Yu-xiang Nan, and Jian-bing Men, (2013) "Numerical study on the shock responses of submunition drop on various mediums." *JOURNAL OF BEIJING INSTITUTE OF TECHNOLOGY* 22 (4):427-431.
114. Wang, Zhiliang, Youpeng Huang, and Feng Xiong, (2019) "Three-Dimensional Numerical Analysis of Blast-Induced Damage Characteristics of the Intact and Jointed Rockmass." *Computers, Materials & Continua* 60 (3):1189 -1206.
115. Wang, Zhiliang, Haochen Wang, Jianguo Wang, and Nuocheng Tian, (2021) "Finite element analyses of constitutive models performance in the simulation of blast-induced rock cracks." *Computers and Geotechnics* 135:104172. doi: <https://doi.org/10.1016/j.compgeo.2021.104172>.
116. Wei, Wenpeng, Xiaofeng Huo, Xianyang Qiu, Zhi Yu, Junnian Nong, and Qinghua Li, (2024) "Three-dimensional Finite Element Simulation and Reconstruction of Jointed Rock Masses for Bench Blasting." *Simulation Modelling Practice and Theory*:102975. doi: <https://doi.org/10.1016/j.simpat.2024.102975>.
117. Whittaker, B.N., R.N. Singh, and G. Sun. (1992). *Rock Fracture Mechanics: Principles, Design, and Applications*: Elsevier Publishing Company.
118. WipWare. (2021). *Sampling and Analysis Guide*.

119. Xie, L. X., W. B. Lu, Q. B. Zhang, Q. H. Jiang, M. Chen, and J. Zhao, (2017) "Analysis of damage mechanisms and optimization of cut blasting design under high in-situ stresses." *Tunnelling and Underground Space Technology* 66:19-33. doi: <https://doi.org/10.1016/j.tust.2017.03.009>.
120. Yang, R. L., P. Rocque, P. Katsabanis, and W. F. Bawden, (1994) "Measurement and analysis of near-field blast vibration and damage." *Geotechnical & Geological Engineering* 12 (3):169-182. doi: 10.1007/BF00426985.
121. Yang, Renshu, Chenxi Ding, Liyun Yang, and Cheng Chen, (2018) "Model experiment on dynamic behavior of jointed rock mass under blasting at high-stress conditions." *Tunnelling and Underground Space Technology* 74:145-152. doi: <https://doi.org/10.1016/j.tust.2018.01.017>.
122. Yi, Changping, Jonny Sjöberg, and Daniel Johansson, (2017) "Numerical modelling for blast-induced fragmentation in sublevel caving mines." *Tunnelling and Underground Space Technology* 68:167-173. doi: <https://doi.org/10.1016/j.tust.2017.05.030>.
123. Yi, Changping, Jonny Sjöberg, Daniel Johansson, and Nikolaos Petropoulos, (2017) "A numerical study of the impact of short delays on rock fragmentation." *International Journal of Rock Mechanics and Mining Sciences* 100:250-254. doi: <https://doi.org/10.1016/j.ijrmms.2017.10.026>.
124. Yin, Jian-Hua, Robina H. C. Wong, K. T. Chau, David T. W. Lai, and Guang-Si Zhao, (2017) "Point load strength index of granitic irregular lumps: Size correction and correlation with uniaxial compressive strength." *Tunnelling and Underground Space Technology* 70:388-399. doi: <https://doi.org/10.1016/j.tust.2017.09.011>.
125. Yoon, J, and S Jeon. (2010) "Use of a modified particle-based method in simulating blast-induced rock fracture." Proceedings of the 9th International Symposium on Rock Fragmentation by Blasting, Fragblast.
126. Zhang, Q. B., and J. Zhao, (2014) "A Review of Dynamic Experimental Techniques and Mechanical Behaviour of Rock Materials." *Rock Mechanics and Rock Engineering* 47 (4):1411-1478. doi: 10.1007/s00603-013-0463-y.
127. Zhang, Z. X. (2016). *Rock Fracture and Blasting: Theory and Applications* Amsterdam: Elsevier.
128. Zhang, Z. X., S. Q. Kou, L. G. Jiang, and P. A. Lindqvist, (2000) "Effects of loading rate on rock fracture: fracture characteristics and energy partitioning." *International Journal of Rock Mechanics and Mining Sciences* 37 (5):745-762. doi: [https://doi.org/10.1016/S1365-1609\(00\)00008-3](https://doi.org/10.1016/S1365-1609(00)00008-3).

-
129. Zhao, J., X. B. Zhao, and J. G. Cai, (2006) "A further study of P-wave attenuation across parallel fractures with linear deformational behaviour." *International Journal of Rock Mechanics and Mining Sciences* 43 (5):776-788. doi: <https://doi.org/10.1016/j.ijrmms.2005.12.007>.
130. Zhu, Zhe Ming, (2011) "The Responses of Jointed Rock Mass under Dynamic Loads." *Advanced Materials Research* 230-232:251-255. doi: 10.4028/www.scientific.net/AMR.230-232.251.
131. Zhu, Zheming, Bibhu Mohanty, and Heping Xie, (2007) "Numerical investigation of blasting-induced crack initiation and propagation in rocks." *International Journal of Rock Mechanics and Mining Sciences* 44 (3):412-424. doi: <https://doi.org/10.1016/j.ijrmms.2006.09.002>.

APPENDIX A

ADDITIONAL MAPPING

This section summarizes the information on the structures mapped from the study area; Nyankanga Cut & Eastern pit wall and the Brazilian tensile strength test results done at the University of Alberta, Rock Mechanics Lab.

Table A8-1: Pit wall mapping data

SN	Easting	Northing	Elevation	Dip	Dip Direction	Size	Type	Section
1	50440.91	10621.13	920.00	30.7	239.7	10	Joint	135
2	50482.98	10637.59	923.22	82.0	243.0	2	Joint	13
3	50478.83	10637.69	920.00	69.5	325.0	10	Joint	100
4	50478.56	10638.30	920.00	65.2	311.7	10	Joint	100
5	50481.82	10639.52	922.78	90.0	58.9	0	Joint	13
6	50481.80	10639.63	921.82	58.0	321.2	3	Joint	13
7	50481.57	10640.28	922.71	43.0	306.9	3	Joint	13
8	50477.39	10640.44	920.00	65.2	321.4	17	Joint	100
9	50480.58	10641.50	922.40	77.0	129.7	3	Joint	13
10	50480.20	10642.13	922.26	62.0	141.0	3	Joint	13
11	50479.74	10643.33	923.71	30.0	318.3	4	Joint	13
12	50479.71	10643.46	922.93	21.0	243.0	3	Joint	13
13	50478.94	10644.19	922.16	49.0	136.5	3	Joint	13
14	50478.24	10645.61	921.87	54.0	316.6	3	Joint	13
15	50477.91	10645.65	920.86	58.0	180.4	3	Joint	13
16	50472.10	10648.86	920.00	66.0	348.0	3	Joint	100
17	50468.52	10654.23	920.00	68.0	172.0	3	Joint	100
18	50470.95	10656.48	921.64	55.0	280.0	10	Joint	11
19	50470.66	10656.89	926.36	82.0	170.0	10	Joint	11
20	50470.21	10657.54	924.87	38.0	300.0	10	Joint	11
21	50470.04	10657.79	922.08	47.0	320.0	10	Joint	11
22	50469.95	10657.92	925.59	17.0	335.0	10	Joint	11
23	50469.34	10658.80	924.68	20.0	350.0	10	Joint	11
24	50469.05	10659.22	925.38	20.0	350.0	10	Joint	11
25	50467.97	10660.79	925.47	75.0	120.0	10	Joint	11
26	50467.46	10661.52	924.86	63.0	170.0	10	Joint	11
27	50462.66	10662.87	920.00	79.5	70.4	4	Joint	100

28	50466.47	10662.94	924.85	42.0	145.0	10	Joint	11
29	50408.47	10664.41	920.00	83.9	255.0	7	Joint	100
30	50464.94	10665.16	925.57	45.0	270.0	10	Joint	11
31	50461.04	10665.36	920.00	55.4	226.1	5	Joint	100
32	50464.21	10666.21	925.24	51.0	145.0	10	Joint	11
33	50458.99	10668.38	920.00	85.8	68.6	6	Joint	100
34	50405.20	10668.82	920.00	46.1	221.2	9	Joint	100
35	50457.17	10671.00	920.00	72.6	81.4	7	Joint	100
36	50460.33	10673.77	921.73	70.0	340.0	10	Joint	9
37	50460.32	10673.79	921.55	17.0	345.0	10	Joint	9
38	50460.20	10673.95	923.14	61.0	156.0	10	Joint	9
39	50460.08	10674.10	921.94	47.0	340.0	10	Joint	9
40	50459.83	10674.43	923.43	47.0	330.0	10	Joint	9
41	50459.56	10674.79	921.52	84.0	340.0	10	Joint	9
42	50459.47	10674.91	924.18	86.0	340.0	10	Joint	9
43	50459.47	10674.91	922.16	52.0	335.0	10	Joint	9
44	50459.41	10674.99	924.90	18.0	140.0	10	Joint	9
45	50459.34	10675.09	923.84	30.0	350.0	10	Joint	9
46	50459.27	10675.17	924.24	30.0	350.0	10	Joint	9
47	50459.21	10675.25	924.17	35.0	350.0	10	Joint	9
48	50459.18	10675.28	923.67	40.0	350.0	10	Joint	9
49	50459.18	10675.29	923.93	33.0	350.0	10	Joint	9
50	50459.18	10675.29	924.41	35.0	350.0	10	Joint	9
51	50459.05	10675.47	924.40	30.0	350.0	10	Joint	9
52	50458.84	10675.74	925.00	88.0	135.0	10	Joint	9
53	50458.50	10676.19	923.23	65.0	100.0	10	Joint	9
54	50458.41	10676.30	923.89	35.0	350.0	10	Joint	9
55	50458.21	10676.57	923.52	65.0	100.0	10	Joint	9
56	50458.03	10676.81	923.79	35.0	210.0	10	Joint	9
57	50457.45	10677.56	923.11	85.0	170.0	10	Joint	9
58	50397.91	10678.38	920.00	46.4	222.2	7	Joint	100
59	50455.90	10679.61	921.05	84.0	164.0	10	Joint	9
60	50455.20	10679.78	920.99	34.0	336.5	4	Joint	7
61	50450.42	10679.83	920.00	19.0	8.0	4	Joint	100
62	50455.58	10680.02	922.73	29.0	140.0	10	Joint	9
63	50454.79	10680.04	922.64	21.0	143.0	10	Joint	7
64	50449.95	10680.38	920.00	76.6	300.6	5	Joint	100
65	50454.43	10680.50	923.24	86.0	143.0	10	Joint	7
66	50453.75	10681.39	923.31	63.0	323.0	10	Joint	7
67	50453.65	10681.52	921.45	17.0	323.0	10	Joint	7
68	50448.92	10681.58	920.00	84.0	164.0	8	Joint	100

69	50453.60	10681.58	920.74	6.0	323.0	10	Joint	7
70	50448.49	10682.11	920.00	73.2	301.6	5	Joint	100
71	50452.93	10682.46	921.37	87.0	340.0	10	Joint	7
72	50452.42	10683.12	923.07	89.0	142.0	10	Joint	7
73	50451.19	10684.72	924.06	73.0	323.0	10	Joint	7
74	50445.83	10685.19	920.00	64.4	283.5	3	Joint	100
75	50390.06	10688.13	920.00	47.2	240.7	4	Joint	100
76	50442.30	10689.26	920.00	57.1	295.3	4	Joint	100
77	50388.40	10690.04	920.00	88.4	263.6	14	Joint	100
78	50440.46	10691.35	920.00	34.0	339.0	2	Joint	100
79	50436.85	10695.60	920.00	51.9	201.1	7	Joint	100
80	50435.66	10696.81	920.00	54.2	188.7	5	Joint	100
81	50433.30	10699.58	920.00	57.9	206.4	4	Joint	100
82	50434.05	10706.34	929.78	62.0	298.1	4	Joint	135
83	50433.55	10706.73	923.50	62.0	347.1	3	Joint	135
84	50433.01	10707.16	925.33	42.0	110.3	2	Joint	135
85	50432.80	10707.37	925.60	35.0	123.0	3	Joint	135
86	50433.00	10707.41	923.26	59.0	341.2	3	Joint	135
87	50432.47	10707.78	925.35	42.0	110.3	3	Joint	135
88	50432.28	10707.97	924.91	42.0	106.0	3	Joint	135
89	50432.29	10707.99	925.25	42.0	105.6	3	Joint	135
90	50431.98	10708.61	923.82	48.0	311.5	3	Joint	135
91	50431.30	10708.98	925.05	69.0	87.7	4	Joint	135
92	50431.82	10709.18	925.09	58.0	275.8	4	Joint	135
93	50431.13	10709.30	924.21	69.0	86.9	3	Joint	135
94	50430.32	10710.25	923.71	52.0	99.9	3	Joint	135
95	50430.59	10710.38	924.86	62.0	293.3	3	Joint	135
96	50430.63	10710.49	926.16	58.0	290.4	4	Joint	135
97	50430.07	10710.58	923.34	40.0	125.0	3	Joint	135
98	50430.18	10710.60	922.78	52.0	131.9	3	Joint	135
99	50429.76	10710.99	925.25	41.0	120.7	3	Joint	135
100	50429.85	10711.13	926.74	62.0	307.4	3	Joint	135
101	50429.47	10711.37	922.66	55.0	128.8	2	Joint	135
102	50429.53	10711.40	924.88	66.0	129.7	2	Joint	135
103	50429.42	10711.60	921.51	58.0	325.2	3	Joint	135
104	50428.97	10712.00	926.93	45.0	132.4	3	Joint	135
105	50428.85	10712.09	926.04	45.0	119.4	3	Joint	135
106	50428.70	10712.21	924.23	47.0	117.8	3	Joint	135
107	50428.73	10712.24	922.03	80.0	191.6	5	Joint	135
108	50428.24	10712.89	925.72	59.0	121.9	3	Joint	135
109	50428.43	10712.92	921.79	80.0	21.6	6	Joint	135

110	50427.87	10713.51	926.12	79.0	299.8	4	Joint	135
111	50427.89	10713.52	922.01	80.0	20.9	5	Joint	135
112	50428.42	10713.53	923.07	45.0	353.8	7	Joint	135
113	50426.73	10714.75	921.45	89.0	107.2	3	Joint	135
114	50383.54	10715.23	920.00	53.6	237.3	4	Joint	100
115	50425.87	10715.29	922.90	2.0	185.0	5	Joint	135
116	50426.28	10715.37	923.72	69.0	314.0	4	Joint	135
117	50426.28	10715.43	922.73	67.0	306.5	4	Joint	135
118	50384.47	10715.77	920.00	47.0	228.4	3	Joint	100
119	50426.06	10715.98	929.95	72.0	277.0	5	Joint	135
120	50425.76	10716.03	923.17	60.0	325.8	7	Joint	135
121	50425.35	10716.56	923.32	64.0	305.8	4	Joint	135
122	50424.47	10716.72	920.78	65.0	202.5	7	Joint	135
123	50425.01	10716.78	924.07	85.0	120.6	3	Joint	135
124	50424.70	10717.27	922.88	64.0	306.7	3	Joint	135
125	50424.40	10717.52	927.41	89.0	98.2	5	Joint	135
126	50416.17	10717.63	920.00	78.0	127.0	2	Joint	100
127	50423.03	10719.26	925.19	88.0	233.9	14	Joint	135
128	50422.89	10719.40	921.27	65.0	306.0	5	Joint	135
129	50422.76	10719.74	922.81	67.0	292.2	4	Joint	135
130	50413.53	10720.37	920.00	58.0	122.0	2	Joint	100
131	50422.57	10720.41	924.10	65.0	263.2	13	Joint	135
132	50412.98	10720.93	920.00	66.4	162.9	3	Joint	100
133	50411.43	10722.64	920.00	72.3	158.5	3	Joint	100
134	50410.47	10723.63	920.00	25.0	338.0	9	Joint	100
135	50409.70	10724.51	920.00	74.9	170.4	3	Joint	100
136	50407.54	10726.70	920.00	79.4	172.2	3	Joint	100

APPENDIX B

FURTHER INSIGHT TO ROCK FRACTURING MECHANISMS

Several tests were conducted at the University of Alberta, Rock Mechanics Lab, and in the field to get insight into fracture mechanism, failure modes, and the effect of loading rate on the peak load. For this purpose, rock strength tests such as the Brazilian tensile strength test, the drop weight impact test, and the point load strength index tests were conducted on various rock types.

8.1 Brazilian tensile strength tests

The Brazilian tensile strength tests (splitting tensile strength tests) were conducted on limestone and sandstone using ELE Digital Tritest 50 of 50 kN capacity with spherical loading platens. The equipment setup is shown in Figure B8-1. The spherical loaded Brazilian load-displacement/time curves are classified into three regions; initial compression section (I), elastic loading (II), and post-peak deformation section(III) (Gong et al., 2019). A sample curve for limestone is shown in Figure B8-2. Spherical loading is believed to cause local compression which restricts crack propagation during the loading process and hence higher vertical forces. This results in higher tensile strength as compared to the direct tensile strength method (Gong et al., 2019). Along with the main crack, secondary cracks are formed during the post-peak stage forming multiple central fractures.

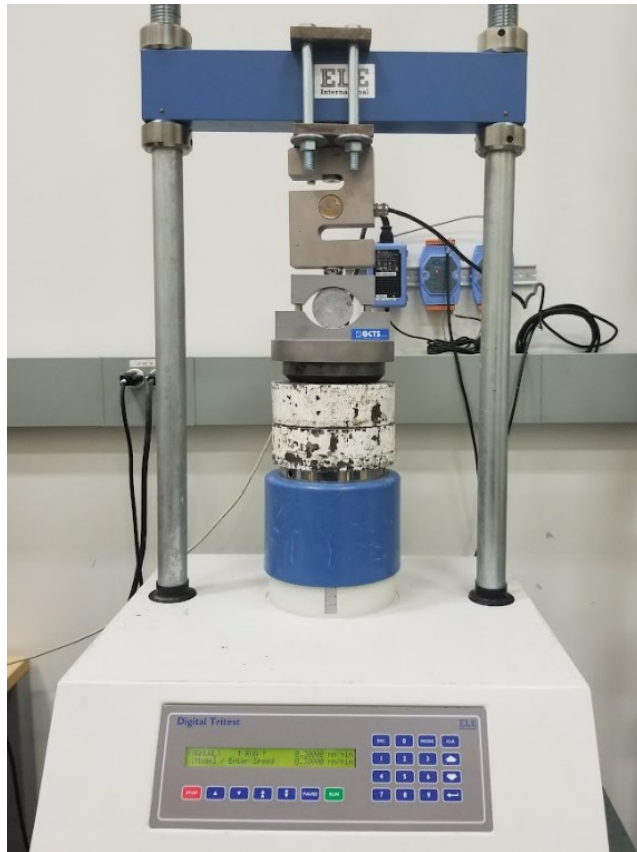


Figure B8-1: Brazilian test setup

As indicated by ASTM standards, samples of around 50 mm diameter and 25 mm thickness were used in this case. Tests were conducted with loading rates varied from 0.015, 0.03 0.05, 0.15, 0.3, to 0.5mm/min. A total of 16 samples of limestone and 13 samples of sandstone were tested. The average tensile strength of limestone is 12.61 ± 2.33 MPa and for sandstone is 9.10 ± 2.1 MPa. Figure B8-3 and Figure B8-4 presents the plots of tensile strength against loading rate. From the plots, it is clear that at lower loading rates which in this case is less than 0.01 s^{-1} the tensile strength is almost constant.

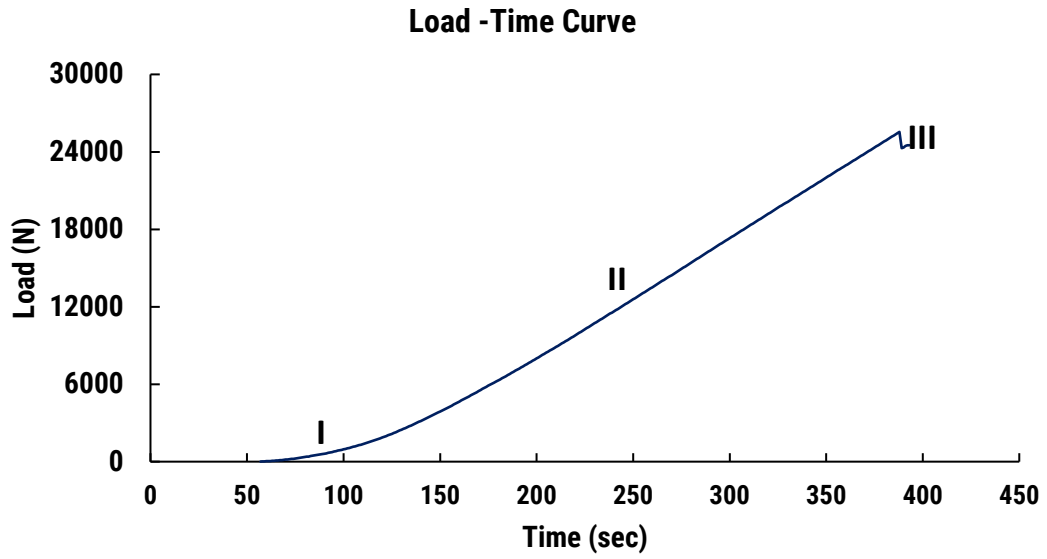


Figure B8-2: Brazilian test load-time curve

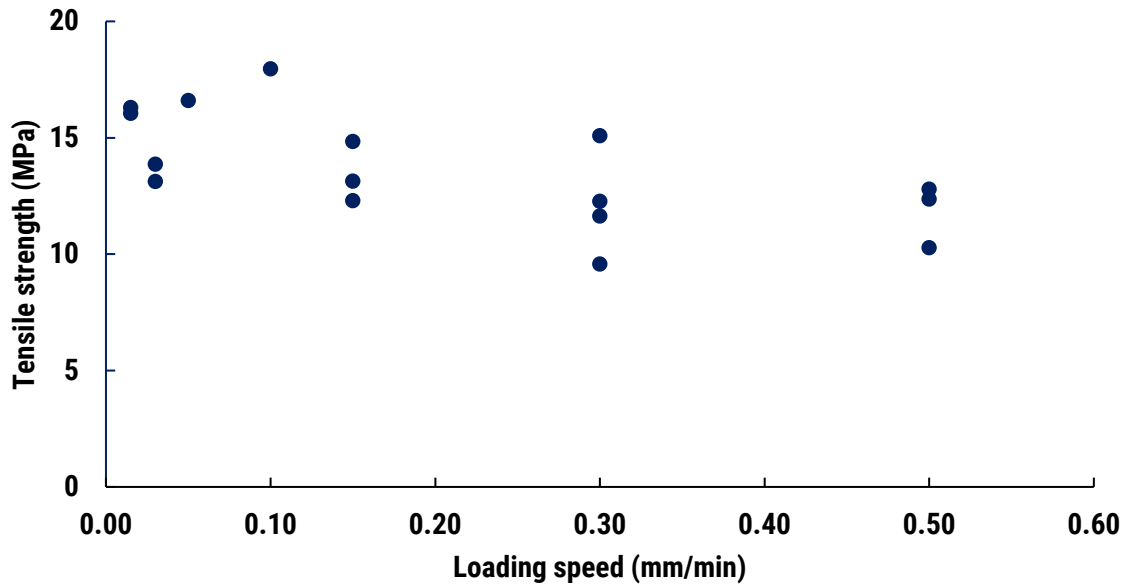


Figure B8-3: Limestone tensile strength vs. loading speed

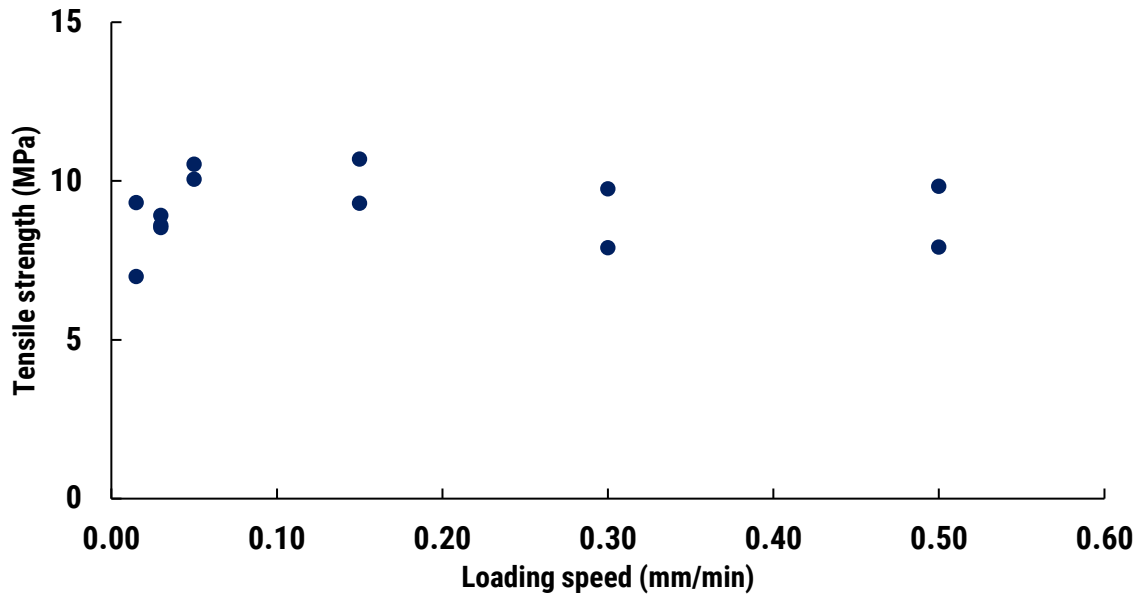


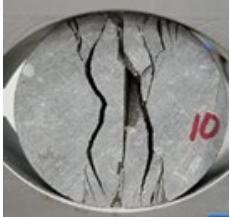
Figure B8-4 Sandstone tensile strength vs. loading speed

Four major fracture modes were observed; central fracture, multiple central fractures, non-central fracture, and layer activation. Central fracture, if it is not associated with structures is the tensile strength of the rock. This type of failure is observed more often in less strong rocks. In the tests conducted, all sandstone samples had central fractures. Central multiple structure is the dominant failure mode in high tensile strength rock where multiple fractures are developed to release stored strain energy. This was observed mostly in the limestone samples.

The other two failure modes were not common but could also be observed from the tests. Non-central fractures were observed on the limestone. Non-central fractures occur as curved lines starting from or around loading platens when the sample fails under high tensile strength. Layer activation occurs when structures are parallel or near parallel to the loading direction. The fracture process uses them because of their weaker mechanical properties of the intact rock and the obtained strength corresponds to the tensile strength of the layer. When the layer is perpendicular

to the loading direction, tensile strength obtained is the strength of intact material. Table B8-2 shows the summary of the failure modes in limestone. The detailed test results are presented in Table B8-4 to Table B8-7.

Table B8-2: Brazilian test failure modes

Failure type	Central fracture failure	Central-multiple fractures failure	Non-Central fracture failure	Layer activation failure
Tensile strength (MPa)	11.32	13.91	12.27	9.57
Images after failure				

8.2 Drop weight test

The drop weight test is an experiment developed to assess breakage characteristics of rock material required for AG/SAG mills and crushers (Napier-Munn, 1996). It is also used to determine the influence of the energy levels on particle size in crushing or blasting. The test operates under the concept that product size distribution is a function of the applied comminution energy. Drop weight tests operate under strain rates ranging from 1s^{-1} to 10s^{-1} . In this range, strain rate effects become considerable although the magnitude can be small and in some cases unsubstantial. This test was performed to estimate energy absorbed by the sample when breaking and determine particle size distribution as a function of energy applied.

Samples were prepared from a 1-inch diameter limestone core cut to a disc of half the diameter thickness. The impacting mechanism for the drop weight test is a weight dropped by gravity on a striker placed on the specimen. A tube is used to guide the falling mass. The load and drop height weight provide a range of impact velocities and energy capacities for impact tests. The energy

absorbed by the test specimen is equal to the impact energy required to fracture the specimen. ASTM rock toughness tester was used in this experiment, with a drop weight (2004 g) falling free by gravity impacting the striker (1008.4 g) placed on the specimen. The test setup is shown in Figure B8-5.



Figure B8-5: Drop weight test setup

Eight (8) samples are tested, varying dropping height from 5cm to 80cm. Each sample's weight (m) and thickness (t) were measured. As the mass falls from initial height h_i to final height h_f the decrease in potential energy is the energy absorbed to create fracture and can be calculated from equation (B1). Table B8-3 shows the results.

$$PE = mg(h_i - h_f) \quad (B1)$$

Table B8-3: Drop weight test results

Sample	Weight (g)	Thickness (mm)	Drop height (cm)	Potential Energy (J)	Specific energy (kWh/t)	Sample after crushing
1	14	11.53	80	15.73	0.285	
2	13.9	11.43	40	7.86	0.156	
3	14	11.51	30	5.90	0.117	
4	14.2	11.69	20	3.93	0.077	
5	14	11.57	10	1.97	0.039	
6	14.5	11.83	5	0.98	0.019	
7	14.3	11.71	5	0.98	0.019	
8	14.9	11.87	5	0.98	0.018	

The crushed samples were collected and sieved for particle size analysis. The results of the sieved samples have slightly less weight than the original samples which can be due to samples being thrown out during impact or errors in the weighing balance. Cumulative weight was calculated for each sample and t_{10} was obtained which is the percentage passing 1/10th of the original sample

size. For the sample of 23.93 mm, t_{10} is between 3.35mm and 2 mm sieves; an interpolation was done to obtain the value. When t_{10} was compared to specific energy input, it was observed that the amount of smaller fragments increased with an increase in specific energy. Figure B8-6 shows the relationship between specific energy and t_{10} obtained for the samples tested.

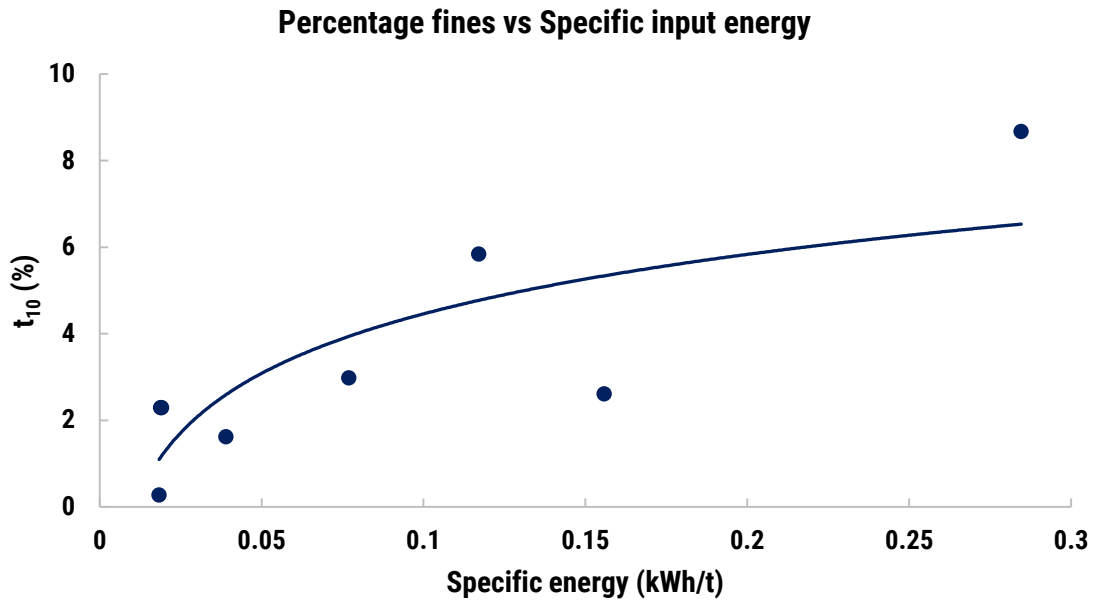


Figure B8-6: Percentage of fines vs fracturing energy

Further analysis into the fragmentation distribution with the variable fracturing energy shows that limestone fractures at a specific energy of 0.019kWh/t. The increase in specific energy increases the production of smaller fragments resulting in a fragmentation distribution curve curving more towards the right-hand side as seen in Figure B8-7; the legend is the specific energy in kWh/t.

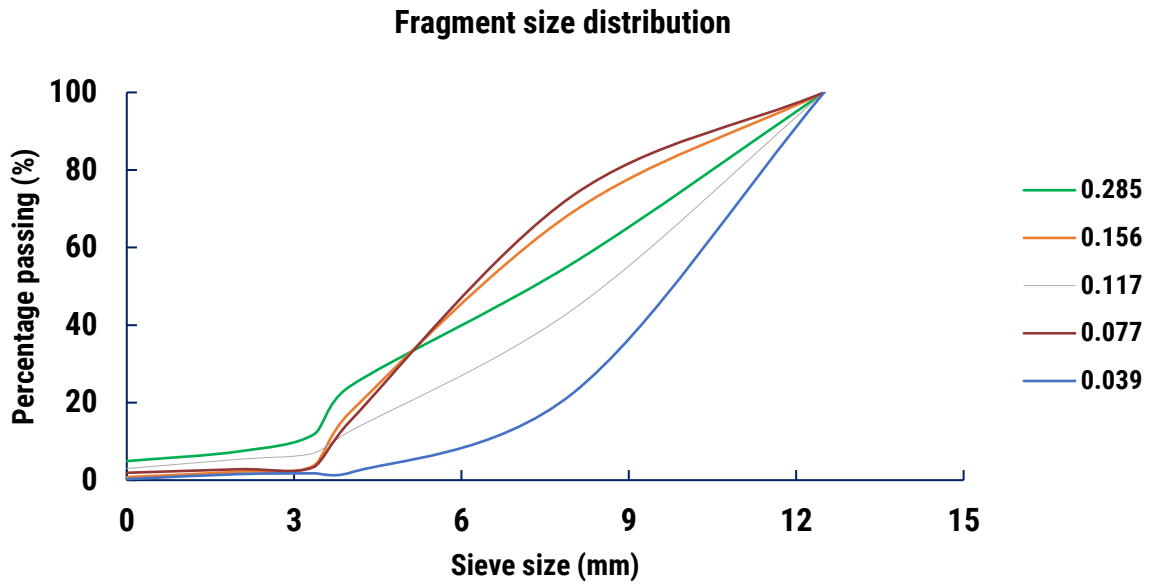


Figure B8-7: Fragmentation size distribution from the drop weight impact test

Table B8-4: Brazilian tests on limestone (1-8)

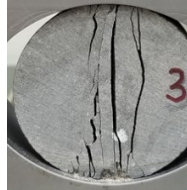
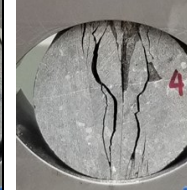
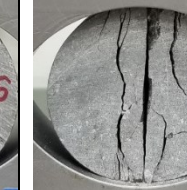
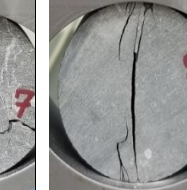
Limestone tests	Sample 1	Sample2	Sample 3	Sample 4	Sample 5	Sample 6	Sample 7	Sample 8
Loading speed (mm/min)	0.15	0.50	0.30	0.15	0.50	0.30	0.15	0.50
Maximum load (KN)	25.54	20.21	28.76	28.76	26.01	24.22	24.77	25.07
Breaking time (sec)	328	228	306	309	302	281	293	267
Loading ratio (N/s)	77.88	88.64	93.98	93.07	86.12	86.21	84.53	93.89
Sample thickness (mm)	24.78	25.04	24.27	24.68	25.90	25.15	25.65	25.83
Tensile Strength (MPa)	13.13	10.28	15.09	14.84	12.79	12.27	12.30	12.36
Fracture mode	Central multiple	Central	Central multiple	Central multiple	Central multiple	Non-central, curved line	Central multiple	Central
Strain rate (s ⁻¹)	5.00E-05	1.67E-04	1.00E-04	5.00E-05	1.67E-04	1.00E-04	5.00E-05	1.67E-04
Sample images after the test								

Table B8-5: Brazilian tests on limestone (9-16)

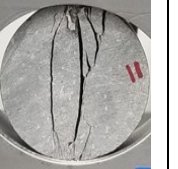
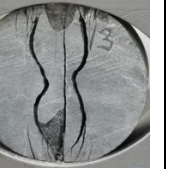
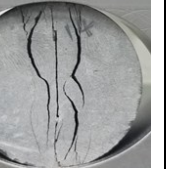
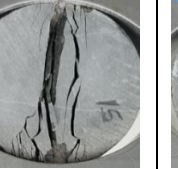
Limestone tests	Sample 9	Sample 10	Sample 11	Sample 12	Sample 13	Sample 14	Sample 15	Sample 16
Loading speed (mm/min)	0.30	0.10	0.3	0.015	0.015	0.03	0.03	0.05
Maximum load (KN)	19.30	35.07	22.35	31.47	32.46	26.13	27.62	32.60
Breaking time (sec)	354	354	265	325	344	344	335	383
Loading ratio (N/s)	54.53	99.06	84.34	96.83	94.36	75.97	82.44	85.12
Sample thickness (mm)	25.69	24.87	24.46	24.97	25.37	25.36	25.37	25.01
Tensile Strength (MPa)	9.57	17.96	11.64	16.06	16.30	13.13	13.87	16.61
Fracture mode	Layer activation	Central multiple	Central multiple	Central multiple	Central multiple	Central multiple	Central multiple	Central multiple
Strain rate (s ⁻¹)	1.00E-04	3.33E-05	1.00E-04	5.00E-06	5.00E-06	1.00E-05	1.00E-05	1.67E-05
Sample images after the test								

Table B8-6: Brazilian tests on Sandstone (1-7)

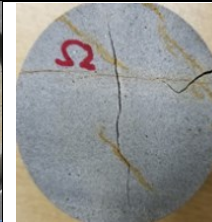
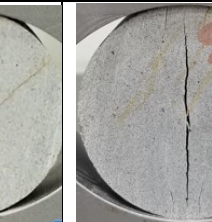
Sandstone tests	Sample 1	Sample2	Sample 3	Sample 4	Sample 5	Sample 6	Sample 7
Loading speed (mm/min)	0.50	0.30	0.15	0.05	0.03	0.015	0.50
Maximum load (KN)	15.68	15.81	21.22	20.14	17.23	15.31	19.53
Breaking time (sec)	215	222	268	264	232	238	272
Loading ratio (N/s)	72.91	71.23	79.19	76.29	74.25	64.32	71.82
Sample thickness (mm)	25.2	25.5	25.3	25.5	25.7	27.9	25.3
Tensile Strength (MPa)	7.92	7.90	10.69	10.06	8.54	7.00	9.84
Fracture mode	Central	Central	Central	Central	Central	Central	Central
Strain rate (s ⁻¹)	1.67E-04	1.00E-04	5.00E-05	1.67E-05	1.00E-05	5.00E-06	1.67E-04
Sample images after the test							

Table B8-7: Brazilian tests on sandstone (8-13)

Sandstone tests	Sample 8	Sample 9	Sample 10	Sample 11	Sample 12	Sample 13
Loading speed (mm/min)	0.30	0.15	0.05	0.03	0.03	0.015
Maximum load (KN)	19.97	18.91	21.49	18.75	19.60	20.48
Breaking time (sec)	282	271	292	261	281	276
Loading ratio (N/s)	70.83	69.78	73.59	71.85	69.76	74.21
Sample thickness (mm)	26.1	25.9	26.0	27.8	28.0	28.0
Tensile Strength (MPa)	9.75	9.30	10.52	8.60	8.91	9.32
Fracture mode	Central	Central	Central	layer activation	Central	Central
Strain rate (s ⁻¹)	1.00E-04	5.00E-05	1.67E-05	1.00E-05	1.00E-05	5.00E-06
Sample images after the test						

APPENDIX C

POWDER FACTOR AND BOREHOLE PRESSURE ESTIMATION

This section summarizes the calculations to estimate powder factor and borehole pressure as stipulated in section 6.2.

C1. POWDER FACTOR ESTIMATION

As discussed in section 5.6.3, the powder factor is estimated from the rock properties and explosive energy after deciding on the size of the fragmentation. For the hard rock, the size of the crushed zone formed is 0.3 m maximum with the fracture zone covering the rest. The crushed zone fragments are formed when the shock wave exceeds the dynamic compressive strength of the rock and the fracture zone from the dynamic tensile strength. Data required to estimate fracture toughness in both regions are presented in Table C8-8. The powder factor is estimated to achieve a 5 mm fragment size in the crushed zone and a 200 mm fragment size in the fracture zone. The estimation is done for the B x S x BH dimensions of 5.5 m x 6.5 m x 10 m. Table C8-9 presents the summary of calculations to estimate the powder factor.

Table C8-8: Powder factor estimation parameters

K_{1csc} (MPam ^{0.5})	K_{1cst} (MPam ^{0.5})	σ_{cd} (MPa)	σ_{td} (MPa)	K_{1cdc} (MPam ^{0.5})	K_{1cdt} (MPam ^{0.5})
1.46	1.79	310.51	27.17	2.57	3.18
E_d (GPa)	VOD (m/s)	ρ_e (kg/m ³)	ρ_r (kg/m ³)	V_p (m/s)	
122.73	4789.125	1207.75	2680	4369	

Table C8-9: Powder factor estimation

Geometric dimensions		
Parameter	Value	Units
rock volume per blasthole	5.5 x 6.5 x 10	(m)
Crushed zone	0.3 x 0.3 x 10	(m)
Fracture zone	the rest	
Initial surface area total	311.5	m²
Surface area calculations for the crushed zone		
Initial crushed surface area	12.18	m ²
Initial crushed volume	0.9	m ³
Crushed zone fragment size	0.005	m
volume of each fragment	0.000000125	m ³
Number of fragments	7,200,000	
New surface area of each fragment	0.0001875	m ²
Total of the new surface area	1,350	m²
Surface area calculations for the fractured zone		
Initial fracture area	299.32	m ²
Initial fracture volume	356.6	m ³
Fractured zone fragment size	0.2	m
Volume of each fragment	0.008	m ³
Number of fragments	44,575	
New surface area of each fragment	0.24	m ²
New surface fracture zone	10,698	m²
Fracture energy requirements		
Crushed zone	36,276.86	J/m ³
Fractured zone	438,877.53	J/m ³
Total energy	475,154.39	J/m ³
Powder factor estimation		
rock impedance	11,708,920	kg/m ² s
Explosive impedance	5,784,066	kg/m ² s
Energy transfer coefficient	0.89	
Fracture energy efficiency	0.18	
Total energy	3.98	MJ/kg
Powder factor	0.76	kg/m³

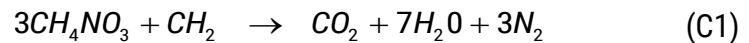
C2: BOREHOLE PRESSURE ESTIMATION

Borehole pressure can be estimated from the heat of explosion which is obtained from the difference between the heat of formation of the products to the heat of breakdown of elements after detonation. The information in section 2.3.2 and equations 2.1 to 2.5 will be used in this section to estimate the borehole pressure produced from the detonation of ANFO. The inference of the borehole pressure produced from emulsion detonation will also be made using BWD. The heat of the formation of ANFO compounds is as shown in Table C8-10, (Hustrulid, 1999).

Table C8-10: Heat of formation of ANFO

Compound	Chemical Formula	Molecular weight (g)	Number of moles	Heat of formation (kCal/mole)
Ammonium Nitrate	HNO ₄ O ₃	80	3	-87.3
Fuel Oil	CH ₂	14	1	-7
Carbon dioxide	CO ₂	44	1	-94.1
Water	H ₂ O	18	7	-57.8
Nitrogen gas	N ₂	28	3	0

A chemical reaction in explosive detonation is used to calculate the energy released using equation (C1). For standard ANFO explosives with the composition of 94.5% Ammonium nitrate and 5.5% Fuel oil (CH₂), the chemical reaction is presented as follows;



The heat of formation of reactants

$$3(-87.3) + (-7) = -268.9 \text{ kCal/ mole} \quad (C2)$$

The heat of the formation of products

$$(-94.1) + 7(-57.8) + 0 = -498.6 \text{ kCal/ mole} \quad (C3)$$

From the equation (C2) and (C3) heat of the explosion, Q_E is -229.7 kCal/mole which is equivalent to -903.3 kCal/kg. Standard ANFO has a density of 0.8 g/cm³ and an effective energy of 2.30 MJ/kg making the initial volume occupied by one kilogram of gases 1.25 litres. The number of moles of gaseous products per kilogram of ANFO is derived as shown in Table C8-11 with the molar heat capacities obtained from Cook (1958). The linear relationship between the heat of explosion (Q_E) and final explosion temperature (T_E) is plotted in Figure C8-8 and for $Q_E = 904.3$ kCal/kg T_E is obtained to be 2789.5 °K. Gas pressure from the explosive reaction is calculated from Equation (2.5) to be 803.96 MPa.

Table C8-11: Ideal Molar Heat Capacities

Gases		CO ₂	H ₂ O	N ₂	Q_E (kCal/kg)
Temperatures (°K)	2500	11.293	8.656	6.082	780.66
	2750	11.456	8.862	6.155	886.97
	3000	11.600	9.045	6.219	994.66
Number of moles per kg		3.94	27.56	11.81	-

The velocity of detonation of standard ANFO is estimated using the thermodynamic formulae by Hustrulid (1999) to be 4529 m/s, making the detonation pressure 4102.36 MPa from equation (2.6). Therefore, the ratio of gas pressure to detonation pressure is estimated to be 19.6%.

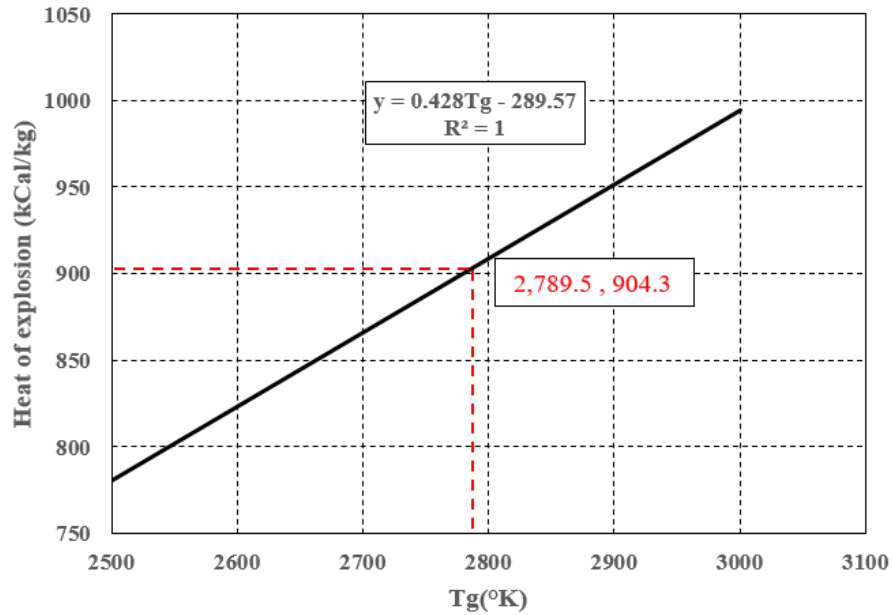


Figure C8-8: The plot of the heat of explosion vs temperature

Relative bulk effective energy (REE) is the effective energy of an explosive compared to the effective energy of an equal volume of standard ANFO and can be estimated from the relative weight strength (RWS) using Equation (C4). For the density of 1.207 g/cm³ of Fortis Extra used, the REE and explosive bulk energy (BE) are interpolated as presented in Table C8-12. Using REE to estimate borehole pressure from Fortis Extra from the borehole pressure produced by ANFO, it is obtained as 1,415 MPa which is 20% of the detonation pressure.

$$REE = RWS \times \frac{\rho_e}{\rho_{ANFO}}, \quad BE_e = REE \times BE_{ANFO} \quad (C4)$$

Table C8-12: Explosive bulk energy

Explosive density (g/cm ³)	Relative weight strength, RWS (%)	Relative bulk energy, REE (%)	Bulk energy, BE (MJ/kg)
1.1	1.1	1.51	3.48
1.25	1.21	1.89	4.35
1.207	1.17	1.76	3.98